Numerical Modelling of
Vehicle Loads on Buried Orthotropic Steel Shell Structures

by

Luke MacDonald

Submitted in partial fulfilment of the requirements
for the degree of Master of Applied Science

at

Dalhousie University
Halifax, Nova Scotia
October 2010

DALHOUSIE UNIVERSITY

DEPARTMENT OF CIVIL AND RESOURCE ENGINEERING

The undersigned hereby certify that they have read and recommend to the Faculty of Graduate Studies for acceptance a thesis entitled “Numerical Modelling of Vehicle Loads on Buried Orthotropic Steel Shell Structures” by Luke MacDonald in partial fulfillment of the requirements for the degree of Master of Applied Science.

Dated: October 18, 2010

Supervisor: _____

Readers: _____

_____

DALHOUSIE UNIVERSITY

DATE: October 18, 2010

AUTHOR: Luke MacDonald

TITLE: Numerical Modelling of Vehicle Loads on Buried Orthotropic Steel Shell Structures

DEPARTMENT OR SCHOOL: Department of Civil and Resource Engineering

DEGREE: MASc CONVOCATION: May YEAR: 2011

Permission is herewith granted to Dalhousie University to circulate and to have copied for non-commercial purposes, at its discretion, the above title upon the request of individuals or institutions.

_____

Signature of Author

TABLE OF CONTENTS

LIST OF TABLES

LIST OF FIGURES

ABSTRACT

An investigation was performed for live load forces applied to soil-steel structures under shallow backfill depths, specifically a long span deeply corrugated box culvert. The work was also relevant to other types of flexible buried structures and loading scenarios. The investigation involved the application of both a robust experimental testing process and the development of 3-D finite element models. Full scale live load tests, performed in Dorchester NB, were executed to obtain a large sample of experimental data. The testing program was designed specifically to fully characterize the structural response of a long span box culvert to CHBDC design truck live loads. The program included live load testing at six different backfill depths with 21 unique truck positions per lift, with instrumentation at four separate rings. The experimental data was used to assess and calibrate the finite element models being developed to predict structural effects. The finite element software package ADINA was used to model the test structure in 3-D. The basics of model development, such as element types, boundary conditions, loads, and other analysis options were discussed. An orthotropic shell modeling approach to accurately describe the corrugated plate properties was developed. A number of soil constitutive models, both linear and nonlinear, were examined and evaluated. The data obtained from experimental testing was compared to the results obtained by the finite element modeling and the various soil models were evaluated. A parametric study was performed examining the sensitivity of modeling parameters. The impact of various assumptions made regarding the model was quantitatively established. The thesis provided guidance on the 3-D modeling of soil-steel structures allowing future researchers to study the factors which were significant to their design and field applications.

LIST OF ABBREVIATIONS AND SYMBOLS

A	Area of plate (mm2/mm)
A_A, A_B, A_{AB}	Axial stiffness of panel
A_{actual}	Area of tire footprint
A_{model}	Area of tire footprint used in FEM model
B	Bulk Modulus
B_A, B_B, B_{AB}	Bending stiffness of panel
B_i	Initial bulk modulus (MPa)
B_t	Tangent bulk modulus (MPa)
c	Chord distance of one half wave of corrugation (mm)
C	Cohesion intercept (MPa)
CHBDC	Canadian Highway Bridge Design Code
d	Depth from top of soil mass to layer of interest (mm)
E	Modulus of elasticity (MPa)
E_i	Initial modulus based on confining stress (MPa)
E_o	Modulus at the ground surface
E_t	Tangent modulus (MPa)
Ex	Young's Modulus in the x direction (MPa)
f	half depth of corrugation (mm)
F_A	Axial thrust (KN/m)
F_B	Bending moment (KN-m/m)
Fy	Steel Yield Strength (MPa)
G_{ij}	Shear modulus in the ij direction (MPa)
H	Depth from the surface to the crown of structure (mm) or Total section depth (mm)
I	Moment of inertia of plate (mm4/mm)
K	Dimensionless magnitude of Young's Modulus

K_B	Bulk modulus number
K_{LA}	Spring constant for axial compression (MPa)
K_{LB}	Spring constant for bending (MPa)
kN	Kilonewtons
L	Circumferential length of one half wave (mm)
m	Bulk modulus exponent or Modulus gradient
MPa	Megapascals
n	Power Law Coefficient
NCHRP	National Cooperative Highway Research Program
OHBDC	Ontario Highway Bridge Design Code
p	Radial pressure (kPa)
P_a	Atmospheric pressure
P_{actual}	Pressure of actual tire footprint
P_H	Pressure at the crown due to an applied patch load
P_{model}	Pressure load used in FEM model
P_P	Pressure of the applied patch load
P_s	Pressure at the crown of the structure due to an applied strip load
P_p	Pressure at the crown due to an applied patch load
R	Radius of curvature of plate (m)
r	Live load reduction factor
R_f	Ratio of soil failure stress to ultimate stress
S	Section Modulus (mm3/m)
t	Section thickness (mm)
T	Thrust in the conduit wall (kN/m)
$\bar{t}$	Equivalent shell thickness (mm)
W	Width of the applied patch load (mm)
$\bar{y}$	Centroid of section measured from the inner fiber (mm)

Z	Plastic Section Modulus (mm3/mm)
z	Depth below ground surface (m)
$\Delta\phi$	Reduction in friction angle for a ten-fold increase in confining stress (Degs)
ε_1	Measured strain from gauge 1 (με)
ε_2	Measured strain from gauge 2 (με)
ε_2'	Measured strain from gauge 2 extrapolated to the extreme fiber (με)
ε_u	Failure strain
θ	Longitudinal live load dispersion angle
ν_{ij}	Poisson's ratio in the ij direction
σ_1	Stress at extreme inner fiber or Vertical Stress (MPa)
σ_2	Stress at extreme outer fiber (MPa)
σ_3	Triaxial confining stress or Horizontal Stress (MPa)
σ_A	Component of section stress from axial compression (MPa)
σ_m	Mean stress - $(\sigma_1 + \sigma_3)/2$ (MPa)
$\phi_\circ$	Initial soil friction angle (Degs)
γ	Unit weight of soil (N/mm^3)
ϕ	Soil friction angle (Degs)

ACKNOWLEDGEMENTS

I would like to acknowledge NSERC and AIL for providing funding for this research, my supervisor Dr. Newhook, and my friends and family for all of their support.

CHAPTER 1 - INTRODUCTION

1.1 GENERAL

Corrugated soil-steel bridges are unique structures used for a variety of purposes including culverts, highway overpasses, service tunnels, and utility conduits. Structural plate corrugated steel products, (SPCSP), are a specific type of corrugated steel product. This type of structure is constructed from steel sheets that are manufactured into corrugated plates of various lengths and assembled on site. This results in large span structures which can be constructed using equipment which is much lighter than would be required for traditional bridge structures.

Such a crossing exhibits many benefits over more conventional bridges constructed from steel plate girders or pre-cast concrete beams. A primary advantage is material savings. The use of engineered backfill as a structural material allows the steel to carry significantly more load than if it were not buried. Another advantage is that construction time is usually shorter than for traditional bridges. Generally they contain little concrete, and construction can take place in almost all weather conditions. The lifetime costs of SPCSP structures are also extremely competitive. They require very little maintenance once constructed and can be quite durable. Galvanizing the plates before assembly can increase the lifespan of structures even further.

A great deal of flexibility is available to create a variety of structural geometries, including arches, (high profile, low profile, or semi-circular), box culverts, pipe-arches, as well as various circular and elliptical configurations. The structure being examined in this thesis is a box culvert. Box culverts are not particularly efficient structural shapes, as the tight radius at the haunches and long crown sections can produce large bending moments. In fact, axial thrust very rarely governs design, as it does with arches.

However their low profile and large end areas make them an attractive alternative for many applications where conventional bridges would normally be considered. No other corrugated steel product comes as close to mimicking traditional bridges, with nearly vertical sides and horizontal crown. In recent years, the maximum span for such structures has increased rapidly.

Despite the fact that corrugated steel structures have been available for many years their behavior is still not fully understood. The soil and steel interact to form a complex system which is not easily analyzed by analytical or simplified methods. Engineers traditionally dealt with this complexity through the use of high factors of safety. However, modern computing technologies have given engineers the ability to analyze structures with much greater accuracy and confidence. Finite element software is a valuable tool for engineers but naturally has its own limitations; the wide array of input options can be overwhelming and produce poor results when used by the inexperienced engineer. Specialized software packages, such as CANDE 2007, (Katona *et al.*), are available but typically use a 2-D plane-strain approach. These approaches cannot directly model 3-D phenomena such as vehicle live loads.

1.2 RESEARCH METHODOLOGY

The focus of the thesis involved the investigation of live load forces applied to soil-steel structures under shallow backfill depths, specifically a long span deeply corrugated box culvert. The work was also relevant to other types of flexible buried structures and loading scenarios. The investigation involved the application of both a robust experimental testing process and 3-D finite element modelling.

Full scale live load tests, performed in Dorchester NB, were executed to get a large sample of experimental data, as described in Chapter Chapter 4 -. The testing program

was designed specifically to fully characterize the structural effects of live loads. This was provided by performing live load tests at six different backfill depths with 21 unique truck positions per lift, and by instrumenting four separate rings. The data was presented in a variety of formats which examined the 3-D effects. The experimental data was also used throughout the thesis to gauge the ability of the finite element models to predict structural effects.

The subsequent section, Chapter Chapter 5 -, described the process of modelling the aforementioned long span box test in 3-D using the finite element software package ADINA. The basics of model development, such as element types, boundary conditions, loads, and other analysis options were discussed. The development of the orthotropic shell model to accurately describe the corrugated plate was discussed in some detail. A number of soil constitutive models, both linear and nonlinear, were examined and evaluated. The advantages and disadvantages of each were briefly examined.

Chapter Chapter 6 -, experimental validation, compared the various soil models to experimental data. The data was presented in plots designed to show the results both transversely and longitudinally. Standard plots were shown for all soil models while additional plots were displayed for the layered linear elastic model.

A parametric study was performed and was presented in Chapter Chapter 7 -, examining the effects of changing some of the parameters used in the analysis. The impact of various assumptions made regarding the model was quantitatively established, allowing future researchers to study the factors which were significant to the final solution.

The final chapter presented a summary of findings and some conclusions regarding the modelling of culverts. Recommendations for future work were also revealed.

CHAPTER 2 - SOIL STEEL STRUCTURES

2.1 TYPES OF CORRUGATIONS AND CROSS SECTIONS

Although some pipes may be smooth walled it is far more common for soil-steel structures to be fabricated from corrugated plates. These corrugations produce plates which are highly orthotropic; that is, their stiffness varies depending on their orientation. In the strong axis direction, corrugated metal offers greatly increased bending stiffness and increased area. This structural efficiency is achieved at the expense of some hydraulic efficiency, but this is seldom an issue in long span structures. In the longitudinal direction corrugated plates are comparatively flexible and support very little moment or axial load. Typical corrugations consist of a series of crests and valleys formed by straight tangent sections connecting smooth, single radius arcs. A corrugation profile is usually described by its pitch and depth, as well as the thickness of the steel itself. The terminology used to describe corrugated profiles is shown in Figure 2-1.

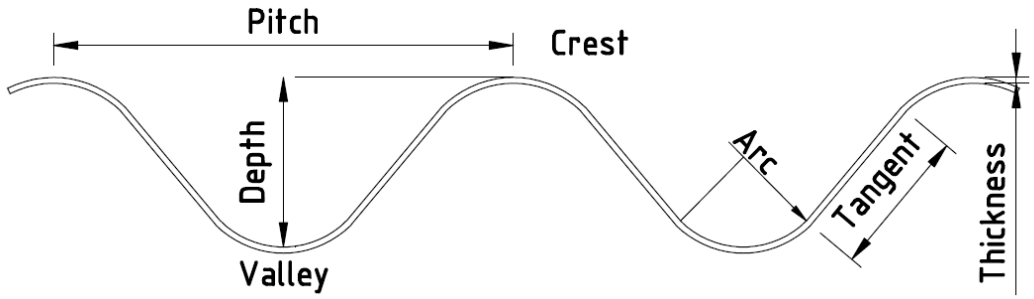

Figure 2-1 – Corrugation profile geometry and terminology

Smaller corrugations are used on culverts which are fabricated as discrete segments of pipe. A seam, usually welded, holds the pipe together in either a helical, (spiralled), or annular, (segmented), fashion. The pipe is assembled by laying the discrete segments

end to end and fastening the pieces together into a continuous culvert. The larger the diameter of the pipe, the deeper the corrugation profile required for the pipe to maintain its shape. Corrugation profiles range from 38 x 6.5 mm for very small pipes to 125 x 25 mm for larger diameter pipes. Because the pipes are welded together with a continuous seam cross sectional shapes are normally round, although it is possible to fabricate some other simple closed shapes as well. The maximum span for this type of pipe rarely exceeds 4 m without special construction provisions, (Abdel-Sayed *et al.*, 1993).

Larger corrugations exceeding those previously described are used to produce a different type of culvert; colloquially called structural plate corrugated steel products, SPCSP. Instead of manufacturing discrete pipe segments these structures are fabricated by bolting together a series of corrugated plates to form the desired shape. The seams are staggered to reduce the stress on the bolts. This allows much greater flexibility with respect to available cross sections, sizes, and corrugation profiles. Also because the structure is delivered to the site in pieces, span limitations are not based on transportation issues. Two common corrugation profiles exist for corrugated structural plate structures; 152 x 51 mm and 381 x 140 mm, (deeply corrugated), (CSPI, 2009). The latter profile exhibits significantly greater bending stiffness, and blurs the line between flexible conduits, usually made from corrugated metals, and rigid conduits, typically fabricated from concrete.

A wide variety of cross sectional shapes exist to meet an array of needs. Cross sections may be classified as closed sections or open sections. Closed sections include round, elliptical, (horizontally or vertically), pipe arches and underpasses. Open sections include arches, (high profile, low profile, and semi-circular), and box culverts. These shapes are displayed in Figure 2-2. Further details regarding the corrugation profile and geometry

of the structure considered in this thesis is provided in Chapters 4.1.2 and 4.1.3, respectively.

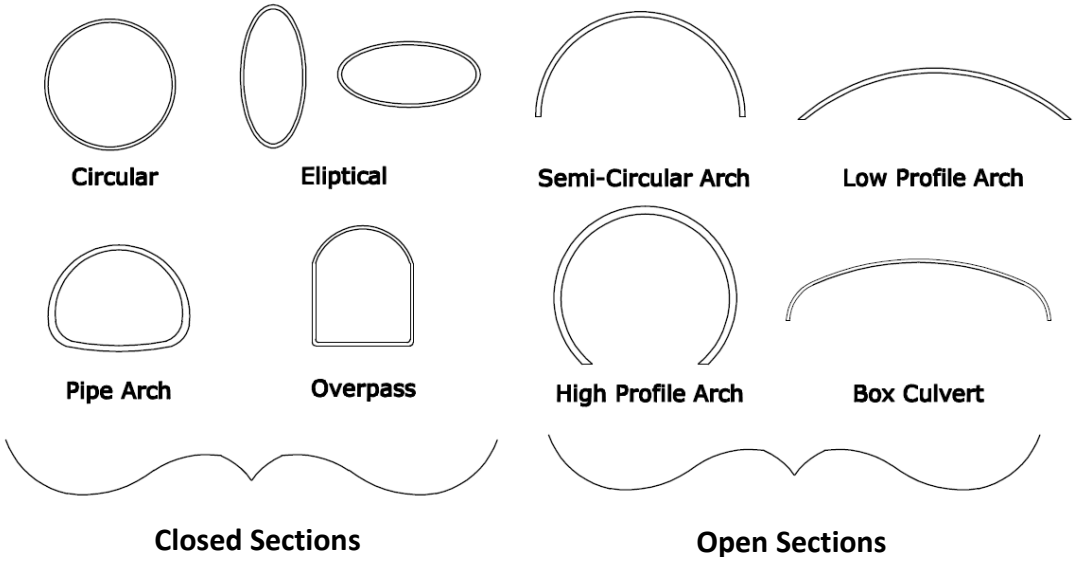

Figure 2-2 – Types of available sections

Regardless of the cross section selected there is some common terminology used to describe the various elements of a buried conduit. These terms are displayed in Figure 2-3 for a box culvert. The crown and invert represent the highest and lowest points in the structure respectively. The springline is the point of the pipe where the largest horizontal distance may be measured. This horizontal distance represents the span, while the distance between the invert and crown refers to structures rise. The haunches represent the tightly radiused corners of the box culvert, although other publications, (Abdel-Sayed *et al.*, 1993), use the term haunches to refer to the region between the invert and the springline.

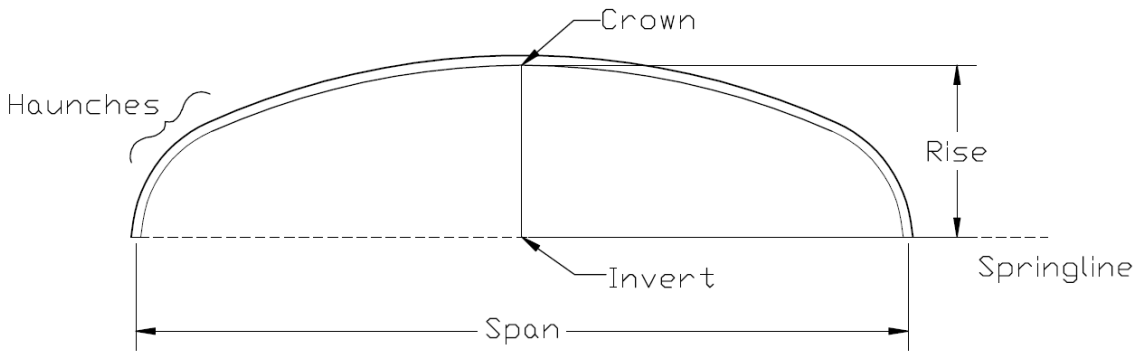

Figure 2-3 – Box Culvert Terminology

The terms transverse and longitudinal are frequently used in this thesis, and refer to the axes of the pipe as shown in Figure 2-4. For example, a transverse plot would show the structural forces acting around the periphery of the structure at a given cross section. A longitudinal plot displays structural forces or displacements along the axis of the pipe.

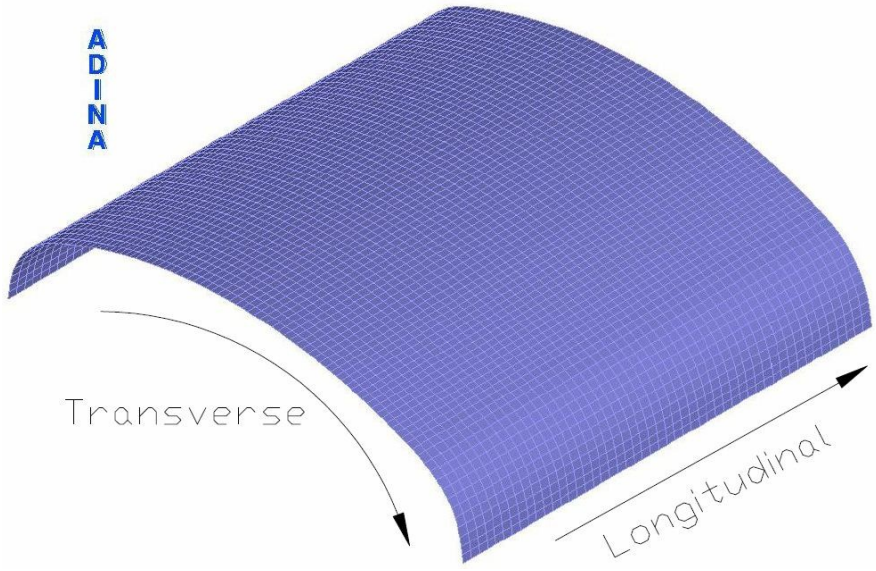

Figure 2-4 – Transverse and longitudinal axis of pipe

Some soil-steel structures also make use of special features to increase their stiffness and capacity. The most common special feature is transverse stiffening plates. These are usually comprised of the additional corrugated plates which are bolted directly to the top of a structure, doubling the area and more than doubling the moment of inertia of the section. These stiffeners may be installed only at certain areas of the structure, for example at the crown, or they may be installed on the entire structure. To increase the stiffness further, the void between the corrugations may be filled with concrete, for a structure known as “encased concrete rib”, (EC rib). Usually shear fasteners are used for this type of a structure which produces a fully composite condition and a very stiff structure. Thrust beams, which run along the structure longitudinally, usually at the haunches, were once popular but are not often used today. Additional details regarding stiffeners and other special features are described by Bakht, Jager and Abdul-Sayed, (1993).

2.2 CONSTRUCTION PROCEDURE

Perhaps more so than other traditional structures, the construction process of soil-steel structures is of critical importance to the health and viability of the structure. Many soil-steel structures experience greater loads during construction than during their service lives. Additionally, if proper construction procedures are not followed, the capacity of the completed structure can be seriously compromised. The installation process takes place over three stages; site preparation, structure assembly, and backfilling.

The site preparation procedure consists of clearing the area around the culvert installation, excavation and dewatering of the site area, and casting or placement of the foundation. The structure may be installed in a trench or soil may be piled on the sides forming an embankment. Selection of the proper foundation depends on the type of

cross section. For open cross sectional shapes, the foundation may consist of un-radiused corrugated steel, for smaller structures, or concrete spread footings, (either cast-in-place or pre-cast), for larger structures. The purpose of these foundations is to increase the bearing area beneath the structure to control settlement. Foundation size is dependent on the size and shape of the structure being erected, total backfill depth, and the integrity of the soil on which the foundation is to be placed. Closed cross sectional shapes rely on a different type of foundation. A bedding of loose gravel is placed to cradle the bottom of the structure and the plates are placed onto this bedding such that the bottom of the structure and the gravel maintain close consistent contact. In regions of very poor in-situ soil or inadequate bearing capacity, pile foundations may be employed. Proper foundation installation is essential to ensure projects proceed at the scheduled pace. As proper bridge alignment depends on a well poured foundation, it is important that a fine tolerance be maintained for vertical and horizontal placement.

Upon completion of the foundation, the structure is then assembled. Cranes are used to hold the pieces in place and the bolting is performed by hand with impact wrenches. A typical assembly process would proceed by completing the end ring on a structure and placing the remaining rings one at a time. The rings may be completed on the ground and lifted into place whole, or they may be assembled piece by piece on the foundation. The structure is either bolted to the foundation, in the case of an open cross section, or placed on the gravel bed, in the case of a closed shape. Depending on the size and stiffness of the structural plates, proper lifting procedures may be required to ensure the plates are not damaged prior to erection. Additionally, if the structure is large and flexible, struts and ties may be required to hold the shape during backfilling.

The final stage of the construction process is the backfilling stage. Following proper backfilling procedures, as well as prudence in structure and backfill monitoring, is key to a successful project. Backfill for a soil-steel structure is comprised of two parts, the

critical backfill zone and all other soils, including in-situ soils and additional fill used a distance away from the structure. The critical backfill zone is the envelope of soil directly adjacent to the structure. The various parts of a typical soil-steel structure are displayed in Figure 2-5.

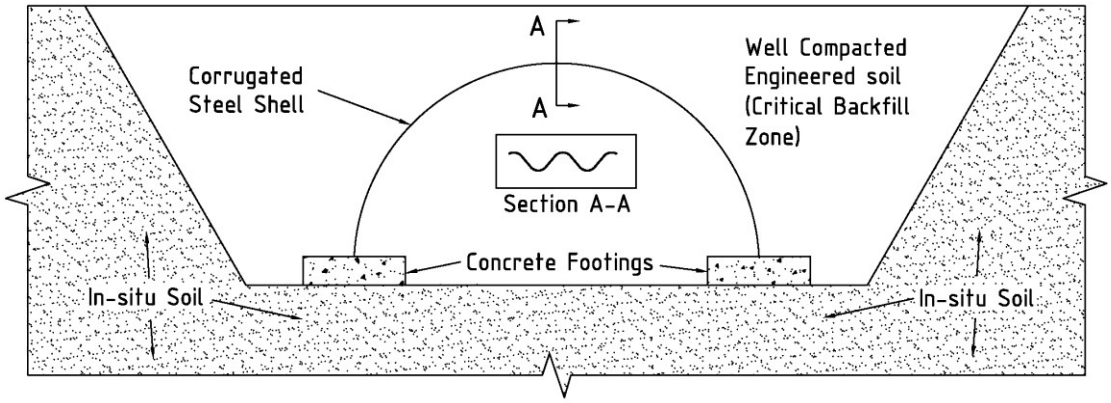

Figure 2-5 – Soil-steel structure terminology

The size of a structure determines the width of the critical backfill envelope, with larger structures requiring extra support. As this soil is part of the structural system, soil materials in this zone have to comply with the standards from the specification. Before a soil not specified in the contract documents is used, it must be approved by an engineer. The soil in this zone is compacted in layers that are typically 200 – 350 mm thick. Layers are built up on both sides of the structure simultaneously, to avoid asymmetric displacements from developing. The required density of structural backfill is typically 95% standard proctor density, corrected for moisture. Density measurements can be taken on site as construction commences by using a nuclear densometer or plate load test. This compaction can be achieved through mechanical tampers or vibratory rollers. On closed shapes hand tamping is often required at the bottom corners of the structure where heavy equipment cannot access. Heavy construction equipment should only be

driven over the structure when the backfill has reached a satisfactory height above the crown, as many construction vehicles exceed the design loads.

2.3 BASIC MECHANICS OF SOIL-STEEL STRUCTURES

Soil-steel structures are composite systems which utilize both the thin walled conduit and engineered backfill to support loads. The restraint provided by the compacted fill prevents the steel conduit from deforming, thus reducing bending moments and supporting the load in axial thrust. This allows the structure to support a much larger load than if it had not been buried. Given the relatively low cost of engineered backfill compared to steel, the economy of soil-steel structures is apparent.

During the backfilling process, the structure undergoes a number of interesting stages. At the commencement of backfilling procedures, soil is piled up the side of the structure and compacted. This action “pinches” in the sides and causes the crown to rise, or peak, resulting in a negative moment at the crown and positive moments at the haunches. The magnitude of this peaking behaviour depends to a large extent on both the type of corrugations used and the cross sectional shape, with stiffer structures resisting these deformations. For flexible structures, however, this peaking can be significant, and produce very high moments at the crown. As soil is placed higher up the structure, the crown falls back down. The moment in the crown and haunches reverses, with negative moments at the haunches and positive moments at the crown. This peaking behaviour is for the most part beneficial to the structure, as the final moments at the haunches and crown tend to be reduced. Figure 2-6 displays three graphics illustrating the behaviour during backfilling.

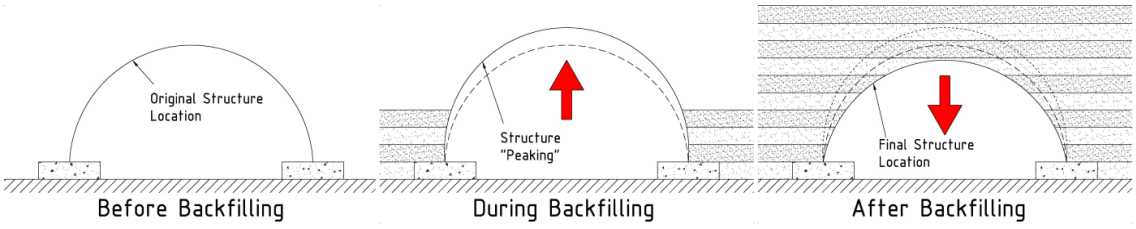

Figure 2-6 – Stages of backfilling process

A soil-steel structure responds to live loads in a similar manner to backfill being placed atop the crown, although the loads are distributed over a smaller area. Loads placed on the backfill above a buried structure are transferred through the soil as stresses and are supported by the corrugated shell. The most effective buried structures are able to maximize axial thrusts whilst minimizing bending moments. Hence semi circular arches are more efficient than box structures. When vertical loads are applied to a buried arch, the tendency of the haunches is to deflect outwards. If the backfill is properly compacted, this horizontal deflection is restrained by the passive engagement of the surrounding soil. This increases the thrust in the structure thus increasing the load carrying capacity.

Stresses travel through a soil mass in a manner that is influenced both by the buried conduit, (its shape, stiffness, and orientation), and backfill properties of the soil mass itself. Generally the stiffer the backfill, the lower the structural forces are which act on the culvert. Increasing backfill depth also decreases structural forces, as the loads acting on the culvert are distributed to a wider area. Because of this, live load effects quickly become dwarfed by dead load effects as backfill depth increases. Live load effects occurring under low cover are usually significant. The characterization of live load effects was an important part of this thesis.

Soil arching is a poorly understood but significant part of the analysis of soil-steel structures. It may occur when a structure is subjected to either dead loads or live loads. Soil arching may be defined as the transfer of loads from the structure to the surrounding soil columns, (positive arching condition), or vice versa, (negative arching condition). A general schematic of soil arching effects may be seen in Figure 2-7. Soil arching effects occur when differences exist between the stiffness of the soil and the stiffness of the conduit. One can appreciate that designing a structure with exactly the same stiffness as its adjacent soil envelope is for all practical purposes impossible. Soil arching may be induced in the transverse or longitudinal directions. However longitudinal arching only takes place under very specific conditions, such as a large change in the foundation stiffness along the culvert length. Positive arching is induced when a structure is less stiff than the surrounding soil columns. The culvert deflects or otherwise settles to a greater degree than the surrounding soil, and thus relieves itself of some of the load. Negative arching is the opposite effect, and is caused by burying a stiffer structure than the surrounding soil. As the soil settles around the structure, the structure remains in the same position. The soil columns on either side of the structure may be imagined to “pull down” the soil above the culvert, thus increasing axial thrusts and bending moments.

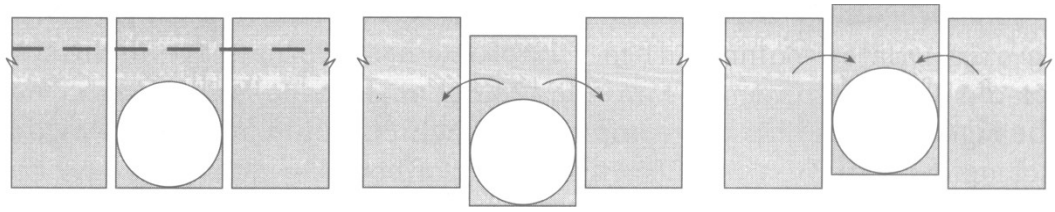

Figure 2-7 - Schematic drawing of soil arching effects, (Abdul-Sayed *et. al.* 1993)

The low stiffness associated with soil-steel structures suggests soil arching can be taken advantage of, especially when it is considered from the project inception. If a structure is properly configured, dead loads may be permanently reduced. Soil arching effects

may be considered to be part of the reason that the development of 'simplified design Equations' are still complex for buried structures, and why analysis software is generally extremely sophisticated.

2.4 RESEARCH OBJECTIVES

The overall objective of this research was to improve the analysis and general understanding of live load forces acting on corrugated soil-steel structures. This purpose was realized through both experimental, empirical analysis of a test structure, and through the application of three-dimensional modelling using finite element software.

The research objectives may be outlined as follows:

- Use empirical data to study and understand live load distribution in corrugated soil-steel box culverts;
- Develop a procedure for the creation of three dimensional models, and;
- Use computer models to further help understand live load distributions and factors affecting it;

CHAPTER 3 - LITERATURE REVIEW

3.1 INTRODUCTION

This literature review presents the history of techniques past researchers have employed when attempting to model the distribution of live loads acting on soil-steel structures. The review has been broken down into three sections detailing the various procedures used as well as the success and practicality of each proposed method.

The first section describes some of the experimental work engineers have employed in an effort to characterize live load distributions. This is followed by two sections on finite element analysis, in two and three-dimensions, examining how numerical models have allowed engineers to finally capture many of the complexities associated with soil-steel structures, while appreciating the limitations of such research.

3.2 EMPIRICAL MODELLING

Researchers have long relied on experimentation to determine structural forces in soil-steel structures. There are many thousands of culverts installed today which were designed entirely from empirical data. The studies referenced in this section are large scale, extremely rigorous, and have been designed primarily to improve the understanding of live load distributions.

In 2002, the National Cooperative Highway Research Program, (McGrath *et al.*, 2002), produced a comprehensive report from a series of experimental tests. The purpose of the testing was to develop recommended design and construction specifications for both rigid and flexible pipes. The test involved the construction of a 9.5 m metal box culvert with a shallow corrugation profile; 152 x 51 mm. No stiffening features were included in the structure, which was unusual for structures built at this time. The

structure was extensively monitored; strains, displacements, and interface soil pressures were collected during backfilling and live load testing. Webb *et al*. (1999) described the instrumentation used in much greater detail. Live load testing was performed using design vehicles placed at three different backfill depths; 0.3 m, 0.6 m, and 0.9 m. Tests were performed under both compacted and uncompacted backfill conditions.

Culvert deflections were monitored at the crown, haunch and footing locations, although only crown locations showed any significant displacements. Deflections were measured by a laser device mounted on a track which allowed the displacements to be determined at nearly every bolt location. The researchers noted that as the live load vehicle passed over the culvert, a "wave-type" motion was observed (Webb *et al.*, 1999). As the vehicle began crossing the bridge, the crown pushed up and away from the wheels. When the truck was over the crown, the crown moved back to the centerline, and deflected downwards. As the truck drove away from the culvert, the crown moved up and away in the opposite direction.

Figure 3-1 displays the longitudinal displacement profile under 0.3 m of cover. This figure shows that adjacent truck tires longitudinally cannot be analyzed independent of one another, as the graph clearly shows the longitudinal profile of the culvert "dishing" under the applied truck loads. The maximum displacement typically took place between the tires. It is also worth noting that regardless of the truck location the longitudinal displacement profile did not shift any appreciable amount. These trends, although less pronounced, were present in the live loads performed on higher backfill heights.

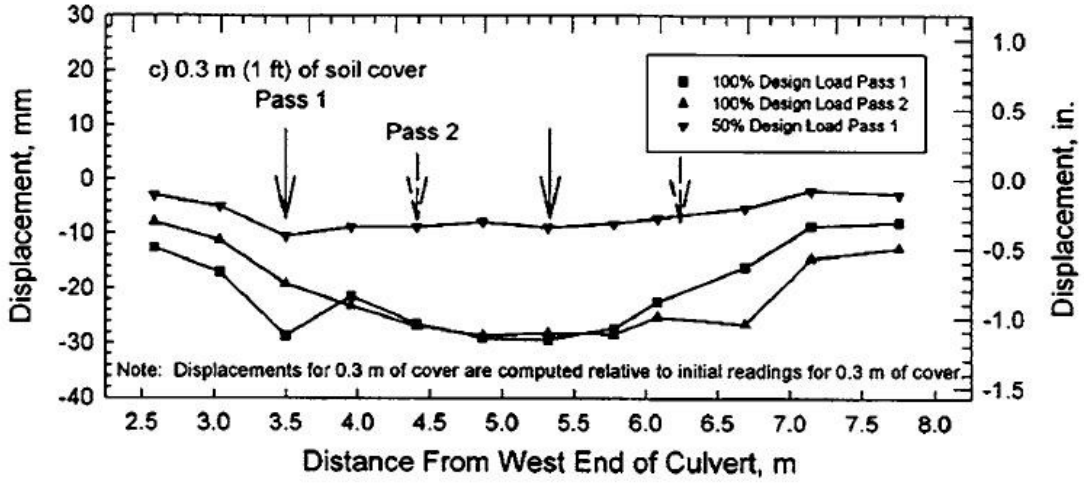

Figure 3-1 – Longitudinal deflection profile under live load, (McGrath *et al.*, 2002)

As expected the bending moments were similar to deflections. Bending moments were found to be heavily influenced by the depth of cover, being significant on the lower covers and practically negligible as the backfill depth increased. Maximum bending moments due to live loads in the transverse direction were found to occur not directly beneath the heaviest loads, (tandem axles), but instead at points on either side. As per the "wave movement" analogy, large loads over the crown produced high bending moments in the haunches, while large loads over the haunches produced large bending moments in the crown. This was because the live loads tended to reverse bending moments already present in the structure due to dead loads.

Radial soil pressures were also measured during these tests, which provided some insight into the soil-structure interaction taking place. Researchers computed the thrust in the wall from the radial pressures using ring compression theory, described in Equation 3-1.

$$T = pR \qquad \textbf{3-1}$$

Where:

T = Thrust in the conduit wall (kN/m)

p = Radial soil pressure normal to structure (kPa)

R = Radius of curvature of plate (m)

Axial thrusts computed by this equation were in good agreement with the thrusts computed from strain gauges, thus verifying the accuracy of the pressure transducers. Radial pressure readings, (soil pressure normal to the structure), were also plotted at various points around the cross section and at different longitudinal positions. Figure 3-2 shows the longitudinal pressure distribution of soil at the crown under 0.9 m of cover. Each plot represents a different transverse load position. However the truck loads were placed at the 7 ft and 11 ft positions on the horizontal axis for all load cases. The greatest pressures measured from this plot, (filled in circle), are when the truck tires are placed over the crown.

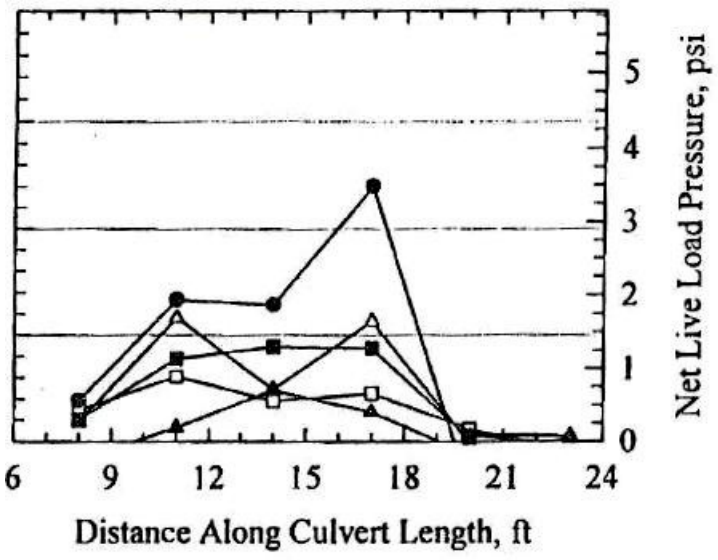

Figure 3-2 – Longitudinal soil pressure profile at crown under various load cases (McGrath *et al.*, 2002)

Viacon performed live load testing on box culverts in Sweden, (Flener, 2006). Two culverts were erected adjacently for experimental testing; one with a crown stiffener and one with no special stiffening features. All plots displayed in this section are taken from the structure without the stiffening rib unless otherwise stated. The structures were comprised of galvanized steel utilizing Super-Cor deep corrugations. Each structure had a span and rise of 8 m and 2.4 m respectively. The structures were instrumented with displacement and strain gauges. Live load tests were performed at various cover depths ranging from 0.45 m to 1.2 m above the crown. Truck positions were designed in such as a way that transverse load spreading could be carefully examined, as transverse truck positions were evenly spaced. A smaller truck with a front axle and a one tandem axle was used.

Displacements measured during the live load testing indicate the relationship between cover heights and deflections; deflections reduce dramatically with increases in cover height. Figure 3-3 displays the crown deflection when the truck is located at various distances away from the crown. Put another way, the first data point represents the crown deflection when the rear tandem axle is 5 m away from the crown. The numbers shown in the legend represent various backfill depths in cm while the “R” represents the presence of the crown stiffening rib. One interesting thing to note about this figure is how increases in cover depth offset deflections at the crown until the vehicle is closer. Some small upward deflection is noticed when the truck is 3 to 4 m away, again owing to the “wave type” motion which pushes the crown up when loads are placed a distance away.

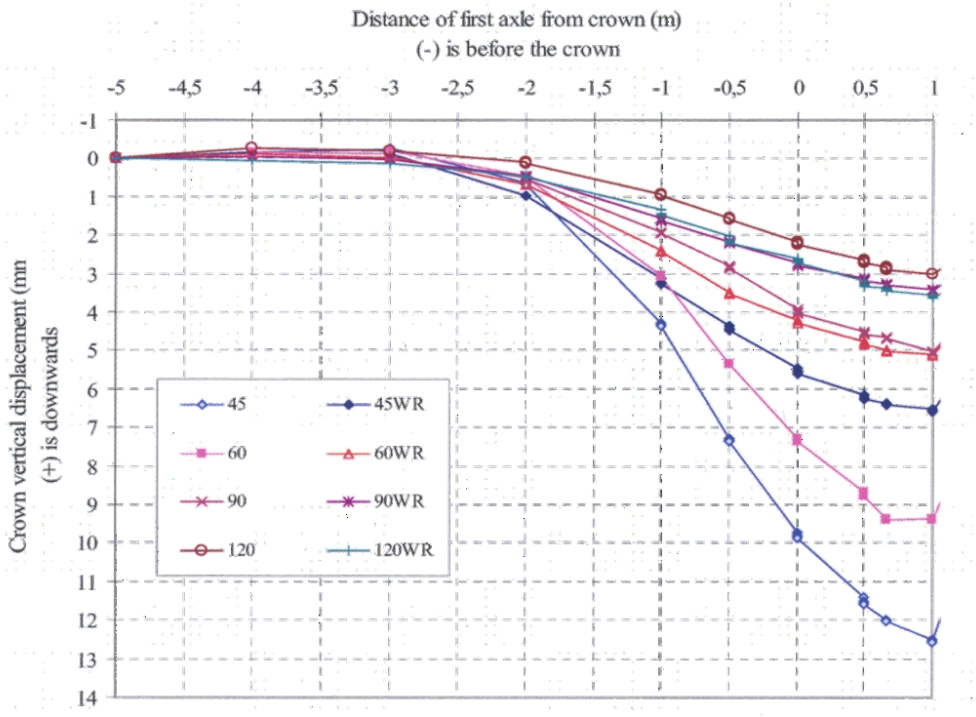

Figure 3-3 – Vertical crown displacements at various truck positions & cover depths (Flener, 2006)

A similar plot is presented for inner fiber strains in Figure 3-4. The trends for strains are similar to the trends seen for deflection. The response appears to be slightly more sensitive than for deflection, with a noticeable response when the truck is 3 m from the crown and a significant response when the truck is 2 m from the crown. The worst strain condition was induced by the position where the tandem axles were placed slightly offset from the crown, (position indicated by 1 m in Figure 3-4). Positions to the left and right of the crown were instrumented in this study as well as the centerline, and it was determined that strains across the entire crown were generally high. Also, the highest strains did not necessarily occur at the centerline.

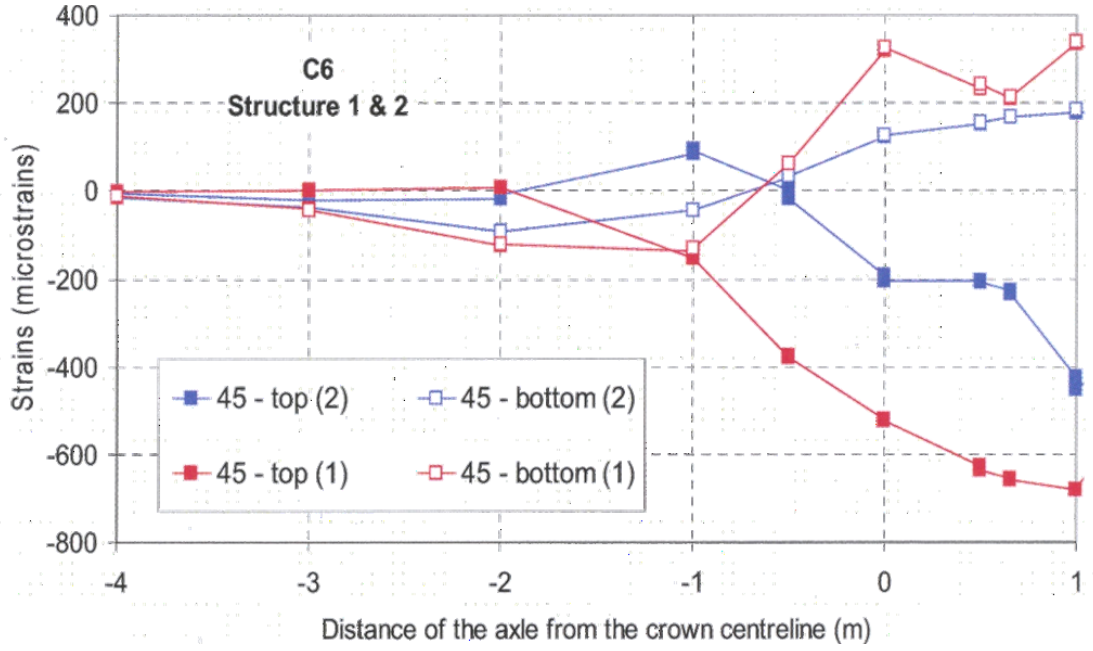

Figure 3-4 – Strains at the crown for live loads under 0.45 m of cover (Flener, 2006)

A plot which displays bending moments at various transverse truck positions is presented as Figure 3-5. Station C6 represents the crown, while C5 and C4 are one and two bolt spacings away from the crown respectfully. When the truck is 1 m away from the crown, gauge C4 is being loaded directly. Crown moments, even away from the centerline are unexpectedly uniform. The differences in moment between the 3 crown gauge locations decrease as cover increases, as the load is spread out more evenly.

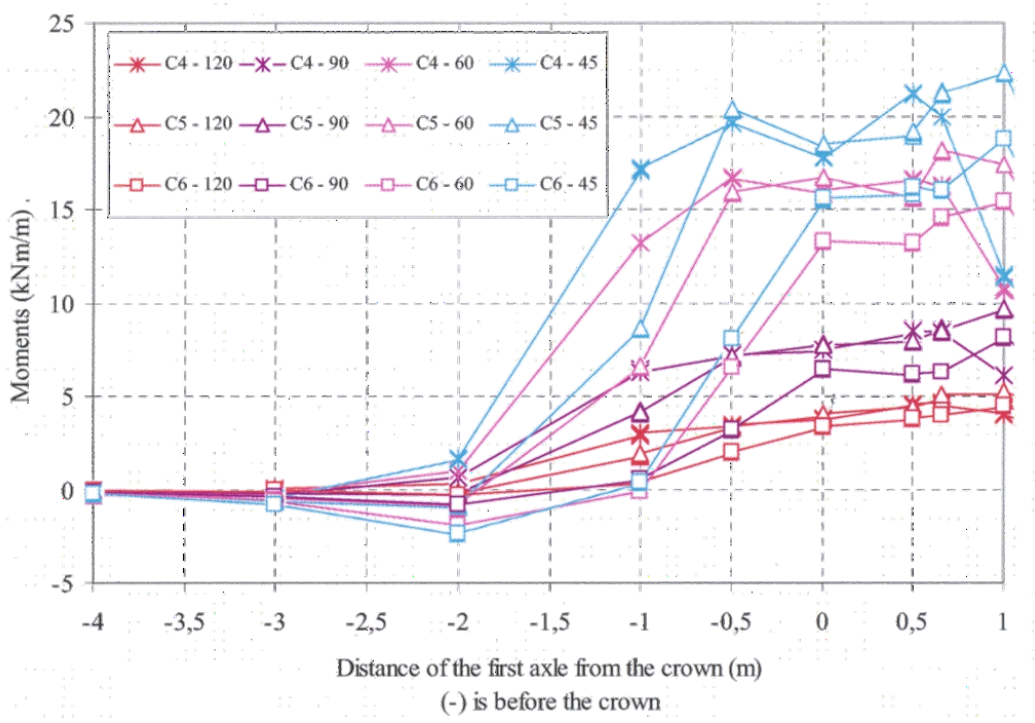

Figure 3-5 – Bending moments around the crown at various cover depths and truck positions (Flener, 2006)

Figure 3-6 displays axial thrusts in the haunches and crown at various truck positions and backfill depths. The thrust plots are generally smoother than those for bending moment. In the -4.0 m position, the trucks axle is placed almost directly over the haunches and shows very little response. When the truck is placed 3 meters from the crown, compressive thrusts increase in the haunches. As the tandem axle moves closer to the crown, large compressive axial thrusts are induced in the crown while the haunches show large tensile thrusts. This effect seems unusual as compressive thrusts were expected from all loading positions. The probable cause for this irregularity is that in the load positions where tensile forces are at a maximum, (-0.5 m), the rear tandem axle and front axle are straddling the gauge.

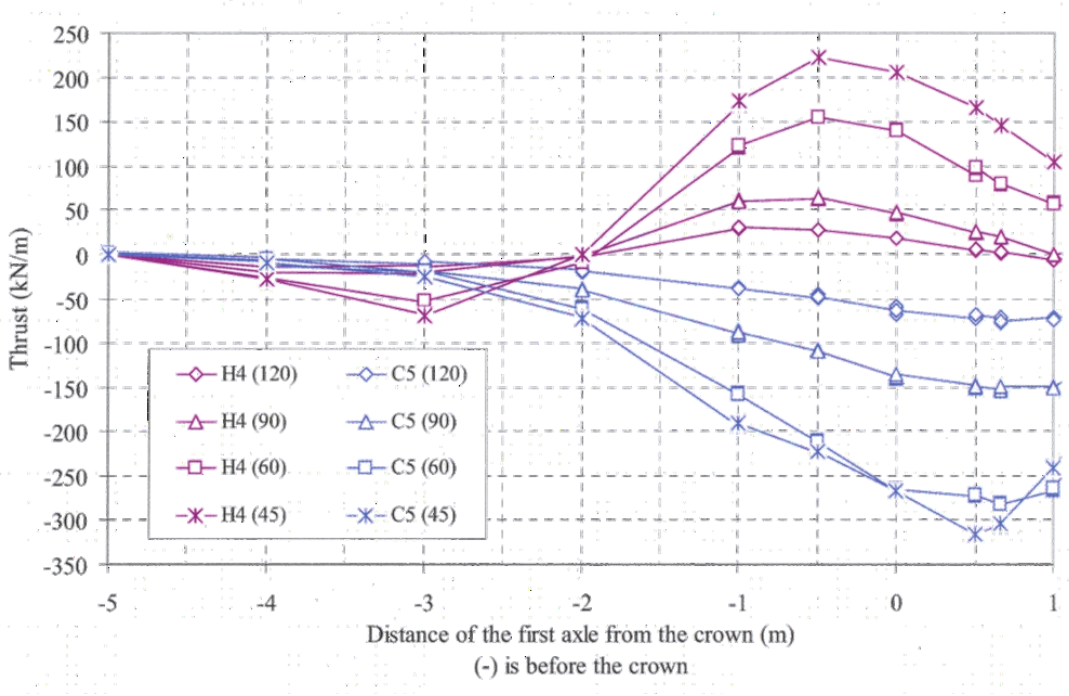

Figure 3-6 – Axial thrusts at the crown and haunches at various cover depths and truck positions (Flener, 2006)

Price Creek, (Au & Lam, 2005), was another box culvert structure which was extensively instrumented and monitored during live load testing. It was a large span structure, at 14.2 m, with encased concrete, (EC), stiffeners cast into two of every three corrugations which run all the way down to the foundation. The structure was required to undergo a proof test because the specifications, specifically the span, were outside code limits. Given that the structure was undergoing a proof test, the majority of the report was focused on ensuring that the structure remained well below plastic strains under a variety of load cases. Five load lines, (two of which contained two load vehicles side by side), and seven load steps each were used to capture the maximum response of the structure. The structure was built on a 15˚ skew, meaning that live load positions spanned across several instrumented rings, rather than running parallel. The backfill depth for all tests was 1.3 m in the center of the structure and 0.85 m at the open ends. The instrumented areas of the arch were located under the larger backfill depth.

Figure 3-7 displays the longitudinal deflection profile at various transverse truck positions. The truck line in this figure straddles “Ring C”, putting the actual tire centerline positions at approximately 0.9 m and -0.9 m on the x-axis. The maximum deflection occurs at Ring C, directly between the tires. Given the maximum deflection occurred at Ring C, the response again shows the interaction of multiple tires placed side by side. Although the overall deflections are quite small for such a large truck load, the longitudinal response is felt in this structure at a distance that is quite distant, greater than 5 m.

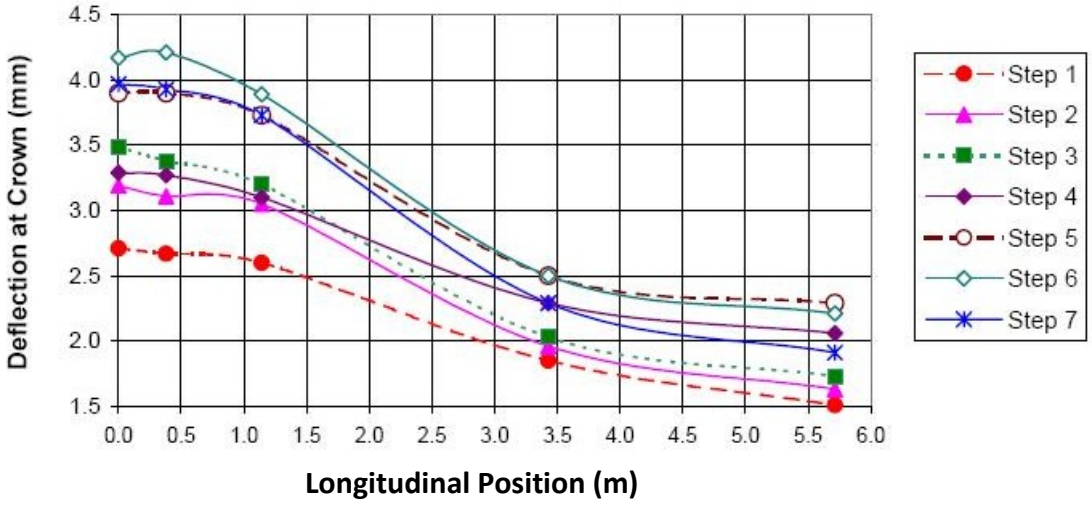

Figure 3-7 – Longitudinal deflection profile at various truck positions (Au & Lam, 2005)

Longitudinal strain profiles, with the truck on the same line as the previous figure, are displayed in Figure 3-8. Strains displayed are taken from the extreme inside fibre of the EC rib sections, as the concrete prevented gauges from being placed on the outer plate. All of the strains are positive, indicating positive bending at the crown, with the exception of load step four. Load step four is unique in that two sets of tandem axles are placed straddling the centerline of the structure. These tandem axles induce positive moments on either side of the crown and negative moments directly over the crown. It is worth noting that in load lines where two test trucks sat on the bridge side by side, the longitudinal strain profile was relatively constant.

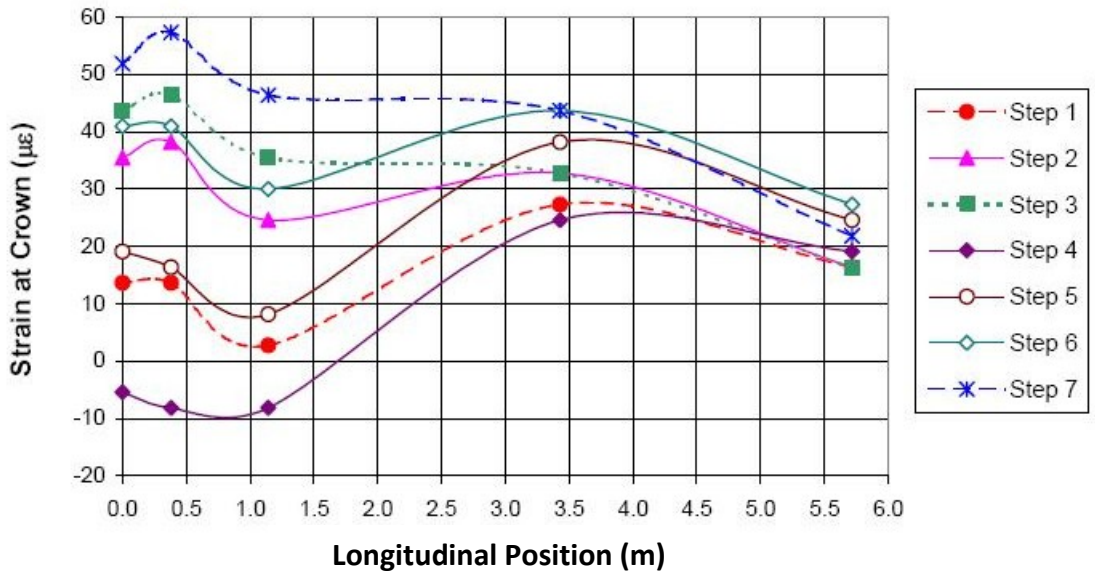

Figure 3-8 – Longitudinal crown strain profile at various truck positions (Au & Lam, 2005)

At some crown locations, researchers included both longitudinal and transverse strain gauges. Figure 3-9 displays both the transverse and longitudinal strains on "Ring D", which is non-EC. Longitudinal strains in this structure were greater than transverse strains for the same load cases, in some cases more than five times higher. The longitudinal and transverse strains were inversely related, that is, increases in longitudinal tension resulted in increases in transverse compression. This trend is consistent with Poisson's ratio effects. The large magnitude of longitudinal strain, however, is unusual given that the transverse bending stiffness is literally hundreds of times greater than the longitudinal bending stiffness.

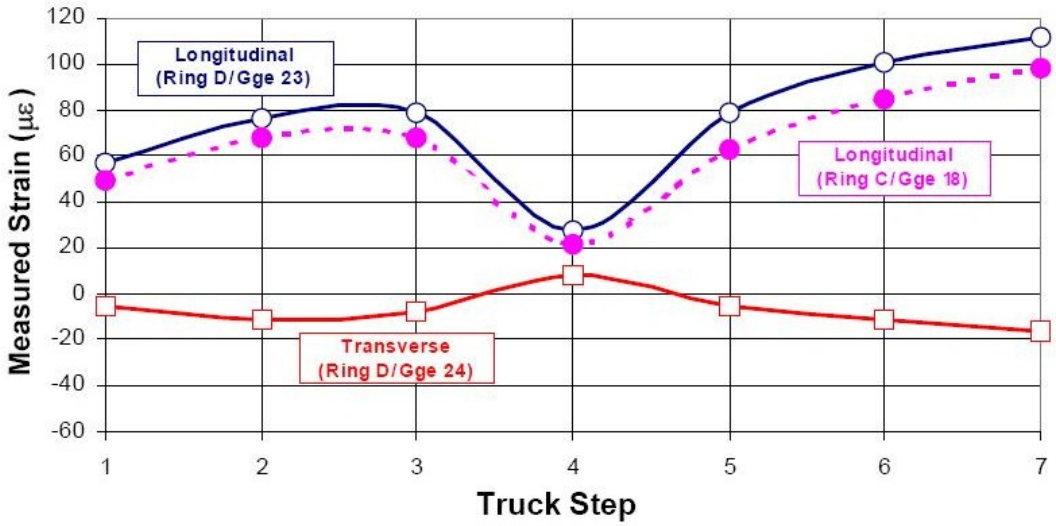

Figure 3-9 – Longitudinal vs. Transverse strains at the crown for non-EC rib (Au & Lam, 2005)

3.3 2-D Finite Element Modelling

Soil-steel structures have traditionally been modelled using a 2-D plane strain approach, as it is an efficient and reasonably accurate solution technique for a large variety of problems. Problems which satisfy the plane strain condition, that is, no loading variation in the longitudinal direction, can often be modelled with reasonable accuracy. In addition, the low required computing power means that significant nonlinearity can be incorporated into the solution while still running in a reasonable amount of time. Problems such as a dead load analysis, including construction steps, or live loads being applied over a deep cover are particularly suited for a plane strain analysis. Certain types of live loads, such as those applied as a strip load along the longitudinal culvert axis are also approximated well by plane strain techniques.

However the live loads applied to a soil-steel structure are typically patch loads applied

on the soil surface which have a finite length and width, such as a truck tire. These loads cannot be easily represented by a 2-D model. If the load applied to a 2-D model is taken to be the same magnitude as the pressure of the tire patch load, the plane strain model will treat it as though it were an infinitely long strip load, which would produce significantly greater load effects than the patch load which was intended. To compensate for this, the applied load in a plane-strain model must be reduced such that the applied load is better represented by the strip load. Typically this involves multiplying the applied patch load pressure by a reduction factor, r. This reduction factor can be determined by a number of approaches, two of which are discussed below.

The first approach is an analytical approach based on Boussinesq's theory of stresses travelling through a homogenous, elastic half-space. Analytical equations may be derived to determine the maximum stress occurring under a patch load at a distance H from the ground surface, corresponding to the depth to the crown of the structure. Additionally, an equation can be derived for the same loading case with the exception that the patch load has one of its sides of infinite length. The reduction ratio is then given as the ratio of these two calculated stresses, as given in Equation 3-2.

$$r = \frac{P_p}{P_s} \qquad \textbf{3-2}$$

Where:

r = live load reduction factor
P_s = pressure at the crown of the structure due to an applied infinite strip load
P_p = pressure at the crown due to an applied patch load

Although this technique can be used to predict reasonably good results, (Katona *et al*., 2007), there are some limitations. The primary problem with this approach to live load

distribution is that it neglects the contribution of the culvert itself, the stiffness of which is typically drastically different than the stiffness of the surrounding soil. Abdel-Sayed and Bakht, (1982), showed that by using different assumptions in the analysis, for example stresses travelling through a finite layer, the stress distributions can vary drastically. It is not difficult to imagine that the presence of a buried soil-steel arch would similarly alter the distribution of stresses in the soil.

The second approach to reducing the live load applied at the surface is described by Bakht, (1981). This approach involves the assumption that patch or point loads placed on a soil mass above a buried conduit spread out at a measureable and constant angle, regardless of conditions such as soil stiffness, culvert size, shape and span, or depth of the backfill. Bakht's research suggests that this is at least partially true, and can result in good approximations of stress distributions. The load spreading is only applied in the longitudinal direction, as the transverse load spreading is handled inherently by the 2-D finite element software. The reduction ratio in this case is found by equating the pressure at the surface to the pressure at the crown, after the stresses have travelled through the soil. A schematic of this longitudinal load spreading is shown in Figure 3-10.

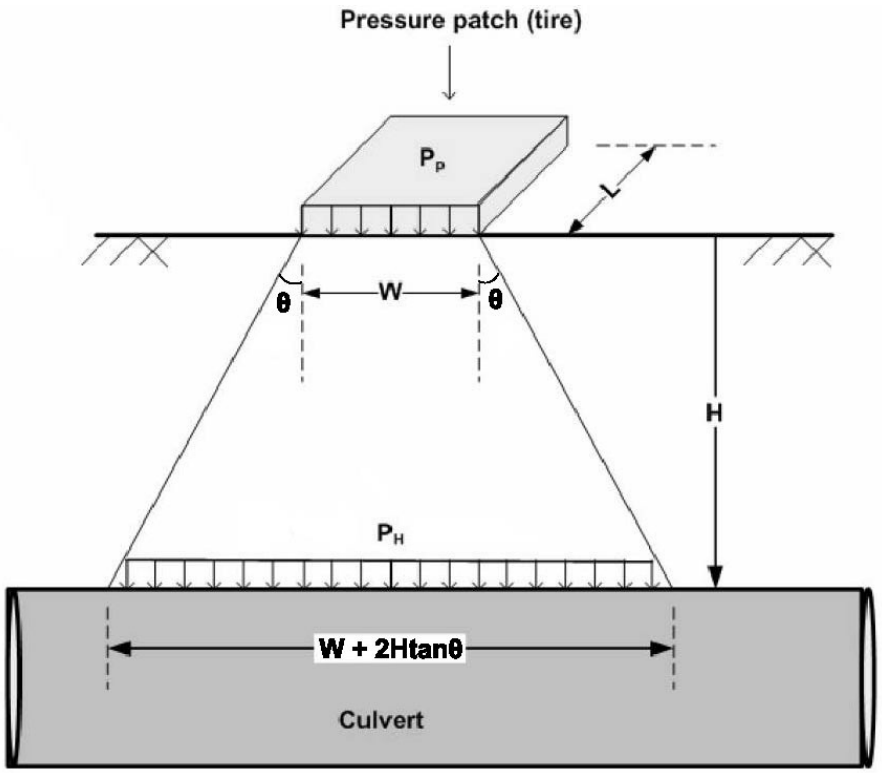

Figure 3-10 – Longitudinal Load spreading (CANDE, 2007)

The live load reduction ratio in this case is similar to Equation 3-2, and is shown in Equation 3-3.

$$r = \frac{P_H}{P_P} = \frac{1}{1 + \frac{2\mathrm{H}}{\mathrm{W}} \tan\theta} \qquad \textbf{3-3}$$

Where:

r = live load reduction factor
P_P = pressure of the applied patch load
P_H = pressure at the crown due to an applied patch load
θ = longitudinal live load dispersion angle
W = width of the applied patch load
H = depth from the surface to the crown of structure

It can be appreciated that as the backfill height increases, an equivalent pressure at the crown will decrease accordingly. By adjusting the angle of dispersion, the presence of the culvert can be taken into account in the analysis. Unlike the elasticity approach, multiple adjacent wheels can be easily accounted for using this technique. The sections of "overlap" are simply added to the total load. Generally this method produces more accurate and less conservative approximations of live load than the elasticity approach, and is also used by most design codes including the American Association of State Highway and Transportation Officials, (AASHTO), as well as Canadian Highway Bridge Design Code, (CHBDC), although the dispersion angle varies.

3.4 3-D Finite Element Modelling

As the size and scope of soil-steel structures has matured, the need for a more robust analytical tool has arisen. There are many situations where a 3-D representation of the problem is necessary to fully capture the structural effects in the culvert. For example, variations in cover depth in the longitudinal direction, culvert end effects, orientation changes and live loads applied to structures with a low backfill depth are all situations that violate the plane strain condition and require a 3-D analysis.

Various factors and techniques may be applied to a plane strain model to simulate three dimensional effects as described in Chapter 3.3. Three-dimensional finite element modeling provides a means to calibrate such plane-strain approximations, and may be performed without the expense and effort required of an experimental test structure. In this way the 3-D models are useful not necessarily for everyday design, but for the improvement of design codes and plane-strain modeling procedures. Despite this fact few researchers have published their efforts to model these structures in 3-D. This section will describe the evolution of 3-D analysis techniques and findings from various researchers.

Moore and his colleagues were the first researchers to recognize a need for 3-D models and develop a technique for analysing culverts with longitudinal variation, (Moore & Brachman, 1994). Additional improvements were made in 1999, (Moore & Taleb, 1999). The development of this analytical procedure was a result of limitations in computing power at the time. Moore developed a "pseudo 3-D analysis" which used traditional two dimensional finite element modeling in the transverse direction combined with analytical Fourier transforms to spread the load out longitudinally. Because of the analytical components of this modeling technique, it contains certain inherent limitations. Firstly, the culvert must be sufficiently long to be modelled as having infinite length. Secondly, because the principles of superposition are utilized, the models must be fully linear. There are some benefits, however, specifically its application is simple once the math is understood and because only plane strain FEA models are being run, it is highly efficient.

Moore, (1999), analysed several circular culverts using both isotropic and orthotropic material models. Although a linear soil model was required, some "nonlinearity" was simulated by varying the stiffness values with depth, to simulate the increase in stiffness associated with soil dead weights. This linear variation is included as Equation 3-4.

$$E(z) = E_o + mz \qquad \textbf{3-4}$$

Where:

E = Young's modulus at depth z (MPa)

z = Depth below ground surface (m)

m = modulus gradient

E_o = modulus at the ground surface

The approach was generally useful and provided some insight into three dimensional effects. Although the analysis produced good accuracy when predicting the shape of the moment and thrust diagrams, the values were often off by more than 50% in magnitude compared to measurements. Moore attributed these inaccuracies to the lack of nonlinearity in the soil model and the finite culvert lengths of the actual structures. The differences between isotropic and orthotropic plates did not appear to be important; however further studies in 3-D FEA showed that the differences can be significant.

An interesting artefact of this research, which has implications for true 3-D FEA modeling, was that modeling live loads under shallow covers can be very difficult. The FEA results grossly underestimated thrust and moment values under the wheel, while overestimating them at longitudinal points away from the load application. Moore speculated that this was due to local shear failure occurring under the wheel which had the effect of providing little to no load distribution through the soil. The situation was rectified by reducing the stiffness of the soil beneath the wheel by a factor of 5, which produced results which were closer to the experimental values. Although Moore was able to get slightly better results under certain conditions than a traditional 2-D approach with line load approximations, the limitations of these techniques are significant. With the advent of faster computing technologies this method has been abandoned for more traditional finite element models.

One of the first published accounts of using a fully 3-D finite element model to analyse a soil-steel culvert was performed by Girges and reported in his thesis, (Girges Y. F., 1993), and later published by Girges & Abdul-Sayed, (1995). The primary purpose of the study was to compare 2-D and 3-D meshes and correlate the results to experimental testing. The culvert was circular and had a span of 7.6 m. 8-noded linear translation brick elements were used for the soil continuum elements while 4-noded reduced integration shell elements were used to model the culvert. Both linear elastic and elastic-plastic

material model were used to model the soil, while the steel portions were modelled elastically. Because of the computational expense of applying the soil in discrete construction lifts, Girges instead applied the soil dead load in one large step but varied the density such that the maximum axial thrust predicted by the OHBDC (Ontario Highway Bridge Design Code) was achieved. Also, multipoint constraints were used to attach the culvert elements to the soil elements, mimicking the translations but allowing the shell elements to rotate freely, creating essentially a fully bonded condition.

Vertical pressure distributions, an important parameter for the determination of live load distributions, were computed explicitly by examining the vertical pressures in elements at the culvert surface. Girges found that in the transverse direction, the dispersion angle was between 43˚ and 47˚ degrees, with an average of 45˚. This value conformed well with published code values. In the longitudinal direction the load dispersion was significantly steeper, at 80˚, or 5V:1H. The 3-D analysis showed the greatest soil pressure directly beneath the wheel, while in the 2-D analysis soil pressures were greatest on either side of the load with a dip directly beneath the load. The transverse vertical pressure distribution at crown level due to live load forces is shown in Figure 3-11.

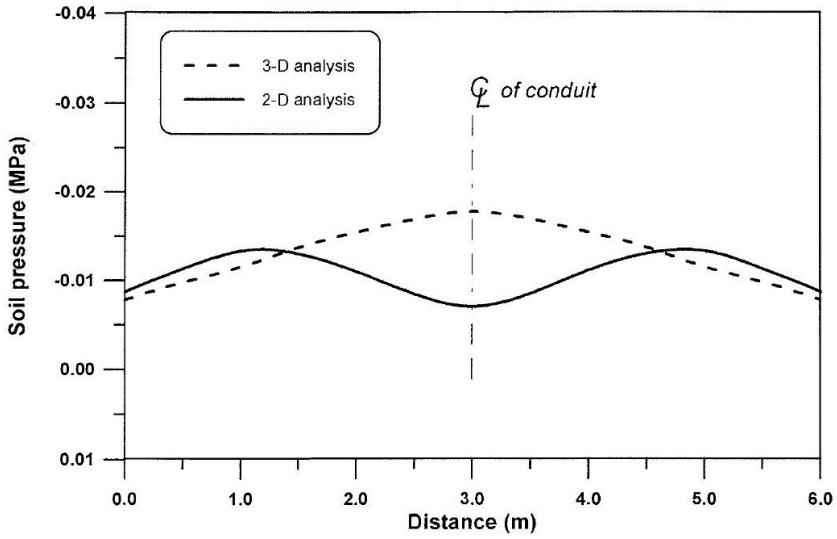

Figure 3-11 – Transverse vertical pressure distribution at crown level (Girges & Abdel-Sayed, 1995)

Thrust and bending moments were also compared. Thrusts due to live loads were lower and more uniform in the 3-D than the 2-D model, as shown in Figure 3-12. The same trend continued for bending moments, as shown in Figure 3-13. At the haunches the bending moment was 20% lower in the 3-D model and in the crown the moment was more than 50% lower.

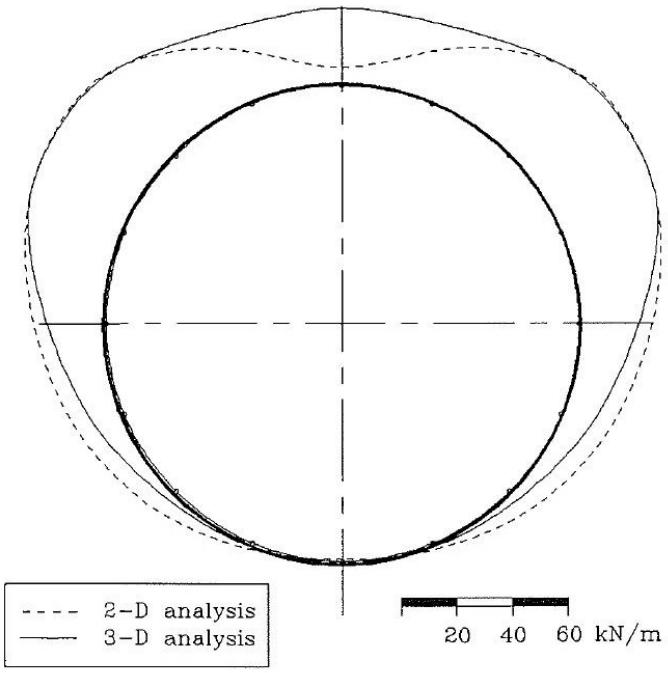

Figure 3-12 – Live load axial thrust distribution (Girges & Abdel-Sayed, 1995)

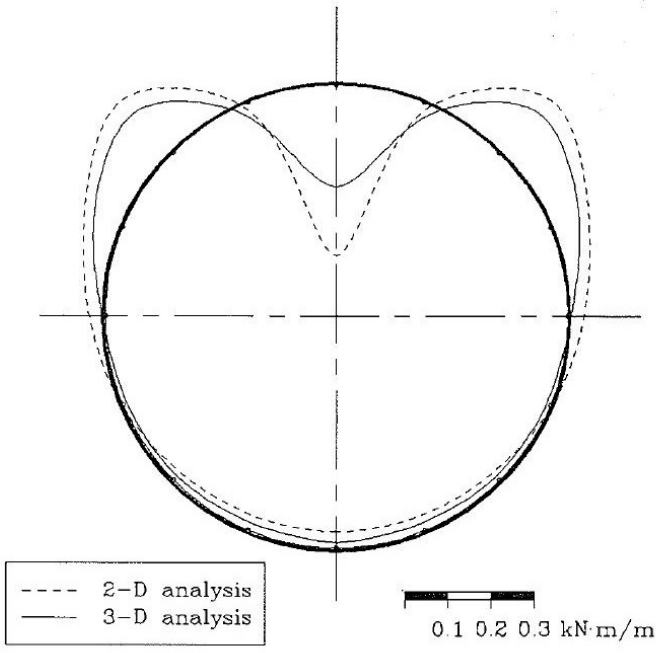

Figure 3-13 – Live load bending moment distribution (Girges & Abdel-Sayed, 1995)

To examine elastic buckling capacity, an eigenvalue analysis was performed. The eigenvalue, λ, was taken as the multiplier to the live load, which when combined with dead load, produced elastic buckling in the structure. The 3-D analysis resulted in an additional 10% capacity when compared to the 2-D. This is probably due to the additional support provided by the unloaded portions of the culvert on either side of the critical ring, which cannot be properly represented in the 2-D analysis.

Another recent study of the 3-D effects of live loads was performed by El-Sawy, (2003). El-Sawy developed 3-D finite element models for two culverts which had previously been studied by Bakht, (1981). One culvert was circular with a span of 7.77 m and the other was horizontally elliptical with a span of 7.24 m. The circular pipe was the same pipe studied by Moore and Brachman, (1994), which allowed a comparison to be made between Moore's semi-analytical technique and a fully 3-D finite element model. The investigation was undertaken primarily to validate the use of 3-D FEA modeling for live loads under shallow cover.

20-noded isoparametric brick elements were used to model the soil, with some 10-noded tetrahedral elements to fill in irregular zones. The culvert itself was modelled using 8-noded quadrilateral with 6-noded triangular elements in irregular zones. Boundary conditions simulated smooth walls on the sides and bottom. No dead load modelling was performed on either culvert due to a lack of detailed soil information. Instead the investigation focused on the linear response of the culvert due to live load forces.

Both isotropic and orthotropic material models were analyzed for the culvert to determine their effect on structural forces. A plane strain FEA model was used to determine the disparity of stiffness between the longitudinal and transverse directions, similar to the method described in Chapter 5.2. The axial stiffness, rather than bending

stiffness, was used to compute the longitudinal stiffness values. In a circular culvert where bending moments are seldom computed during design and axial thrusts are significant, this decision was rational. Unlike Moore and his semi-analytical modeling technique, El-Sawy found significant differences between the isotropic and orthotropic cases. A diagram showing the circumferential thrust under both the isotropic and orthotropic cases is displayed as Figure 3-14. It is readily apparent that the orthotropic model differs significantly from the isotropic model. The isotropic model significantly overestimates the crown thrust and underestimates thrust in the haunches. The orthotropic model slightly underestimates the thrust in the crown and slightly overestimates the thrust in the haunches, where the maximum thrusts are expected to occur. The shape of the orthotropic thrust distribution is much closer to experimental values, and thrust is conservative in the critical zones. Also shown in this figure is the difference between actual culvert geometry and “infinitely long” prismatic geometry, to test Moore’s theory that the assumption of infinite culvert length can have a significant impact on structural forces. As is shown, the differences are not appreciable.

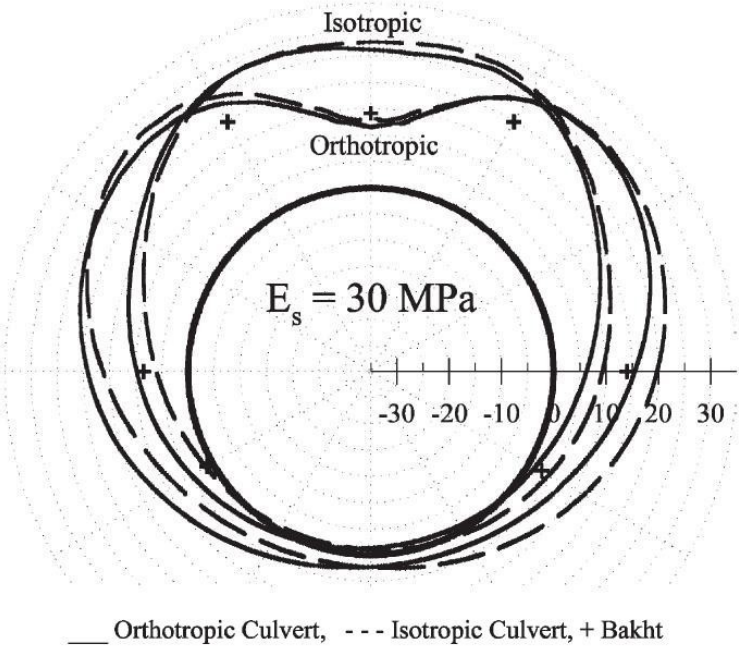

Figure 3-14 – Circumferential thrust in Deux Rivieres culvert (El-Sawy, 2003)

El-Sawy also provided several longitudinal plots which show how thrusts decay in the longitudinal direction. Two plots are included; Figure 3-15 displays the circumferential thrust while Figure 3-16 displays the longitudinal thrust. In each plot the live load is applied at the zero point on the x-axis. The circumferential thrust decay shows differences between the isotropic and orthotropic cases. When there is no longitudinal stiffness, then thrusts become insignificant a very short distance from the applied load, approximately 1.2 times the culvert diameter. Figure 3-16 displays the unrealistic longitudinal thrusts which occur when an isotropic model is used. For the orthotropic model, longitudinal thrusts are negligible.

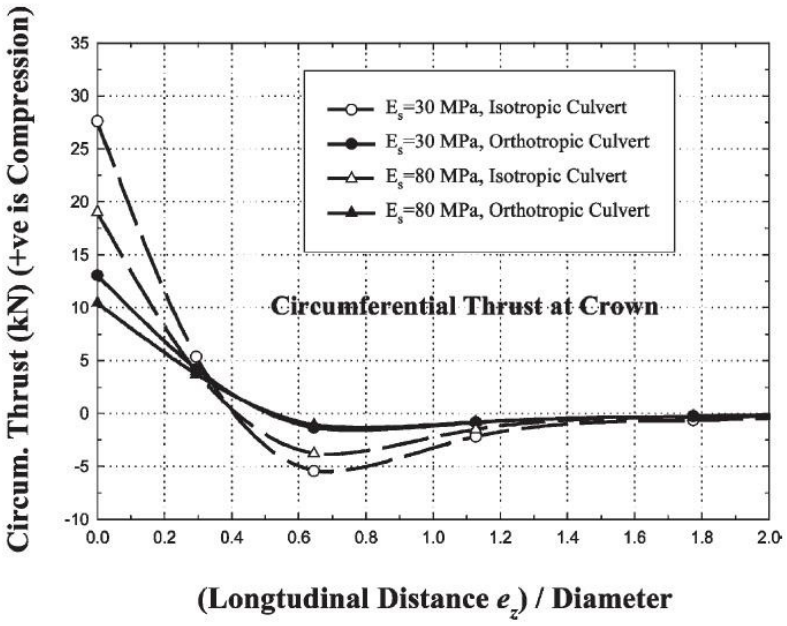

Figure 3-15 – Circumferential thrust at crown gauges in Deux Rivieres culvert (El-Sawy, 2003)

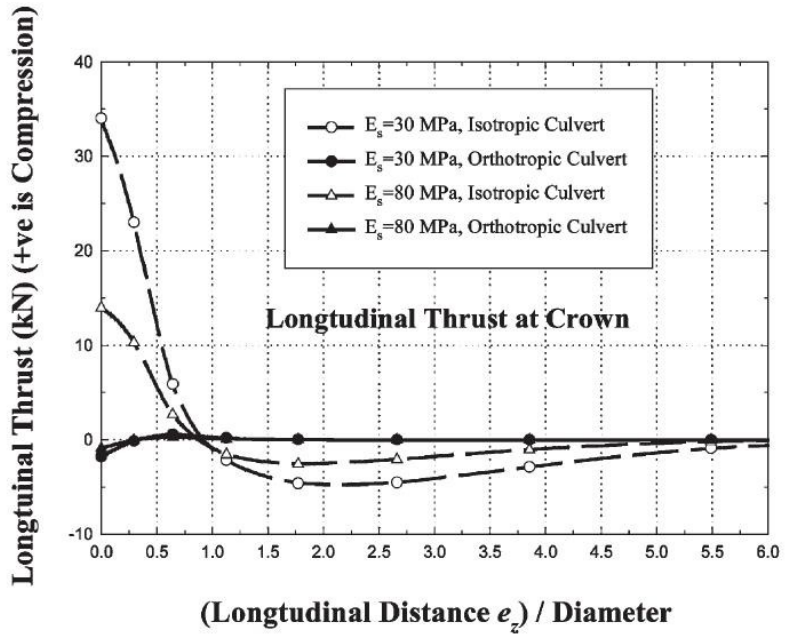

Figure 3-16 – Longitudinal thrust at crown gauges in Deux Rivieres culvert (El-Sawy, 2003)

The deficiencies of El-Sawy's research include the lack of nonlinearity and accurate soil constitutive models. Since thrusts are less sensitive to soil properties, the results obtained were quite good. However, without proper soil properties neither bending moments nor displacements would display the same degree of accuracy.

The most recent effort by researchers to study live loads using 3-D finite element models was performed by Peterson *et al.* (2010). The study was produced by NCHRP as "Report 647". The purpose of this report was to improve the simplified design equations, (SDE), for live loads, especially under low covers, and to provide engineers with guidelines for using both 2-D and 3-D finite element software to design culverts. The report also details the authors' attempts to calibrate their 3-D models to experimental data obtained by Webb *et al.*, (1999). This review of the research focuses on the calibration efforts.

Researchers began by selecting a number of soil models in an effort to determine a model with an appropriate balance of simplicity and sophistication. The researchers compared the models using a 2-D plane strain approach. The models used were, in order of complexity, linear elastic, Mohr-Coulomb, and a hardening model developed for the Plaxis 3D Tunnel Version 2.0 software package. The linear elastic model contained stratified soil layers and utilized a graduated stiffness based on the depth of each layer. Stiffness values were calculated based on research performed by Selig, (1990). The Mohr-Coulomb model was similar to this but also included shear plasticity and tensile cutoff using a non-associated and associated flow rule respectively. The hardening model was a robust soil model which included shear hardening due to primary deviatoric loading and compression hardening due to primary compression. This model was similar to the Duncan-Selig model used in CANDE. The hardening model parameters were determined by performing finite element triaxial tests with the Duncan-Selig model created using known parameters taken from soil testing, and

selecting the hardening model parameters by matching the behaviour.

The first series of models were performed on a shallow corrugated, (152 x 51 corrugation profile), box culvert with a span and rise of 9.6 m and 3.66 m respectively. The backfill depth was 760 mm. The structure was an “off-the-shelf” culvert and no physical version had been experimentally tested. Dead load effects were included in the nonlinear soil models but were subtracted out such that the final results displayed only live load effects. The sequence used for the addition of dead load used the following four steps. The in-situ soil was loaded under gravitational effects. The structure itself was then added with gravity effects. The backfill was added in one monolithic layer, including gravitational effects, and finally the live loads were applied to the surface of the backfill. This sequence ensured that gravitational effects did not incorporate unrealistic load effects such as distortion of the culvert before being buried. Bending moment and axial thrust diagrams for each soil model and loading case are shown in Figure 3-17, Figure 3-18, Figure 3-19, and Figure 3-20

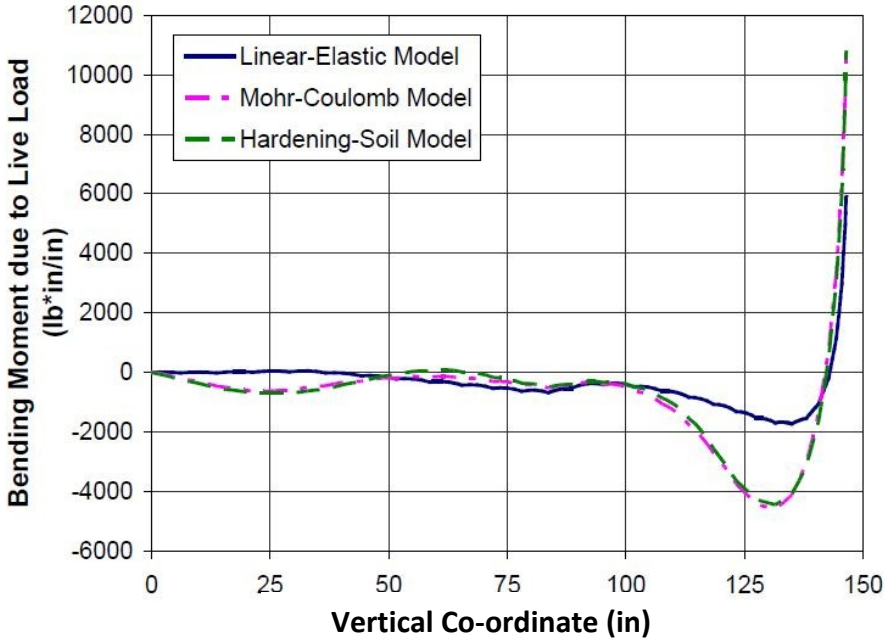

Figure 3-17 – Bending moment diagram with 2' of cover (Peterson *et al.,* 2010)

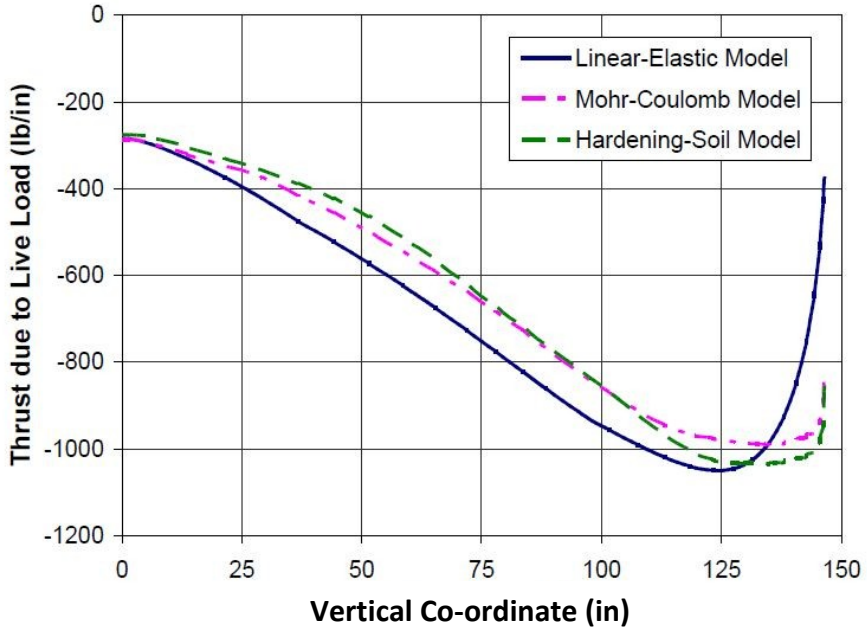

Figure 3-18 – Axial thrust diagram with 2' of cover (Peterson *et al.,* 2010)

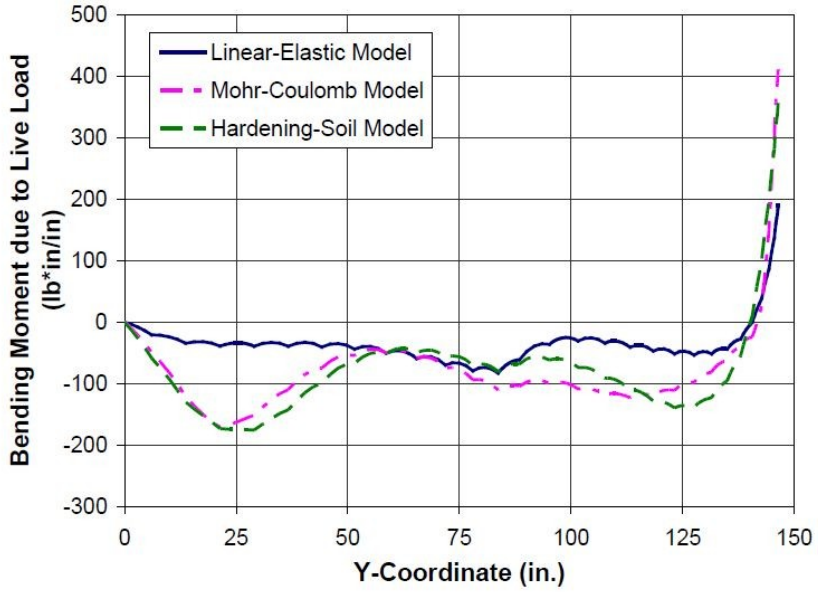

Figure 3-19 – Bending moment diagram with 6' of cover (Peterson *et al.,* 2010)

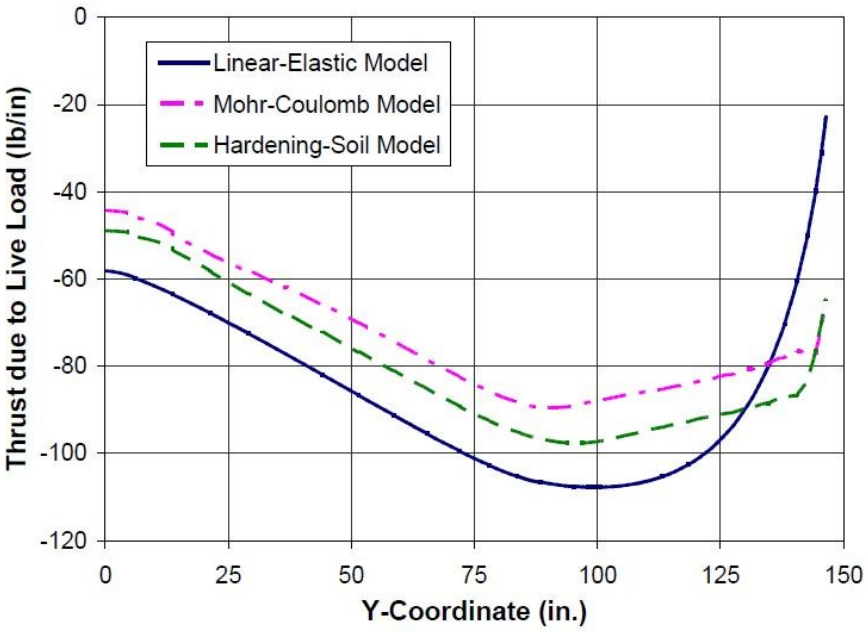

Figure 3-20 – Axial thrust diagram with 6' of cover (Peterson *et al.,* 2010)

The non-linear models performed similarly, most of the time predicting the exact same structural forces. The linear model deviated, at times significantly, from the non-linear models. Peak positive and negative moments were generally lower in all cases for the linear model due to the greater stiffness associated with no plastic behaviour. Results from the axial thrust diagrams showed that all of the models produced similar results, with the exception of the crown station, where the linear soil model took a significant dip in magnitude while the other models did not. When comparing the non-linear models, generally the agreement was good. In most cases, the Mohr-Coulomb model predicted larger moments and less thrust than the hardening model, due to the stress dependant stiffness. The nonlinear soil models displayed a high degree of plasticity and nonlinearity, with many instances of soil failure. Without this plasticity, the Mohr-Coulomb model and linear elastic model should have produced identical results.

The researchers postulated that due to the similarities between the nonlinear models and deviance of the linear model that the nonlinear models must be correct. It was concluded that the less rigorous of the nonlinear soil models, the Mohr-Coulomb model, was the best suited model to run the 3-D analysis.

Validation for the models and procedures used was provided by comparing the 3-D finite element model with experimental data acquired by Webb *et al.*, (1999). A cross section of the structure is displayed in Figure 3-21 which shows the instrumented locations. This test is described in more detail in Chapter 3.2. The Mohr-Coulomb model was used, although some preliminary modelling using the hardening model suggested that the results would be similar. The linear elastic model was not used.

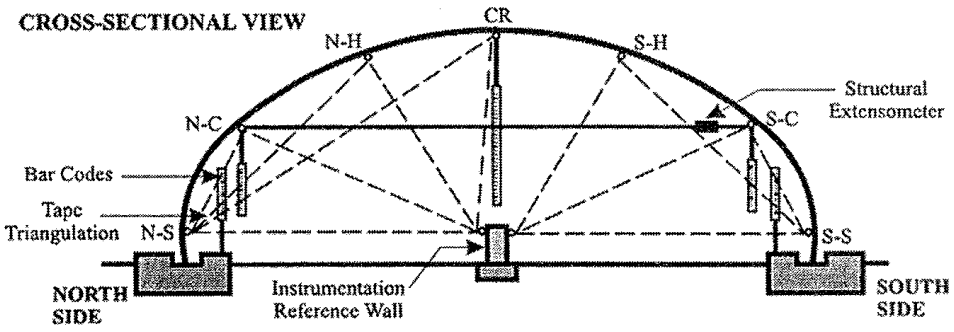

Figure 3-21 – Instrumentation stations

Dead loads were applied as previously described for the 2-D plane strain models. Four models were analyzed; two different cover depths, 1' and 3', and two backfill stiffness's, SW95, (Test 1), and SW85, (Test 2). A novel orthotropic model was constructed for the steel shell as Plaxis did not contain a proper orthotropic material model. Shell elements with the proper circumferential properties were fastened together longitudinally via small flexible elements, effectively reducing the longitudinal stiffness. Axial thrusts and bending moments are displayed in Figure 3-22 and Figure 3-23 respectively. The shapes of these diagrams are consistent with those obtained from the 2-D plane strain analysis.

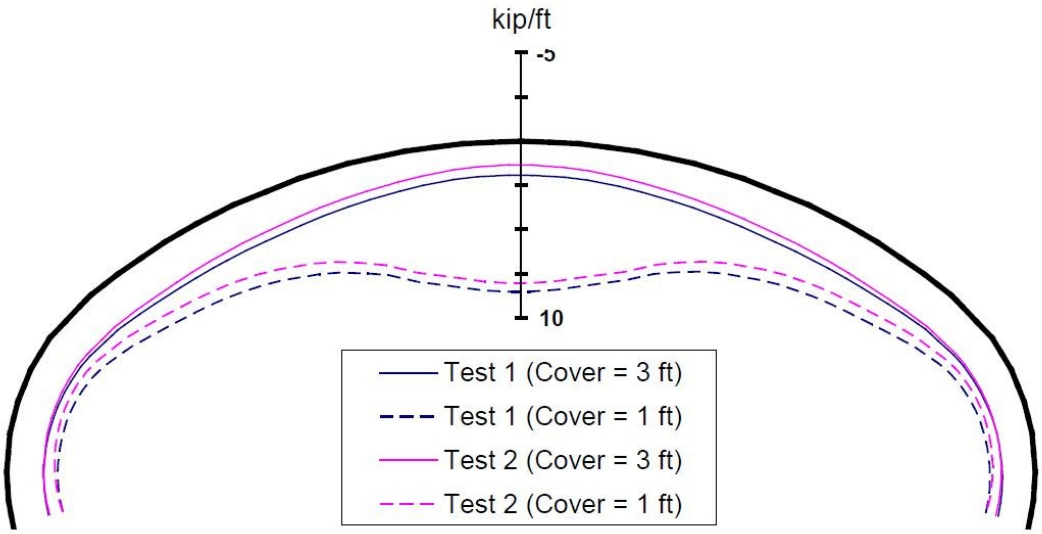

Figure 3-22 – Axial thrust of culvert under various conditions

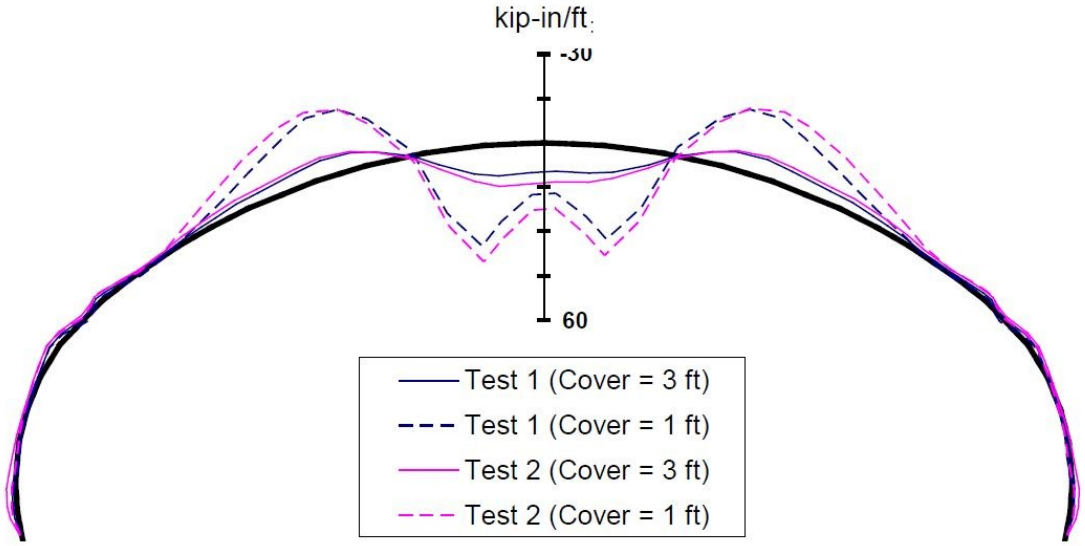

Figure 3-23 – Bending moment of culvert under various conditions

The results, however, were very inconsistent when compared to the experimental data. Axial thrusts in most cases were highly conservative at the springline while being slightly

more accurate at the crown. Negative bending moments were reasonably well predicted by the model. The maximum positive moment, however, was poorly predicted by Plaxis, over-predicting the value by 2 to 7 times the experimental data. Plots which display the predicted and experimental data at six different points on the structure were constructed from data tables in the report, and are presented in Figure 3-24 and Figure 3-25. The X-Axis labels correspond to various cross sectional locations, defined in Figure 3-21.

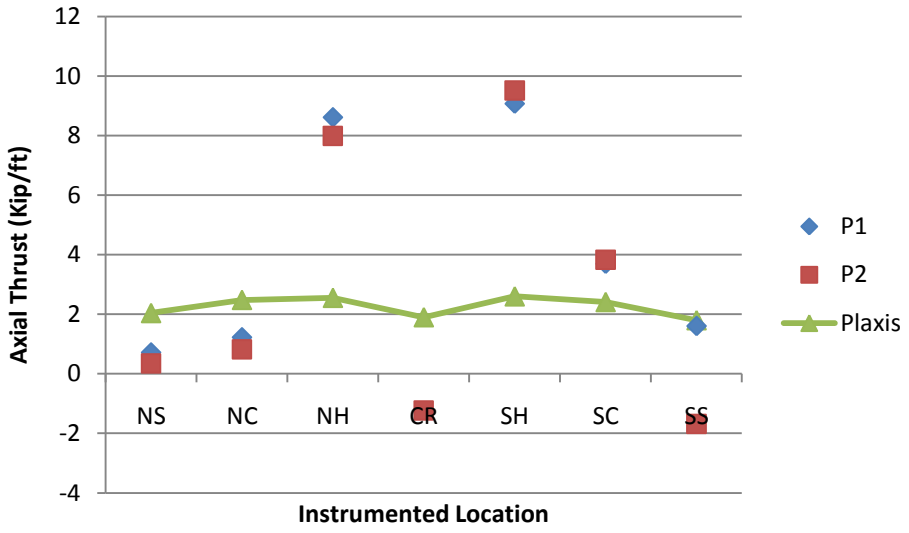

Figure 3-24 – Axial thrust – Test 1, 3' of cover

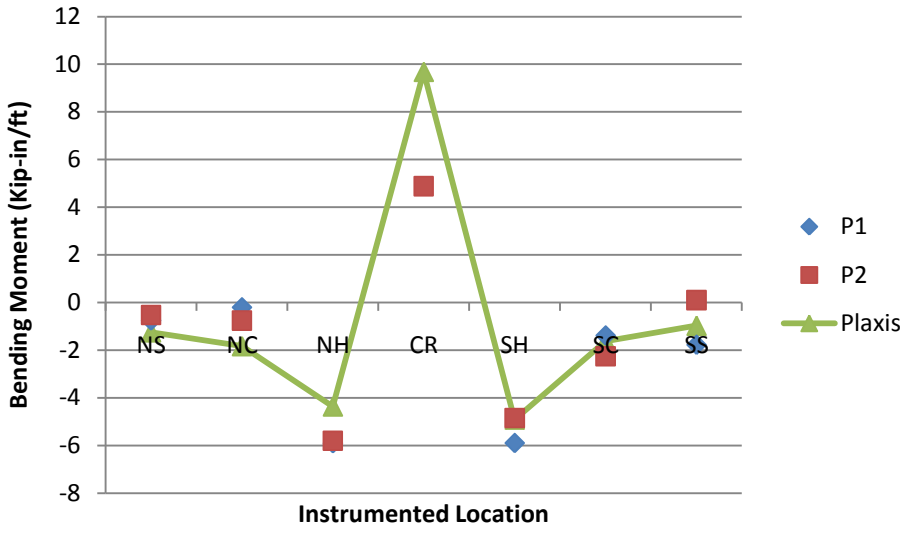

Figure 3-25 – Bending moments – Test 1, 3' of cover

The lack of further validation of the modelling methods used in the NCHRP Report 647 highlights the significance of the empirical and modeling work in this thesis.

CHAPTER 4 - EMPIRICAL ANALYSIS

4.1 LONG SPAN BOX TEST APPARATUS

4.1.1 General

A box culvert, manufactured and assembled in Dorchester, NB, was constructed for the purposes of testing a variety of live load conditions. The structure was a deeply corrugated steel long span box culvert with a span of 15 m and a rise of 3.5 m. The structural shell was comprised of Super-Cor corrugated plates, as described in Chapter 4.1.2. Figure 4-1 displays the steel structure, including the "Bolt-A-Bin" end treatment, while Figure 4-2 shows the structure partially buried. More precise dimensions are included in Chapter 4.1.3. Because this structure was built with the sole purpose of experimental testing, a robust testing sequence was designed which included extensive structural monitoring.

Figure 4-1 – Unburied structure with "Bolt-A-Bin" end treatment

The structure was monitored during backfilling and tested under a range of live load conditions, including various backfill depths and truck positions. The backfill depths tested, as measured from the top of the barrel plate to the roadway surface, were 0.45, 0.6, 0.75, 1.05, 1.35, and 1.55 m.

Figure 4-2 – Partially Buried Test Stucture

4.1.2 Structural Plate Details

The corrugation profile of this structure is known under the trade name Super-Cor, developed and manufactured by Atlantic Industries Limited. The exact dimensions of individual corrugated plates as well as cross sectional geometries are displayed in Figure

4-3 and Figure 4-4 respectively.

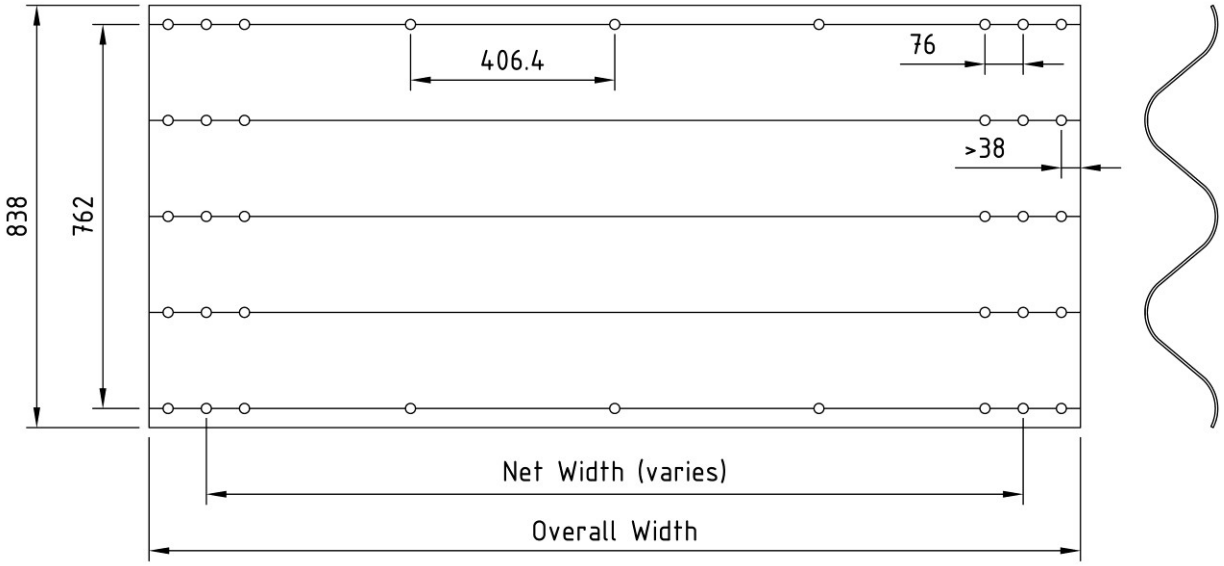

Figure 4-3 – Plan view of corrugated plates

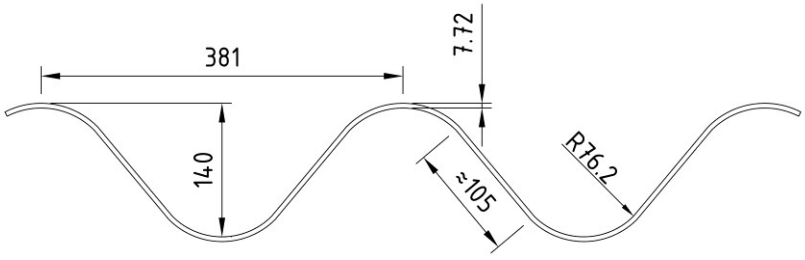

Figure 4-4 – Corrugated plate section

Specific material properties of the structural steel and various other sectional properties are provided in Table 5-1. The material properties were obtained through coupon testing of samples performed at Dalhousie University. The yield strength represents an average as taken from various locations in the plate cross section.

4.1.3 Test Structure Geometry

The span of the test structure was 15 m, and was comprised of 18 transverse rings giving a total length of 13.7 m. The haunch radius was 2.5 m and the crown radius was 15 m. The cross section is shown in Figure 4-5.

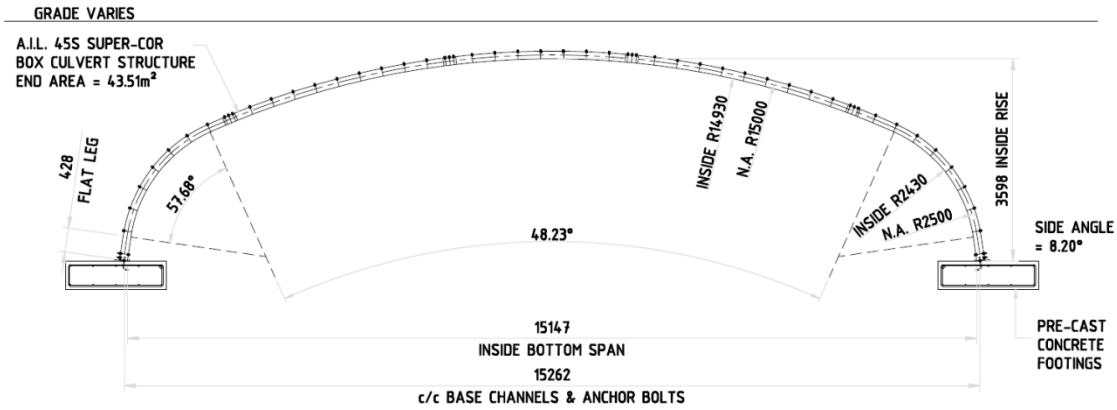

Figure 4-5 – Geometry of Test Structure

The end treatments for the test structure were chosen such that they simulated a bevelled end; which often produces the maximum structural response. The East face end condition was a Super-Cor retaining wall. The Super-Cor Retaining wall was a typical cantilevered retaining structure comprised of un-radiused Super-Cor plates bolted adjacent to one another. The West face end treatment was comprised of large steel bins filled with sand. These bins were designed and manufactured by AIL and are known by the trade name “Bolt-A-Bin”. Tension cables connecting the two end treatments provided additional support for the Super-Cor Retaining wall. The main purpose of the retaining structures on each face was to contain the soil such that a short length of structure could be constructed.

The structure was assembled in a manner typical of a standard field assembly. As per many culvert installations of this size, the footings were comprised of pre-cast, reinforced concrete, with a cross section 1.8 m wide by 0.5 m deep. Each side of the structure sat on five segmented footings, four of which were 3 m long, (holding 4 steel rings), and one of which was 1.6 m long, (holding 2 steel rings). The footings were cast with anchor bolts to which a steel channel was attached. The structure was bolted to the channel to maintain its position during backfilling. Figure 4-6 displays the footing configuration during structure assembly. Some differential settlement is also seen between precast units.

Figure 4-6 – Precast Footings

The structure was manufactured in Dorchester, NB, and assembled on site by Atlantic Underground Services Ltd. Bolt torque was specified to 200 – 400 N-m, however checks performed on random bolts indicated that the actual torque used was greater than this

range. Bolt torque limiters were not utilized during construction, making it difficult to achieve specific torque values. It is also worth noting that the structure was assembled and instrumented several months before backfilling and testing operations commenced. This exposed the unburied structure to large temperature gradients.

Engineered backfill was installed in an envelope that extended three meters from the base of the structure. The engineered backfill was comprised of soil with properties that allowed it to be well compacted and resist various soil failure modes. Specific soil properties as obtained through geotechnical testing are provided in Chapter 5.3.1. In addition to laboratory soil tests, in-situ density and moisture content tests were performed on selected lifts. The density and moisture content were measured with a Nuclear Densometer using services provided by Acadia Consultants & Inspectors Ltd. Relative standard proctor density was maintained above 95%, as per the test procedure specifications. The soil outside the engineered backfill envelope was native and was characterized as gravel with silt and sand. No geotechnical testing was performed on soil in this zone.

4.1.4 Instrumentation

4.1.4.1 Data Acquisition

Data was acquired from the strain gauges by routing them into six Campbell Scientific AM-16/32A multiplexers. Each multiplexer had the capacity for 16 quarter bridge strain gauges. The data was collected from the multiplexors via a bridge completion unit attached to a Campbell Scientific CR-3000 data logger. Power to the data logger was provided from a Campbell Scientific PS100 12V power supply. Battery charge levels were collected with the data to ensure that the voltage was within acceptable limits to ensure data accuracy. The data was stored on a Campbell Scientific CFM100 compact flash

memory module.

The protocol for reading each gauge was to switch to the channel and delay for 150 μs, excite the gauge, and allow it to settle for 20 μs. The logger then acquired 15 readings, averaged the last 10, and wrote that average to the data file. This process was repeated for each of the 96 channels. The process was selected to minimize noise in the strain readings.

Data was collected from the gauges in both raw voltage and microstrain. Readings were triggered manually via a laptop located outside the structure, which also collected the raw data from the memory. Each time a manual reading was to be taken, the system was triggered three times and the results were averaged. This further reduced the possibility of error in the measured strain. In addition to manual data readings, automatic readings were triggered every 6 hours at 0:00, 6:00, 12:00 and 18:00. The data acquisition system is shown in Figure 4-7.

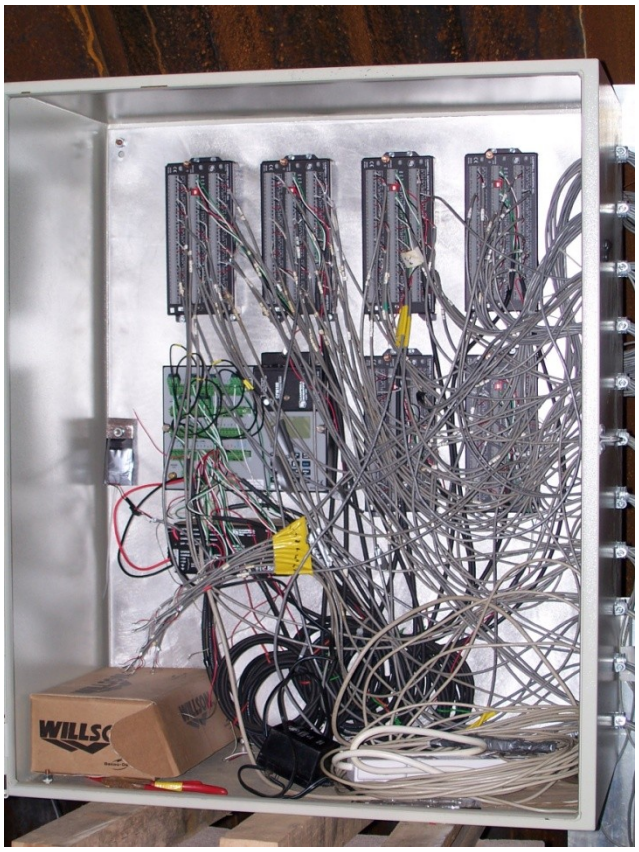

Figure 4-7 – Data acquisition system

4.1.4.2 Strain

Strain gauges were attached to both the barrel and crown stiffening rib of the structure. The gauges were “Micro-Measurement” quarter bridge 350 Ω model CEA-06-125UW-350. These gauges were bonded in the transverse direction to the inside of the barrel. Figure 4-8 shows a typical strain gauge.

Figure 4-8 – Typical strain gauge

The strain gauges were labelled according to their position on the structure. They were identified by the ring they were installed on, peripheral location relative to the transverse bolts, as well as their placement in the cross section. The labelling convention used is displayed in Figure 4-9. For example, A-12-1 is located on “Ring A”, at a transverse bolt spacing of 12 counted from the North side footing, and is located at the extreme inner fiber of the structure on the barrel.

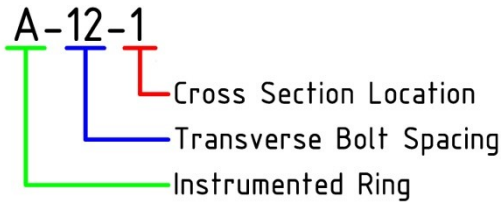

Figure 4-9 – Strain gauge abbreviation

The strain gauges were arranged in four rings on the barrel, labelled Ring A through Ring D. Each ring consisted of a single plate two corrugations wide. The ring locations are shown in Figure 4-10.

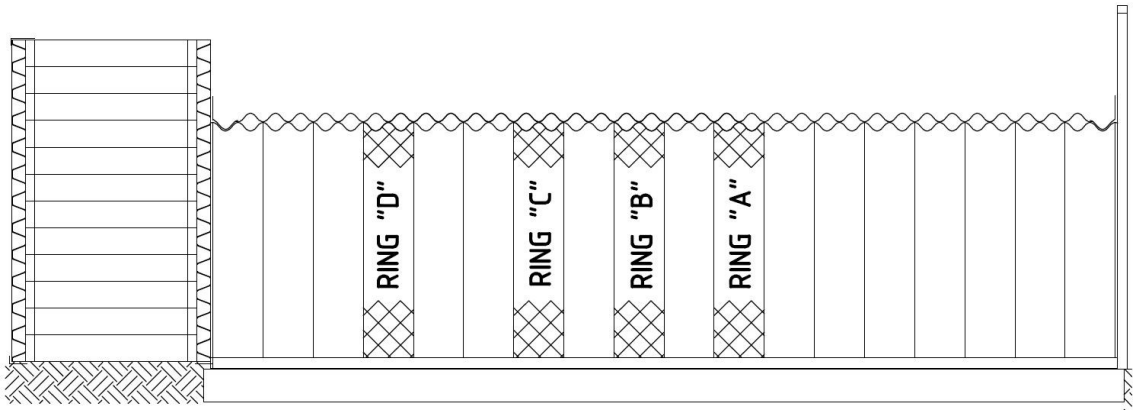

Figure 4-10 – Instrumented ring locations

Peripheral gauge locations are shown in Figure 4-11 at each of the instrumented rings. The positions were numbered 0 through 45, referenced from the North side footing to the South side footing. Gauges were placed at the midpoint between transverse bolts, except at the crown.

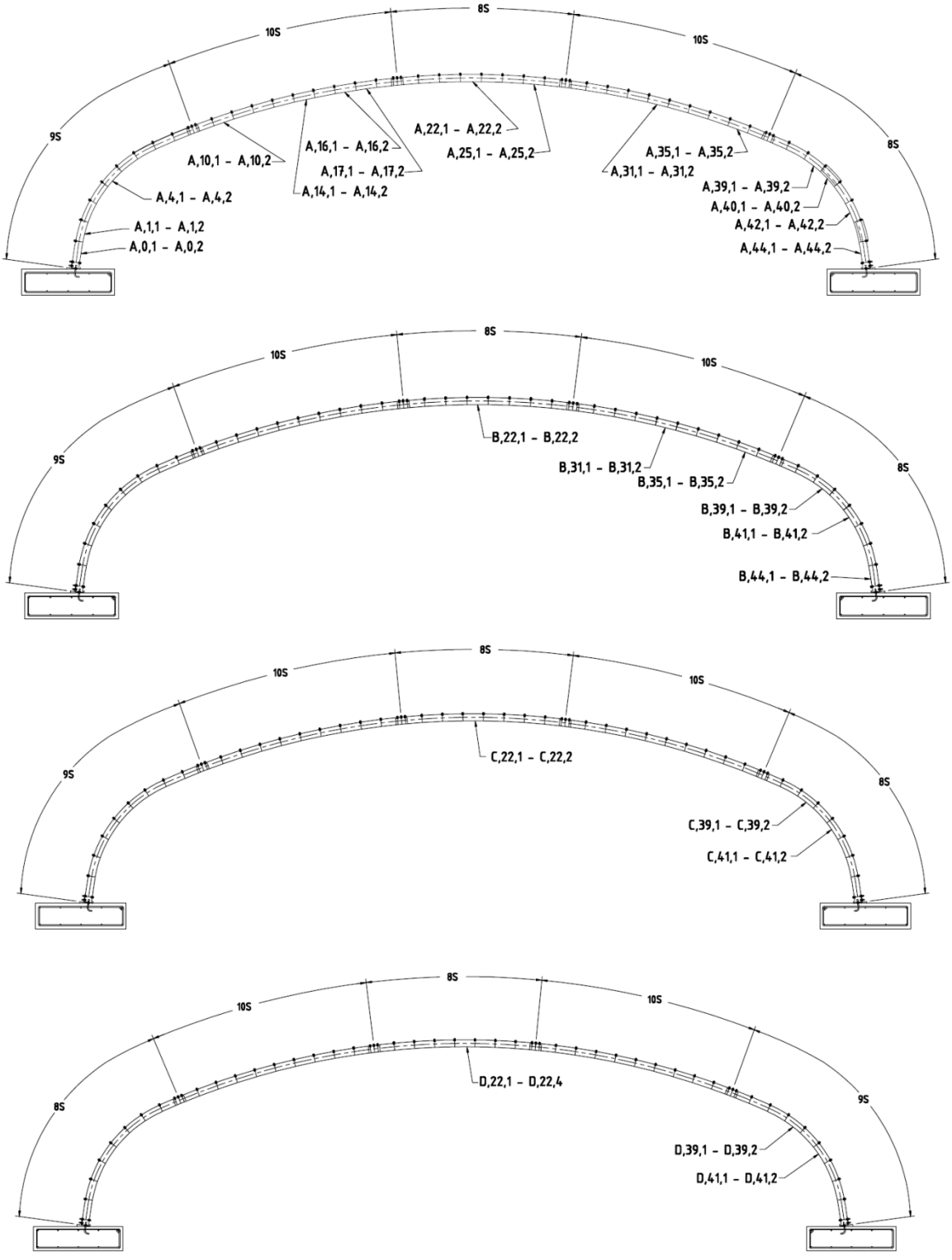

Figure 4-11 – Gauge locations on instrumented rings

At each peripheral station gauges were installed at the crest and valley of the cross section and labelled G2 and G1 respectively, as shown in Figure 4-12.

Figure 4-12 – Strain gauge location in structure cross section

4.1.4.3 Deflections

Flat bottomed plum bobs sitting atop manual dial gauges were used to measure precise deflections. In the crown location only vertical movement was measured. At the haunches the plumb bob was fixed to the structure at an angle, allowing both lateral and vertical deflections to be calculated. To measure lateral footing displacements, a dial gauge was placed directly against the structure approximately 100 mm above the footing. Examples of each of these gauges are shown in Figure 4-13.

Figure 4-13 – Manual deflection gauges at the footing, crown, and haunch

On “Ring A” five manual dial gauges were installed at the footings, haunches and crown. In addition, Rings B, C, and D contained instrumented crown locations. During live load testing readings were taken from the crown gauges only due to time constraints.

For more global deflection measurements, typical survey equipment including a total station was used. The survey equipment was referenced to two external points outside the structure. Eleven reflectors were installed inside the structure; nine around the periphery of Ring A and two stationary targets used for reference. The movement of these points was monitored for both vertical and horizontal deflection. Figure 4-14 displays the location of these reflectors.

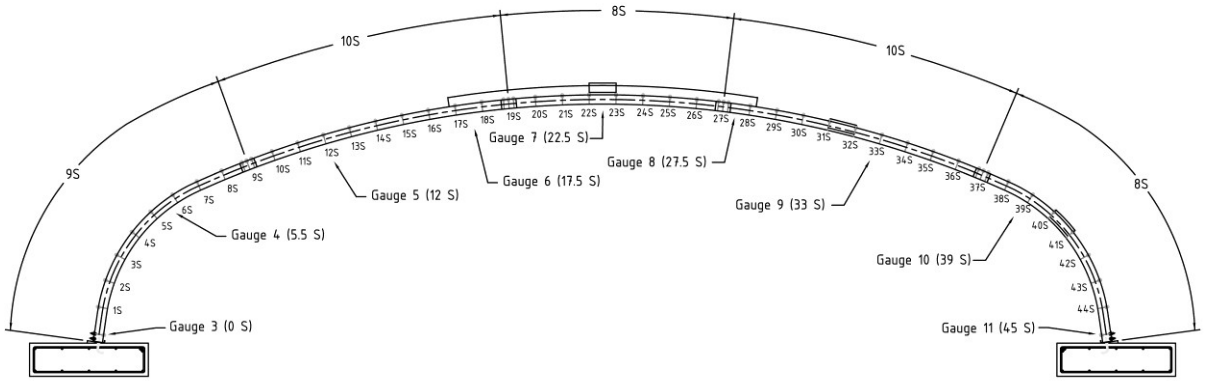

Figure 4-14 – Location of reflectors for survey measurements

4.1.5 Testing Procedure

Backfill was placed on both the North and South face of the structure and then compacted with vibratory plates and rollers. The fill was placed in lifts of approximately 200 mm compacted until the top of the crown was reached. Above the crown level, the backfill was placed at 0.45 m, 0.6 m, 0.75 m, 1.05 m, 1.35 m, and 1.55 m above the top of the barrel.

Live load testing was performed using a vehicle configured to replicate a CL-625, as referenced in CAN/CSA-S6-06 Canadian Highway Bridge Design Code (2006), although the rear axle was not included because it falls outside of the structure footprint. The testing vehicle was a Volvo model DD S60 370 with a specially designed trailer, shown in Figure 4-15.

Figure 4-15 – Testing vehicle

To obtain the proper wheel loads, concrete blocks were stacked onto the load frame. Figure 4-18 shows concrete blocks being loaded onto the bed of the test vehicle. Individual wheels were weighed using portable scales with an accuracy of 1% of displayed loads. The results from these measurements are shown in Table 4-1.

Table 4-1 – Wheel and axle weights of test truck

Axle	Testing Vehicle			CL-625
	Drivers Side (kN)	Passenger Side (kN)	Total (kN)	Total (kN)
Front	26.5	26.3	52.8	50
Front Tandem	66.8	66.4	133.2	125
Rear Tandem	68.5	61.3	129.8	125
Rear	83.6	85.5	169.1	175

Longitudinal test truck dimensions were measured directly from the vehicle. Tire pressures were adjusted to 690 kPa, thus the transverse tire footprint was assumed to match the CL-625 design truck. Dimensions of the assumed tire footprint are shown in Figure 4-16.

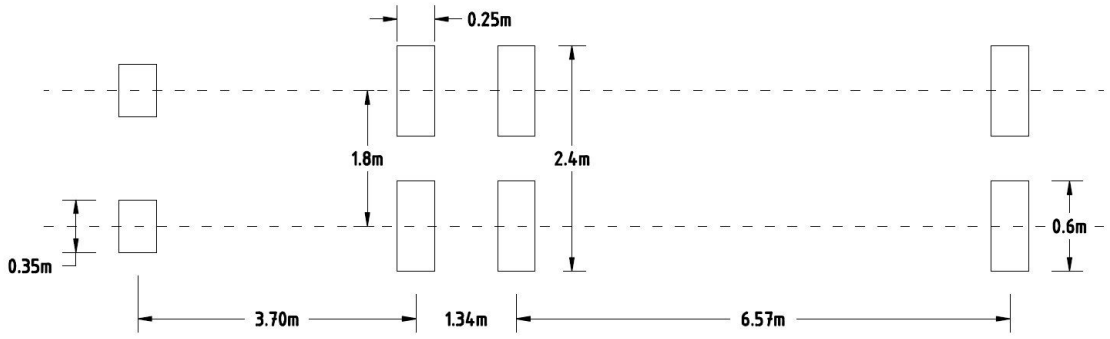

Figure 4-16 – Assumed tire footprint of test vehicle

Three transverse lines were considered in this test, representing various distances from the instrumented rings. For each of these transverse lines, seven truck positions were used, providing 21 unique truck positions per test. These positions are shown in Figure 4-17.

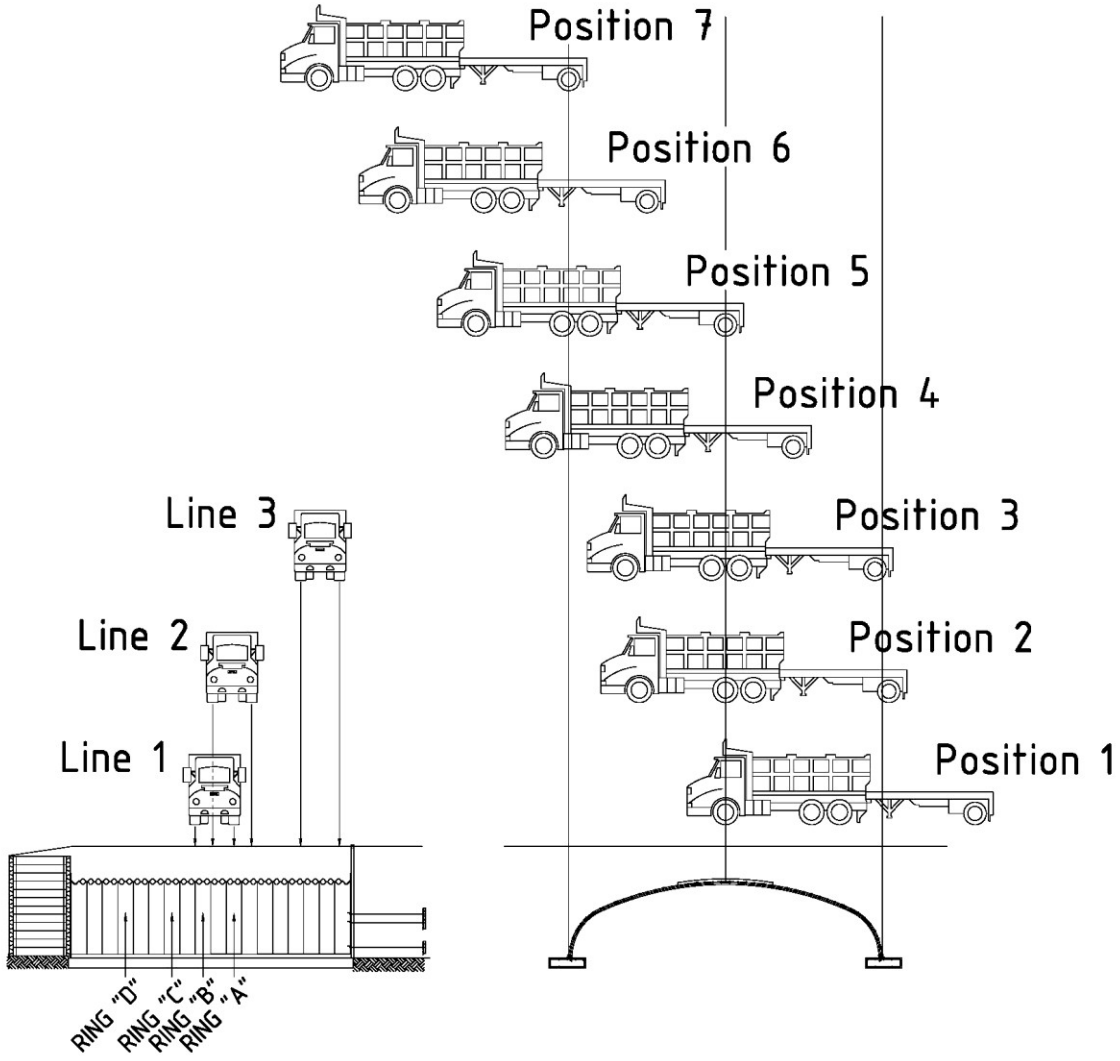

Figure 4-17 – Live load truck lines and positions

The test truck was stopped in each specified position while strain and crown deflection were measured. Zero readings, (that is, a reading without live load), were taken prior to the commencement of each test. Zero readings were also taken before each line, and upon the conclusion of the live load test once the loads were removed.

Figure 4-18 – Test frame during loading

4.2 LIVE LOAD RESULTS

4.2.1 Analysis

Strain gauges adhered to the peaks and valleys of the corrugated plate were used to compute bending moments and axial thrusts at instrumented sections. The following procedure was used for computing structural forces in the barrel plate. It was assumed that plane sections remained plane during bending. A schematic of the strain gauge locations, stresses acting on the plate, as well as labelling conventions is shown in Figure 4-19.

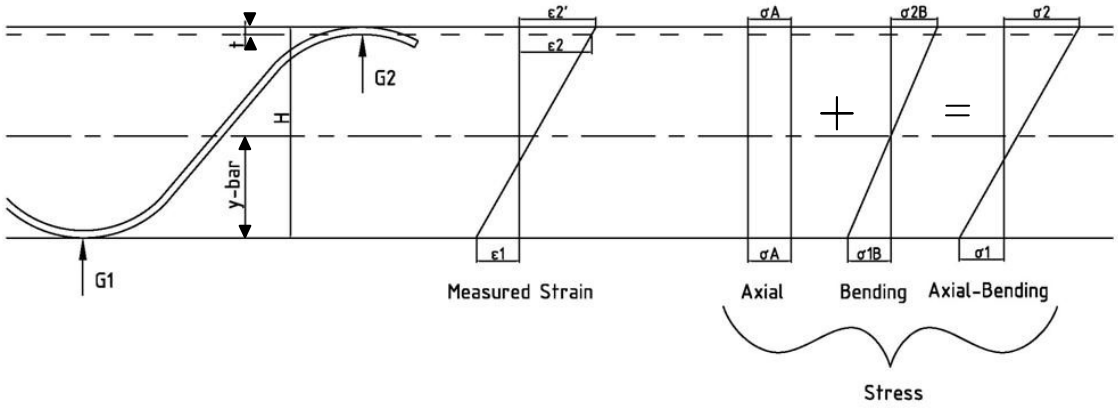

Figure 4-19 – Gauge locations and stresses acting on the barrel plate

To account for gauge 2 being located on the inner surface of the structure, rather than the extreme fiber, Equation 4-1 was applied to linearly interpolate the strain.

$$\varepsilon_2' = \left[\frac{\varepsilon_2 - \varepsilon_1}{H - t}\right] H + \varepsilon_1 \qquad \textbf{4-1}$$

Where:

ε_1 = Measured strain from gauge 1 ($\mu\varepsilon$)

ε_2 = Measured strain from gauge 2 ($\mu\varepsilon$)

ε_2' = Measured strain from gauge 2 extrapolated to the extreme fiber ($\mu\varepsilon$)

H = Total section depth (mm)

t = Section thickness (mm)

Tensile strains were taken as positive while compressive strains were taken as negative. The strains were then converted to stresses by multiplying by the modulus of elasticity, as per Equations 4-2 and 4-3.

$$\sigma_1 = E\varepsilon_1 \qquad \textbf{4-2}$$

$$\sigma_2 = E\varepsilon_2' \quad \textbf{4-3}$$

Where:

σ_1 = Stress at extreme inner fiber (MPa)

σ_2 = Stress at extreme outer fiber (MPa)

E = Modulus of elasticity (MPa)

These stresses were converted to axial and bending stresses at the extreme fiber using Equations 4-4, 4-5 and 4-6. Two expressions were used for bending as the bending stresses at the top and bottom of the section were different. Since the neutral axis was located slightly above mid-depth the bending moment was computed from the extreme inner fiber stress, or σ_{1B}.

$$\sigma_A = \frac{\sigma_2 + \sigma_1 Z}{1 + Z} \quad \textbf{4-4}$$

Where:

σ_A = Component of section stress from axial compression (MPa)

$\bar{y}$ = Centroid of section measured from the inner fiber (mm)

$Z = \frac{H-\bar{y}}{\bar{y}}$

$$\sigma_{1B} = \frac{\sigma_1 - \sigma_2}{1 + Z} \quad \textbf{4-5}$$

$$\sigma_{2B} = -\sigma_{1B}\left(\frac{H - \bar{y}}{\bar{y}}\right) \quad \textbf{4-6}$$

Where:

σ_{1B} = Stress of extreme inner fiber from bending (MPa)

σ_{2B} = Stress of extreme outer fiber from bending (MPa)

Equations 4-7 and 4-8 were used to compute the structural forces in the barrel plate.

$$F_A = \sigma_A A \quad \textbf{4-7}$$

$$F_B = \frac{\sigma_{1B} I}{\bar{y}} \quad \textbf{4-8}$$

Where:

F_A = Axial thrust (KN/m)

F_B = Bending moment (KN-m/m)

A = Steel cross sectional area (mm^2/m)

I = Cross sectional moment of inertia (mm^4/m)

4.2.2 Bending Moments

For most long span box culverts, bending moments are significant and typically govern the structural design.

During backfilling the magnitude of bending moment at the haunches was nearly twice that of the crown, however, during live load testing this trend was reversed. Figure 4-20 displays the bending moment envelope acting on the structure from all truck positions and backfill depths. The largest bending moments occurred on the crown radius and tapered towards the footings of the structure.

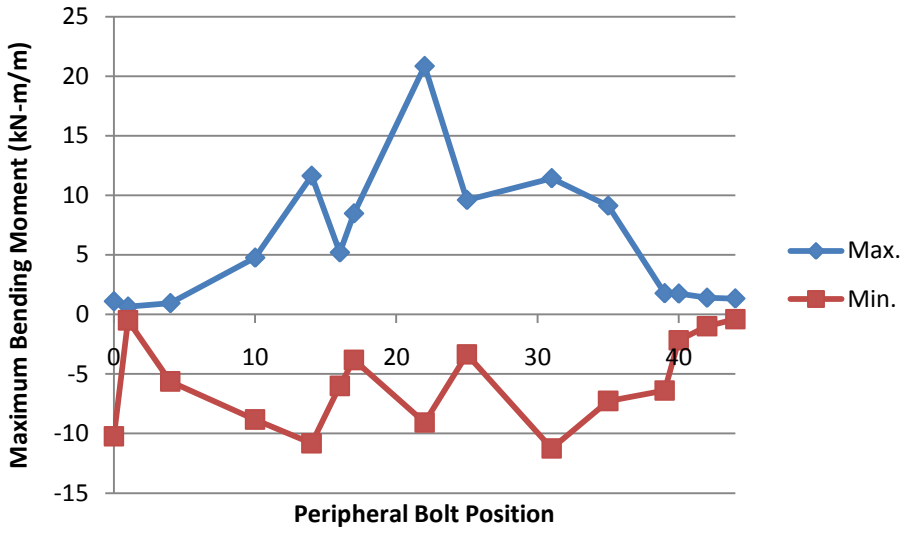

Figure 4-20 – Bending moment envelope from all truck positions and backfill depths

Peripheral bending moments at various truck positions are presented in Figure 4-21. Peripheral bolt positions are displayed in Figure 4-11. In a general sense, positive bending was induced under wheel loads and negative bending induced between wheel loads. In this sense the box culvert behaved as a traditional plane frame. The largest bending moments were induced at the crown in load cases where an axle or axles were placed at the centerline; such as positions 2, 3, and 5. In Truck position 4, where the tandem axle and rear axle straddled the crown, negative bending occurred at the crown and positive bending occurred under the tires. A large negative moment was observed at the base of the structure, (peripheral bolt position 0), for load positions 2 and 3, where the rear axle was placed directly above the footing.

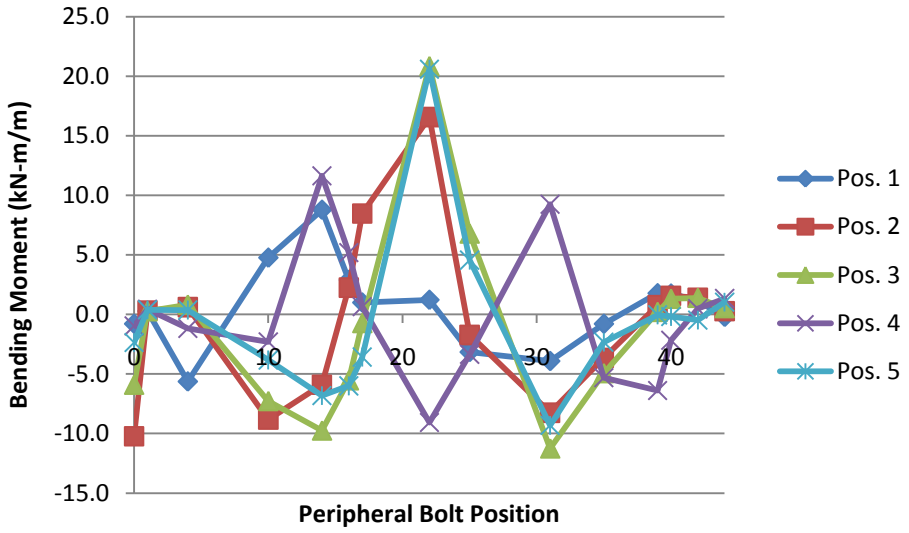

Figure 4-21 – Peripheral bending moment; 0.45 m of cover, line 2, at various truck positions

Backfill depth was found to have a significant impact on bending moment. The reduction in bending moment as backfill depth increased loosely resembled a sine curve, with large decreases in bending moment taking place between 0.6 and 1.05 m of cover. Figure 4-22 displays crown bending moments for some heavily loaded truck positions of both positive and negative moment. Stations 22 and 31 were loaded under position 3 while stations 39 and 14 were loaded under position 4. Under lower cover the live load produced significant bending moments which accounted for a large proportion of the total moment. Under higher backfill depths, live load bending moments were entirely eclipsed by the moment due to dead loads.

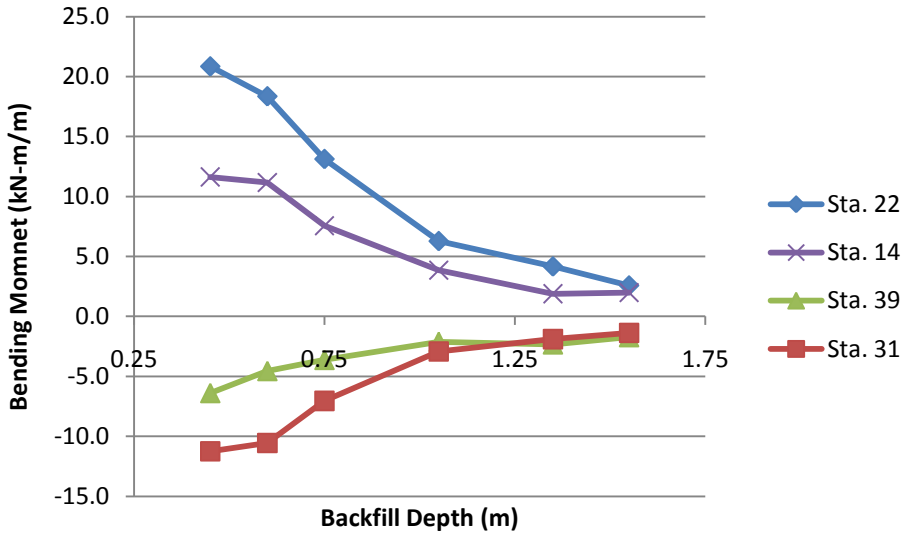

Figure 4-22 – Maximum positive and negative bending moments at various backfill depths

Figure 4-23 and Figure 4-24 displays longitudinal bending moment profiles at the crown and haunches, respectively. Bending moments were only significant directly under the load and decreased rapidly 2-4 meters away. The haunch moments were selected based on maximum magnitude, rather than gauge location. The maximum haunch moment occurred in a variety of peripheral locations between stations 38 to 42. The unusual shape of Figure 4-24 was likely a result of failure to capture the maximum haunch moment at “Ring A”, reducing the apparent maximum moment at the ring. Given the high moment gradient at the haunches, the maximum moment on “Ring A” likely occurred adjacent to the strain gauges installed in this region.

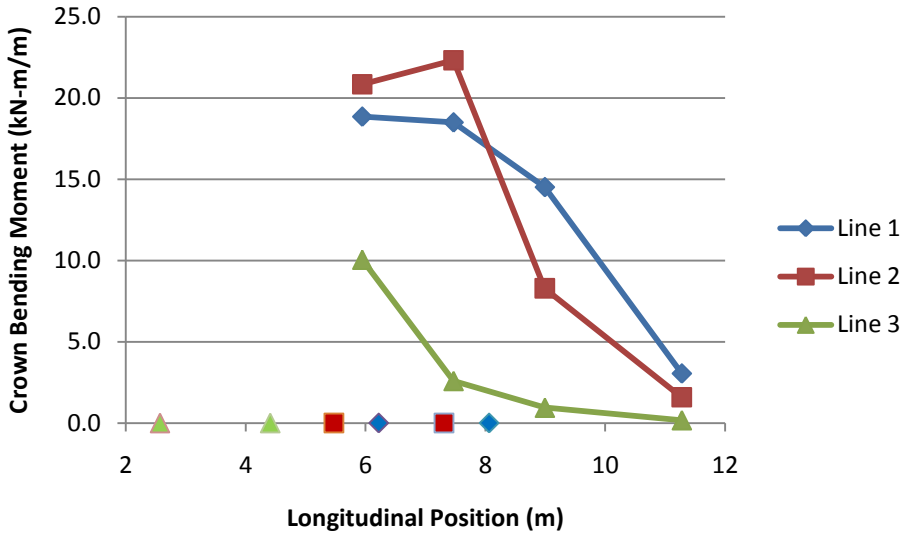

Figure 4-23 – Longitudinal crown bending moment; 0.45 m of cover, position 3 at various lines

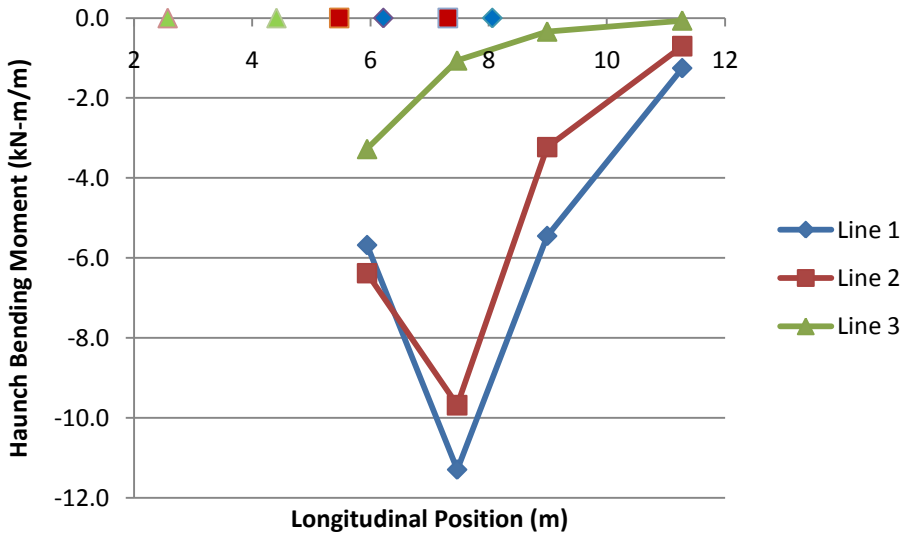

Figure 4-24 – Longitudinal maximum haunch moment; 0.45 m cover, position 4 at various lines

4.2.3 Axial Thrust

Although axial thrust rarely governs the design of corrugated box culverts, it is a cause of significant stress which can significantly increase compressive bending stresses. The thrust contributions from live loads were low when compared to the maximum thrust values from the dead load effects. Axial thrust around the periphery of the structure was more uniform than bending moments.

Figure 4-25 shows the maximum recorded minimum and maximum thrust values as recorded from all truck locations and backfill depths. Live loads did little to relieve axial thrust, as shown by the relatively low “positive” thrust values registered during testing. Compressive axial thrusts were generally greatest at the crown of the structure and decreased to a minimum at the base. A clear exception to this trend occurred at the footing of the structure; the maximum recorded thrust at station 0 was twice that of all other measured values. The data point appears to be erroneous, as it does not seem possible that the structure could incurred such a massive axial force at the base, and then mere inches away at station 1 register a thrust nearly 6 times lower. Also unusual was that such behaviour occurred on only one side of the structure, despite load cases which were nearly identical on the other side. That being said, the data was included as there was no electronic evidence that the gauges at this station were malfunctioning.

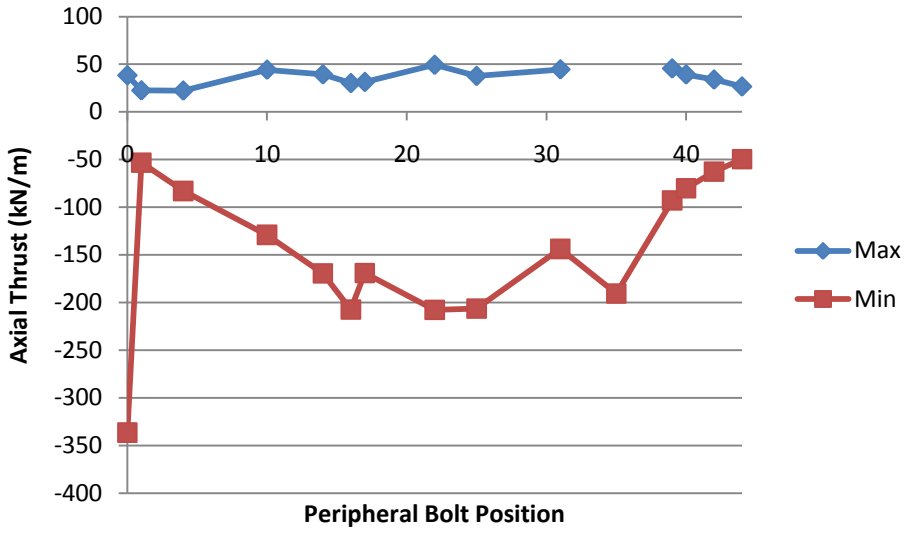

Figure 4-25 – Maximum and minimum thrust from all truck positions and backfill depths

Figure 4-26 shows the axial thrust values around the periphery of the structure at various truck positions. Generally the largest axial thrust values occurred directly under and around the load application. Most maximum thrust values at the crown, and resulted from loads placed directly above the crown. The large axial thrust observed at Station 0 at the base of the structure occurred in load cases where the rear axle was placed directly atop the footing. Despite the variety of truck positions displayed, the axial thrusts appeared very uniform.

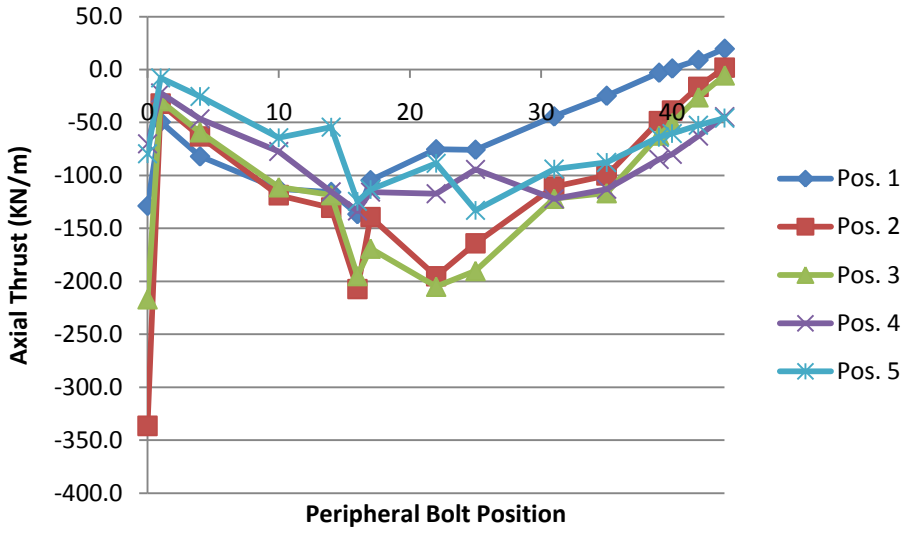

Figure 4-26 – Peripheral thrust profile; 0.45 m cover, line 2 at various truck positions

Longitudinal plots of thrust are provided in Figure 4-27 and Figure 4-28 for the crown and haunches respectively. At the crown, thrust values deteriorated very rapidly within 2 meters of the load. Axial thrust values consistently went into “tension”, meaning the thrust was relieved, a short distance away from the load. The data at the crown was slightly erratic, indicating some sensitivity to the load conditions. Small changes in the position of the truck or shear failure of the soil beneath the tires may have contributed to these irregular values. The maximum thrust in the haunches was more predictable. The maximum haunch thrust occurred under load position 4, where most of the truck’s mass was over the span of the culvert, causing the haunches and legs to carry nearly the entire weight of the vehicle. Thrust in the haunches deteriorated more gradually in the haunches than the crown. The tensile thrusts located away from the load at the crown were absent in the haunches. Generally thrust in the haunches was relatively low compared to the crown.

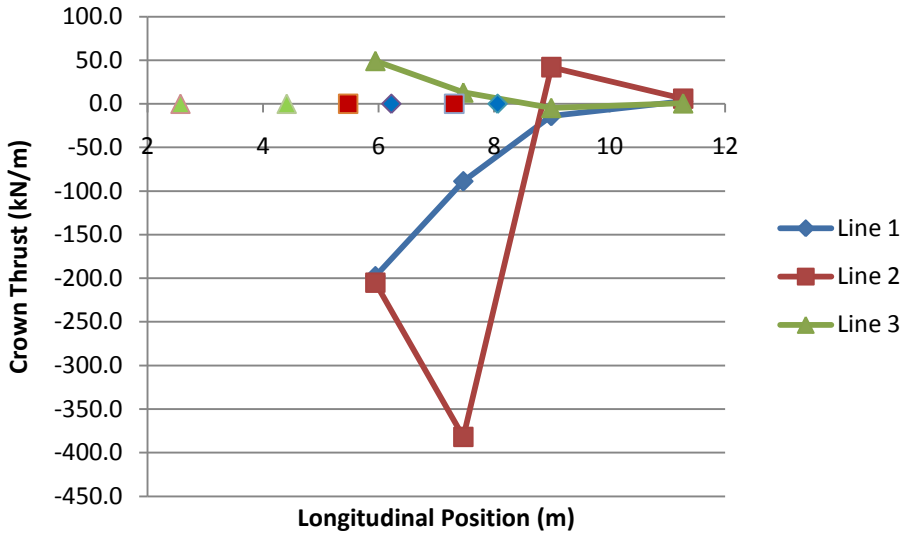

Figure 4-27 – Longitudinal crown thrusts; 0.45 m cover, position 3 at various lines

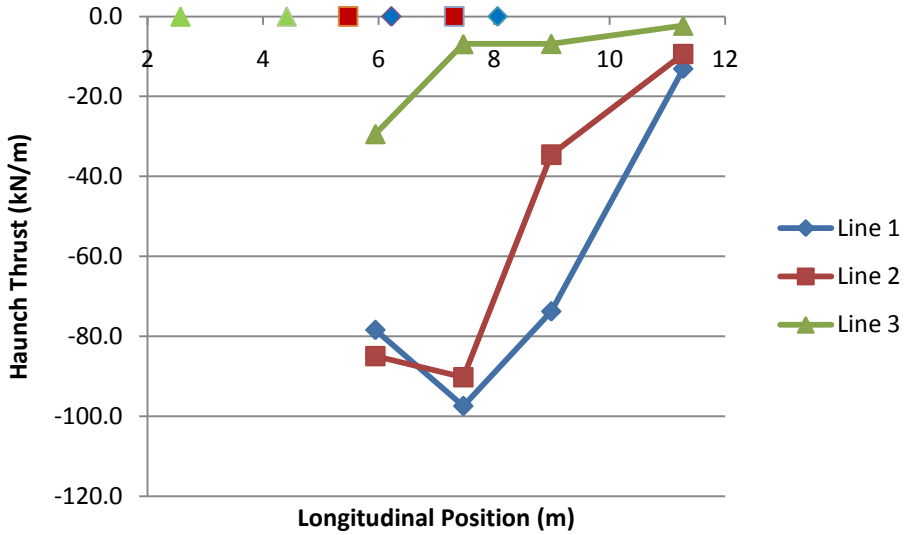

Figure 4-28 – Longitudinal maximum haunch thrust; 0.45 m cover, position 4 at various lines

4.2.4 Deflections

Deflections captured in this section were measured from manual dial gauges attached to the crown at each of the four instrumented rings. Only vertical measurements were taken during live load testing, as the survey equipment was not a practical means to measure the fine movements which occurred during testing.

Figure 4-29 displays the effects on backfill depth on crown deflection. Displacements increased significantly as the backfill depth decreased. Deflections diminished rapidly a short distance away from the load in the longitudinal direction. Significant reductions were observed two meters from the load and the deflection was negligible at four meters. The rate at which the deflection diminished in the longitudinal direction was much greater under shallow backfill depths. This was likely due to the wider load distribution under the deeper fills. This plot also showed the interaction between adjacent tires. The structure experienced only one longitudinal deflection wave despite two patch loads.

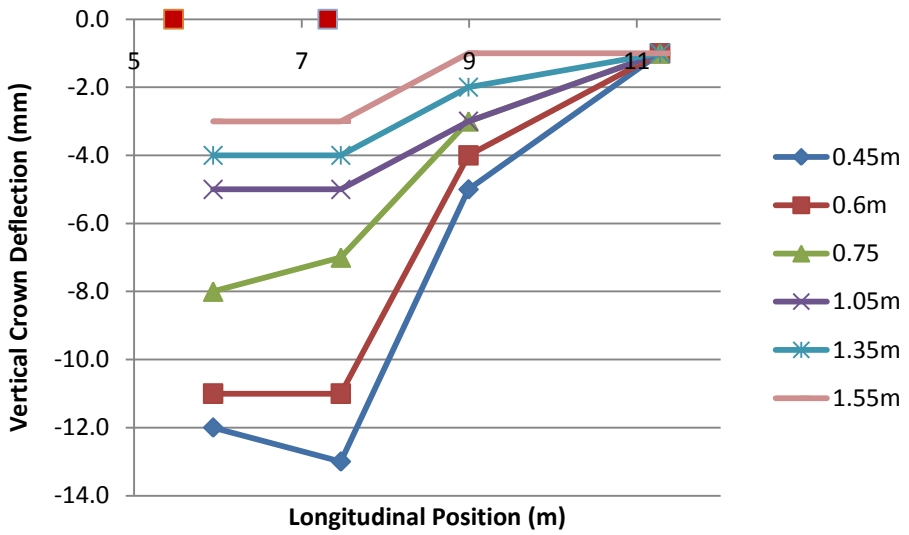

Figure 4-29 – Longitudinal crown deflection; line 2, position 3 at various backfill depths

Figure 4-30 shows the effects of placing the load at various longitudinal distances from the instrumentation. The magnitude of deflection decreased as the load was placed further from the instrumented rings in a nonlinear but consistent manner. When the lines were plotted at a constant distance from the load, as displayed in Figure 4-31, this consistency was further emphasized.

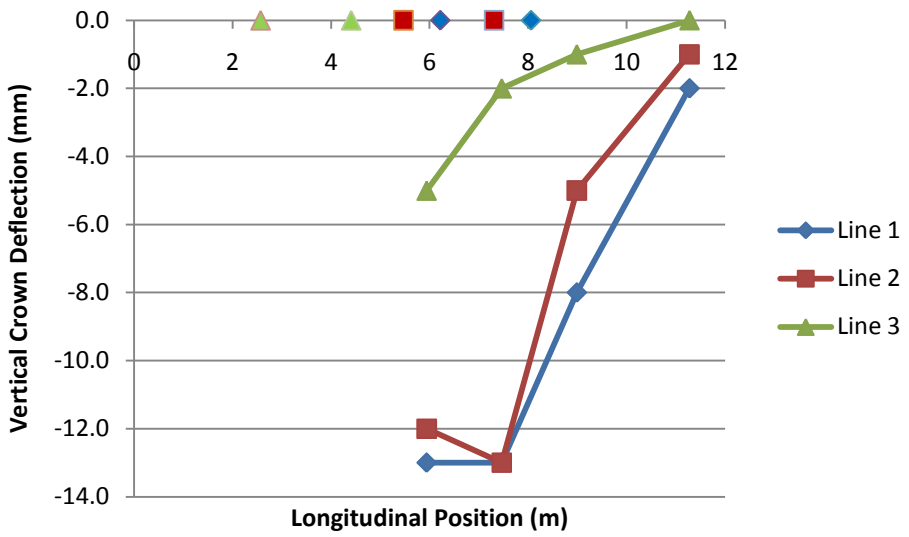

Figure 4-30 – Longitudinal crown deflection; 0.45 m cover truck position 3 at various lines

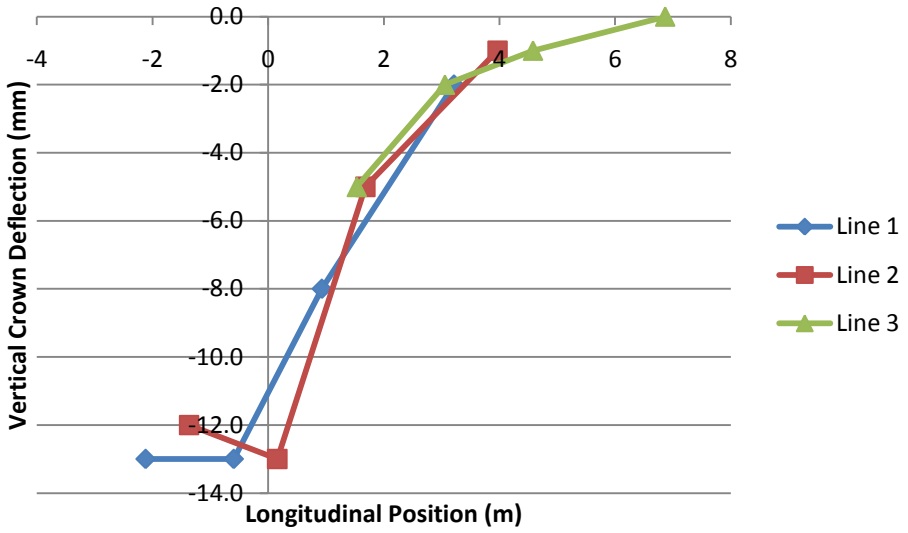

Figure 4-31 – Longitudinal crown deflection; 0.45 m cover truck position 3 with tire placed at 0.0 m

CHAPTER 5 - 3-D FINITE ELEMENT MODEL DEVELOPMENT

5.1 FEM OPTIONS

5.1.1 General

ADINA, (Automatic Dynamic Incremental Nonlinear Analysis), is a robust general purpose finite element package which may be used for a wide variety of structural, fluid, and heat transfer problems, both linear and nonlinear. To model the long span box culvert both linear and nonlinear analysis were performed. During a nonlinear analysis, the user breaks up the load application into a series of steps which are then iterated by the solver until certain convergence criteria are met. ADINA also features "Automatic Time Stepping" (ATS), which divides a solution into a smaller load step if the solver fails to find a solution in the specified number of iterations. If a solution still cannot be reached, ADINA subdivides the time step even further. Other features contained in Adina which are useful for the analysis of a soil-steel structures include element birth/death, (to model construction increments), and a wide variety of linear and nonlinear elements and material models.

ADINA contains a number of matrix solving algorithms, including sparse solver, 3-D iterative, iterative, multigrid, direct, and non-symmetric sparse. The default solver, and the solver used for this research, is the sparse solver. The sparse solver is both efficient and robust and cuts down on solution time, memory, and disc space when compared to other algorithms (ADINA R & D, Inc., 2008).

The "Full Newton Method" was employed for solving the nonlinear system of equations. This solver formulates a new stiffness matrix at the beginning of each load step and iteration, making it ideal for most structural applications. Energy was used as the convergence criteria, and the maximum number of iterations per time step was 15.

5.1.2 Elements and Meshing

Two different element types were used for the model; 3-D elements for the soil and shell elements for the orthotropic steel shell. Figure 5-1 and Figure 5-2 display the elevation and isometric views of the mesh used to model the long span box test. Groups of elements with different properties are shown in different colors. Regardless of element type, small displacements and small strains were used in all formulations.

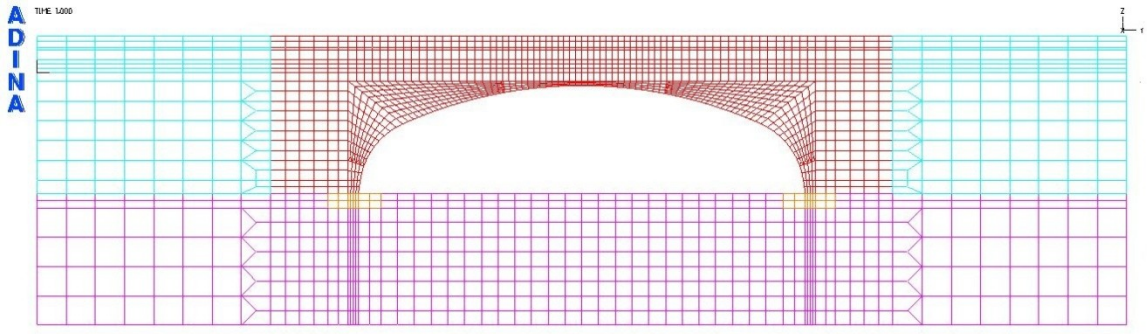

Figure 5-1 – Elevation view of FEA mesh

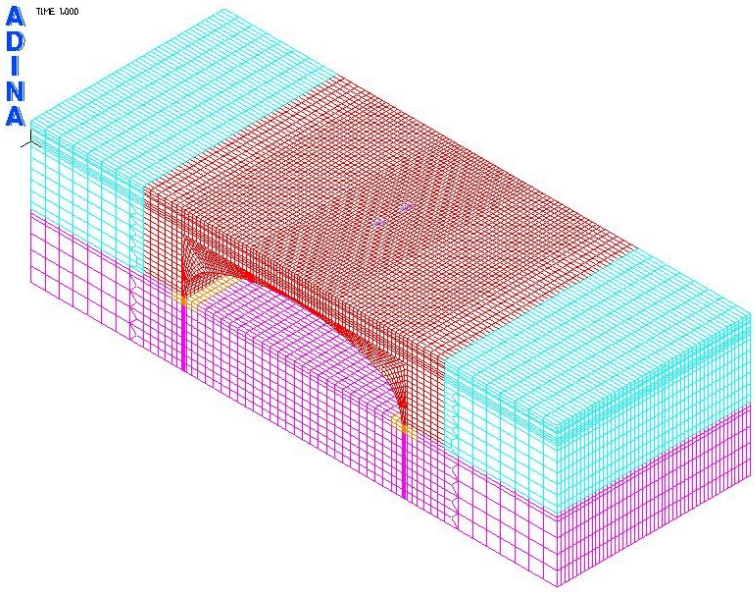

Figure 5-2 – Isometric view of FEA mesh

The corrugated steel plate was modelled using 4-noded isoparametric shell elements with a uniform thickness with equivalent section properties. The development of these equivalent elements is discussed in detail in Chapter 5.2. These elements are capable of modelling both out-of-plane bending and axial “membrane” forces. Thin, or “Kirchhoff” bending behaviour was used, which does not include deformations due to shear. Each node contained 5 active degrees of freedom; translations X, Y, and Z, and rotations α and β. The rotational degree of freedom corresponding to a vector normal to the shell surface was restrained, as the element contained no stiffness in this direction. The mesh density of shell elements was correlated to the bolt spacing, with approximately two elements between each transverse bolt (203.2 mm). The model was extruded the full longitudinal length of the original test (13700 mm) into 50 subdivisions, providing the shell elements with an aspect ratio of 1.3.

Soil and concrete elements were modeled with isoparametric displacement based 3-D solid elements. Most elements were 8-noded hexahedral elements, although some 6-noded degenerate triangular prism elements were used for element mesh density transition zones. These elements contain three translational degrees of freedom per node. Higher order elements were used for the Mohr-Coulomb material model, as described in Chapter 5.3.4.3. The element types are shown in Figure 5-3 – Elements used for FEM model

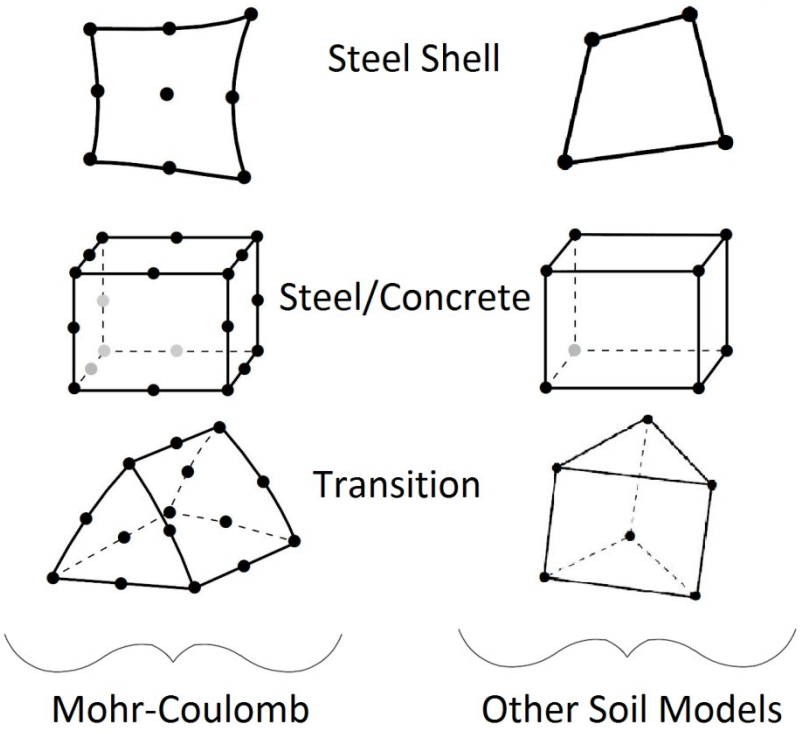

Figure 5-3 – Elements used for FEM model (ADINA R & D, Inc., 2008)

Nodes were shared between the shell elements and adjacent 3-D solid elements, creating a "fully bonded" condition between the steel and the soil. This assumption was chosen for several reasons. The main purpose of the study was specific to the structures live load response, where soil-steel slip was expected to be negligible, (Peterson *et al*., 2010). In addition, contact and friction would increase the non-linearity of the problem and make convergence significantly more difficult, and take much longer, to attain.

Mesh densities for the 3-D solid elements were varied from coarse to fine depending on the complexity and importance of the regions being modelled. Generally mesh density was increased around and above the structure, to be able to capture the soil-structure interaction as well as live load distributions.

5.1.3 Boundary Conditions and Loads

Boundary conditions for the long span box model were analogous to the soil being contained in a "smooth-sided" box. Nodes were restrained on each of the four vertical faces such that they did not displace in the direction normal to that face. Nodes on the underside of the model were restrained in the X, Y, and Z directions. These boundary conditions were selected to simulate the conditions in the field. The "open" ends of the structure were restrained with Super-Cor and Bolt-a-Bin retaining walls, which likely behaved more elastically normal to their faces than the infinitely rigid boundary conditions imposed in the finite element model. However it would have been difficult to quantify elastic boundary conditions and would most likely have had a negligible impact.

During the dead load analysis density values were input and used to calculate mass properties for the soil elements. Gravity loads were imposed resulting in model deformations. Soil densities were applied only to the critical backfill zone soil and the noncritical backfill zone soil. Dead loads from the steel barrel were not captured in the strain gauges as the gauges were zeroed following structure erection, therefore mass properties were not included for the steel section. Mass properties were not calculated for the elastic foundation soil or concrete elements as well, as loads in this region would have little impact on structural forces, and can unrealistically alter the shape of the culvert without special considerations. Rather than use explicit construction increments, the load was applied incrementally while the structure was in its fully buried condition. The size of each load step corresponds to the total gravity load divided by the number of

time steps, typically five. This method of dead load application deviates significantly from the actual field conditions, where the soil is added to the structure in discrete backfill lifts which are then compacted. As such some important behavioural effects were not accounted for, such as the model peaking and subsequent moment reversals in the haunches and crown. However as the main focus of this study relates to live load responses, the dead load procedure was simplified and used mainly to achieve proper stiffness values for the stress dependent nonlinear soil models.

Live loads were applied to elements on the top of the model as pressure loads closely resembling the conditions in the field. Tire footprints, weights, and live load truck positions are discussed in Chapter 4.1.5. The truck footprint could not be perfectly aligned with the truck position as the finite element mesh is composed of discrete areas; however the tire footprints were added to the approximate locations on the mesh. The applied pressure was scaled up or down to account for the tire footprint being sized differently from the on the mesh footprint, as per Equation 5-1. Additionally, constraint equations were applied to the patch load such that of each of the nodes in the tire footprint moved with the same vertical displacement. Without these constraints the deformation under the patch loads became unrealistically “pointy”.

$$P_{Model} = \left(\frac{A_{Model}}{A_{Actual}}\right) P_{Actual} \qquad \textbf{5-1}$$

Where:

P_{model} = Pressure load used in FEM model

P_{actual} = Pressure of actual tire footprint

A_{model} = Area of tire footprint used in FEM model

A_{actual} = Area of tire footprint

5.2 ORTHOTROPIC PLATE MODEL

The long span box culvert was comprised of CSPSP plates 7.72 mm thick with 381 x 140 mm corrugations, (Super-Cor^{TM}). Each corrugated plate consisted of two corrugations, as shown in Figure 3-3. Section and material properties are displayed in Table 5-1. Properties were calculated per unit width of plate.

Table 5-1 – Material and section properties for Super-Cor plate

Property	Symbol	Value	Unit
Yield Strength	F_y	306	MPa
Young's Modulus	E	200	GPa
Poisson's Ratio	ν	0.3	N/A
Plate Thickness	t	7.72	mm
Area	A	10.81	mm^2/mm
Moment of Inertia	I	25092	mm^4/mm
Section Modulus	S	322.9	mm^3/mm
Plastic Section Modulus	Z	466.4	mm^3/mm

Corrugated plates made from a variety of materials are commonly analysed as orthotropic plates. In the case of a corrugated sheet metal, both axial and bending stiffness' along the strong and weak axes are drastically different. In soil-steel structures the strong axis is always oriented to bend in the transverse direction, providing little stiffness in the longitudinal direction. If an isotropic material model were to be used instead the structure would support unrealistically large longitudinal bending moments and thrusts, (El-Sawy, 2003).

In a three-dimensional finite element analysis one of the simplest ways to simulate an orthotropic plate was to define the shell elements with a uniform thickness and employ an orthotropic material model to vary elastic properties in the transverse and longitudinal directions. Either the bending stiffness, EI, or the axial stiffness, EA, may be approximated by the orthotropic model, but not both simultaneously, (although the bending and axial stiffness are often inherently similar). The orthotropic material axes used in ADINA were labelled as “A”, “B”, and “C”. The “A” material direction ran parallel to the corrugation axis, while the “B” direction ran perpendicular to the corrugation axis. Direction “C” was perpendicular to the plane which both “A” and “B” lie on, that is, it was normal to the corrugated plate. Figure 5-4 displays the material axes naming convention. This convention was used when describing the various elastic properties. A summary of elastic properties is included in Table 5-2. For E_C and G_{BC} no values were specified. This does not indicate that a value was not required, but rather the value has no effect on the final solution.

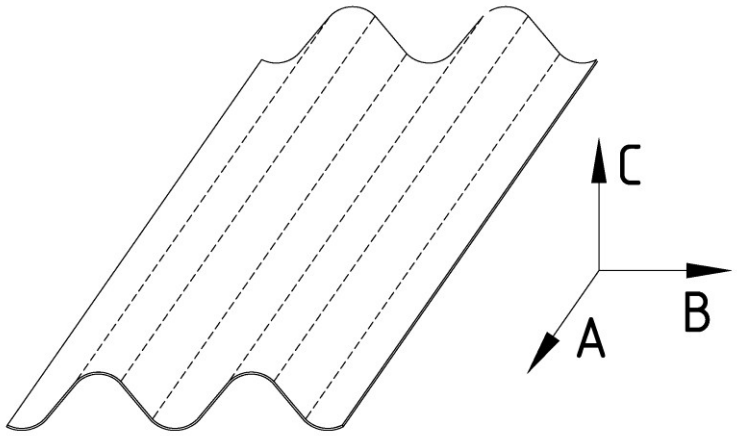

Figure 5-4 - Orthogonal axes system convention

Table 5-2 - Geometric and elastic properties for steel constitutive model

Parameter	Symbol	Unit	Value
Shell thickness	t	mm	166.9
Young's Modulus	E_a	MPa	12953
	E_b		16.2
	E_c		N/A
Poisson's Ratio	ν_{ab}	-	0
	ν_{ac}		0
	ν_{bc}		0
Shear Modulus	G_{ab}	MPa	20.3
	G_{ac}		20.3
	G_{bc}		N/A

To determine the appropriate elastic parameters to be used for this orthotropic model, research from a variety of sources was invested. Abdel-Sayed, (1970), treated shallow corrugated plates as orthotropic shells and derived expressions for axial and bending stiffness in both the transverse and longitudinal directions. Although some of the expressions Abdel-Sayed used were simplifications that do not work well with deeply corrugated plates, derivations were included which allowed the expressions to be modified. Biancolini, (2005), studied corrugated paper products, and derived similar bending and axial expressions for weak and strong axis bending, albeit with drastically different nomenclature. The Canadian Highway Bridge Design Code (Canadian Standards Association, 2006) provided some additional expressions to characterize the bending stiffness of sinusoidally corrugated plates, although axial stiffness was neglected. Weak and strong axis bending stiffness values showed good correlation with Abdel-Sayed. Expressions used to calculate axial and bending stiffness and the resultant values are shown respectively in Table 5-3 and

Table 5-4.

Table 5-3 – Corrugated plate axial and bending stiffness expressions

Value		Abdel-Sayed	Biancolini	CSA – S6-06
Bending	B_A	EI	$\frac{Et^3}{12(1-\nu^2)}+\frac{1}{2}Etf^2$	EI
	B_B	$\frac{c}{L}\frac{Et^3}{12(1-\nu^2)}$	$\frac{c}{L}\frac{Et^3}{12(1-\nu^2)}$	$\frac{c}{L}\frac{Et^3}{12(1-\nu^2)}$
	B_{AB}	$\frac{L}{c}\frac{Et^3}{12(1+\nu)}$	$\frac{L}{c}\frac{Gt^3}{12}$	0
Axial	A_A	$\frac{L}{c}tE$	$\frac{L}{c}tE$ *	N/A
	A_B	$\frac{E}{6(1-\nu^2)}\left(\frac{t}{f}\right)^2 t$	$\frac{Et}{1+6(1-\nu^2)\left(\frac{f^2}{t^2}\right)\left(\frac{c}{L}\right)^2-\frac{(c/L)}{2\pi}\sin\left(2\pi\left(\frac{c}{L}\right)\right)}$	N/A
	A_{AB}	$\frac{Et}{2(1+\nu)}\frac{c}{L}$	$Gt\frac{c}{L}$ *	N/A

*Errors in original publication have been corrected

Where:

A_A, A_B, A_{AB} = axial stiffness of panel

B_A, B_B, B_{AB} = bending stiffness of panel

E = Young's modulus for steel (MPa)

G = shear modulus for steel (MPa)

L = circumferential length of one half wave (mm)

f = half depth of corrugation (mm)

c = chord distance of one half wave (mm)

I = Moment of inertia per unit length of corrugated plate, (mm^4/mm)

ν = Poisson's Ratio

Table 5-4 – Corrugated plate axial and bending stiffness values

Value		Abdel-Sayed	Biancolini	CSA – S6-06
Bending	B_A (N/mm)	5.02E+09	3.79E+09	5.02E+09
	B_B (N/mm)	6.32E+06	6.32E+06	6.32E+06
	B_{AB} (N/mm)	7.86E+06	7.87E+06	0
Axial	A_A (N/mm)	2.06E+06	2.06E+06	N/A
	A_B (N/mm)	3.44E+03	6.20E+03	N/A
	A_{AB} (N/mm)	445.4E+03	445.4E+03	N/A

El Sawy, (2003), developed a three-dimensional finite element model for several soil-steel structures using an orthotropic shell model. To compute the longitudinal axial stiffness, El Sawy used a numerical approach to determine the ratio of stiffness between the longitudinal and transverse directions.

Transverse and longitudinal geometry and stiffness values were calculated based on a combination of finite element modelling and analytical approximations. Bending stiffness, as opposed to axial stiffness, was used to formulate the orthotropic model as bending effects are typically more sensitive than axial thrust in box culverts. To select an appropriate uniform shell thickness, Equation 5-2 was applied.

$$\bar{t} = \sqrt{\frac{12I}{A}} \qquad \textbf{5-2}$$

Where:

$\bar{t}$ = Equivalent shell thickness (mm)

A = Area per unit length of corrugated plate (mm^2/mm)

This equation was derived from the unit moment of inertia for a rectangular plate, and allowed both the bending stiffness and equivalent area to be incorporated into the expression. The equation allowed the ratio of the primary axial and bending stiffness to remain consistent.

The corresponding Young's modulus value was also computed based on an analytical approach, as displayed in Equation 5-3.

$$E_A = \frac{12EI}{\bar{t}} \quad \textbf{5-3}$$

Where:

E_A = equivalent stiffness in the "A" direction (MPa)

This expression was derived from the simple proportionality $(EI)_{equivalent} = (EI)_{Actual}$, and ensured that bending stiffness in the transverse direction was realistic.

To compute the shear modulus, G_{AB}, another analytical expression was used. There was good agreement between all of the researchers for this value, despite small differences in the proposed formulas. The expression stated in Equation 5-4 is a modified form taken from Abdul-Sayed, (1970), expressed as a ratio of the modulus E_A.

$$G_{AB} = \frac{E_A}{\left(\frac{L}{C}\frac{Et^3}{12(1+\nu)}\right)} \quad \textbf{5-4}$$

where:

G_{AB} = equivalent shear modulus (MPa)

Young's modulus in the longitudinal direction, E_B, was determined by the finite element method. An analysis was undertaken to determine the ratio of stiffness between the transverse and longitudinal directions. A plane strain model of a single corrugation was loaded with either a unit load or moment, as shown in Figure 5-5, and the 'spring' constant, k, was computed from the force/deflection and moment/deflection, respectively.

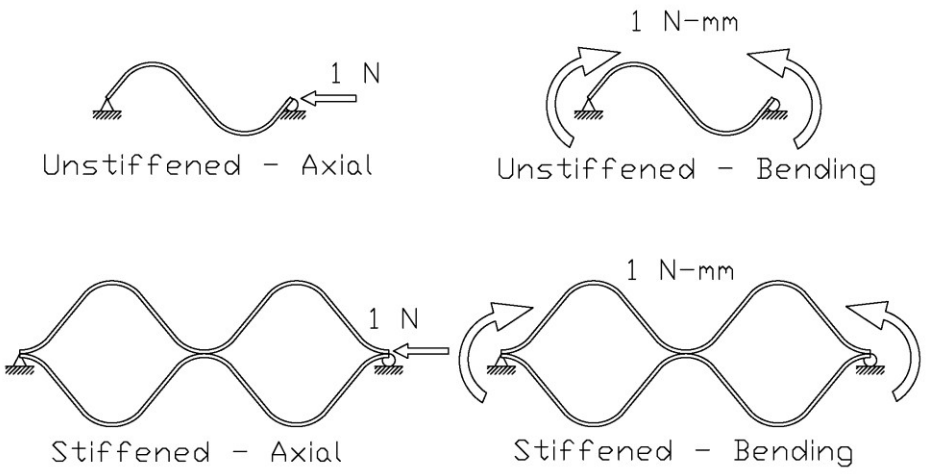

Figure 5-5 – Loads and boundary conditions for longitudinal corrugation profile

The equivalent beam spring constants can be determined from simple mechanics by Equation 5-5 and 5-6, respectively.

$$K_{LA} = \frac{P}{\Delta} = \frac{EA}{L} \quad \textbf{5-5}$$

$$K_{LB} = \frac{M}{\Delta} = \frac{8EI}{L^2} \quad \textbf{5-6}$$

where:

L = length of a single corrugation (mm)

The value of axial stiffness, EA, and bending stiffness, EI, were computed from the FEA values of K_L and Equations 5-5 and 5-6. These longitudinal values were compared against the transverse values of EA and EI, computed from the expressions in Table 5-1. The comparison is presented in Table 5-5 and for a 7.72 mm plate and various steel gauges respectively. Figure 5-6 and Figure 5-7 displays these stiffness values graphically.

Table 5-5 – Ratio of longitudinal to transverse stiffness in bending and axial compression

Type		Transverse Stiffness Values	Longitudinal		Transverse to Longitudinal
			FEA (K_L)	Equivalent Stiffness	
Unstiffened	Axial (N/mm)	$(EI)_t$ = 2.16E06	$\frac{F}{\Delta}$ = 6.89	$(EI)_l$ = 2.62E03	$\frac{1}{823.6}$
	Bending (N-mm/mm)	$(EA)_t$ = 5.02E09	$\frac{M}{\Delta}$ = 353.2	$(EA)_l$ = 6.41E06	$\frac{1}{783.0}$
Stiffened	Axial (N/mm)	$(EI)_t$ = 4.32E06	$\frac{F}{\Delta}$ = 4.45	$(EI)_l$ = 3.39E03	$\frac{1}{1275.2}$
	Bending (N-mm/mm)	$(EA)_t$ = 33.5E09	$\frac{M}{\Delta}$ = 591.7	$(EA)_l$ = 42.9E06	$\frac{1}{780.6}$

Table 5-6 – Longitudinal/transverse stiffness values for all steel gauges

Thickness (mm)		Transverse		Longitudinal		Longitudinal/Transverse	
		EA	EI	EA	EI	EA	EI
Non-Composite	2.81	0.74E+06	1.82E+09	128	0.31E+06	$^1/_{5808}$	$^1/_{5849}$
	3.53	0.96E+06	2.34E+09	254	0.62E+06	$^1/_{3769}$	$^1/_{3799}$
	4.27	1.17E+06	2.87E+09	448	1.09E+06	$^1/_{2610}$	$^1/_{2627}$
	4.79	1.31E+06	3.21E+09	632	1.54E+06	$^1/_{2067}$	$^1/_{2083}$
	5.54	1.53E+06	3.75E+09	977	2.38E+06	$^1/_{1562}$	$^1/_{1573}$
	6.32	1.74E+06	4.29E+09	1448	3.54E+06	$^1/_{1204}$	$^1/_{1212}$
	7.11	1.96E+06	4.83E+09	2058	5.04E+06	$^1/_{954}$	$^1/_{959}$
	7.72	2.16E+06	5.02E+09	2626	6.41E+06	$^1/_{824}$	$^1/_{783}$
Composite	2.81	1.49E+06	11.2E+9	168	1.98E+06	$^1/_{8856}$	$^1/_{5657}$
	3.53	1.91E+06	14.5E+9	332	3.96E+06	$^1/_{5761}$	$^1/_{3670}$
	4.27	2.34E+06	17.9E+9	585	7.05E+06	$^1/_{3998}$	$^1/_{2539}$
	4.79	2.62E+06	20.1E+9	824	10.0E+06	$^1/_{3174}$	$^1/_{2011}$
	5.54	3.05E+06	23.7E+9	1270	15.6E+06	$^1/_{2403}$	$^1/_{1517}$
	6.32	3.49E+06	27.2E+9	1878	23.3E+06	$^1/_{1857}$	$^1/_{1169}$
	7.11	3.92E+06	30.9E+9	2663	33.4E+06	$^1/_{1473}$	$^1/_{924}$
	7.72	4.32E+06	3.36E+10	3390	4.29E+07	$^1/_{1276}$	$^1/_{783}$

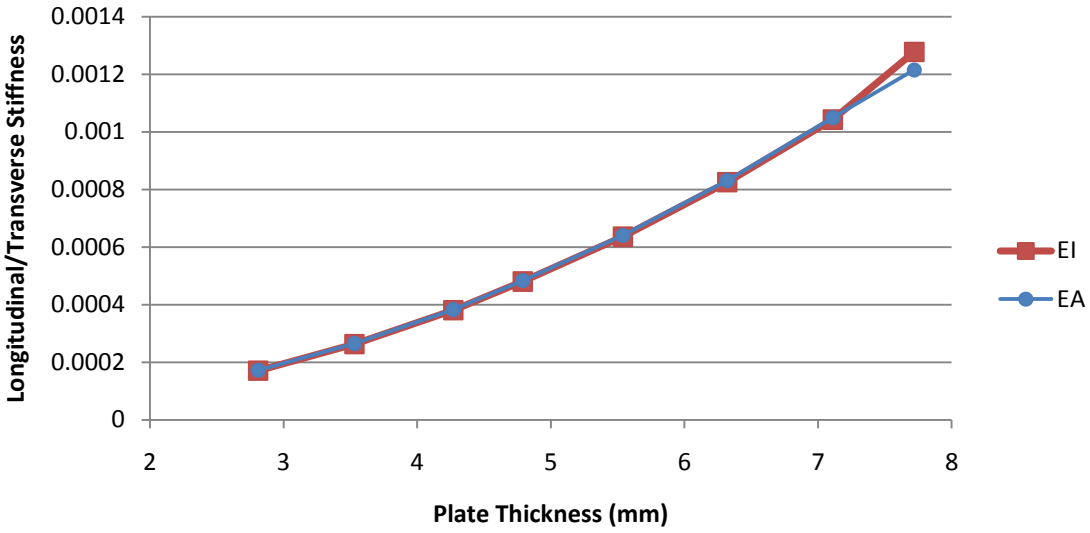

Figure 5-6 – Transverse/Longitudinal stiffness values for unstiffened structure

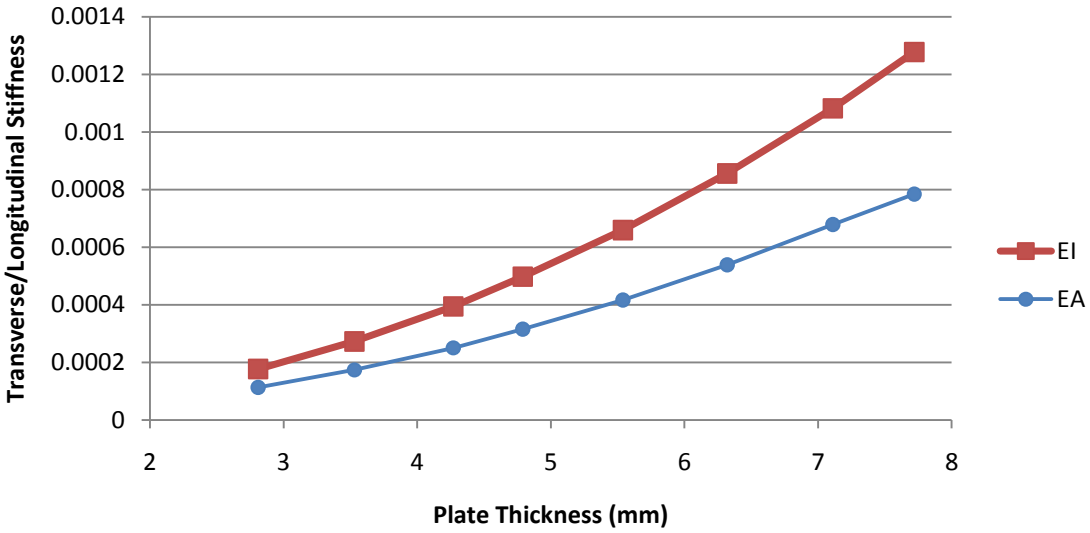

Figure 5-7 – Transverse/longitudinal stiffness values for stiffened structure

For the plate used in the long span box test, the ratio of longitudinal stiffness to transverse stiffness was found to be approximately 1/800, (except for the case of longitudinal axial compression in the stiffened section). The impact of these results was that whether bending or axial stiffness values were used to quantify the longitudinal stiffness, the results would be similar.

Some researchers have postulated that the engineered fill packed into the corrugations may significantly increase the longitudinal stiffness. To investigate these claims the models were run again with linear elastic solid plane strain elements filling the space between the corrugations, as shown in Figure 5-8. Four different elastic modulus values, (from 1MPa to 15 MPa), were used for the soil representing a typical range of soil stiffness values while Poisson's ratio was set to 0.3. No stiffening plates were used for this model.

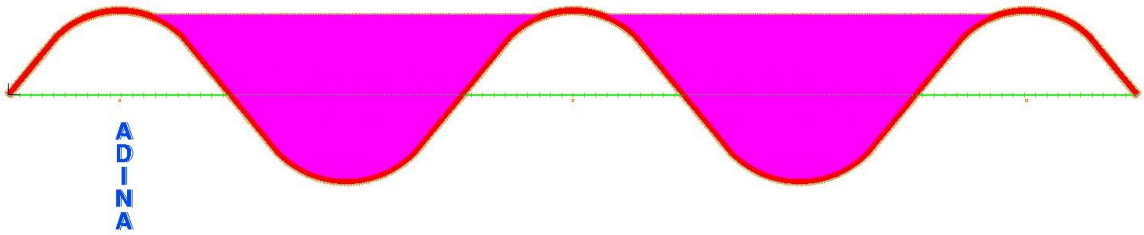

Figure 5-8 – Plane strain model with soil-packed corrugations

The results from this analysis are displayed for bending and axial stiffness in Figure 5-9 and Figure 5-10, respectively. These plots show that including soil in the corrugations does indeed increase the longitudinal stiffness, both in bending and axial compression. As the value of Young's modulus for the soil increases, the longitudinal stiffness also increases. However, longitudinal stiffness was still several orders of magnitude lower than transverse stiffness and hence was not significant enough to affect structural forces acting on the place.

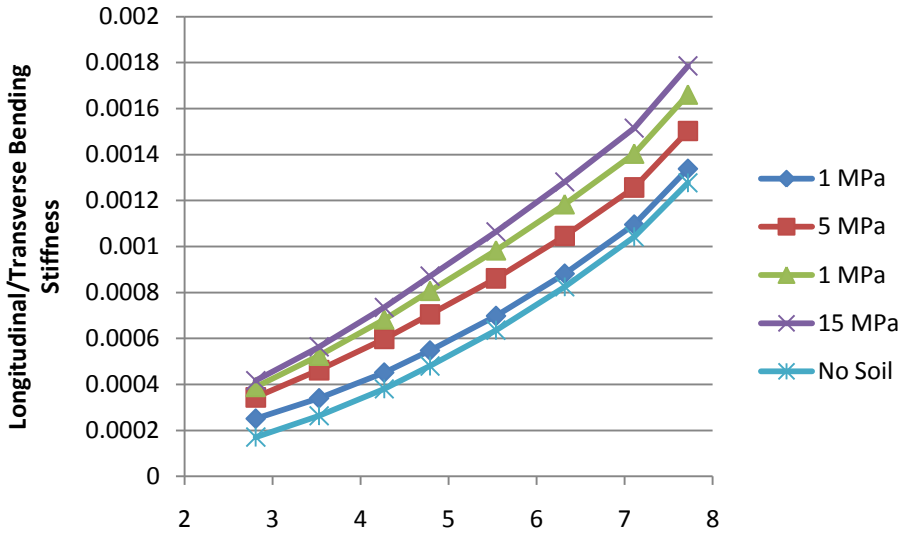

Figure 5-9 – Longitudinal/transverse bending stiffness at various soil modulus values

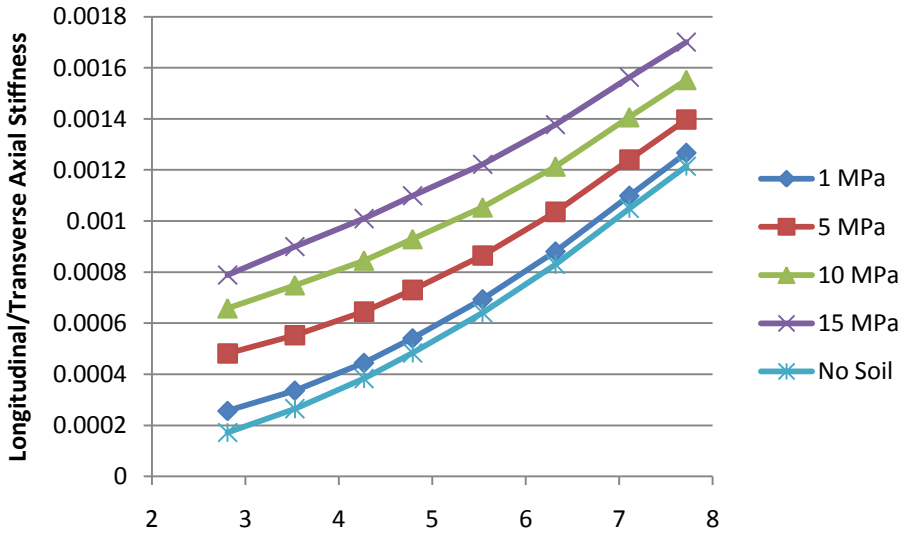

Figure 5-10 – Longitudinal/transverse axial striffness at various soil modulus values

Poisson's ratio used for the orthotropic axes system was taken to be zero in each of the three directions. This was done to satisfy the requirement that the stress-strain constitutive matrix be positive definite, and thus invertible, (ADINA R & D, Inc., 2008). In addition to this requirement, there was also some logic for not including Poisson's ratio effects in the material model. Poisson's ratio effects for a shell of uniform thickness would be poorly representative of Poisson's ratio effects for an actual corrugated plate. Poisson's ratio effects were, however, taken into account in the derivation of each of the orthotropic elastic properties.

5.3 SOIL MODELS

5.3.1 General

Proper characterization of soil properties is important if structural forces are to be computed correctly. This is especially true of the critical backfill zone, the envelope of soil directly in contact with the structure. A robust model was required to capture the complex behavior of the soil.

The most popular soil model used by engineers studying soil-steel structures is the "Duncan/Selig" model; programmed into various soil-structure interaction programs such as CANDE, (Culvert ANalysis and DEsign), SPIDA, (Soil Pipe Interaction Design and Analysis), and NLSSIP, (Nonlinear Soil Structure Interaction Program), although CANDE remains the only software widely used today. The Duncan/Selig constitutive model was the result of a collaboration of researchers working over several decades.

Duncan and others produced the first iteration of the soil model in 1970, at the threshold of the personal computing revolution, (Duncan & Chang, 1970). The premise of the soil model was that many stress-strain relationships in soil masses were

reasonably approximated by hyperbolic mathematical functions. By calibrating the soil model to these functions it was possible to achieve stress dependent stiffness using a piecewise linear curve defined by a simple mathematical expression. By assuming Poisson's ratio to be constant throughout the solution, Duncan formulated an expression for the tangential elastic modulus, E_t, based entirely on the state of stress in the soil. Only six parameters were needed to characterize the soil; the Mohr-Coulomb parameters cohesion, c', and friction angle, ϕ_o, and four additional terms which could be quickly determined from standard triaxial tests. Duncan improved his model in 1980, (Duncan *et.al.*, 1980), by including a variable Poisson's ratio through the introduction of a stress-dependent bulk modulus function. Selig also produced a stress-dependent bulk modulus function, (1988). The functions used in these soil models were used to calculate the stiffness at various soil layers in the layered models in this thesis. Chapter 5.3.4 describes the specific expressions in greater detail.

Consultants performed many soil tests on samples from the critical backfill zone including sieve, hydrostatic, and triaxial tests, (TerrAtlantic Engineering Limited, 2009). The purpose of geotechnical testing was to provide parameters for the previously described Duncan-Selig material model. Unfortunately the Duncan/Selig constitutive model was not available in ADINA, however ADINA provided a number of other geotechnical constitutive models.

The soil constitutive models considered for this thesis include linear elastic, with and without depth dependent stiffness, the elastic perfectly-plastic Mohr-Coulomb model and a user defined "curve-description". Chapter 5.3.5 describes how the non-critical backfill regions were characterized.

5.3.2 Linear Elastic

The model described in this chapter represents an isotropic linear elastic material model with uniform stiffness for the entire critical backfill zone. Despite the relative simplicity of this constitutive model, the results did not significantly deviate from some of the more robust soil models used. Generally the bending moment and axial thrust diagrams were similarly shaped. The model was run four times each with different stiffness values, ranging from 1 MPa to 15 MPa. This represented the full range of stiffness values as calculated in Chapter 5.3.4.2. Poisson's ratio was taken as 0.3. While the model generally performed well, the lack of stress-dependency in the elastic modulus was unrealistic. Further, without experimental test data, it was difficult to quantify exactly which stiffness value was appropriate for the model.

5.3.3 Curve Description Model

The "Curve Description" model is a constitutive model which allows user generated stress-strain curves, allowing for stress dependent stiffness without plasticity. The model allows the user to enter values for the bulk modulus, B, (both loading and unloading), and shear modulus, G, at user specified intervals of volumetric strain. To obtain the bulk modulus curve, the volumetric strain vs. confining stress curve was plotted from the hydrostatic tests. A polynomial regression was applied to the data, and the resulting function was differentiated to provide a curve of the bulk modulus vs. volumetric strain. The stress-strain curve and modulus-volumetric strain curves are provided in Figure 5-11 and Figure 5-12, respectively.

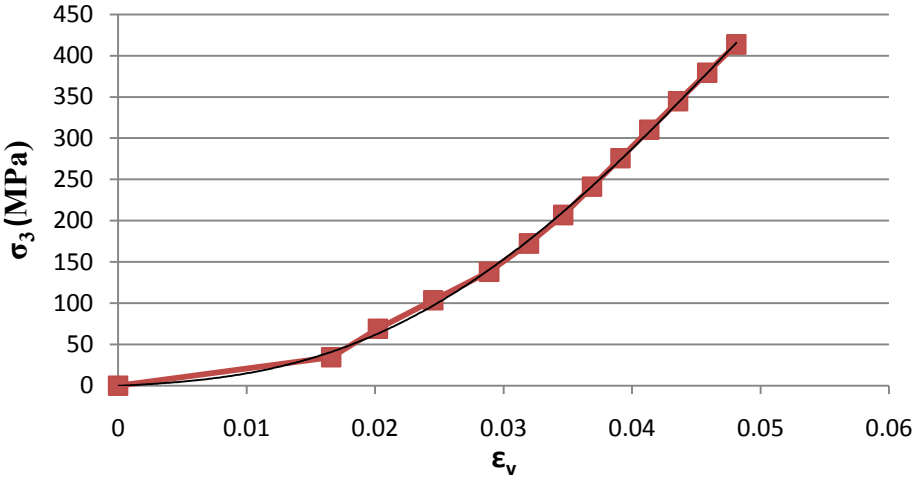

Figure 5-11 - Stress-strain curve for soil in critical backfill zone

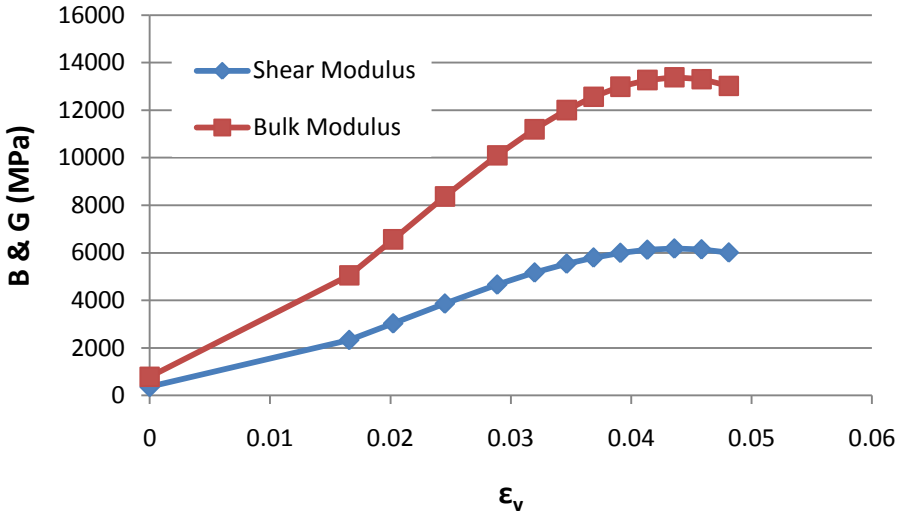

Figure 5-12 – Bulk and Shear modulus curves for critical backfill zone

To obtain the shear modulus from the triaxial test, volume measurements would have had to be taken, which was both uncommon and expensive. Instead Poisson's ratio was assumed to be constant and the isotropic elastic relationship between shear modulus,

bulk modulus, and Poisson's ratio was applied, given as Equation 5-7. Assuming a Poisson's ratio of 0.3, (Bowles, 1996), computes the shear modulus to be equal to 0.461 of the bulk modulus.

$$G = 3B\left(\frac{1-2\nu}{2(1+\nu)}\right) \qquad 5\text{-}7$$

Figure 5-13 shows the bulk modulus formulation graphically. Equations 5-13 and 5-14, along with soil parameters provided by TerrAtlantic, (2009), were used to compute the Duncan and Selig curves, respectively. The curve-description model provided good agreement with the Duncan and Selig models for the service range.

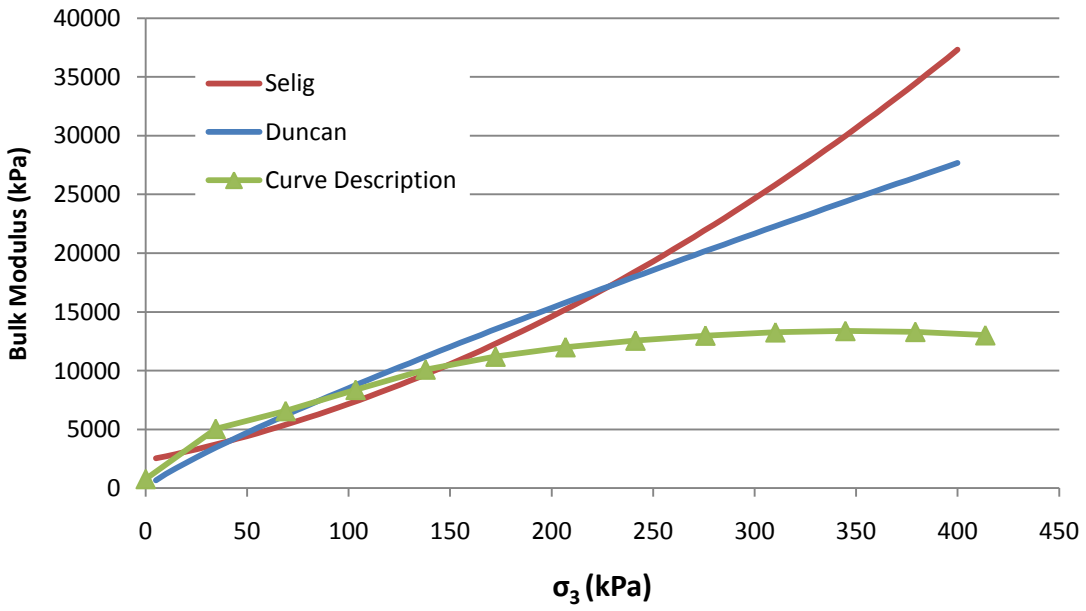

Figure 5-13 – Various bulk modulus functions

5.3.4 Layered Models

5.3.4.1 General

Layered models are those which contained a number of horizontal layers such that soil properties may be manually varied with depth. Using this approach it was possible to quantify the increase in stiffness resulting from the weight of soil, without actually including gravitational load effects on stiffness. As was shown by Selig (1990), the change in modulus and other soil properties can be significant from the top to the bottom of a compacted soil mass. Using a model with uniform properties throughout makes it impossible to capture this gradient. Two constitutive models were used with the layered geometry; isotropic linear elastic and the elastic-perfectly plastic Mohr-Coulomb.

Seven layers were used from the top of the footing to the crest at the crown. An additional layer was utilized for each successive backfill lift. Soil layers are shown in Figure 5-14.

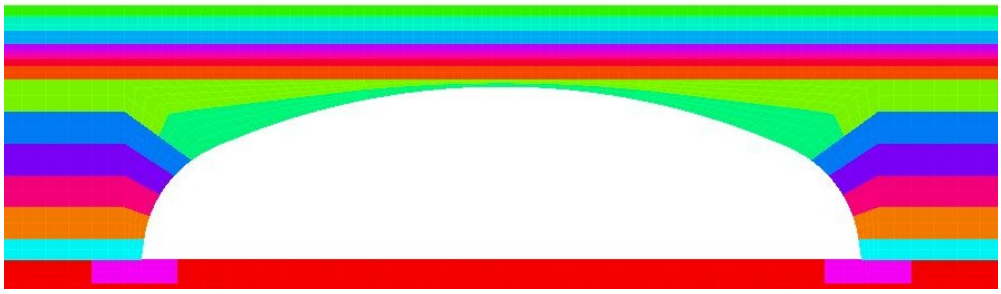

Figure 5-14 – Soil layers used for graduated stiffness models

5.3.4.2 Linear Elastic

As previously described, the elastic soil model is a linear model which represents materials by four elastic constants; Young's modulus, bulk modulus, shear modulus and Poisson's ratio. Of these only two are needed to fully characterize the stiffness. The layered elastic model contains some advantages over its nonlinear counterparts. Rather than using nonlinear-stress dependent models with gravity loads, with or without construction increments, this approach calculated the apparent stiffness based on the depth of the layer to the surface.

The procedure for the determination of soil properties at each layer was developed by Selig, (1990). Recently, researchers have used this approach to study similar engineering problems, (Petersen *et al*., 2010). The soil model used to calculate elastic properties, Duncan/Selig, was developed specifically for soil-structure interaction problems and was considered the most accurate constitutive model for this application, (Katona *et al.*, 2007). Soil properties were computed as a function of depth, more specifically the state of stress linearly related to the depth. Principal stresses were obtained from Equations 5-8 and 5-9.

$$\sigma_1 = \gamma d \qquad \textbf{5-8}$$

where:

σ_1 = Vertical stress (MPa)

γ = Unit weight of soil (N/mm^3)

d = depth from top of soil mass to layer of interest (mm)

$$\sigma_3 = \frac{\sigma_1}{2} \quad \textbf{5-9}$$

where:

σ_3 = Horizontal stress (MPa)

The minimum principle stress, σ_3, was the horizontal stress induced by the confinement of the soil. Selig originally recommended a value of one half to one times the value taken for the maximum principle stress. However for the soil type of interest, well-graded gravelly sand, the value was taken to be one half of the principle vertical stress. This state of stress combined with hyperbolic soil parameters provided by TerrAtlantic, (2009), was used to determine soil properties.

Tangent Young's modulus values, as originally developed by Duncan (1970), are expressed in Equations 5-10 through 5-12. The initial modulus based on confining stress, σ_3, is presented as Equation 5-10.

$$E_i = KP_a\left(\frac{\sigma_3}{P_a}\right)^n \quad \textbf{5-10}$$

where:

E_i = Initial modulus based on confining stress (MPa)

K = Dimensionless magnitude of Young's Modulus

n = Power Law Coefficient

P_a = Atmospheric pressure (101.325 kPa)

The friction angle, defined as the slope of the Mohr-Coulomb failure envelope, is also used in the calculation of the tangent Young's modulus. The formula is provided as Equation 5-11.

$$\phi = \phi_{\circ} - \Delta\phi \log_{10}\left(\frac{\sigma_3}{P_a}\right) \quad \textbf{5-11}$$

where:

ϕ = Soil friction angle (Degs)

$\phi_{\circ}$ = Initial soil friction angle (Degs)

$\Delta\phi$= Reduction in friction angle for a ten-fold increase in confining stress (Degs)

Finally the tangent modulus, the ratio of axial stress to axial strain, may be computed by Equation 5-12.

$$E_t = E_i\left[1 - \frac{R_f(1-\sin\phi)(\sigma_1 - \sigma_3)}{2(\mathrm{C}\cos\phi + \sigma_3 \sin\phi)}\right]^2 \quad \textbf{5-12}$$

where:

E_t = Tangent modulus (MPa)

R_f = Ratio of soil failure stress to ultimate stress

C = Cohesion intercept (MPa)

To compute Poisson's ratio, one additional elastic parameter was required. Duncan *et al.*, (1980), derived a stress-dependent function for bulk modulus after it was shown that volume change behavior can also be accurately modeled by applying hyperbolic mathematical functions. The parameter K_B, can be calculated from triaxial test results. The bulk modulus expression derived by Duncan is shown as Equation 5-13.

$$B_t = K_B P_a \left(\frac{\sigma_3}{P_a}\right)^m \quad \textbf{5-13}$$

where:

B_t = Tangent bulk modulus (MPa)

K_B = bulk modulus number

P_a = atmospheric pressure in the same units as B and σ_3

m = bulk modulus exponent

σ_3 = Triaxial confining stress

Selig had also derived a hyperbolic expression for bulk modulus, similar to the expression used for initial Young's modulus, (1988). Parameters for this function were calibrated using hydrostatic tests, rather than triaxial tests. Ultimately, Selig's function was chosen for the layered models in this thesis due to the increased number of "canned", or previously calculated, soil parameters available for comparative purposes, although the model was known to produce similar results to Duncan's original formulation. Both Duncan and Selig's formulations are popular in practice. Equation 5-14 displays Selig's bulk modulus function.

$$B_t = B_i \left[1 + \frac{\sigma_m}{\left(\frac{B_i}{\varepsilon_u}\right)}\right]^2 \quad \textbf{5-14}$$

where:

B_i = Initial bulk modulus (MPa)

σ_m = Mean stress - $(\sigma_1 + \sigma_3)/2$ (MPa)

ε_u = Failure strain

Using values of Young's and bulk modulus, Poisson's ratio was computed by the isotropic linear elastic expression shown in Equation 5-15.

$$\nu = \frac{3B_t - E_t}{6B_t} \qquad \textbf{5-15}$$

where:

ν = Poisson's ratio

5.3.4.3 Mohr-Coulomb

The Mohr-Coulomb geotechnical material model is an elastic, perfectly plastic model which uses the Mohr-Coulomb yield criteria. The model also features a tension cutoff feature whereby when the tensile limit is exceeded stress components of the failure elements are shifted to pressure components, redistributing the forces. The model uses a non-associated flow rule.

The fully linear elastic layered model was used as a basis for the Mohr-Coulomb model, where the properties of various layers were manually input to represent the stress dependency of the parameters. To fully characterize the soil, the following parameters were used: the modulus of elasticity, E, Poisson's ratio, ν, friction angle, ϕ, cohesion, c, and tension cutoff, T. Young's Modulus and Poisson's ratio defined the elastic portion of the soil behaviour. The friction angle and cohesion were used to characterize the Mohr-Coulomb yielding behaviour. The tensile cutoff represented the maximum stress the soil could support before tensile failure. The soil friction angle, Young's modulus, and Poisson's ratio represented the stress dependent parameters, and were calculated specifically for each layer using Equations 5-11, 5-12, and 5-15, respectively.

Both cohesion and tensile capacity were considered to be very low in a sandy, gravelly soil. The "tension cutoff" was set to zero, preventing the soil from supporting any tensile stresses. The cohesion intercept, although realistically also close to zero, was set to 0.01

MPa, for numerical stability.

Some additional changes were required from the layered linear elastic model due to the non-linearity of the Mohr-Coulomb model. Hexahedral elements were changed from 8-noded to 20-noded, as the lower order shape functions were numerically unstable. Orthotropic shell elements were increased to 9 nodes from 4 nodes. Due to the large computing requirements the mesh also needed to be modified from its original size. Symmetry in the transverse direction was utilized and the mesh density was reduced at a distance away from the point of load application. The mesh used for this model is shown in Figure 5-15.

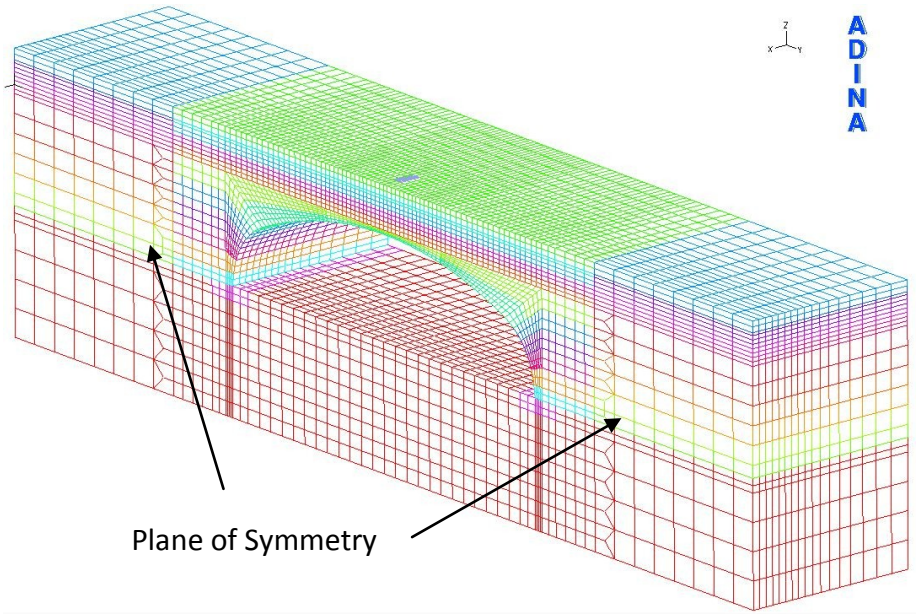

Figure 5-15 – Finite element mesh used with the Mohr-Coulomb material model

The modulus of elasticity of the upper layers was also altered such that the stiffness above the crown was uniformly set to the average value. For example, on the 0.75 m model, all backfill layers above the crown were set to the equivalent stiffness at a depth

of 0.375 m. This was done to prevent excessive deformations and plasticity at surface layers and improve the model stability. Also, to prevent plasticity directly under the tire load, the uppermost layer was changed to a linear elastic model with the same stiffness as the soil. The thickness of the linear elastic layer ranged from 100 – 200 mm. Peterson *et al.* also used a similar elastic surface layer in their Mohr-Coulomb models, (2010).

5.3.5 Non-Engineered Soil

5.3.5.1 Non-Critical Backfill Zone Soil

Soil which was above the foundation yet outside the critical backfill zone was labeled as noncritical backfill zone soil. Soil properties in this zone had a higher impact on structural forces in the culvert than the insitu soil beneath the foundation, but a much lower impact than soil directly in contact with the structure. A linear elastic soil model was employed for this soil group. Generally, increasing the stiffness of this soil provided more support for the structure, thus reducing bending moments and axial thrusts in the shell. Decreasing the stiffness produced the opposite effect; the steel structure carried the loads with reduced support and structural forces increased. The noncritical backfill zone soil was not technically a part of the soil structure system, however it should be viewed analogously to elastic boundary conditions for the actual soil-structure system.

Unfortunately, no quantitative soil tests were performed on soil samples in this region. Based on site photographs the soil was characterized soil as “gravelly silt with sand”, according to the “United Soil Classification System”, (USCS). This soil belongs to the ML, (silty sand), group of soils. Elastic Parameters used for the noncritical backfill zone were estimated from Bowles, (1996). The value for Young’s modulus for the soil in this zone was set to 700 kPa while Poisson’s ratio was taken to be $\nu = 0.3$. Chapter 7.2.1 explores the impact on structural forces when this value is changed.

5.3.5.2 In-situ Soil

In-situ soil properties of the structures foundation were produced by ADI Limited from a series of plate load tests performed in October and November of 2007, (ADI Limited, 2007). The sub-grade beneath the foundation was characterized as “fractured, slightly weathered sandstone bedrock...consisting of large, flat, cobble and boulder sized pieces with smaller sized sandstone particles filling the voids”. The plate load tests were performed using square steel plates which were 12”, 16” and 24”. The plates were pushed against the ground using a hydraulic jack while their displacements were measured. Elastic properties were derived from the resulting load/deflection plots.

The impact of varying the insitu soil was expected to be low, (Katona, 2009). Although global deflections may be impacted by the stiffness of this soil, the deflection between the footing and crown, (and thus bending moments and axial thrusts), showed little impact. The linear elastic material model was selected because of its simplicity and low computational cost. Young’s Modulus was selected as E = 60 MPa from the plate load test, with a Poisson’s ratio of $\nu = 0.35$.

5.4 PRESENTATION OF RESULTS

This section describes some details regarding the plots and data generated from the finite element software and presented in the subsequent two chapters. Sample plots shown in this chapter are taken from the layered linear elastic model under 0.45 m of backfill cover, but other soil models and backfill depths display similar trends.

The structural forces of interest were bending moment, axial thrust, and vertical displacement. The bending moment and axial thrust refer to transverse forces, that is, forces calculated from the strong axis of the corrugated plate, unless otherwise stated.

These forces are given on a per meter basis; bending moment was kN-m/m and axial thrust was kN/m. Because of the orthotropic nature of the plate, longitudinal forces were several orders of magnitude lower, and thus of little interest. Values were calculated at the nodes by averaging the forces of adjacent elements. Load effects, unless otherwise stated, were due to live loads only.

Plots show a single load case; load line 1 truck position 5, (see Figure 4-17 for load cases). The assumed truck footprint is shown in Figure 4-16. This load case consisted of the single rear axle placed in the center of the structure and straddling the longitudinal line of symmetry, producing significant bending moments at the crown. This load case is shown both schematically and as represented by ADINA in Figure 5-16.

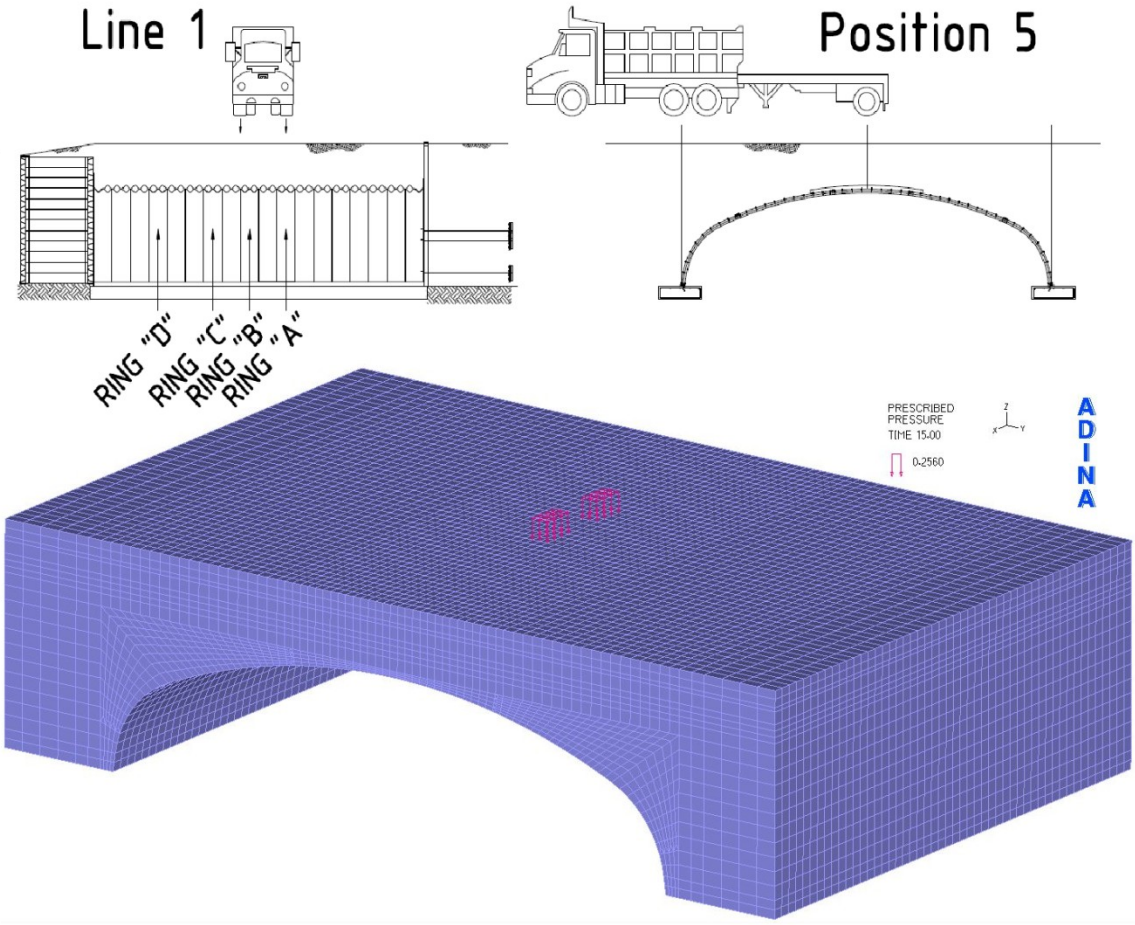

Figure 5-16 – Load position used for FEM analysis

Generally plots were taken as either transverse, longitudinal, or contoured. Transverse plots ran along the periphery of the structure, from footing to footing with the crown at the midpoint. The horizontal axis for these transverse plots represented the distance to the crown, in mm, with the crown shown at zero. Since the maximum structural forces were of interest, transverse plots were taken from the line beneath the tire which produced the maximum load effects. This may be one of six lines shown in Figure 5-17, represented as “Trans1” through “Trans6”.

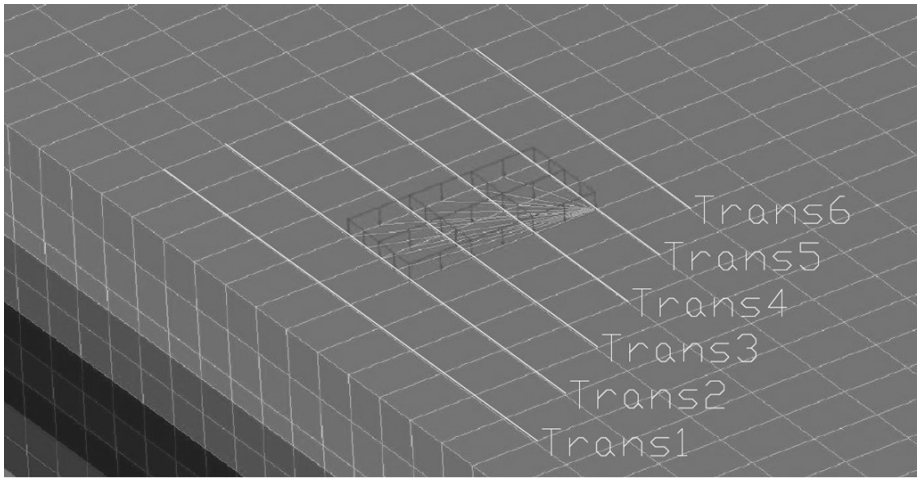

Figure 5-17 – Location of transverse sections

The line which carries the maximum moment did not necessarily correspond to the line which showed the maximum thrust. The maximum moment and thrust line also changed at various backfill depths and to a lesser extent with different soil models. As an illustration of this point, Figure 5-18 and Figure 5-19 display bending moment and axial thrust diagrams at each of the six possible transverse lines. Although the shape of the moment diagram changed little, the shape of the axial thrust diagram changed significantly from one line to the next. For this particular case, the maximum positive moment occurred on line “Trans3” while the maximum negative thrust occurred at “Trans4”.

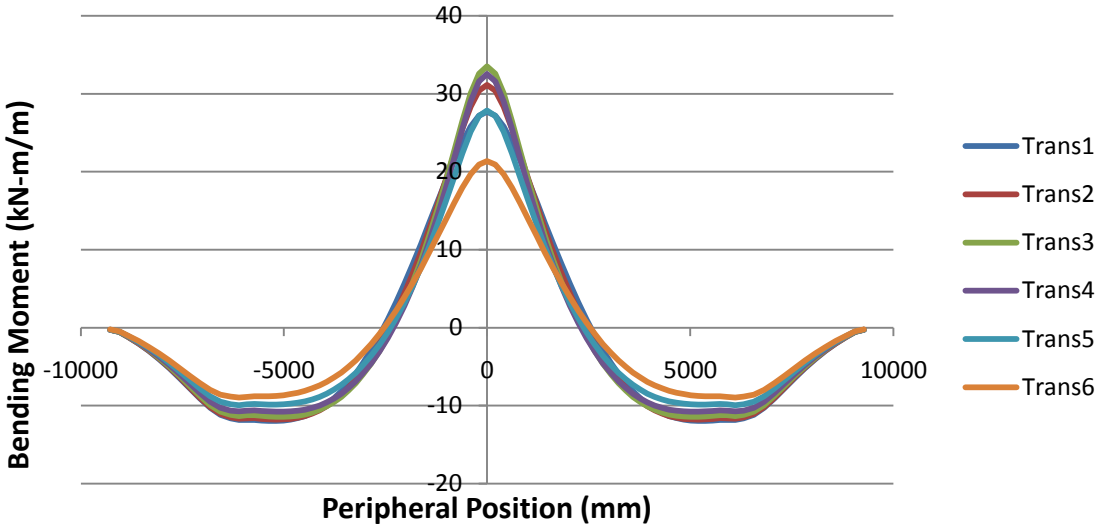

Figure 5-18 – Transverse bending moments at various sections beneath the wheel load

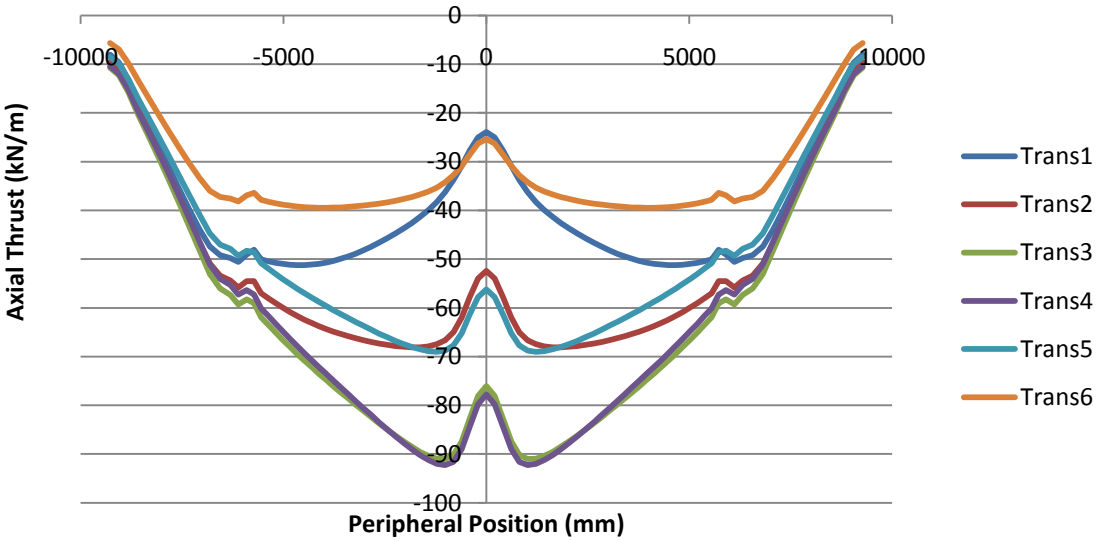

Figure 5-19 – Transverse axial thrust at various sections beneath the wheel load

Longitudinal plots of transverse structural forces ran along the axis of the culvert. Although the maximum positive moment occurred at the crown, the maximum negative moment and axial thrust occurred at various points around the periphery of the structure depending on the backfill depth and soil model used. Unless otherwise stated, all longitudinal plots were shown at the point where the greatest structural effects were observed. Also, longitudinal plots begin at the point directly between tire loads and extend to the edge of the structure.

CHAPTER 6 - EXPERIMENTAL VALIDATION

6.1 LINEAR ELASTIC

The linear elastic model was simple and easily implemented, with no consideration for the gradation of stiffness which naturally occurs in a soil mass. The stiffness values shown represented the full range of soil moduli values calculated in the layered linear elastic model, with the average stiffness value being 7.25 MPa for 0.6 m backfill condition. Despite this unrealistic condition, the model performed surprisingly well. Transverse bending moments shown in Figure 6-1, for the 15 MPa model particularly, displayed an excellent fit with the experimental data. Transverse axial thrust, displayed in Figure 6-2, also showed good correlation to the test data with the exception of crown position, which was significantly under predicted. Longitudinal decay of bending moments displayed a reasonable fit with the experimental values, as shown in Figure 6-3. The longitudinal decay of axial thrust, shown in Figure 6-4, showed similar behaviour to the experimental values but the magnitude was too low. Although the 15 MPa model showed good correlation, without the experimental data it would have been impossible to determine which stiffness value was appropriate.

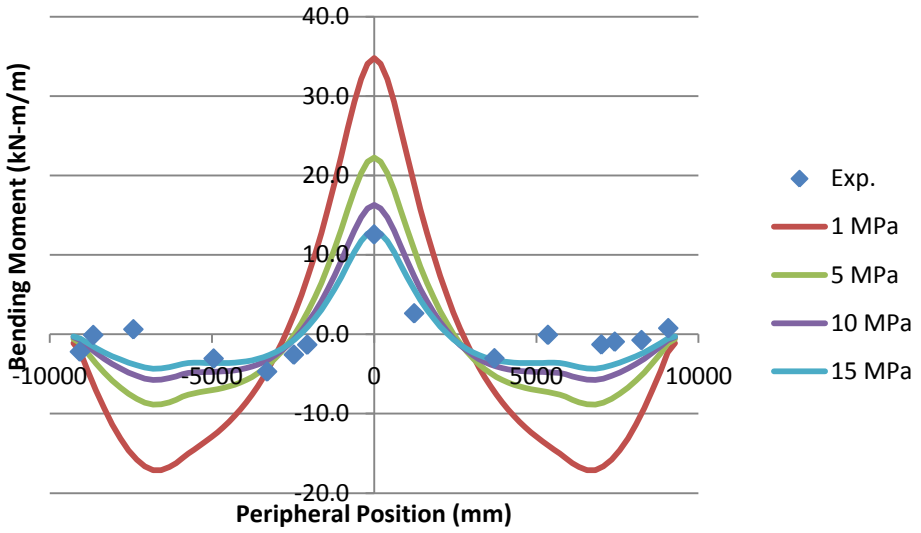

Figure 6-1 – Linear elastic model, transverse bending moments, 0.6 m backfill

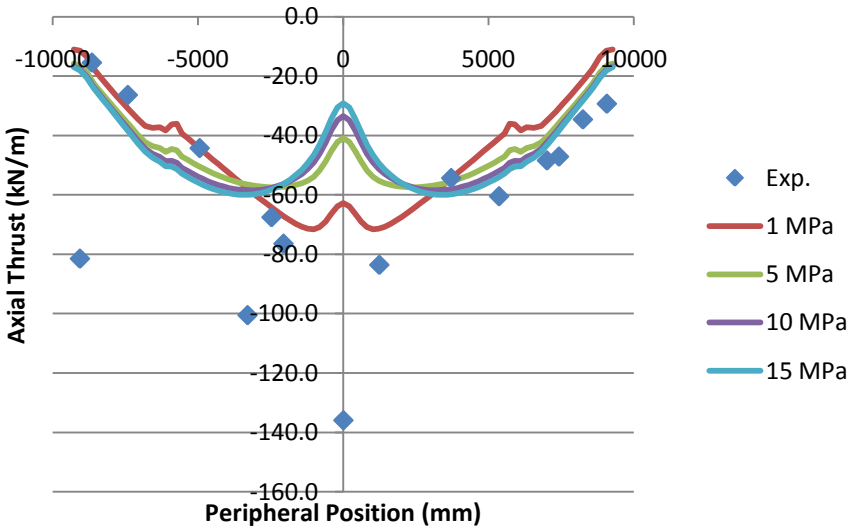

Figure 6-2 – Linear elastic model, transverse axial thrust, 0.6 m backfill

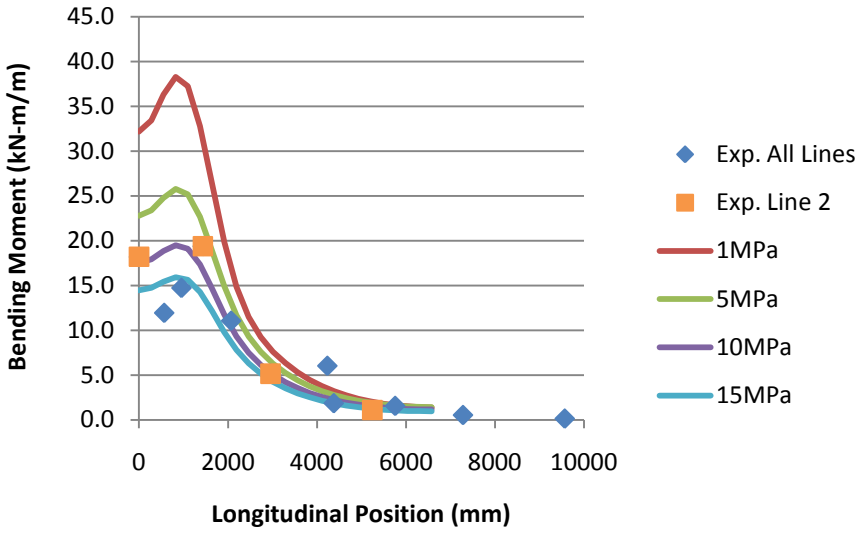

Figure 6-3 – Linear elastic model, longitudinal bending moment profile, 0.6 m backfill

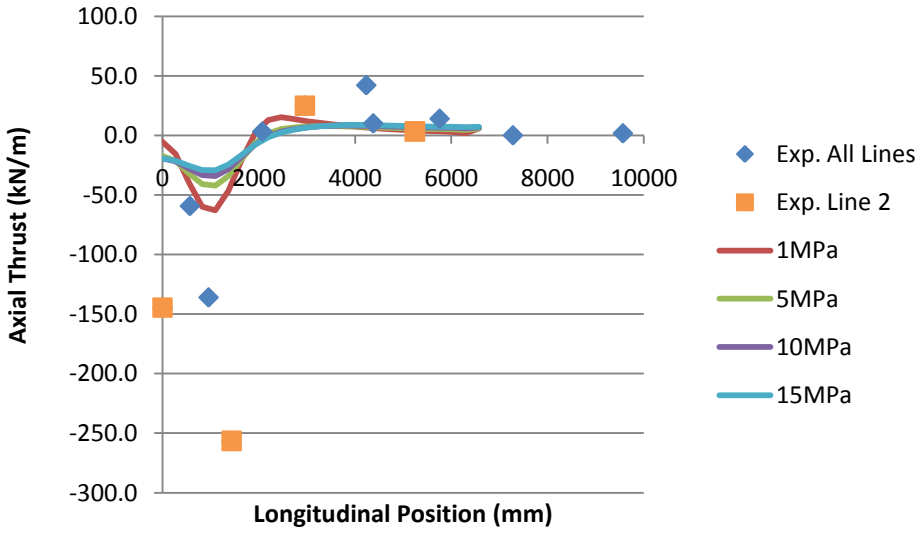

Figure 6-4 - Linear elastic model, longitudinal axial thrust profile, 0.6 m backfill

6.2 CURVE DESCRIPTION

The curve description model, calibrated from hydrostatic testing, provided conservative values for bending moment and non-conservative values for the axial thrust, especially at the crown. Transverse bending and thrust plots are displayed in Figure 6-5 and Figure 6-6 while longitudinal bending and thrust plots are shown in Figure 6-7 and Figure 6-8, respectively. The inclusion of dead load forces provided a better fit to the data, as the additional strains stiffened the soil resulting in a greater distribution of the loads. This was especially apparent for the bending moments. It also may have been useful to apply further strains to simulate the compaction efforts, but these were not fully investigated. Overall the model performed acceptably for design purposes, and the analysis was not particularly inefficient given the lack of plasticity.

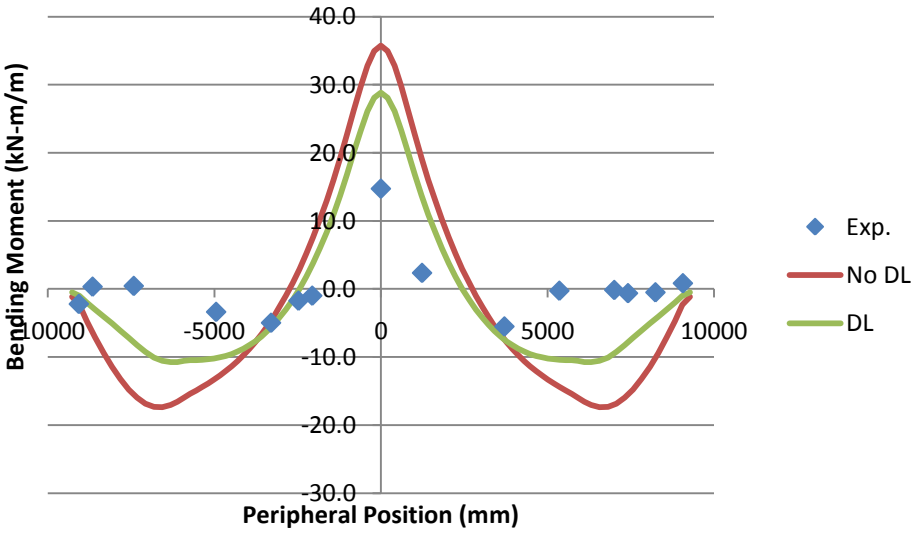

Figure 6-5 – Curve description model, transverse bending moment, 0.6 m backfill

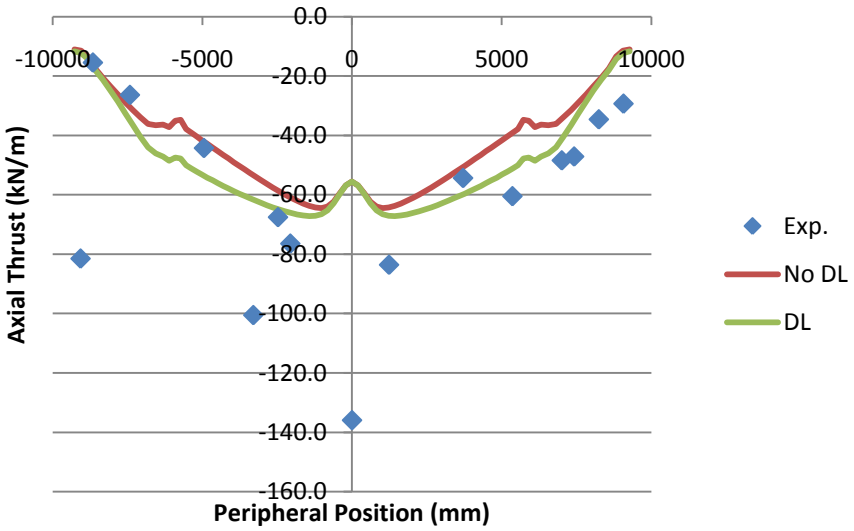

Figure 6-6 – Curve description model, transverse axial thrust, 0.6 m backfill

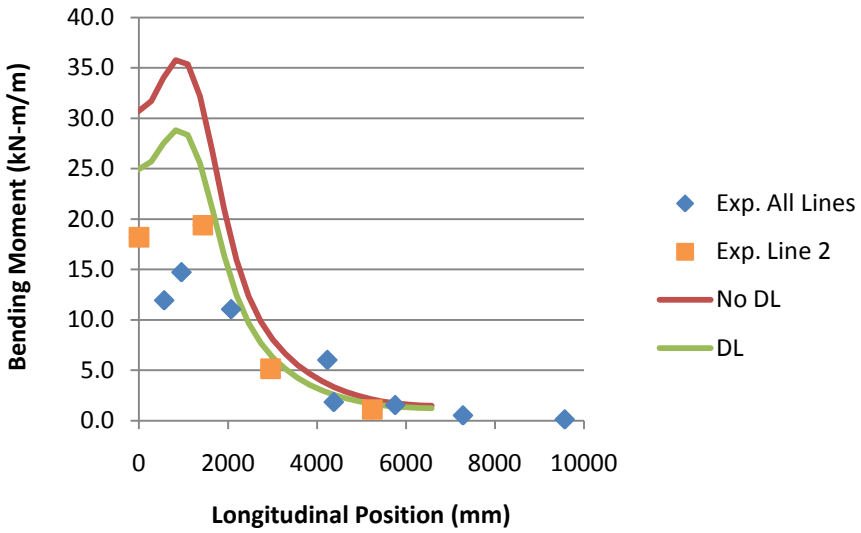

Figure 6-7 – Curve description model, longitudinal bending moment profile, 0.6 m backfill

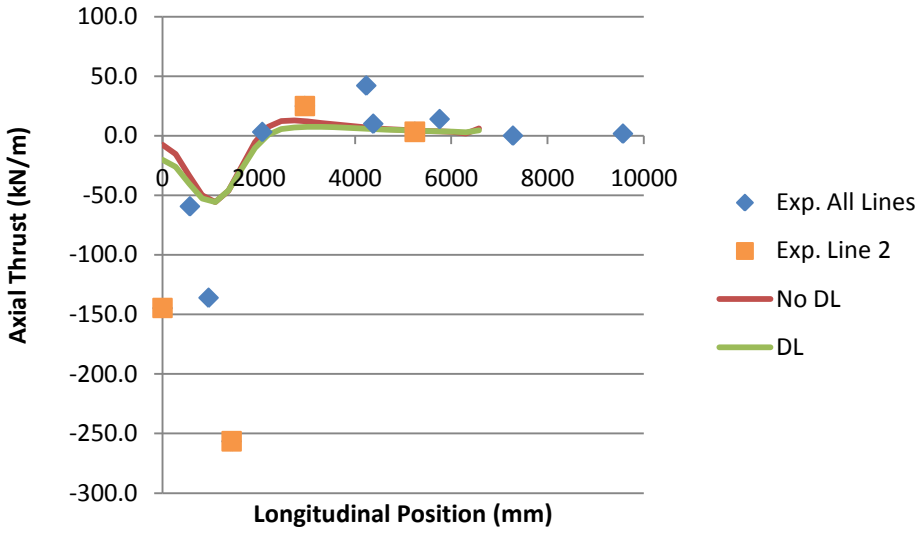

Figure 6-8 - Curve description model, longitudinal axial thrust profile, 0.6 m backfill

6.3 LAYERED LINEAR ELASTIC

The layered linear elastic model was calibrated from Duncan-Selig parameters obtained from geotechnical testing, specifically triaxial and hydrostatic soil tests. Despite the simplicity of the model and the extremely efficient run times, the stiffness was rigorously defined. The results obtained were similar to the curve description model described in the previous section. Transverse bending and thrust plots are displayed in Figure 6-9 and Figure 6-10 while longitudinal bending and thrust plots are shown in Figure 6-11 and Figure 6-12, respectively. The comparison with the "canned" soil models, SW85 and SW95, (well graded sand compacted to 85 and 95 percent standard proctor density), provided some insight into the character of the soil. Each of the soils were characterized as well graded coarse sand, however the soil model computed from soil testing was much softer than the "canned" models. Despite the significant compactive effort applied to the soil during the testing, (at least 95% standard proctor

density), the soil was significantly softer than the SW85 model, which was considered a conservative upper bound for well graded sand compacted to only 85% standard proctor density. Given the excellent experimental correlation of the canned soil models, which were considered conservative, the accuracy of the soil model derived from triaxial testing was questionable. Although the model parameters were accurately derived from the soil tests, the soil behaviour occurring under small scale experimental conditions may not be entirely representative of field conditions. TerrAtlantic, (2009), also noted the unusual softness of the soil. The consultants attributed the behaviour to the atypical roundness of the soil grains producing little grain interlock.

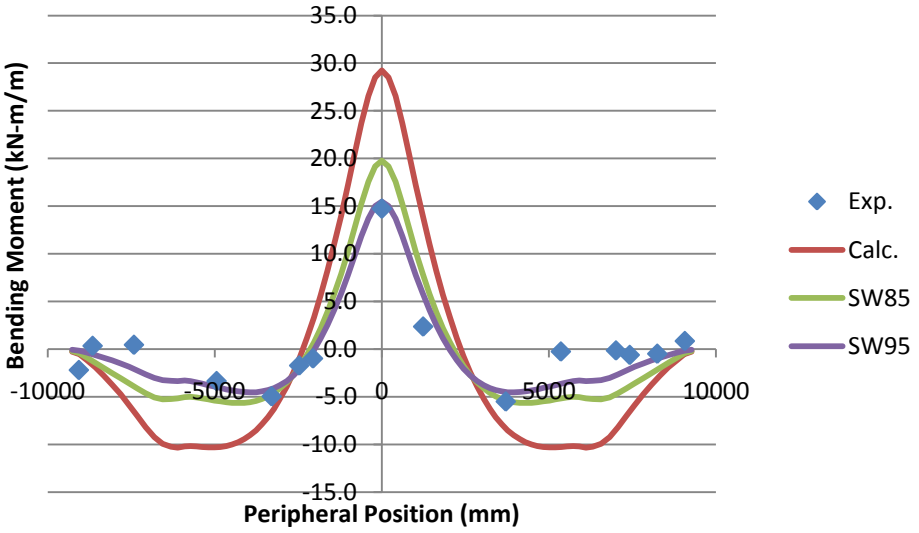

Figure 6-9 – Layered linear elastic model, transverse bending moments, 0.6 m backfill

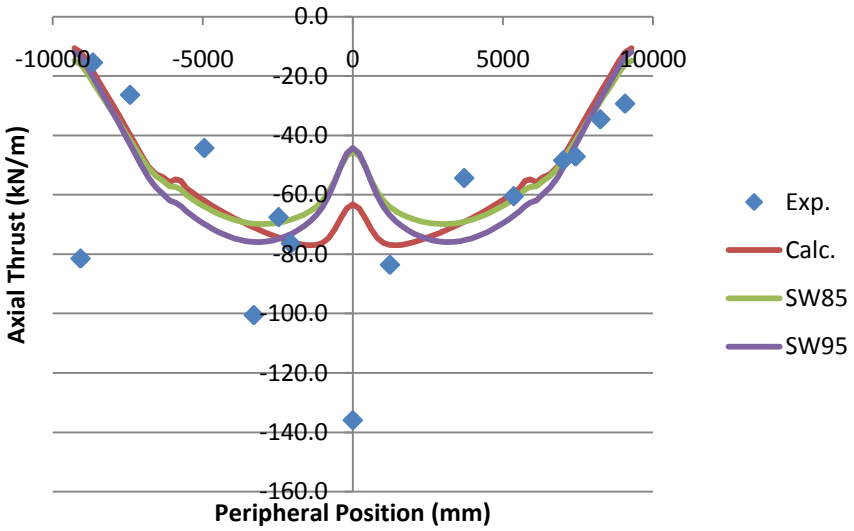

Figure 6-10 – Layered linear elastic, transverse axial thrust, 0.6 m backfill

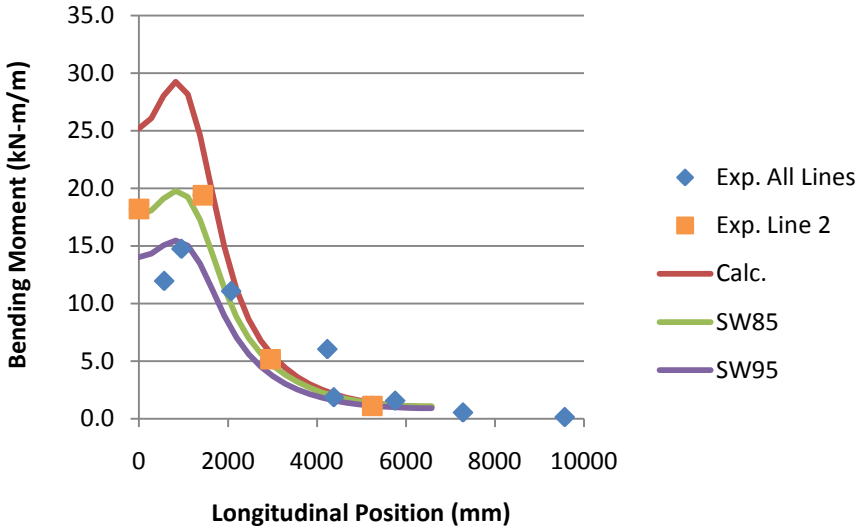

Figure 6-11 – Layered linear elastic model, longitudinal bending moment profile, 0.6 m backfill

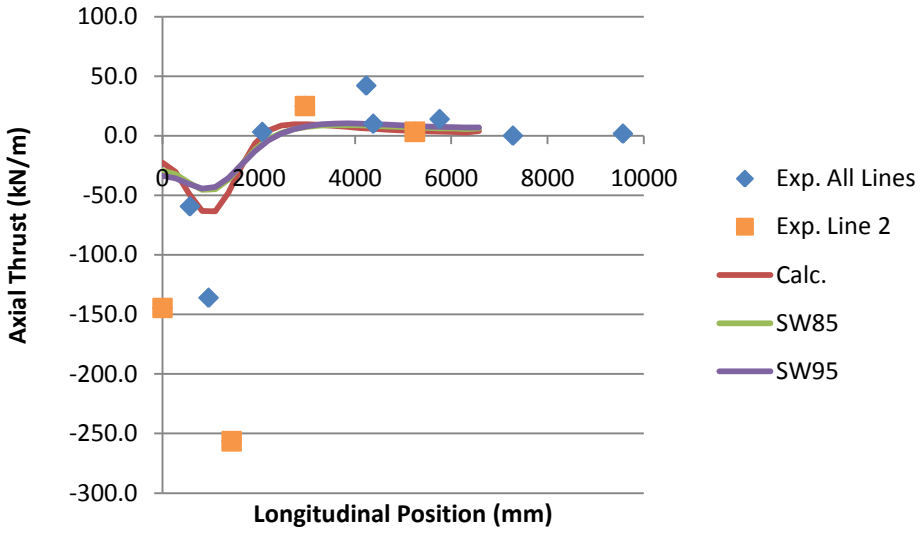

Figure 6-12 - Layered linear elastic model, longitudinal axial thrust profile, 0.6 m backfill

6.4 LAYERED MOHR-COULOMB

The soil properties used for the layered Mohr-Coulomb model were very similar to the layered linear elastic properties, with additional nonlinear behaviour. Transverse bending and thrust plots are displayed in Figure 6-5 and Figure 6-14 while longitudinal bending and thrust plots are shown in Figure 6-15 and Figure 6-16, respectively. In general, these nonlinearities could only produce softer soil behaviour, and thus greater structural forces. Despite significant plastic behaviour, shown in Figure 6-17, this was indeed the result. The structural forces were similar to the layered linear elastic model but were more conservative, especially the bending moments. One observed difference was the unusual "squiggle" occurring near the edges of the crown plate on the transverse axial thrust diagram. This anomaly was an artefact of the plasticity, but it was not entirely clear what mechanism would produce such a result.

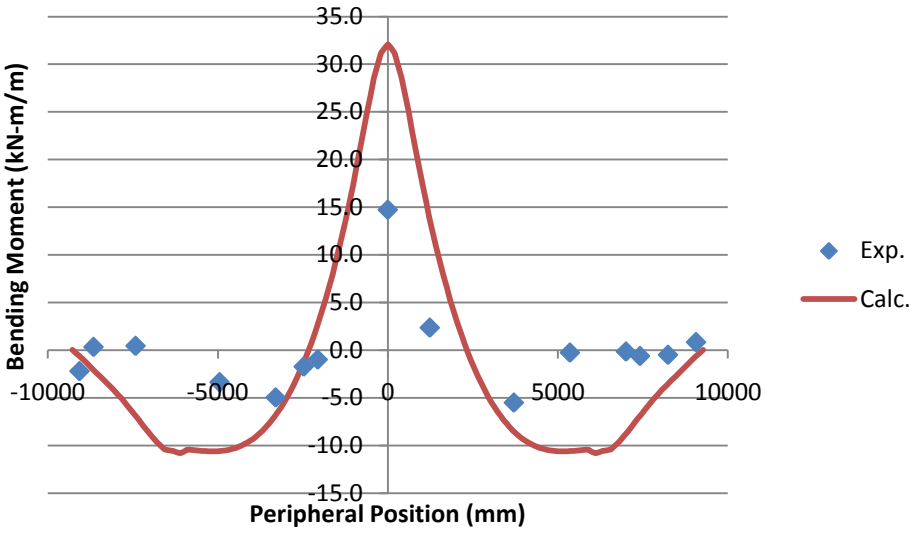

Figure 6-13 – Layered Mohr-Coulomb model, transverse bending moments, 0.6 m backfill

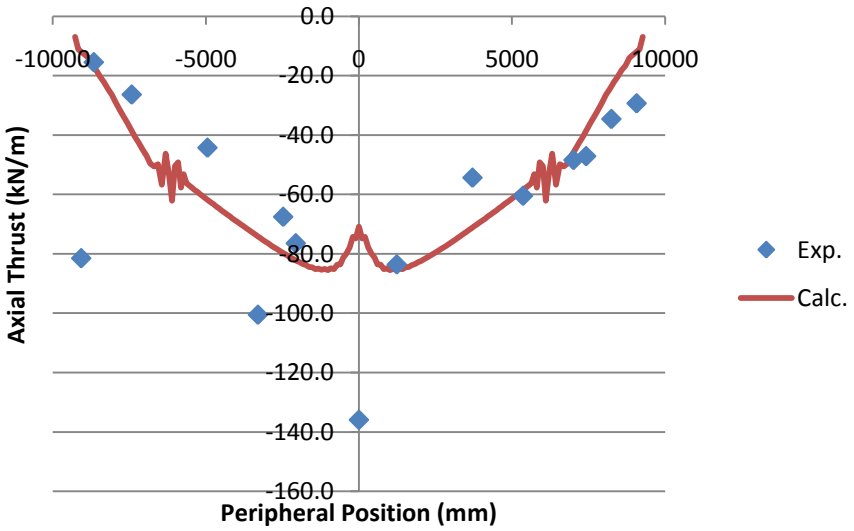

Figure 6-14 – Layered Mohr-Coulomb model, transverse axial thrust, 0.6 m backfill

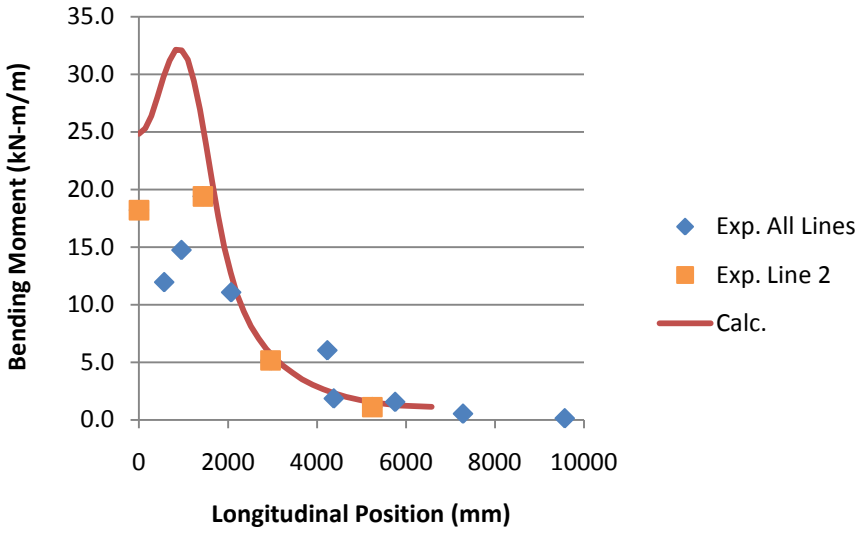

Figure 6-15 – Layered Mohr-Coulomb model, longitudinal bending moment profile, 0.6 m backfill

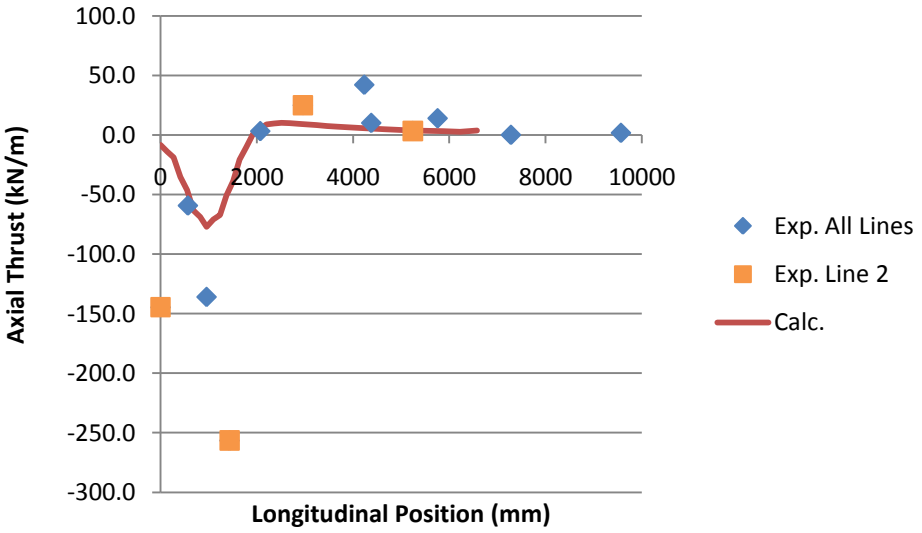

Figure 6-16 - Layered Mohr-Coulomb model, longitudinal axial thrust profile, 0.6m backfill

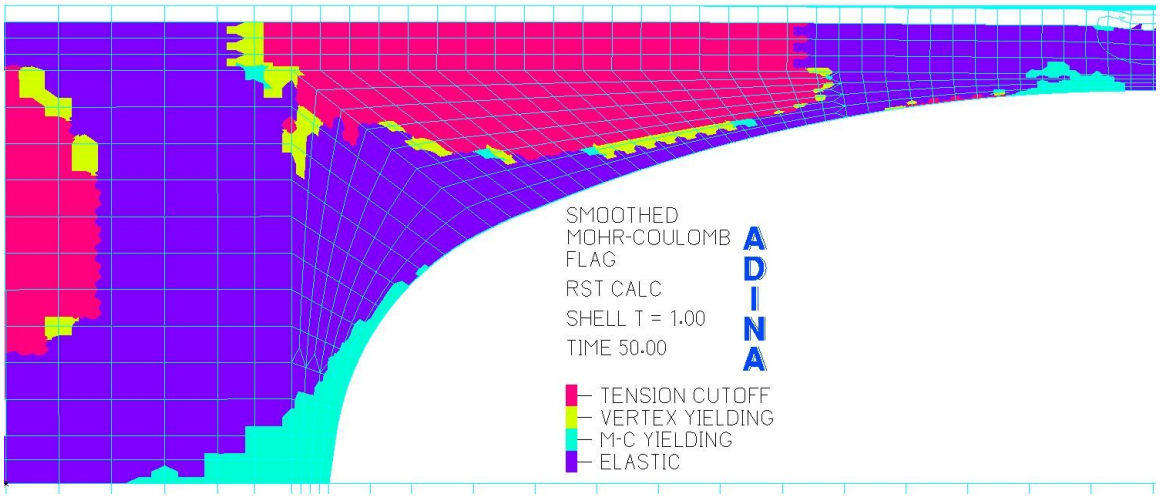

Figure 6-17 – Mohr-Coulomb failure flags, transverse section, 0.6m backfill

6.5 MODEL COMPARISON

The soil models which were derived from geotechnical testing were the curve description model, the layered linear elastic model, and the Mohr-Coulomb model. The structural forces obtained from each of these models were remarkably similar. Figure 6-18 and Figure 6-19 show the transverse bending and thrust diagrams with each model displayed.

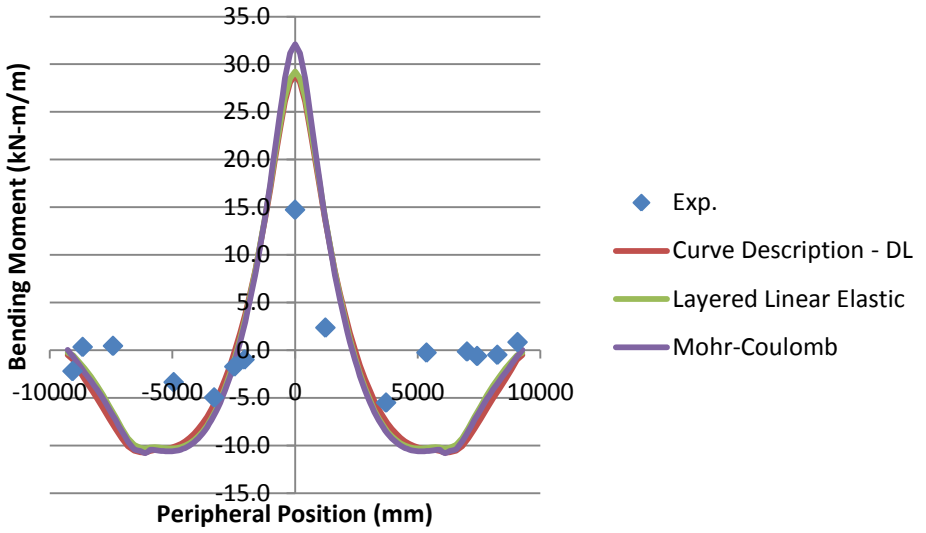

Figure 6-18 – Various soil models, transverse bending moments, 0.6m backfill

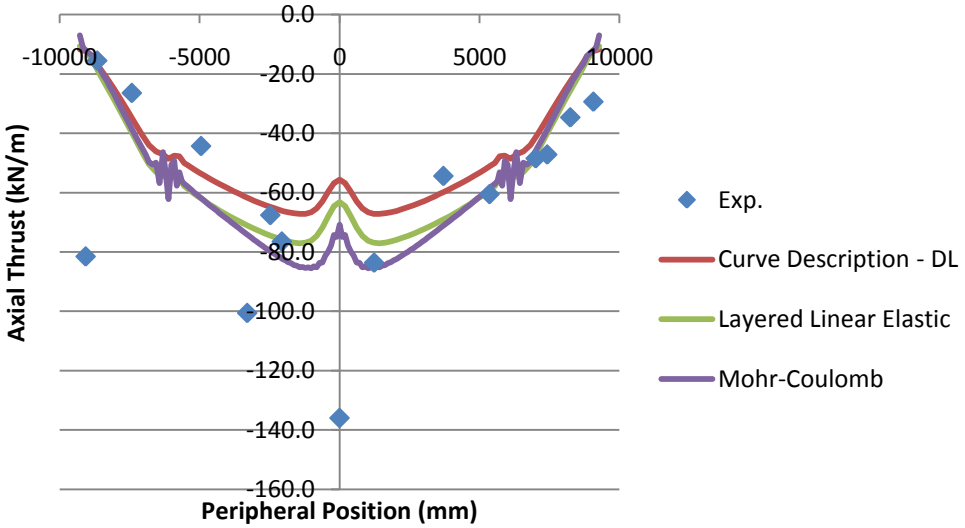

Figure 6-19 – Various soil models, transverse axial thrust, 0.6m backfill

The curve description model and layered linear elastic models produced an almost identical structural response. The curve description model, however, contains many

disadvantages over the layered linear elastic model. Firstly the curve description model required a dead load analysis, and because of the nonlinearity was less computationally efficient. Additionally, characterizing the stress strain curve required raw data obtained from hydrostatic testing. Analysing a structure with no prior soil history would be impossible. The layered linear elastic model, however, has a variety of well tested parameters developed for a number of different soil types and compaction levels. Because of these advantages, the layered linear elastic model would be far more useful for either research or design.

The Mohr-Coulomb model, while being extremely sophisticated, did not offer a more accurate solution than its elastic counterpart. The difference in computational intensity was significant. The linear elastic model could be solved in less than five minutes whereas the Mohr-Coulomb models run time consistently exceeded 10 hours, depending on the number of load steps and the convergence. The Mohr-Coulomb model was also more fastidious. Overall, the layered linear elastic model was the most effective and easily implemented model of those studied, and would be recommended for future live load studies.

6.6 Additional Plots of Layered Linear Elastic Model

6.6.1 Bending Moments

Figure 6-20 displays the longitudinal profile of maximum negative bending under 0.6 m of backfill cover. Negative moments were observed to decay over approximately twice the distance of positive moments at the crown. Experimental values were taken from the load case where the maximum negative moments were recorded. Figure 6-21 displays the maximum positive and negative moments at various backfill depths. Although the magnitudes were poorly correlated, the slopes from the finite element

models were reasonably similar to those taken from the experimental testing. Figure 6-22 shows a contour plot of the bending moments. The moment gradients acting beneath the tire loads were much steeper than those at the negative moment location.

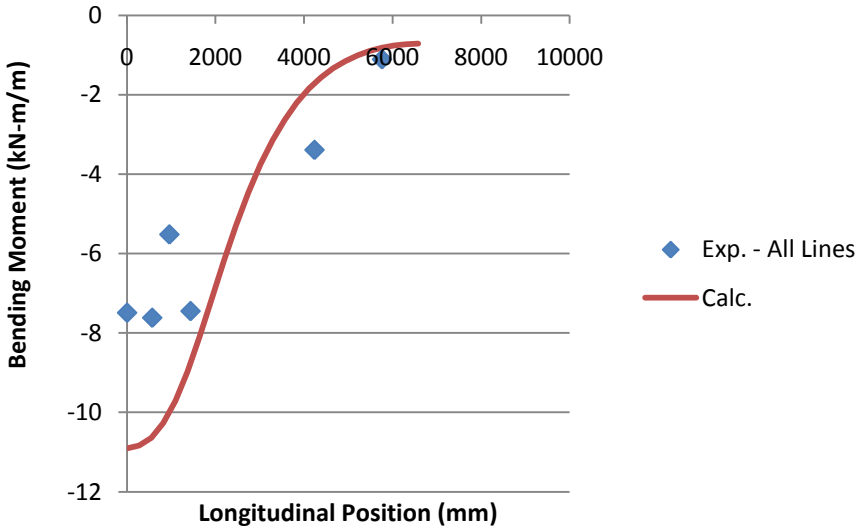

Figure 6-20 – Longitudinal bending moment profile at maximum negative moment, 0.6m

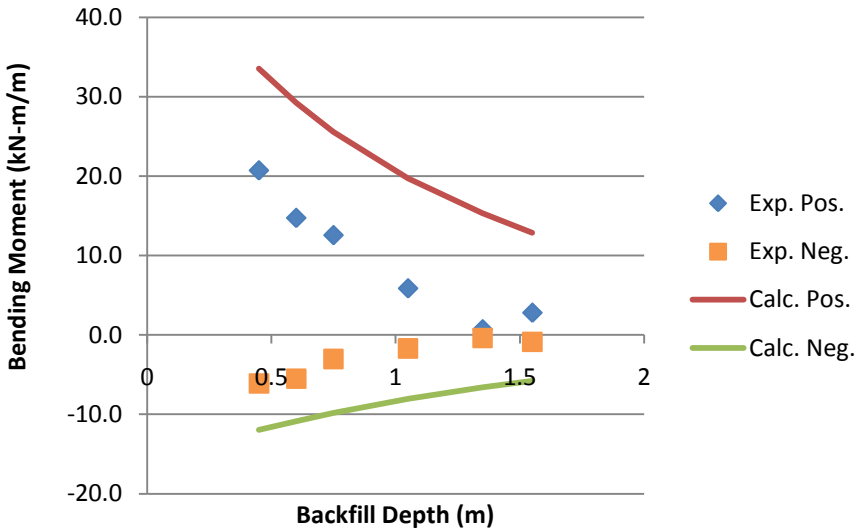

Figure 6-21 – Maximum positive and negative bending moments at various backfill

depths

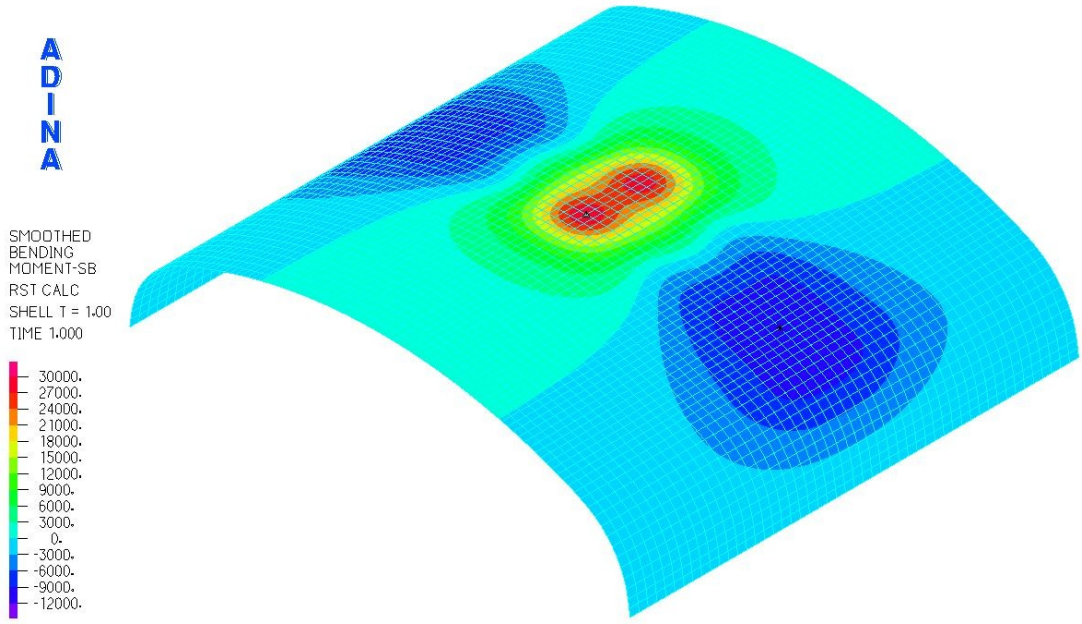

Figure 6-22 – Contour plot of bending moments, 0.6m backfill

6.6.2 Axial Thrust

Figure 6-23 displays the longitudinal profile of axial thrust plotted at the point of maximum axial thrust for each of the backfill depths analyzed. Under shallow backfill depth the thrust was very concentrated beneath the tire. Higher backfill depths showed a wider thrust distribution and much lower magnitudes. Figure 6-24 displays the absolute maximum thrust at various backfill depths. Both the magnitude and slope of this figure were poorly correlated to the experimental values. Figure 6-25 and Figure 6-26 display axial thrust contour plots at 0.45 m and 1.55 m, respectively. The thrusts were concentrated beneath the wheel loads at the lower backfill depth, and were farther from the crown and more evenly distributed in the deeper backfill model.

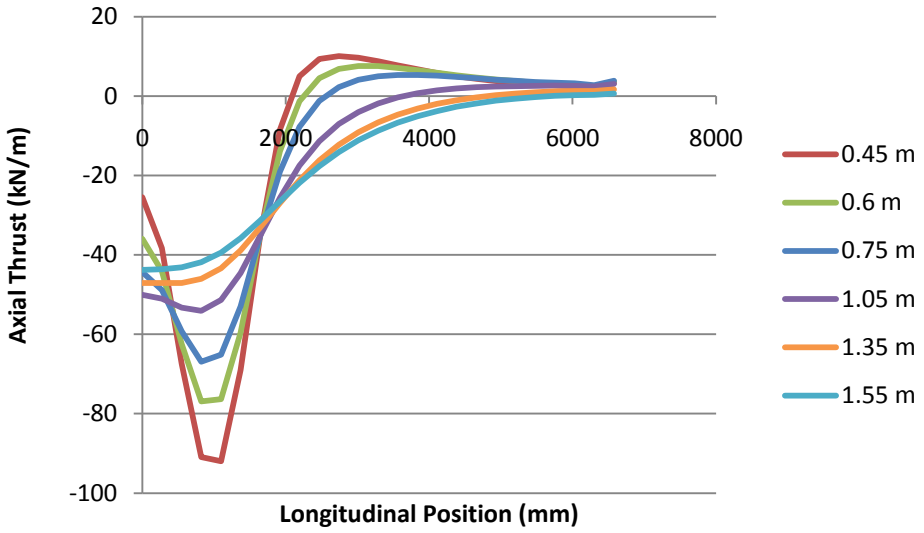

Figure 6-23 – Maximum longitudinal thrust profile at various backfill depths

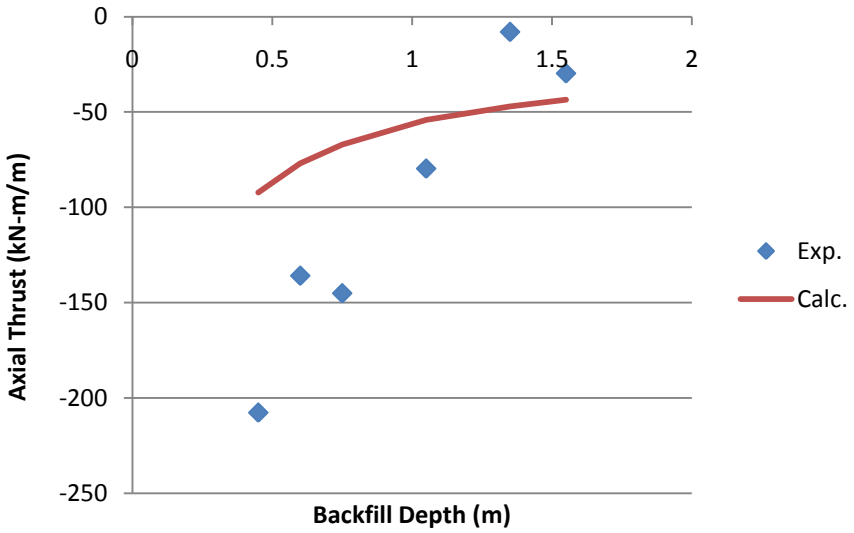

Figure 6-24 – Absolute maximum axial thrust at various backfill depths

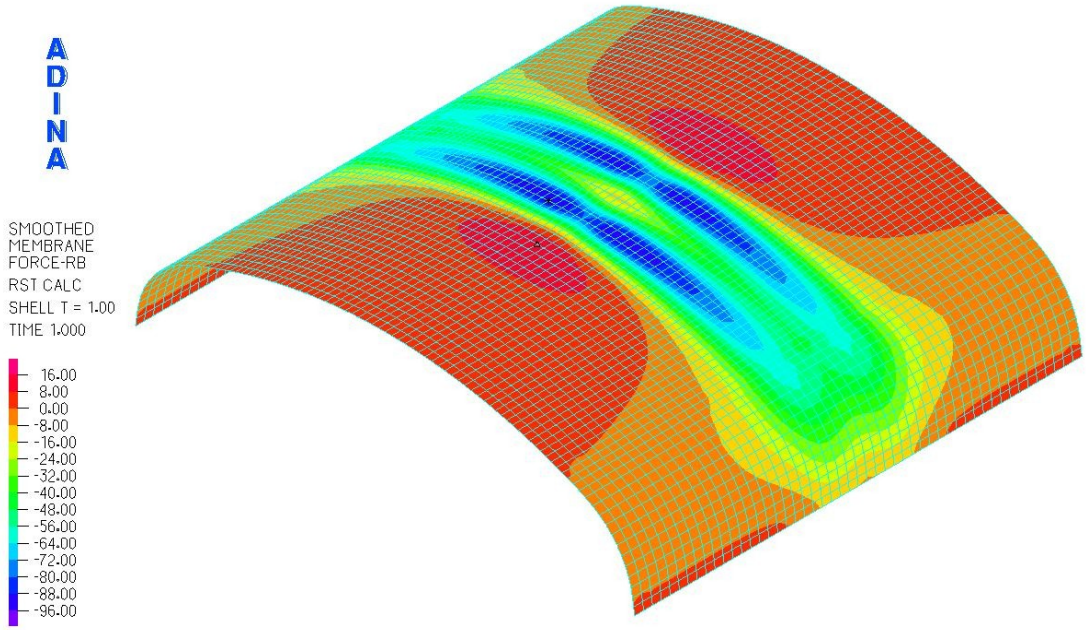

Figure 6-25 – Contour plot of axial thrust, 0.45m backfill

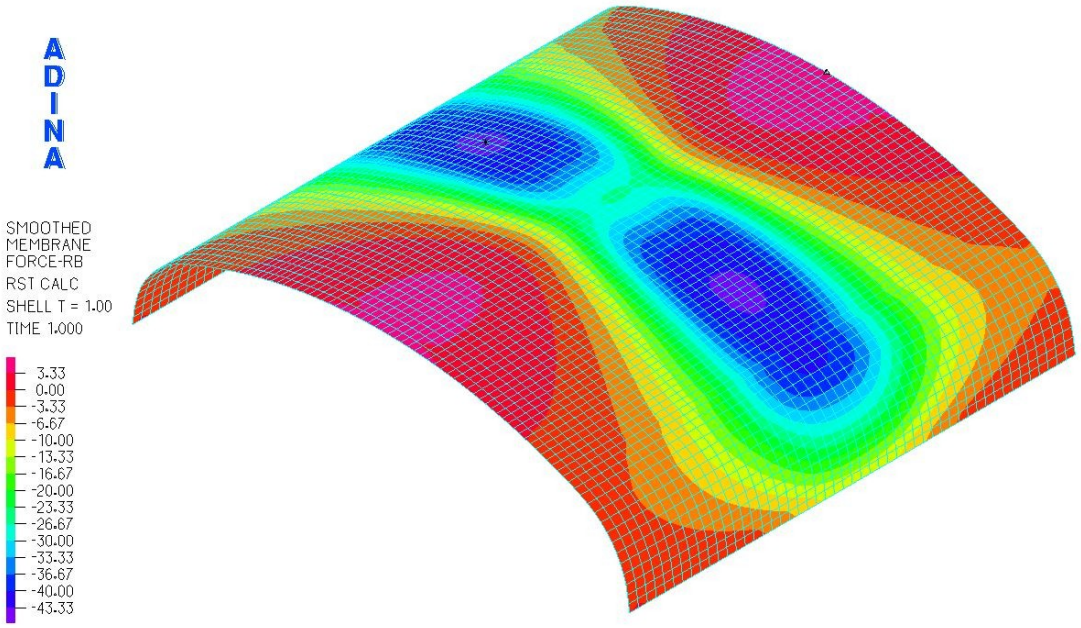

Figure 6-26 – Contour plot of axial thrust, 1.55m backfill

6.6.3 Displacement

In general the displacements calculated by the finite element software were very poorly correlated with experimental data. The finite element models predicted deflections many times in excess of what was recorded experimentally. Figure 6-27 shows the longitudinal displacement profile across the crown at a backfill depth of 0.6 m. Figure 6-28 shows the maximum vertical displacement at each backfill depth. The finite element model conservatively predicted the displacements to be approximately four times greater than the measured values. A contour plot of vertical displacements is shown in Figure 6-29.

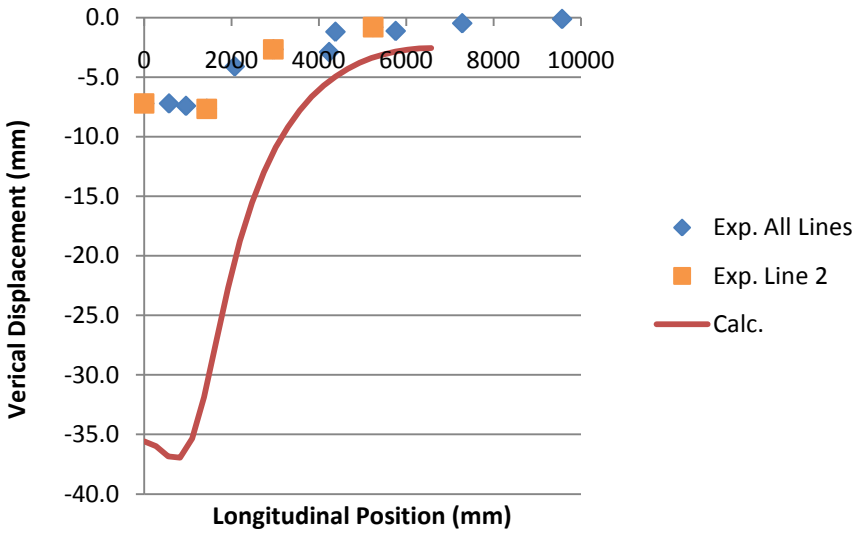

Figure 6-27 – Longitudinal vertical displacement profile, 0.6m

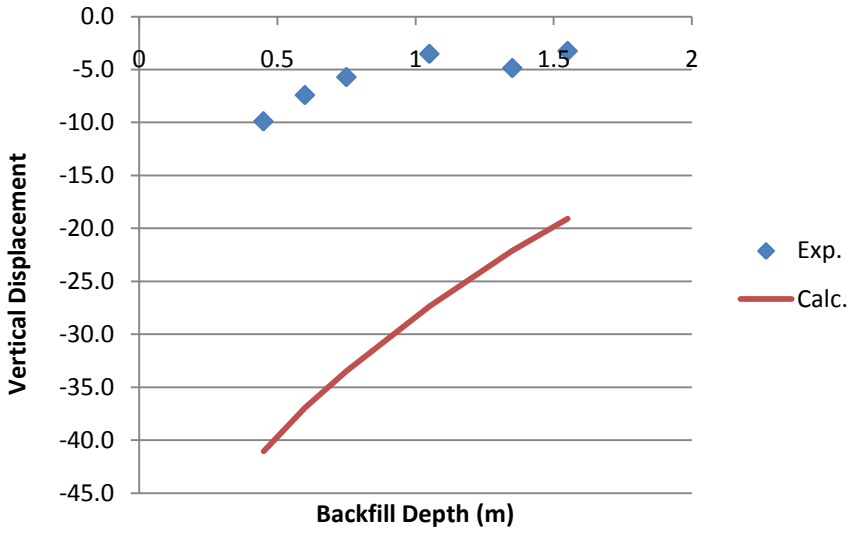

Figure 6-28 – Maximum vertical displacement at various backfill depths

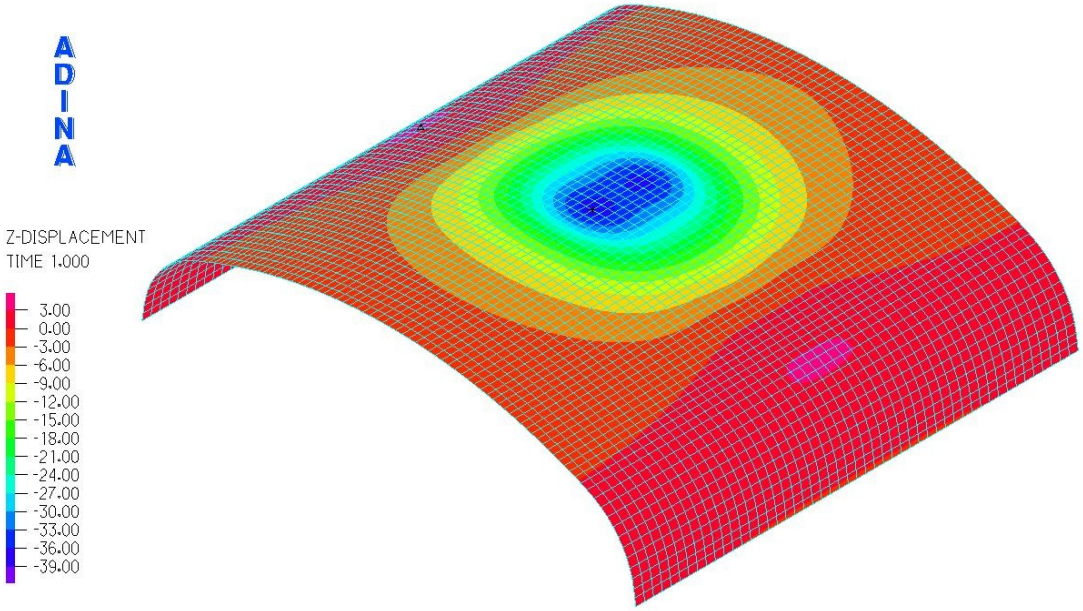

Figure 6-29 – Contour plot of vertical displacement, 0.6m backfill

6.6.4 Strain

Both inner and outer fiber strains were calculated from their respective bending moment and axial thrust values and plotted around the periphery of the structure. These plots are displayed as Figure 6-30 and Figure 6-31. Because the finite element models tended to overestimate the bending moment and underestimate the axial thrust, the strain diagrams showed better correlation to the experimental data. Additionally the models were conservative for both inner and outer fiber strains.

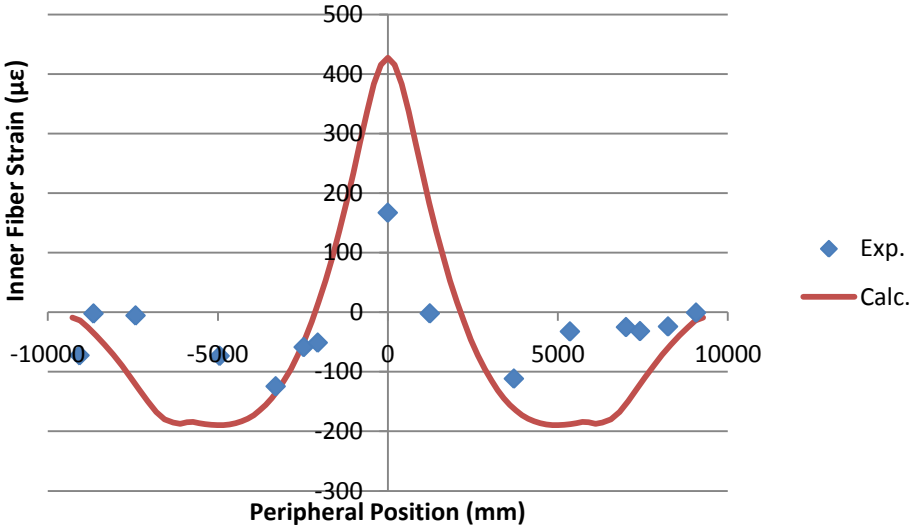

Figure 6-30 – Inner fiber strains around periphery of structure, 0.6m backfill

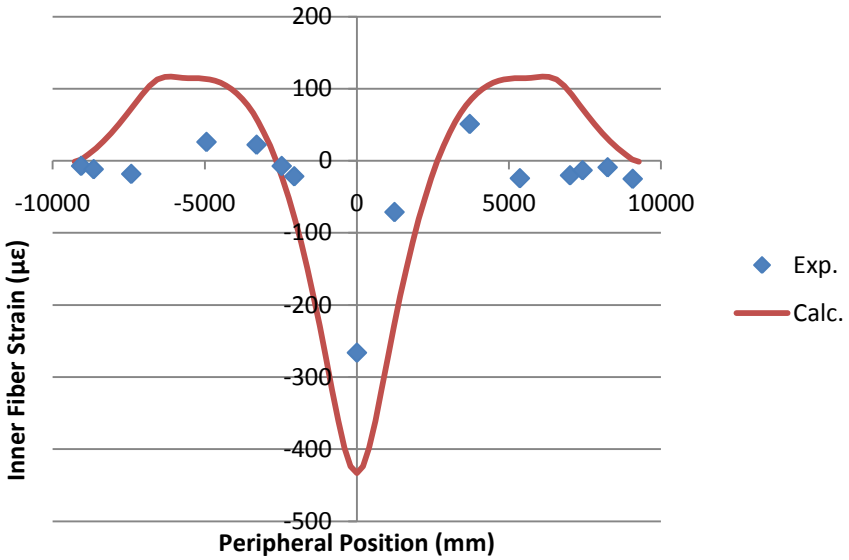

Figure 6-31 – Outer fiber strains around periphery of structure, 0.6m backfill

6.6.5 Soil Stresses

The load distribution through the soil is an important consideration when modelling shallow live loads in two dimensions. Figure 6-32 and Figure 6-33 show vertical soil stresses transversely while Figure 6-34 and Figure 6-35 show vertical soil stresses longitudinally.

Figure 6-32 – Vertical soil stress, transverse section, 0.45m backfill

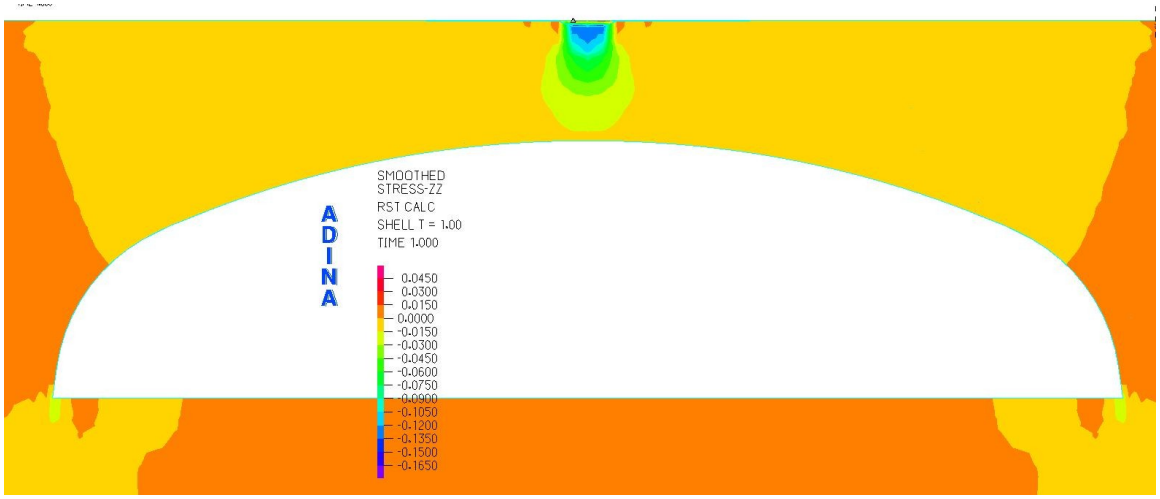

Figure 6-33 – Vertical soil stress, transverse section, 1.55m backfill

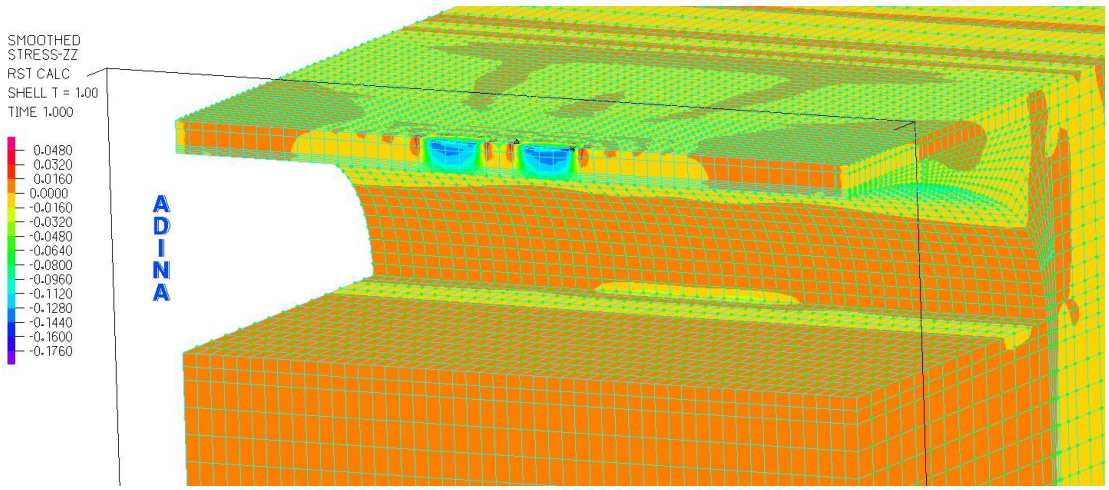

Figure 6-34 – Vertical soil stress, longitudinal section, 0.45m backfill

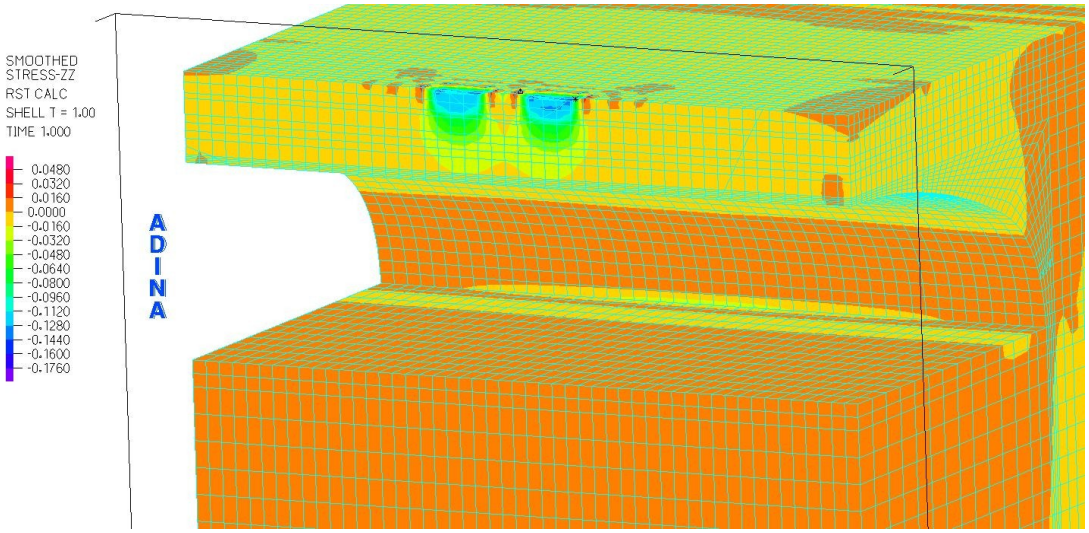

Figure 6-35 – Vertical soil stress, longitudinal section, 1.55m backfill

CHAPTER 7 - PARAMETRIC STUDY

7.1 GENERAL

The parametric study was conducted to determine the influence of each of the various parameters on the structural forces, specifically axial thrust and bending moment. The outcomes of this study established which parameters require the most accuracy when modelling or when designing a soil-metal box structure. The absolute maximum bending moment and axial thrust values were presented unless otherwise specified. For numerical charts, maximum and minimum values were extracted various points around the structure. Typically, the maximum positive moment occurred at the crown directly beneath the tire load while the maximum negative thrust occurred adjacent to the tire load. The maximum negative bending moment occurred between the haunches and crown. The maximum positive axial thrust occurred longitudinally 2 – 3 meters away from the wheel load. The layered linear elastic model using parameters obtained from soil testing was used for the entire chapter. The model was subjected to the same loads described in Chapter 5.4 with a backfill depth of 0.6 m.

7.2 SOIL

7.2.1 Non-critical Backfill

The stiffness of soil in the non-critical backfill zone was analogous to elastic boundary conditions which support the critical backfill stiffness. As such the impact of changing this parameter was low, even when changed by several orders of magnitude. A lower stiffness represented very soft boundary conditions while stiffer values were analogous to fixed boundary conditions. Table 7-2 displays maximum and minimum values of bending moment and axial thrust from the entire structure at various values of noncritical backfill zone stiffness. A graphical display of this data showing only the

absolute maximum bending moment and axial thrust is presented in Figure 7-1. The maximum bending moment, (which occured at the crown), showed the most sensitivity, but the change across the entire range was less than 5%.

Table 7-1 – Variance in non-critical backfill stiffness

Stiffness Value (MPa)	Bending Moment (kN-m/m)		Axial Thrust (kN/m)	
	Max	Min	Max	Min
0.1	29.88	-11.12	10.22	-78.21
0.7	29.63	-10.91	9.63	-78.93
1	29.54	-10.86	9.42	-79.18
5	29.04	-10.53	8.24	-80.62
10	28.84	-10.41	7.78	-81.20
50	28.53	-10.24	7.14	-82.02
100	28.47	-10.21	7.00	-82.20

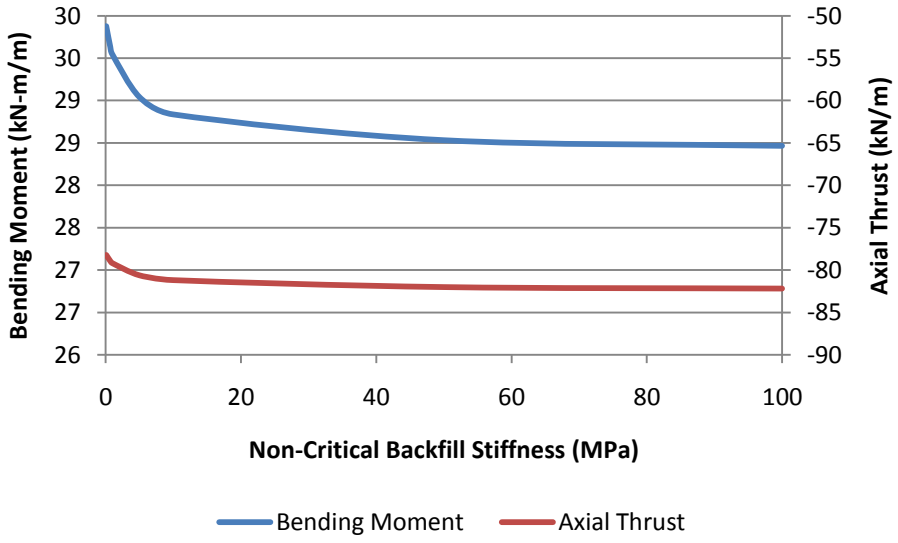

Figure 7-1 – Maximum moment and thrust at various non-critical backfill values

These results were reasonable; increased stiffness provided better support for the culvert and reduced bending moments and thrusts while decreased stiffness provided less support and increased bending moments and thrusts. This relationship held true only for the lower range of values. At stiffness values greater than approximately 10 MPa, the change in both moment and thrust became asymptotic. The impact of this parameter was ultimately low, and determination of geotechnical parameters for soil in this zone was of little importance for vehicular loads.

Foundation stiffness may be considered the boundary condition for the soil beneath the structure. The foundation soil used on the long span box test was characterized by plate loading tests performed by ADI Limited, (2007). The recommended foundation stiffness was found to be 60 MPa. To determine the sensitivity of the model to this parameter wide range of stiffness values was modelled, ranging from 1 – 1000 MPa. The results are displayed in Table 7-2 and Figure 7-2.

Table 7-2 – Variance in foundation stiffness

Stiffness Value (MPa)	Bending Moment (kN-m/m)		Axial Thrust (kN/m)	
	Max	Min	Max	Min
1	32.67	-11.16	14.00	-74.46
10	30.24	-11.08	10.78	-77.77
60	29.63	-10.91	9.63	-78.93
100	29.57	-10.90	9.50	-79.06
500	29.49	-10.89	9.34	-79.22
1000	29.48	-10.88	9.32	-79.25

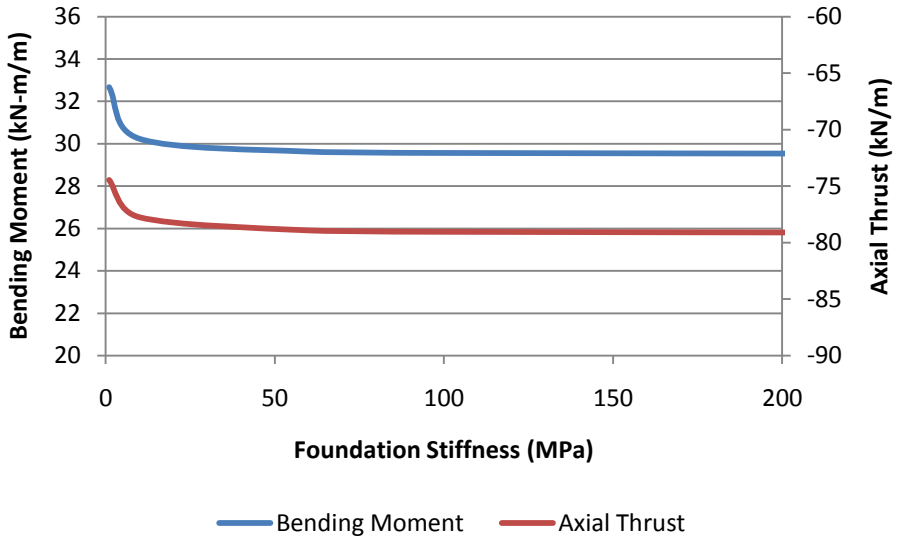

Figure 7-2 – Maximum bending moment and axial thrust at various foundation stiffness values

The results show that foundation stiffness plays a very small role in the accurate calculation of bending moments and axial thrust values under live loads. Very low stiffness values showed moments and thrust increasing by a small amount, but the results were asymptotic throughout the range of realistic foundation stiffness values. Given the time and expense involved with plate load testing, it is difficult to see a direct benefit to performing such tests. Quantifying the foundation stiffness is unlikely to provide additional benefits for live load analysis.

7.2.2 Critical Backfill Zone

The critical backfill zone was the soil in direct contact with the culvert and as such formed part of the "soil-structure" system. Properly characterizing this soil was extremely important in determining structural forces. Critical backfill stiffness affected both how live loads were transferred through the soil and how the structure responded

to these loads by restraining lateral deflections. The stiffness of soil was scaled up and down by a variety of percentages, and the results are shown numerically in Table 7-3 and graphically in Figure 7-3, Figure 7-4, and Figure 7-5.

Table 7-3 – Effect of varying critical backfill stiffness

Percent Change	Bending Moment (kN-m/m)		Axial Thrust (kN/m)	
	Max	Min	Max	Min
100	25.08	-8.54	8.84	-79.98
50	27.00	-9.44	9.02	-79.37
25	28.20	-10.07	9.23	-79.14
10	29.02	-10.54	9.40	-79.02
5	29.32	-10.72	9.49	-78.97
0	29.63	-10.91	9.63	-78.93
-5	29.95	-11.16	9.78	-78.89
-10	30.29	-11.44	9.94	-78.85
-25	31.41	-12.39	10.51	-78.77
-50	33.74	-14.48	11.97	-78.79

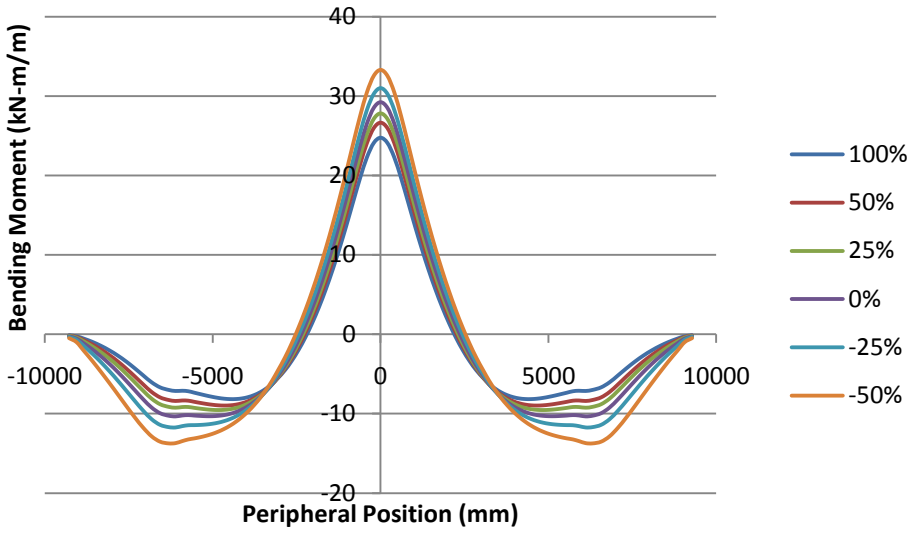

Figure 7-3 – Bending moments at various critical backfill stiffness values

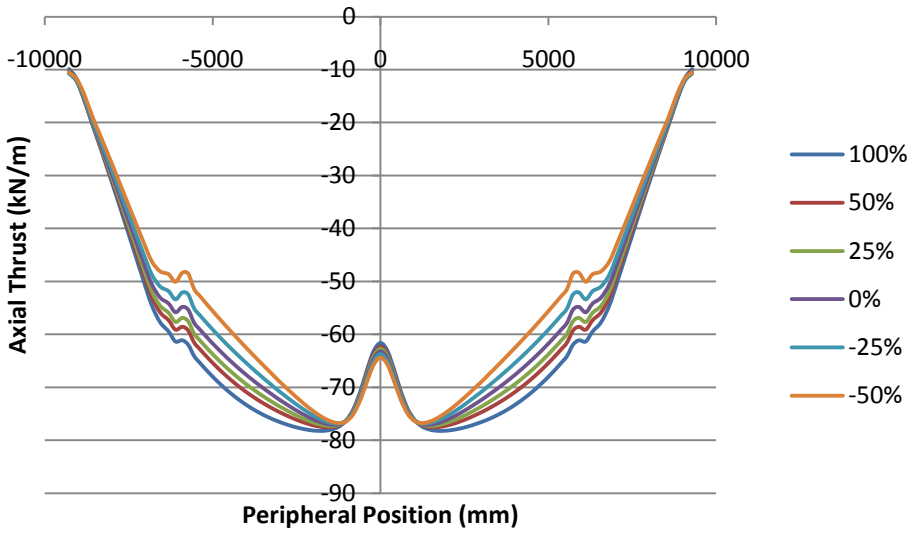

Figure 7-4 – Axial thrust at various critical backfill stiffness values

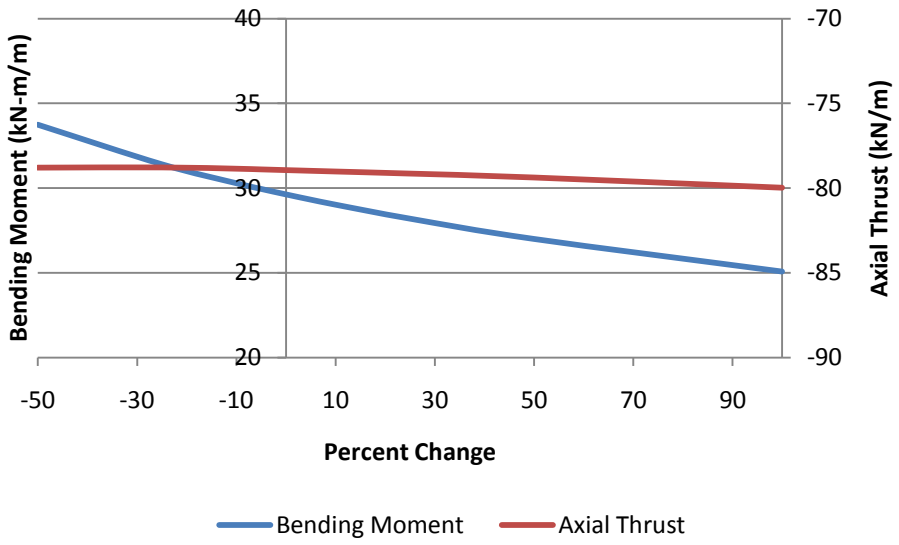

Figure 7-5 - Maximum bending moment and axial thrust at various critical backfill stiffness values

Increasing the critical backfill stiffness resulted in significant decreases in the maximum bending moment while decreasing the stiffness increased bending moments. The axial thrust was largely unaffected.

The critical backfill zone was then divided into two zones; an upper zone encompassing the soil above the haunches over the crown and a lower zone which consisted of the soil around the haunches down to the footings. A schematic representation of these zones is displayed in Figure 7-6. The stiffness of each zone was varied independently to determine which zone had a greater influence on structural forces.

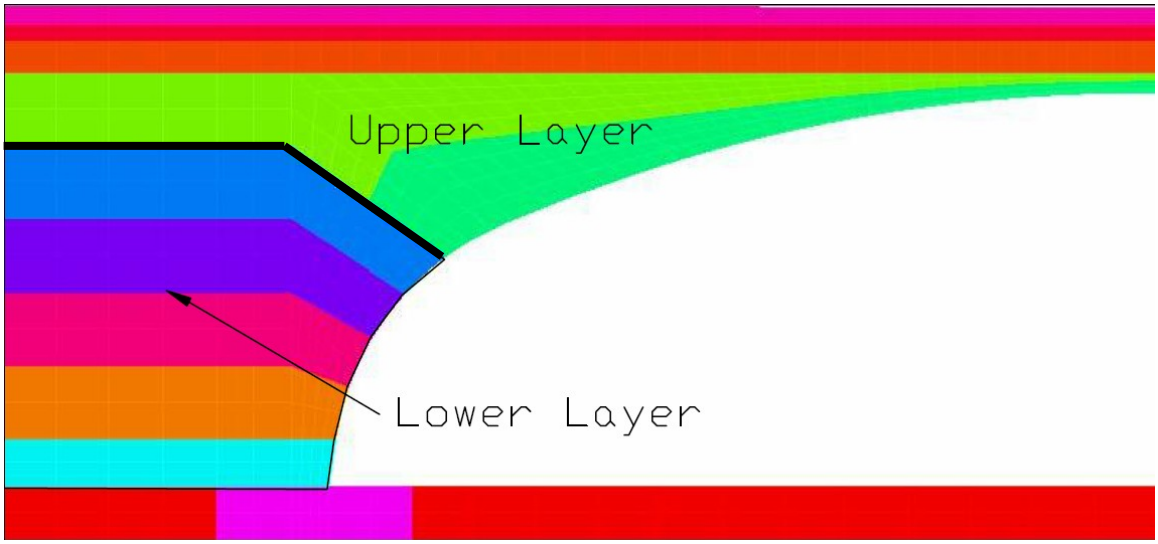

Figure 7-6 – Definition of upper and lower zones

Numerical results are displayed in Table 7-4 while graphical results are displayed in Figure 7-7 and Figure 7-8 for bending moments and axial thrusts respectively.

Table 7-4 – Comparison of effects of changing fill above and below crown

Percent Change	Upper Zone		Lower Zone	
	Moment (kN-m/m)	Thrust (kN/m)	Moment (kN-m/m)	Thrust (kN/m)
100	27.92	-83.96	26.61	-74.50
50	28.62	-81.86	27.96	-76.29
25	29.07	-80.53	28.74	-77.50
10	29.39	-79.61	29.26	-78.33
5	29.51	-79.28	29.44	-78.63
0	29.63	-78.93	29.63	-78.93
-5	29.76	-78.57	29.82	-79.25
-10	29.89	-78.19	30.02	-79.58
-25	30.34	-76.95	30.67	-80.68
-50	31.31	-74.37	31.91	-82.94

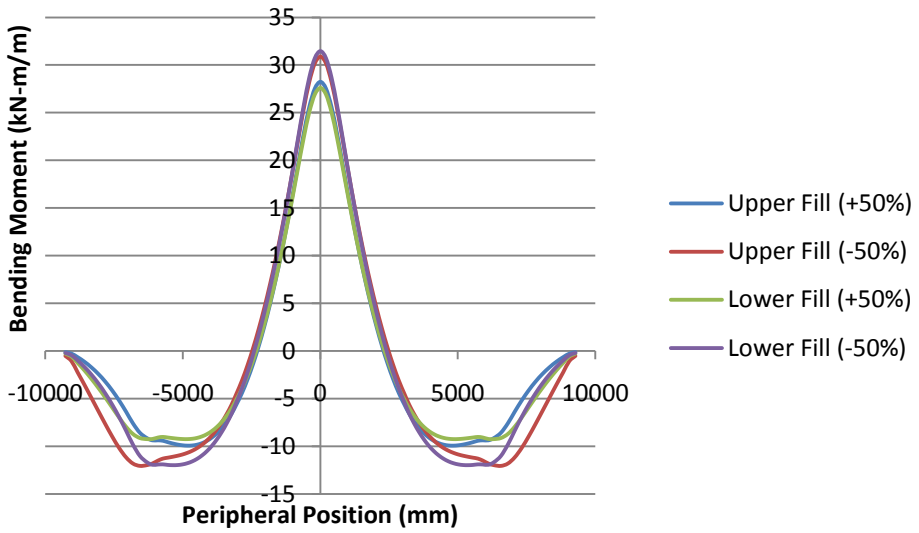

Figure 7-7 – Peripheral bending moments at various backfill stiffness values

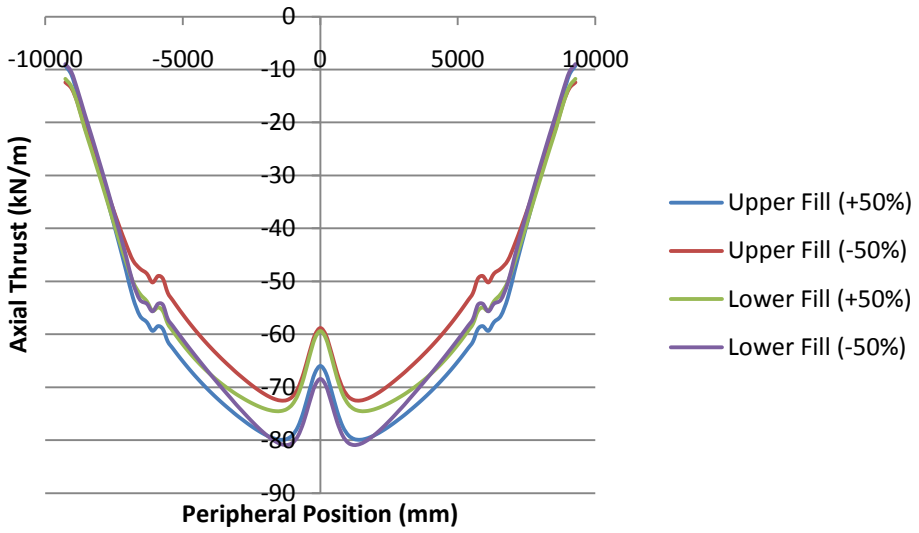

Figure 7-8 – Peripheral axial thrust at various backfill stiffness values

For both zones, increasing the stiffness resulted in corresponding decreases in bending moment. This result was intuitive, and similar to the results shown by varying the stiffness in the entire backfill zone. The upper zone influenced the transfer of stresses through the soil while the lower stiffness provided greater restraint for the haunches. The magnitudes observed were surprisingly similar, such that it was difficult to determine which zone has a greater influence on the structural forces.

The axial thrust response was counter-intuitive. Increasing stiffness in the upper zone resulted in larger values, while increasing stiffness in the lower zone resulted in lower values. The magnitudes observed were also very similar, albeit in different directions. The net result was that changing the stiffness of the entire backfill zone resulted in very little change in the axial thrust values. In effect, the changes “cancelled out” one another.

7.3 STEEL

ADINA's orthotropic material model, described in Chapter 5.2, was ideal for analysing corrugated plates. The structure was characterized by nine elastic constants and a shell element thickness. This chapter discusses how changes in these elastic constants alter the structural forces.

7.3.1 Young's Modulus

Young's Modulus was adjusted along each of the three orthogonal axes. Axes "A" and "B" were in-plane, representing the transverse and longitudinal directions respectively, while axes "C" was normal to the structure. The out-of-plane elastic constant, Ec, had no effect on structural forces.

The transverse in-plane Young's Modulus, E_A, was perhaps the most important variable considered in the steel model. As such its value was selected based on an equivalent flat shell considering the uniform thickness of the plate. That is, the bending stiffness EI was identical to the corrugated plate despite its uniform thickness. The accuracy of this constant was essential for the computation of both axial thrusts and bending moments. To judge the sensitivity of this variable to structural forces its value was scaled up and down by various percentages and the maximum transverse thrust and moment values were recorded. These values are presented in Table 7-5. It is noted that the error in determining this value for an unstiffened structure is practically ± 5% based on simplifications in the sectional analysis or small variation in steel modulus. This small variation would not significantly affect design values. The EI of structures with special stiffening features could vary as high as 50% based on the assumptions about the degree of composite action achieved. For these types of structures more effort should be devoted to characterizing the in-situ composite stiffness.

Table 7-5 – Variance in transverse stiffness

Percent Change	Bending Moment (kN-m/m)		Axial Thrust (kN/m)	
	Max	Min	Max	Min
50	32.07	-12.76	9.88	-77.26
25	30.99	-11.95	9.79	-78.03
10	30.21	-11.35	9.70	-78.55
5	29.93	-11.13	9.67	-78.74
0	29.63	-10.91	9.63	-78.93
-5	29.32	-10.73	9.59	-79.14
-10	28.98	-10.54	9.54	-79.34
-25	27.85	-9.93	9.47	-80.02
-50	25.33	-8.73	9.28	-81.26

Increasing E_A produced both greater axial thrust and bending moments, although changes in axial thrust were much less significant.

The in-plane Young's Modulus in the longitudinal direction was also an important parameter and reflected the axial stiffness along the axis of the culvert. The value was affected by corrugation geometry, plate thickness, and soil stiffness. The finite element analysis described in Chapter 5.2 suggests that regardless of these factors the value of the parameter was less than 1% of the transverse stiffness. Given the low magnitude changing E_B by a percentage directly had little influence on structural forces. E_B was also set to various percentages of E_A, 100%, 50%, and 5%, to gauge the impact of a model with similar stiffness in the transverse and longitudinal directions. Table 7-6 displays maximum and minimum transverse bending moments and axial thrusts from the model. The isotropic condition is represented by E_B = 12953 MPa whereas the orthotropic condition used in the thesis is represented by E_B = 16.2 MPa.

Table 7-6 – Variance in longitudinal stiffness

Parameter	E_B Value (MPa)	Bending Moment (kN-m/m)		Axial Thrust (kN/m)	
		Max	Min	Max	Min
$E_B = E_A$	12953	22.64	-8.30	52.66	-43.37
$E_B = 0.5E_A$	6476	23.81	-8.86	49.91	-47.09
$E_B = 0.05E_A$	647.6	27.11	-10.43	15.21	-60.66
E_B (+10%)	17.8	29.60	-10.91	9.45	-78.52
E_B	16.2	29.63	-10.91	9.63	-78.93
E_B (-10%)	14.8	29.67	-10.91	9.84	-79.38

As E_B was increased, transverse structural forces decreased. This was due to a greater proportion of the load being supported longitudinally. When E_B was low, longitudinal bending moments and thrusts were negligible, while they were significant at higher values of EB. This is illustrated in Figure 7-9, which displays the transverse and longitudinal bending moments around the periphery of the structure.

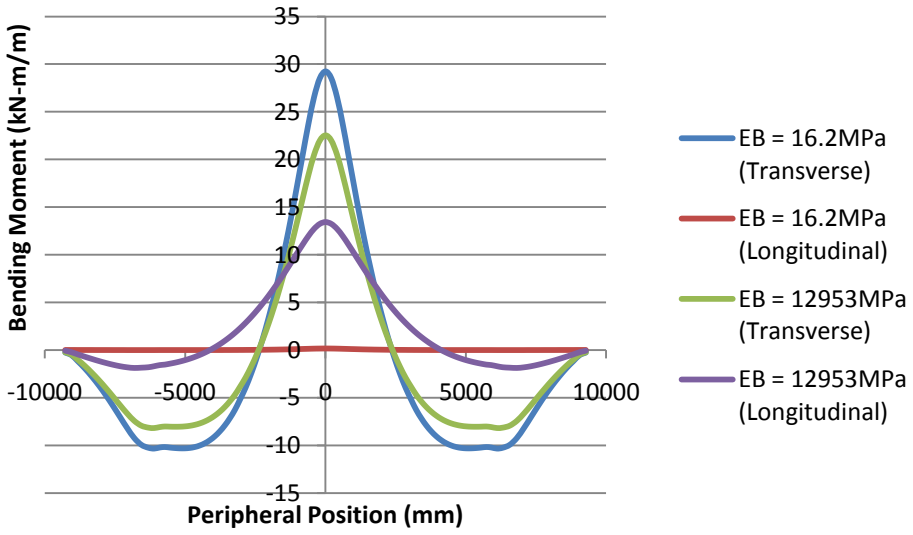

Figure 7-9 – Transverse and longitudinal bending moments

7.3.2 Shear Modulus

Three independent shear modulus constants were used to define shear stiffness in the orthotropic material model; G_{AB}, G_{AC}, and G_{BC}. Figure 7-10 graphically illustrates the shear direction that each constant represents.

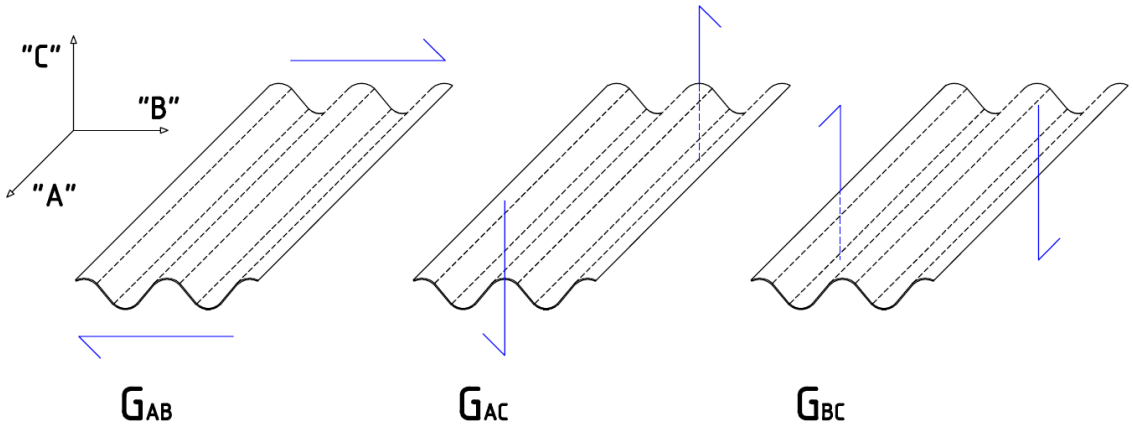

Figure 7-10 – Shear modulus label conventions

In-plane shear stiffness, G_{AB}, was derived from general analytical expressions derived for corrugated plates. The computed value from these expressions was 20.3 MPa. This stiffness value was very low compared to the stiffness of an isotropic plate, which was calculated to be 4982 MPa, assuming a Poisson's ratio of 0.3. Plots of bending moment and axial thrust with G_{AB} represented as a percentage its isotropic value are provided in Figure 7-11 and Figure 7-12 respectively.

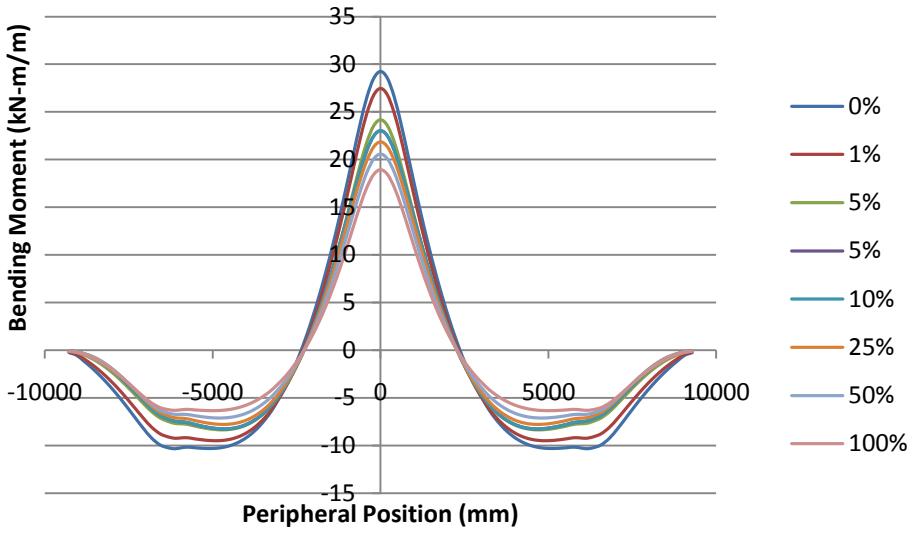

Figure 7-11 – Live load bending moments at various values of G_{AB}

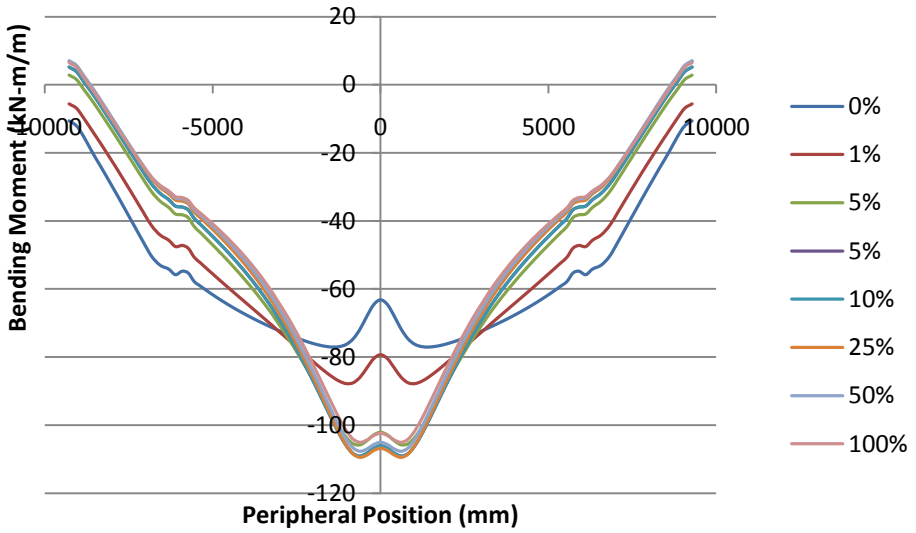

Figure 7-12 – Live load axial thrusts at various values of G_{AB}

As in-plane shear stiffness increased, bending moments decreased. As this elastic constant was important to the transfer of loads from the loaded ring to adjacent rings, this decrease in moment was consistent with the plate behaving more isotropically.

Figure 7-13 displays a contour plot of bending moments, with magnified displacements, showing how changes in G_{AB} affect bending moments across the structure. Empirical data suggests that the figure on the right is poorly representative of structural behaviour, as bending moments tend to decrease rapidly in the longitudinal direction.

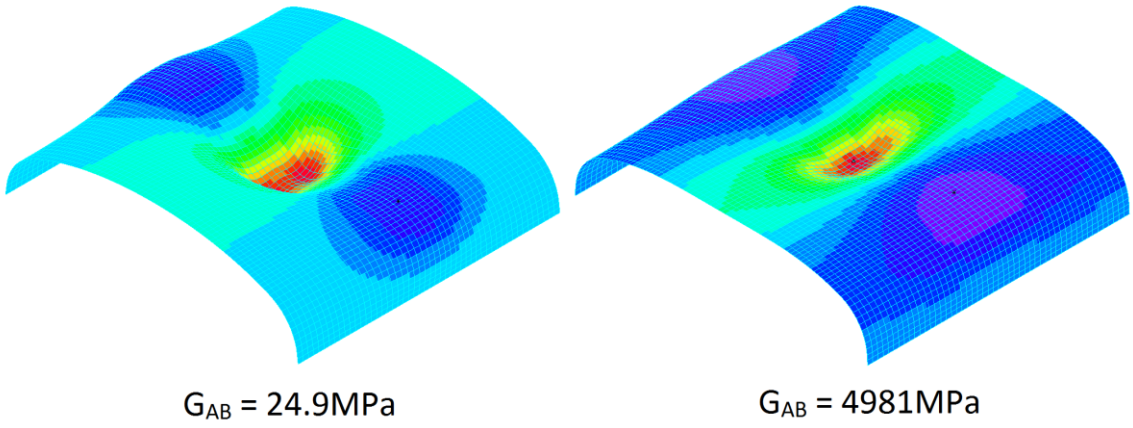

Figure 7-13 – Contour plots of bending moment (magnified 93 times)

Both the shape and magnitudes of axial thrust were affected by the in-plane shear modulus. When the shear modulus was less than 5% of the isotropic condition, the axial thrust diagram displayed a distinctly "flatter" profile, whereas values over 5% showed a profile which peaked near the crown. The "peaking" profile more closely resembled the experimental data, especially under lower backfill depths, thus the value of G_{AB} may be greater than was calculated by the analytical models. The influence of soil packed into the corrugations may increase the in-plane shear stiffness, but this issue was not investigated.

Maximum bending moment and axial thrust are plotted in Figure 7-14 with various values of in-plane shear modulus. Both of these structural forces were sensitive to shear

modulus changes, especially at low values. The maximum thrust occurred at approximately 10% of the isotropic condition. The greater sensitivity occurred in the range of values used for orthotropic criteria. Therefore properly quantifying the in-plane shear stiffness can be important to achieving accurate results.

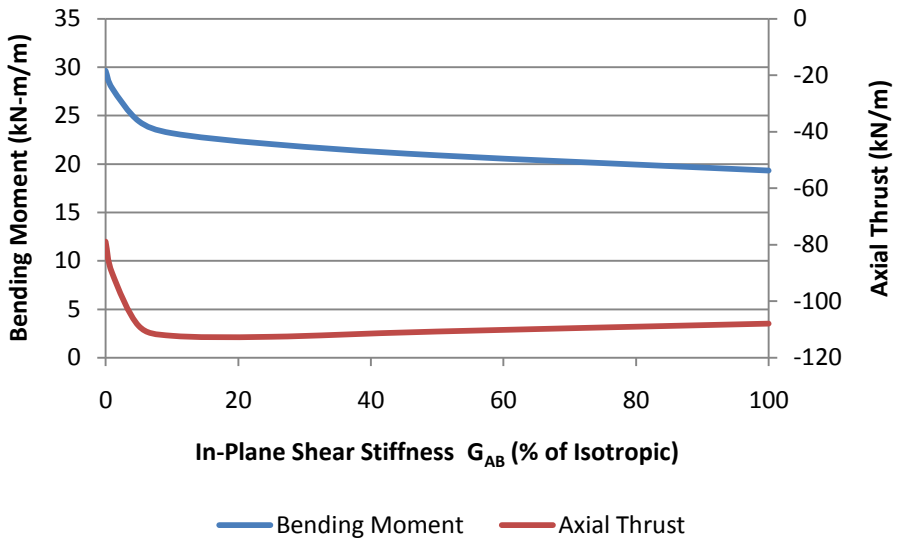

Figure 7-14 – Maximum bending moment and axial thrust at various values of G_{AB}

Out-of-plane shear stiffness had a much lower impact on structural forces. Figure 7-15 displays maximum bending moment and axial thrust as G_{AC} was gradually changed in a similar way to G_{AB}. Although the values selected for G_{AC} do not have the same physical meaning that exists for in plane shear stiffness, they were chosen for their convenience. Increases in G_{AC} resulted in increases in bending moment and decreases in axial thrust, although the differences were not significant. The impact of changing G_{AC} only occurred at low values, with higher values remaining constant.

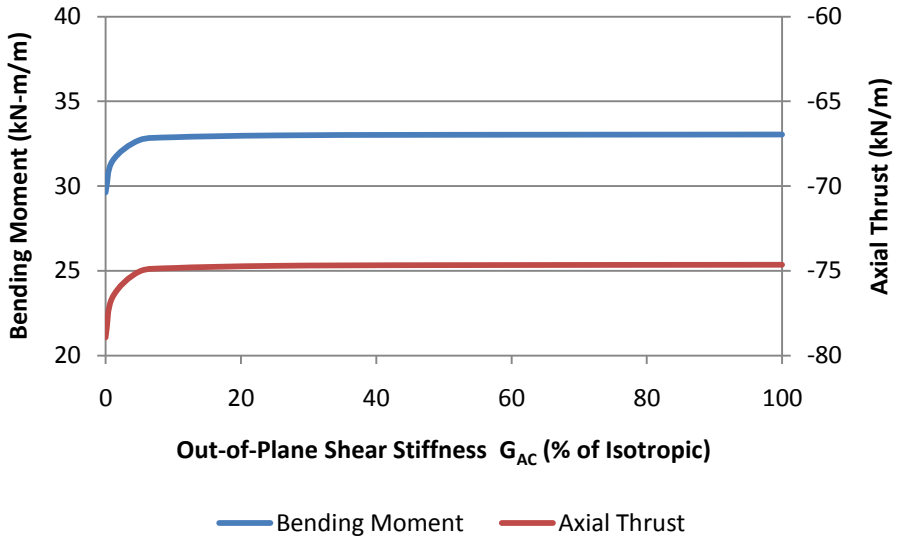

Figure 7-15 - Maximum bending moment and axial thrust at various values of G_{AC}

The final shear constant, G_{BC}, had no impact on structural forces while Poisson's ratio was taken as zero. Even with non-zero Poisson's ratio, its impact on moment and thrust predictions was low.

7.3.3 Poisson's Ratio

Poisson's ratio was taken as zero due to the differences in behaviour between the flat idealized shell used in the finite element model and the corrugated steel plate. In the stiffness matrix, six Poisson's ratio constants were used to characterize the stress-strain response of the steel. Three of these constants, ν_{AB}, ν_{AC}, and ν_{BC}, were input while ν_{BA}, ν_{CA}, and ν_{CB} were calculated automatically by ADINA according to the ratio described in Equation 7-1.

$$\frac{\nu_{ij}}{E_i} = \frac{\nu_{ji}}{E_j} \qquad \textbf{7-1}$$

This ratio ensured that the stiffness matrix was symmetric. Because of the large stiffness difference between E_A and E_B, however, ν_{BA} was only .00125 ν_{AB}.

The acceptable range of values for Poisson's ratio was restricted while using the orthotropic material model due to requirements that the stiffness matrix be positive definite. Equation 7-2 describes the maximum value of Poisson's ratio given the Young's modulus values already computed. This value of Poisson's ratio was too low to have any impact on the structural response.

$$|\nu_{AB}| < \sqrt{\frac{E_B}{E_A}} = \sqrt{\frac{16.2}{12953}} = 0.035 \qquad \textbf{7-2}$$

The out-of-plane Poisson's ratio values, ν_{AC}, and ν_{BC}, had no effect on structural forces. Ultimately Poisson's ratio was of little consideration.

7.4 SUMMARY

Using Chapter 5.3.4.2 as the reference case, normalized values for structural response were calculated as the calculated bending moment over the reference bending moment and calculated axial thrust over reference axial thrust respectively. The percentage change in property represented the reference stiffness scaled up or down by the indicated percentage, with zero percent representing no change. Figure 7-16 and Figure 7-17 display normalized plots of bending moment and axial thrust, respectively, against changes in soil stiffness in each of the zones of soil used in the model. These plots allow the sensitivity of each of the parameters to be compared directly for a range of possible values. The critical backfill zone soil stiffness was found to have the most significant impact on structural forces. An increase in stiffness for soil located in the top half of the

critical backfill zone, (upper), resulted in an increase in axial thrust. An increase in stiffness for soil located in the bottom half of the critical backfill zone, (lower), resulted in a decrease of axial thrust. Soil properties in the non-critical backfill zone and foundation were found to have little influence. The importance of proper soil characterization in the entire soil mass is emphasized by these results.

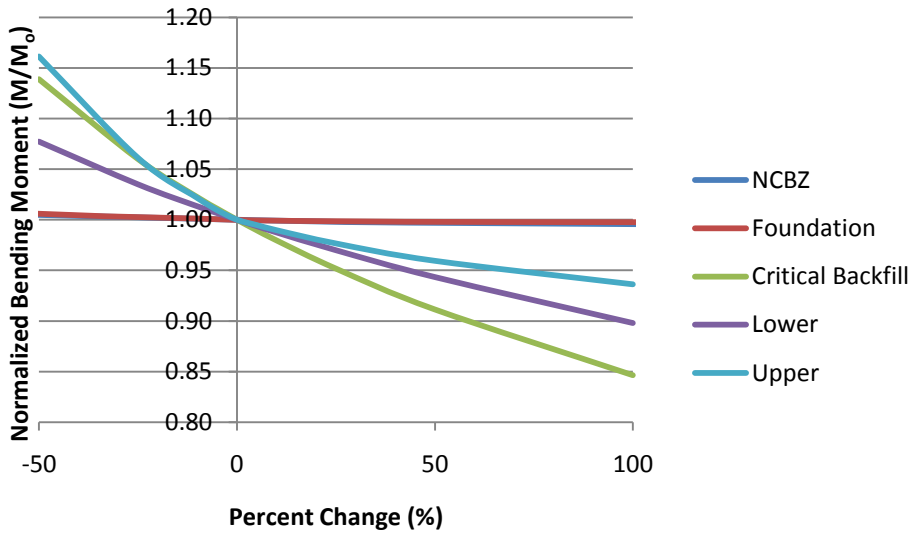

Figure 7-16 – Normalized bending moment for various values of soil stiffness

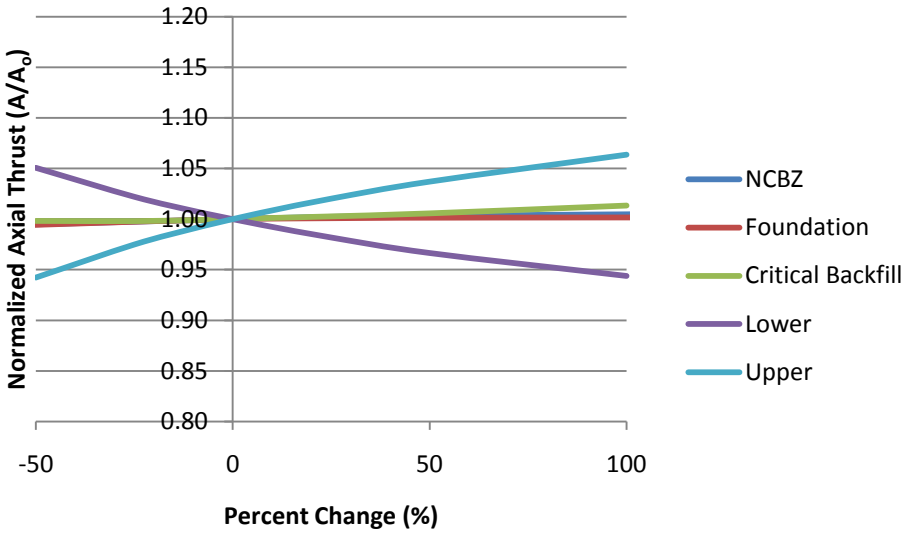

Figure 7-17 – Normalized axial thrust for various values of soil stiffness

Figure 7-18 and Figure 7-19 display normalized plots of bending moment and axial thrust, respectively, for various values of stiffness for the orthotropic steel parameters. Overall the steel parameters had a lower impact on structural forces than soil parameters. The most important parameter was E_A or strong axis stiffness. Although a range of values was used for the parametric study, the actual variance of this parameter was unlikely to exceed 10%. In plane shear stiffness, G_{AB}, had a surprisingly large impact on axial thrust, and thus may be worth investigating further.

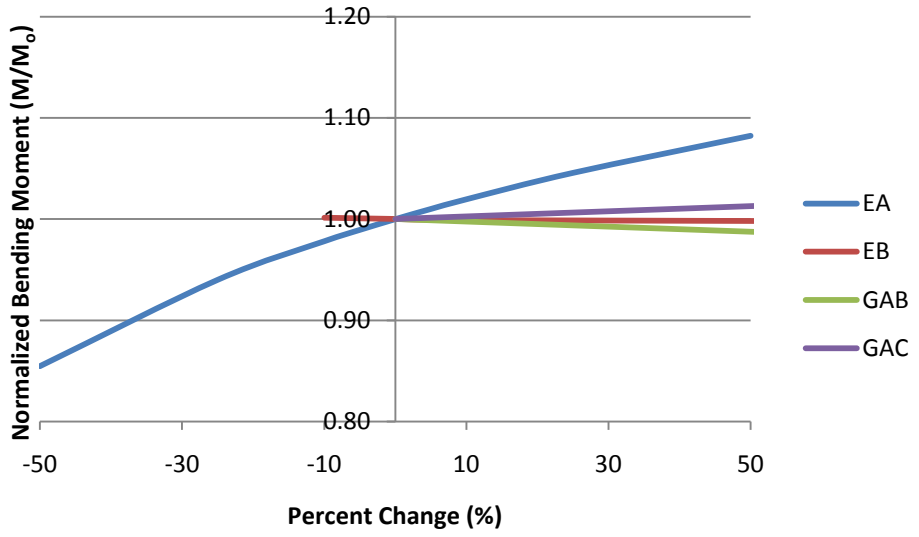

Figure 7-18 – Normalized bending moment at various steel stiffness values

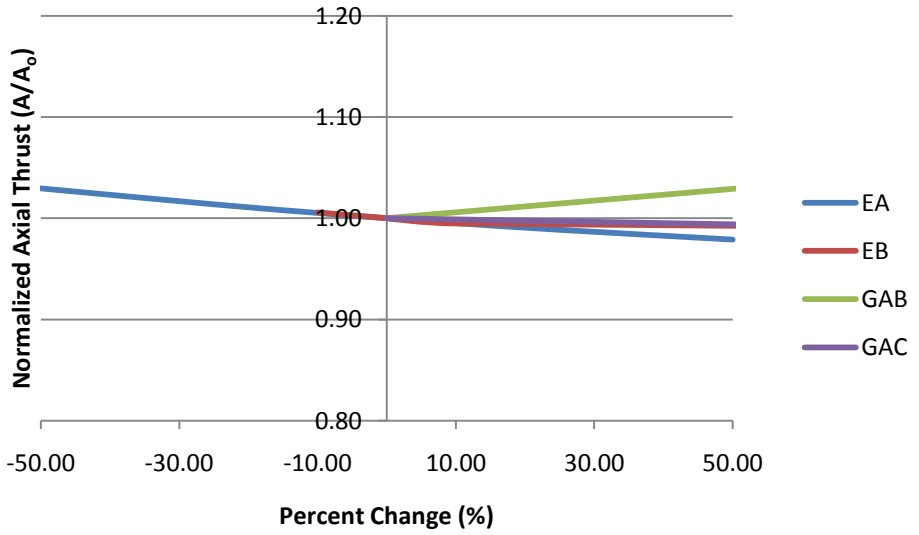

Figure 7-19 – Normalized axial thrust at various steel stiffness values

CHAPTER 8 - CONCLUSIONS

This research covered the characterization of live loads acting on shallow fill on a deeply corrugated box culvert. Both experimental testing and 3-D finite element modelling were used to describe the response.

Maximum positive bending moments observed during experimental testing occurred directly beneath live loads while maximum negative moments occurred adjacent to these positions. In this way the structure behaved similarly to a traditional portal frame. The largest structural response was induced when concentrated loads were placed at or around the crown. Backfill depth played an important role in reducing bending moments. Under shallow backfill depths, bending moments were large and accounted for a significant proportion of the total load acting on the structure. As backfill depth increased, bending moments were sharply reduced; their magnitudes insignificant when compared to the dead load response. Positive bending moments were large directly beneath the wheel loads but decayed rapidly in the longitudinal direction, becoming insignificant 4 – 6 meters from the load.

Axial thrust displayed a more uniform profile than bending moments. Just as with the bending moments, maximum vertical thrusts occurred directly beneath the wheel loads and were greatest when loads were placed at the crown. Maximum haunch thrusts occurred in load cases where the greatest mass was placed over the span. Tire loads placed directly above the instrumented stations resulted in very large thrust measurements which were not predicted by the finite element models. In the longitudinal direction, axial thrusts decayed very rapidly within two meters of the load application. Beyond two meters “positive” axial thrusts were observed, which may be more accurately described as reductions in the compressive thrust due to dead loads.

3-D finite element modelling was found to be a useful tool in the study of live loads applied under shallow backfill depths. The use of linear or nonlinear 3-D solid elements for soil combined with linear orthotropic shell elements for the steel shell was effective for capturing the nature of structural effects. The general stiffness expressions derived generically for corrugated plates provided a good foundation for characterizing the stiffness of the orthotropic shell. Analytical expressions were used for calculating the transverse in-plane Young's modulus and shear modulus while numerical methods calculated the longitudinal stiffness. Longitudinal stiffness was very low and was not increased significantly by the presence of soil packed in the corrugations.

Regardless of the soil model utilized, the results were typically conservative for bending moments and non-conservative for axial thrust, although bending moments resulted in larger strains and thus were of greater consequence. The differences between results obtained from the linear soil models were not appreciably different than those obtained from the nonlinear soil models. When dead load effects were included, the curve description model, a nonlinear model with fully elastic behaviour, produced almost identical results when compared to the layered linear elastic model. Given the model parameters were computed from two different soil tests, hydrostatic and triaxial, this similarity indicates that the model parameters were accurately established. It also established that soil properties for modelling can be obtained from material test results without model calibration which is important for creating reliable 3-D models for structures in which empirical results are not available. The layered linear elastic model was more computationally efficient.

The differences between the layered linear elastic model and the layered Mohr-Coulomb model were also small. The Mohr-Coulomb model resulted in an increase of 8 – 12% in maximum bending moments and axial thrusts. This was most likely a result of the additional plasticity softening the soil and resulting in reduced load distribution. The

shapes of the bending moment and axial thrust diagrams were very similar. Given the significant increase in computational expense for the nonlinear Mohr-Coulomb model, the model was not optimal for studying this particular loading application. The differences for other applications, for example the analysis of dead loads, may be more significant and was not investigated. Ultimately the layered linear elastic model was an efficient and reasonably accurate model and is recommended for future live load studies.

The parametric study was able to help identify those parameters which are highly sensitive to changes. Foundation stiffness and non-critical backfill zone stiffness was found to have very little impact on structural forces. It would be difficult to justify performing soil tests on samples from these areas, as the influence was not great enough to defend the expense. Critical backfill stiffness exerted a much greater impact on structural forces. Generally, increased stiffness resulted in lower bending moments due to the greater load distribution. Altering the critical backfill stiffness had little impact on axial thrust. The soil was divided into upper and lower zones, the lower zone covering the fill from the footings to just above the haunches, and the upper zone covering the fill above the crown. The influence of both of these zones was found to have a nearly equivalent effect on bending moments. Increasing the upper soil zone stiffness increased the magnitude of axial thrust, while increasing the lower soil zone stiffness decreased axial thrust. This phenomenon explained why changing the backfill zone stiffness for the entire critical backfill zone had little impact on axial thrust.

Many of the elastic parameters used for the orthotropic steel model were also sensitive to changes. Young's modulus in the transverse direction was a very important parameter. Increasing Young's modulus in the transverse direction resulted in both greater bending moments and axial thrust values, although the effect was much more significant for bending moments. Young's modulus in the longitudinal direction was the

primary factor for determining the level of orthotropy in the shell. When this parameter was increased, the load was shared between the transverse and longitudinal directions, resulting in lower transverse bending moments and axial thrust values. Increasing this parameter by a significant amount, for example to the same value as was used for the transverse stiffness, created unrealistic longitudinal bending moments and thrusts, which were negligible when the value was kept low. This established the importance of using an orthotropic model for 3-D analysis. The in-plane shear modulus, G_{AB}, was found to be an important factor in the transfer of forces from the loaded ring to adjacent rings. Increasing the value resulted in a decrease of bending moments as a greater width of the plate was engaged to support the load. Increasing the in plane shear stiffness resulted in an increase in the magnitude of axial thrust.

REFERENCES

Abdel-Sayed, G. (1970). Critical Shear Loading of Curved Panels of Corrugated Sheets. *ASCE - Engineering Mechanics Division* , 895-912.

Abdel-Sayed, G., & Bakht, B. (1982). Analysis of Live-Load Effects in Soil-Steel Structures. *Transportation Research Record* , 49-55.

Abdel-Sayed, G., Bakht, B., & Jaeger, L. G. (1993). *Soil-Steel Bridges - Design and Construction.* New York: McGraw-Hill Inc.

ADI Limited. (2007). *Results of Plate Load Test.* Dorchester, NB.

ADINA R & D, Inc. (2008). *Adina Theory and Modelling Guide - Volume I:Solids & Structures* . Watertown, MA: ADINA R & D, Inc.

Au, A., & Lam, C. (2005). *Load Test Report - Price Creek Culvert.* Toronto: Government of Ontario.

Bakht, B. (1981). Soil-Steel Structure Response to Live Loads. *Journal of Geotechnical Engineering Division* , 779-798.

Boscardin, M. D., Selig, E. T., Lin, R.-S., & Yang, G.-R. (1990). Hyperbolic Parameters for Compacted Soils. *Journal of Geotechnical Engineering* , 88-104.

Bowles, J. E. (1996). *Foundation Analysis and Design - 5th ed.* Peoria, Illinois: McGraw-Hill.

Canadian Standards Association. (2006). *Canadian Highway Bridge Design Code.* MISSISSAUGA, ON.

CSPI. (2009). *Handbook of Steel Drainage & Highway Construction Products.* Washington: Corrugated Steel Pipe Institute.

Duncan, J., & Chang, C.-Y. (1970). Nonlinear Analysis of Stress and Strain in Soils. *Journal of the Soil Mechanics and Foundations Division* , 1629-1653.

Duncan, J., Byrne, P., Wong, K. S., & Mabry, P. (1980). *Strength, Stress-Strain and Bulk Modulus Parameters for Finite Element Analyses of Stresses and Movements in Soil Masses.* Berkeley, California: University of California.

El-Sawy, K. (2003). Three-dimensional Modeling of Soil-Steel Culverts Under the Effect of Truckloads. *Thin-Walled Structures* , 747-768.

Flener, E. B. (2006). *Full-scale Testing of Two Corrugated Steel Box Culverts with Different Crown Stiffness.* Stockholm, Sweden: KTH Byggvetenskap.

Girges, Y. F. (1993). *Three-Dimensional Analysis of Composite Soil-Steel Structures.* Windsor, Ontario: University of Windsor.

Girges, Y., & Abdel-Sayed, G. (1995). Three-dimensional Analysis of Soil-Steel Bridges. *Canadian Journal of Civil Engineering* , 1155-1163.

Katona, M. (2009, January 20). Comments on Results of Plate Load Test.

Katona, M., Mlynarski, M., & McGrath, T. (2007). *Cande 2007 - Solution Methods and Formulations.* National Cooperative Highway Research Project.

M.E. Biancolini, C. B. (2005). Numerical Evaluation of Buckling and Post-Buckling Behavior of Corrugated Board Containers. *Associazione Italiana Per L'Analisi Delle Sollecitazioni.* Milan: Politechnico Di Milano.

McGrath, T., Moore, I., Selig, E., Webb, M., & Taleb, B. (2002). *Recommended Specifications for Large-Span Culverts.* Washington, D.C.: National Academy Press.

Moore, I. D., & Brachman, R. W. (1994). Three-Dimensional Analysis of Flexile Circular Culverts. *Journal of geotechnical engineering, v 120, n 10, p 1829-1844, Oct 1994* , 1829-1844.

Moore, I. D., & Taleb, B. (1999). Metal Culvert Resonse to Live Loading: Performance of Three-Dimensional Analysis. *Transportation Research Record* , 37-44.

Petersen, D. L., Nelson, C. R., Li, G., McGrath, T. J., & Kitane, Y. (2010). *NCHRP Report 647 - Recommended Design Specifications for Live Load Distribution to Buried Structures.*

Washington: Transportation Research Board.

Selig, E. T. (1988). Soil Parameters for Design of Buried Pipelines. *Pipeline Infrastructure* , 99-116.

Selig, E. T. (1990). Soil Properties for Plastic Pipe Installations . *Buried Plastic Pipe Technology, ASTM STP 1093* , 141-158.

TerrAtlantic Engineering Limited. (2009). *Results of Soil Testing.* Fredericton, NB.

Webb, M. C., Selig, E. T., & McGrath, T. J. (1999). Instrumentation for Monitoring Large-Span Culverts. *ASTM Special Technical Publication* , 66-88.

Webb, M. C., Selig, E. T., Sussman, J. A., & McGrath, T. J. (1999). Field Tests of a Large-Span Metal Culvert. *Transportation Research Record* , 14-24.

Williams, K., & Voros, R. (2009). *Long Span Box Test - Report #5 Dead Load Analysis.* Dorchester, NB: Atlantic Industries Limited.

APPENDIX A - ADDITIONAL PLOTS FOR VARIOUS SOIL MODELS

1. Linear Elastic

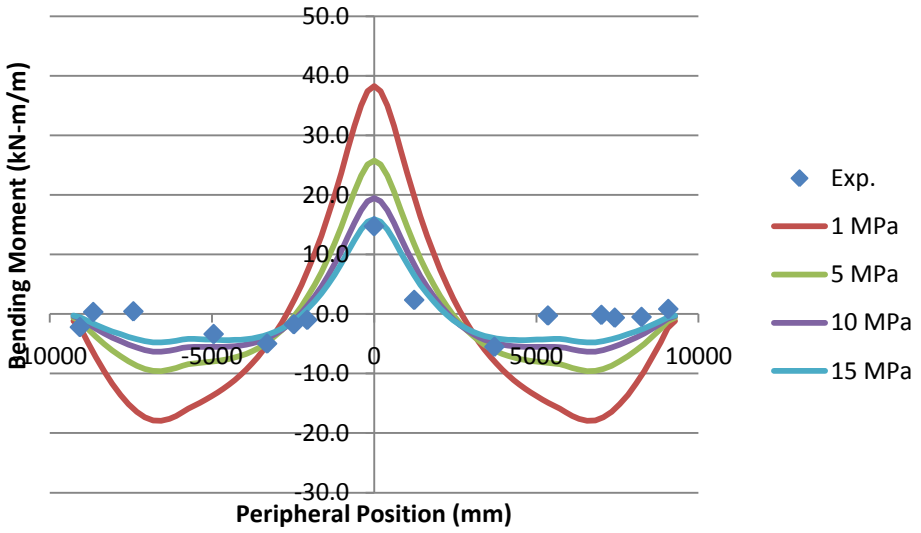

Figure 1 – Linear elastic model, transverse bending moments, 0.45 m backfill

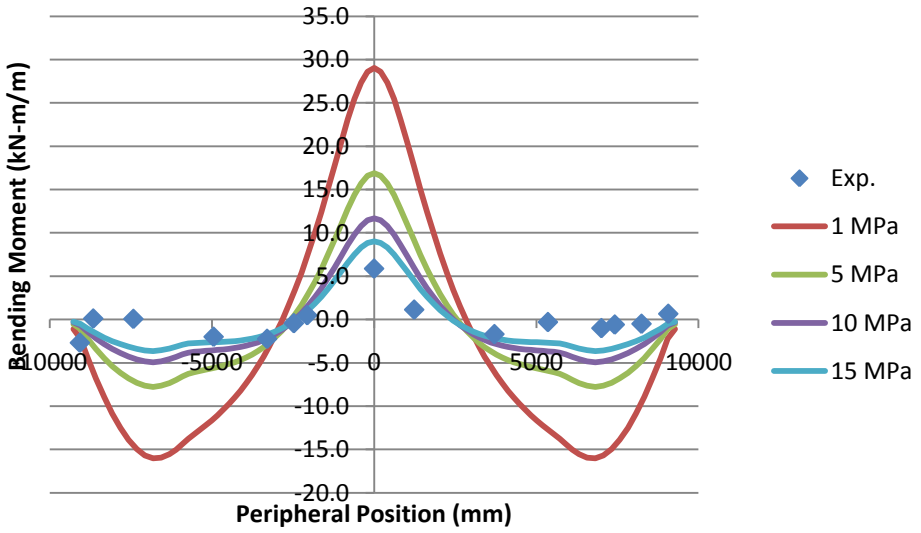

Figure 2 – Linear elastic model, transverse bending moments, 0.75 m backfill

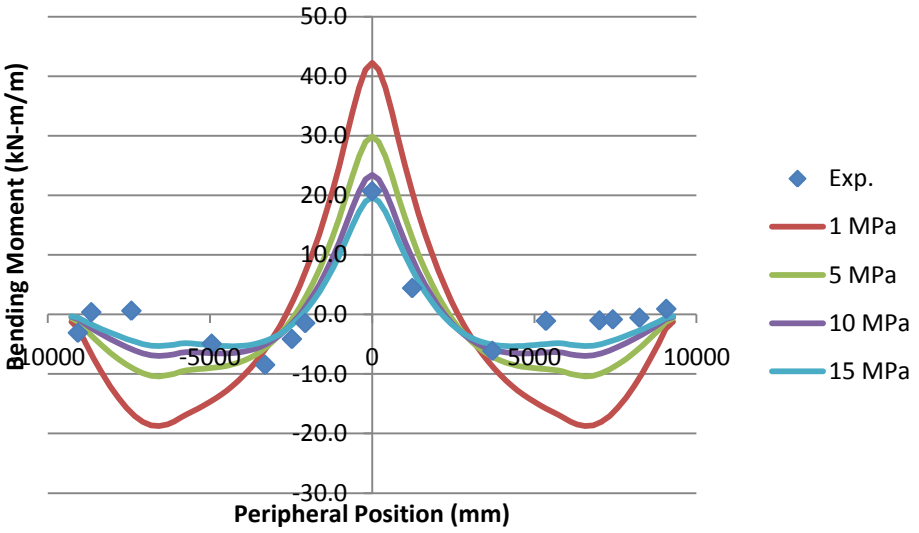

Figure 3 – Linear elastic model, transverse bending moments, 1.05 m backfill

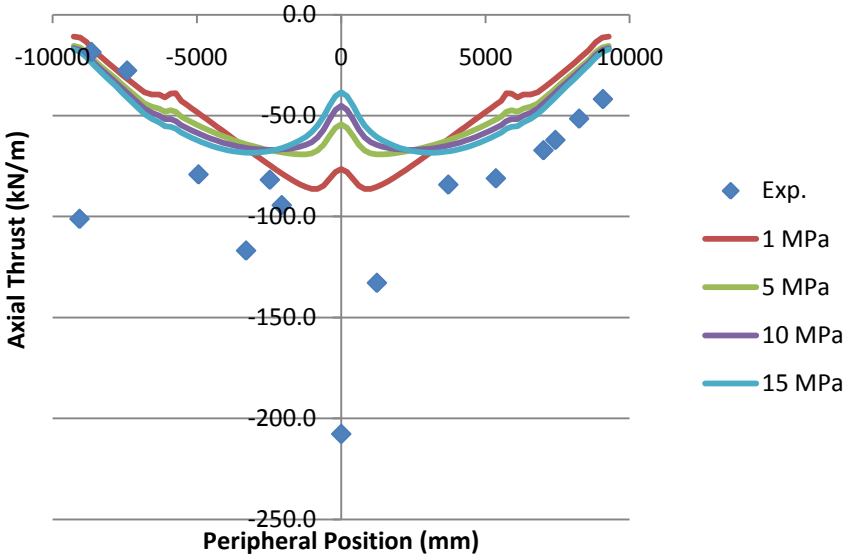

Figure 4 – Linear elastic model, transverse axial thrust, 0.45 m backfill

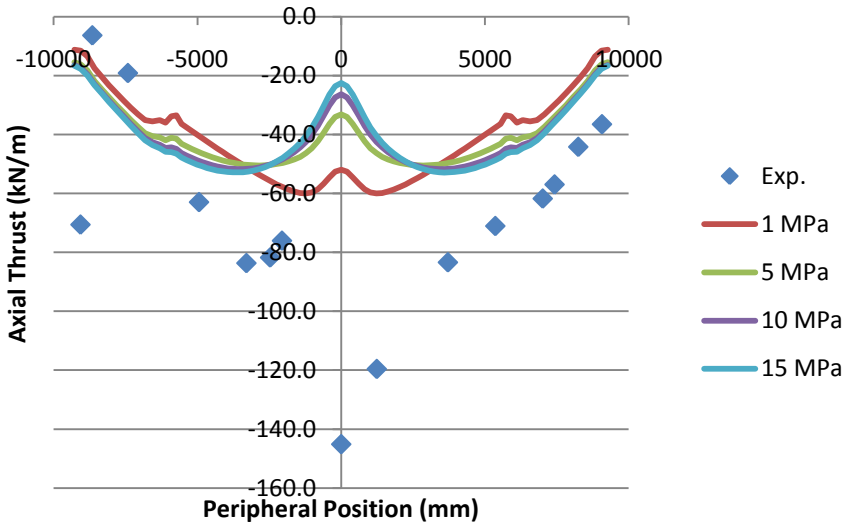

Figure 5 – Linear elastic model, transverse axial thrust, 0.75 m backfill

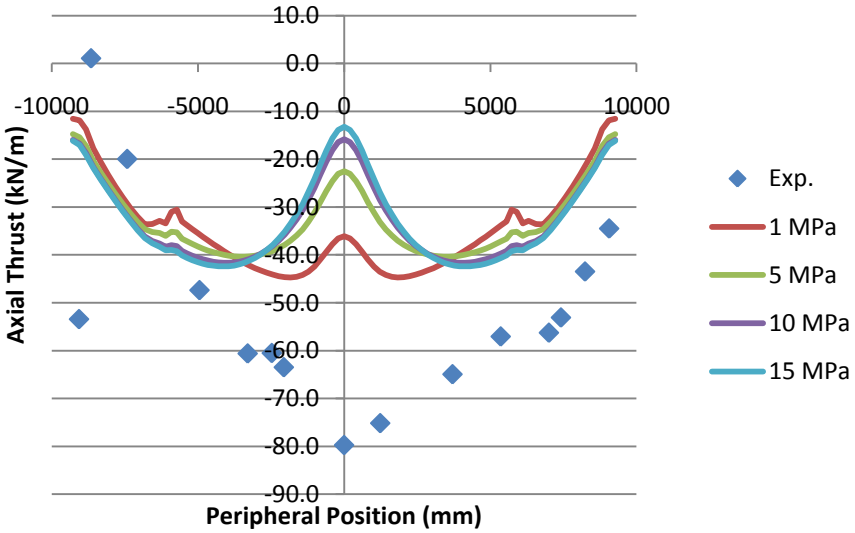

Figure 6 – Linear elastic model, transverse axial thrust, 1.05 m backfill

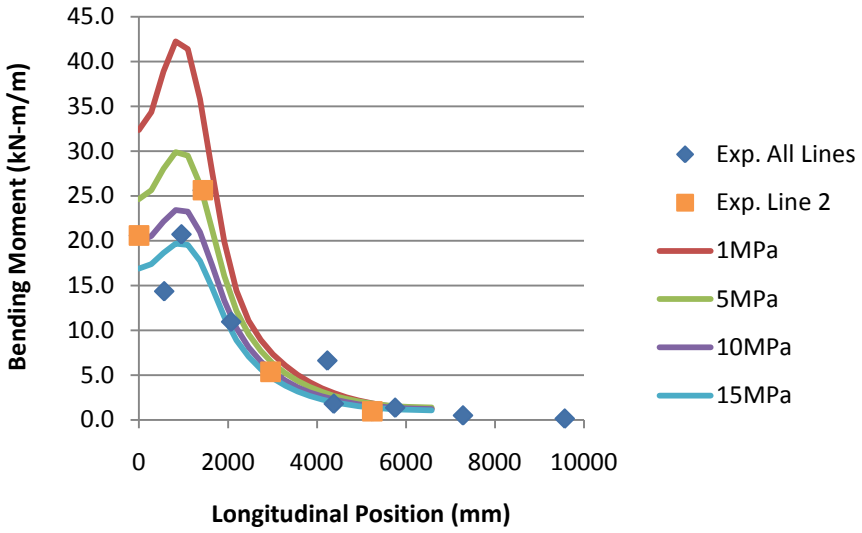

Figure 7 – Linear elastic model, longitudinal bending moment profile, 0.45 m backfill

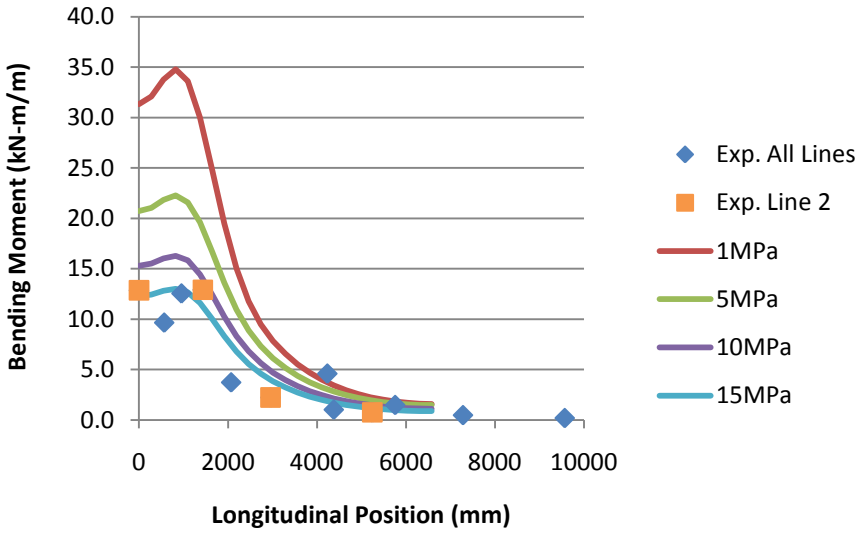

Figure 8 – Linear elastic model, longitudinal bending moment profile, 0.75 m backfill

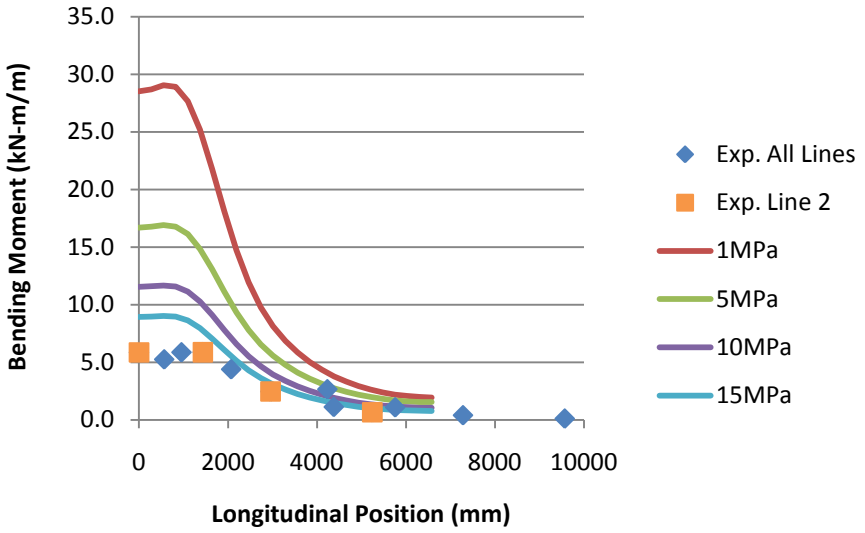

Figure 9 – Linear elastic model, longitudinal bending moment profile, 1.05 m backfill

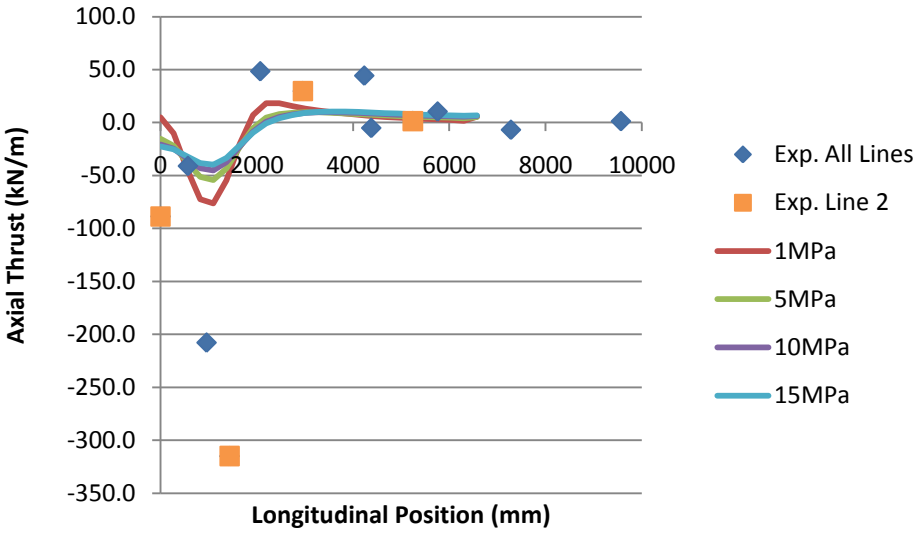

Figure 10 – Linear elastic model, longitudinal axial thrust profile, 0.45 m backfill

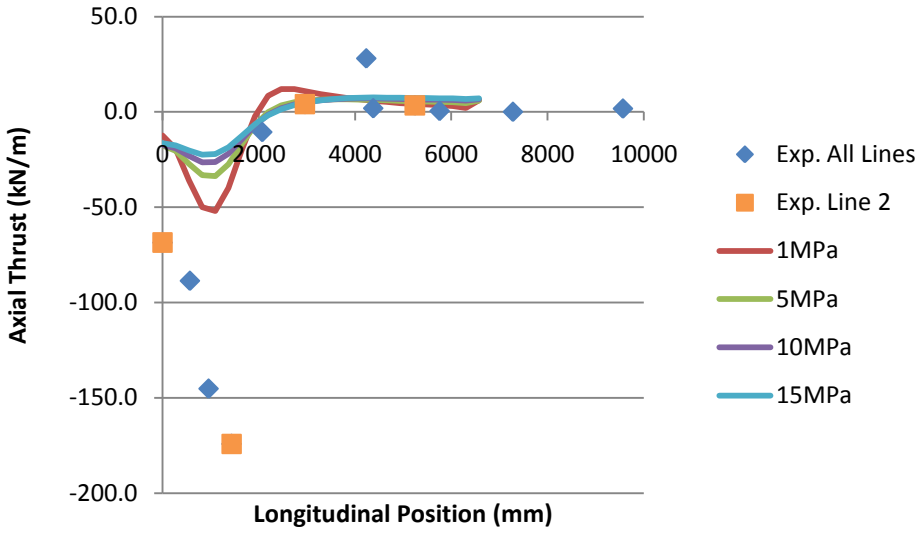

Figure 11 – Linear elastic model, longitudinal axial thrust profile, 0.75 m backfill

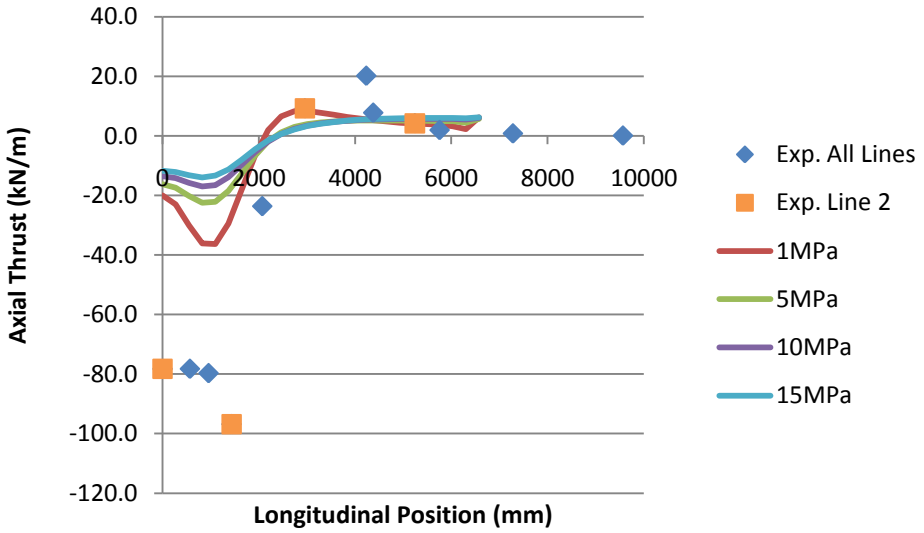

Figure 12 – Linear elastic model, longitudinal axial thrust profile, 1.05 m backfill

2. Curve Description

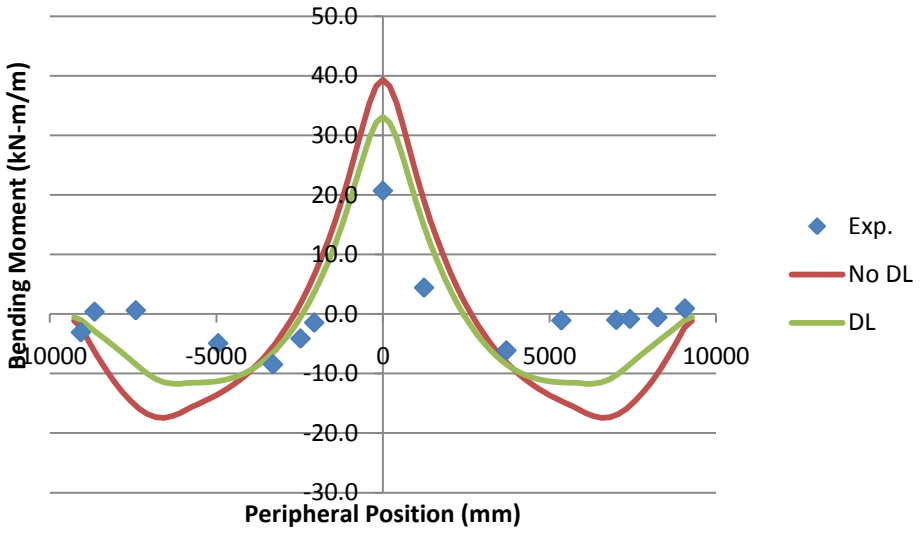

Figure 13 – Curve description model, transverse bending moments, 0.45 m backfill

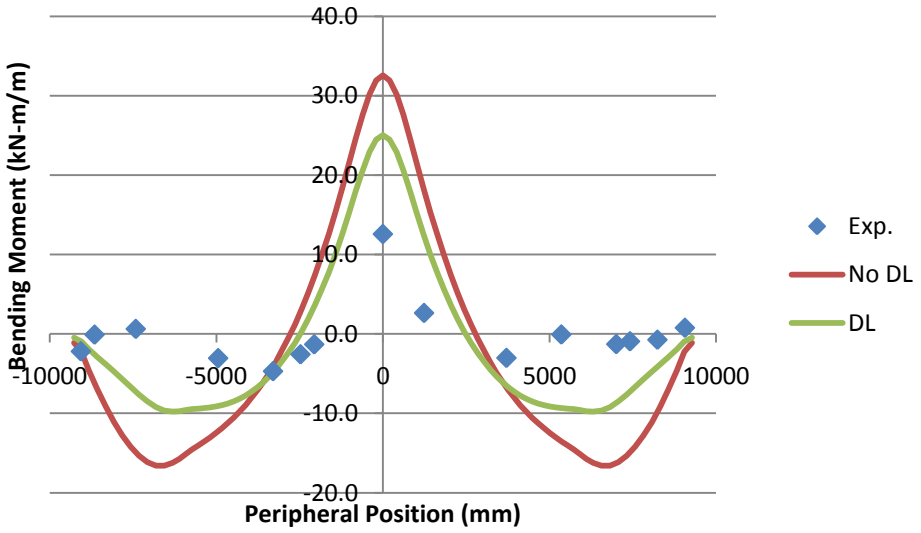

Figure 14 – Curve description model, transverse bending moments, 0.75 m backfill

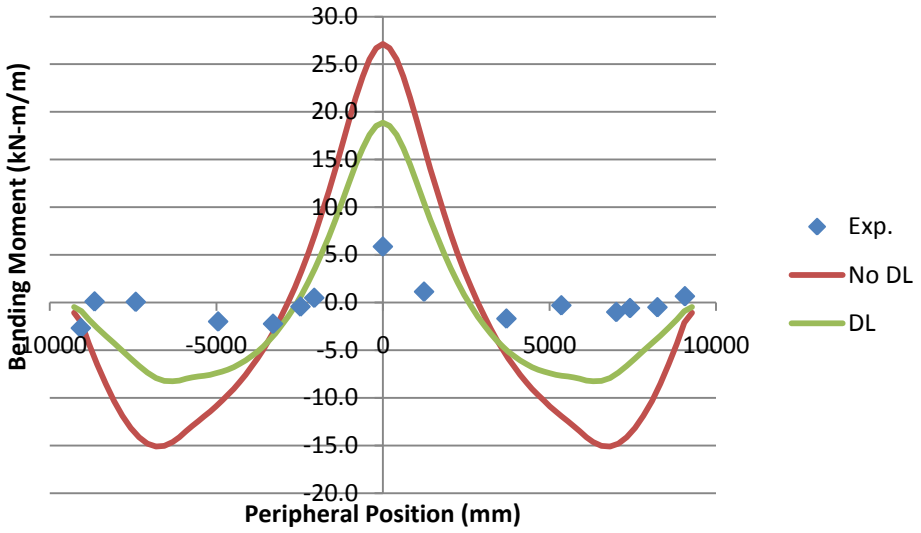

Figure 15 – Curve description model, transverse bending moments, 1.05 m backfill

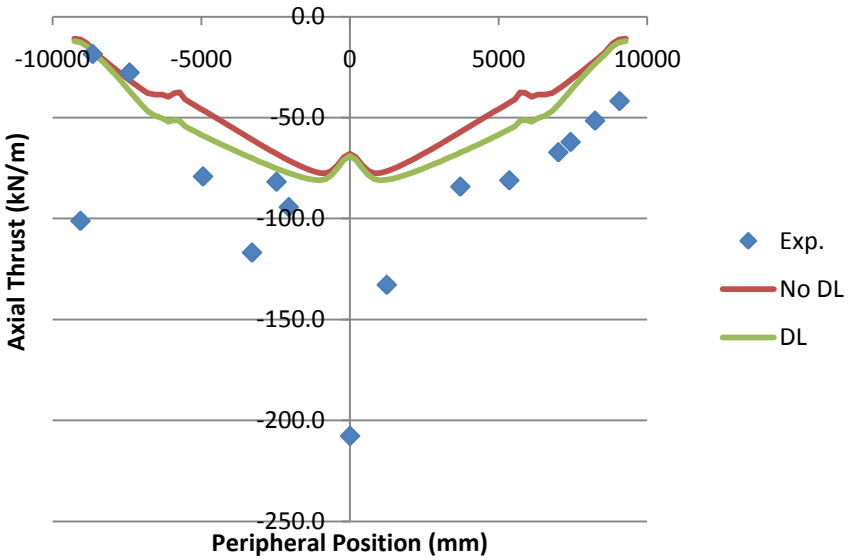

Figure 16 – Curve description model, transverse axial thrust, 0.45 m backfill

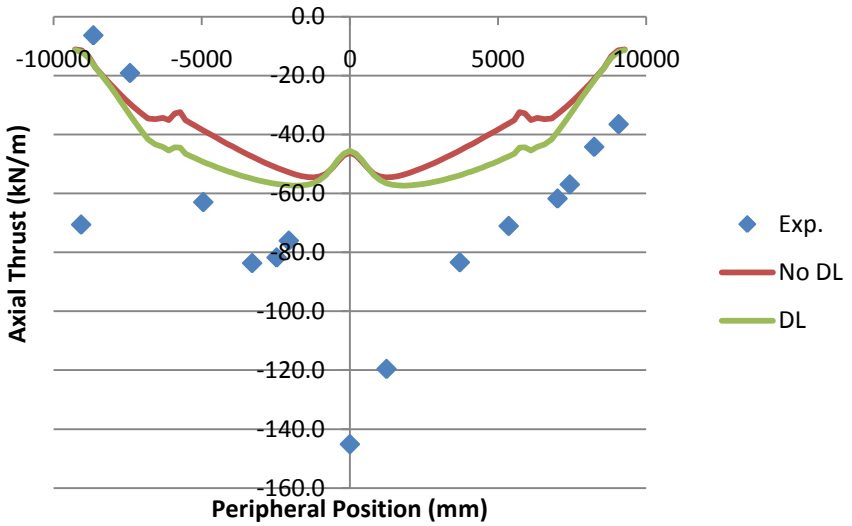

Figure 17 – Curve description model, transverse axial thrust, 0.75 m backfill

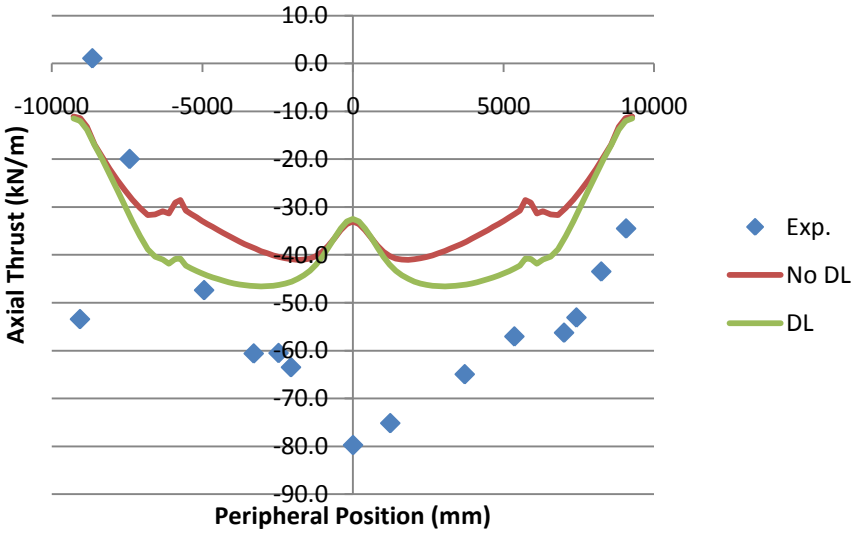

Figure 18 – Curve description model, transverse axial thrust, 1.05 m backfill

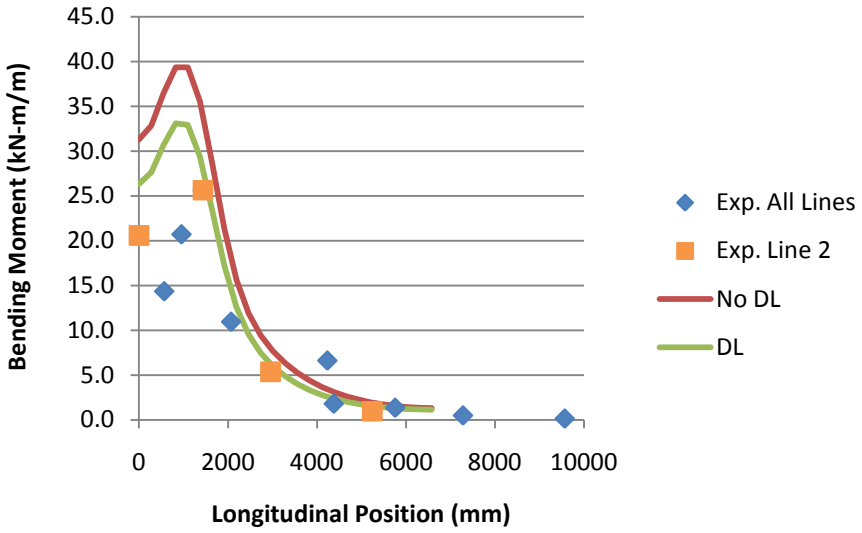

Figure 19 – Curve description model, longitudinal bending moment profile, 0.45 m backfill

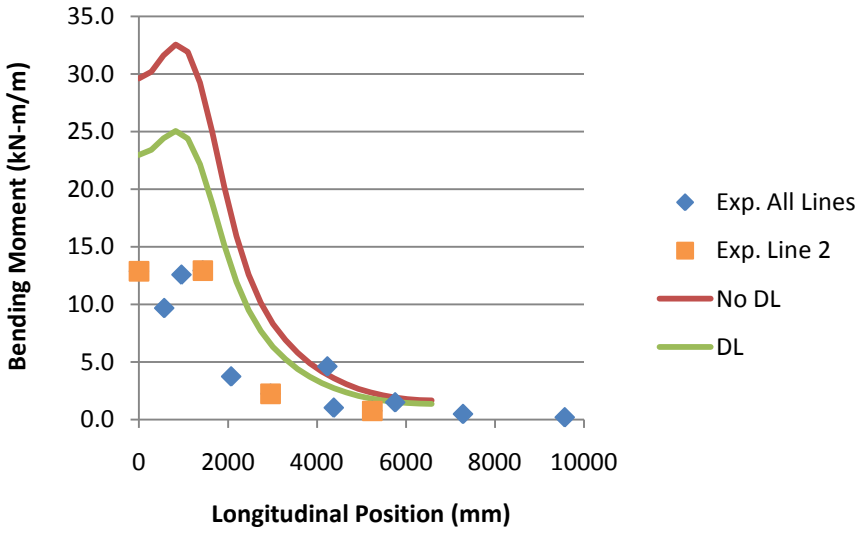

Figure 20 – Curve description model, longitudinal bending moment profile, 0.75 m backfill

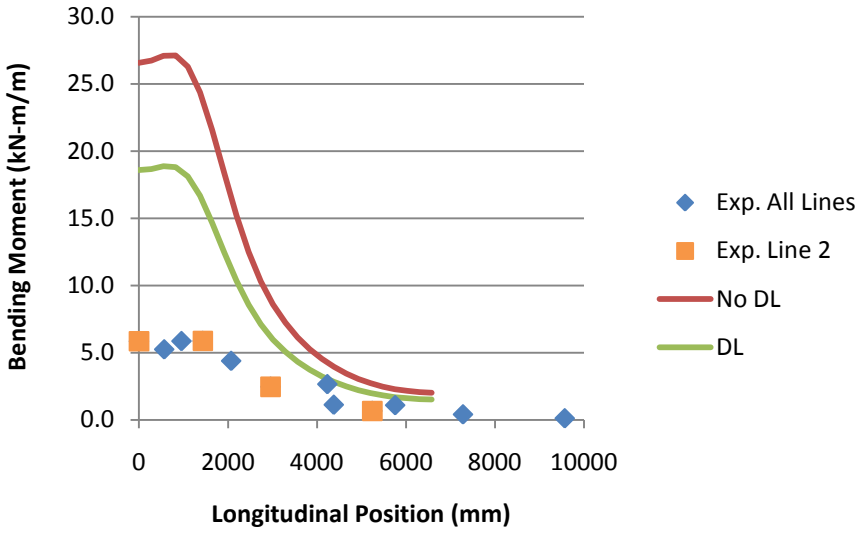

Figure 21 – Curve description model, longitudinal bending moment profile, 1.05 m backfill

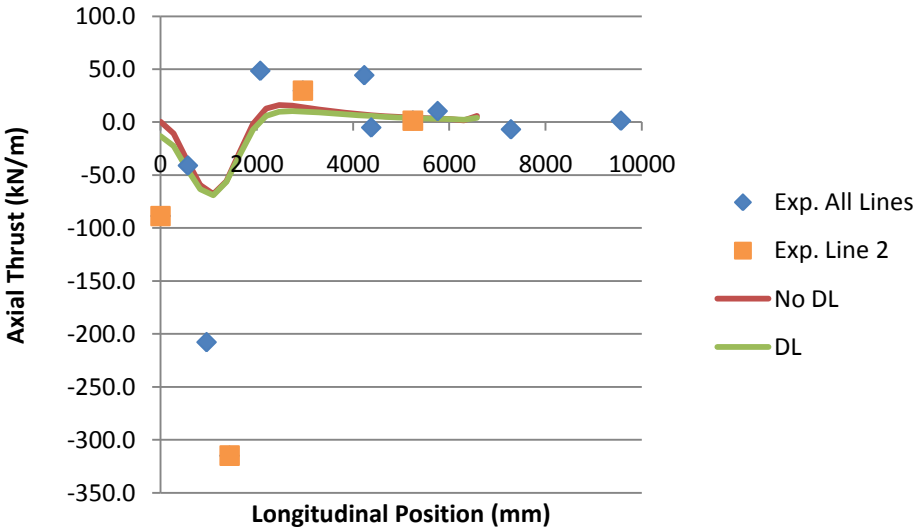

Figure 22 – Curve description model, longitudinal axial thrust profile, 0.45 m backfill

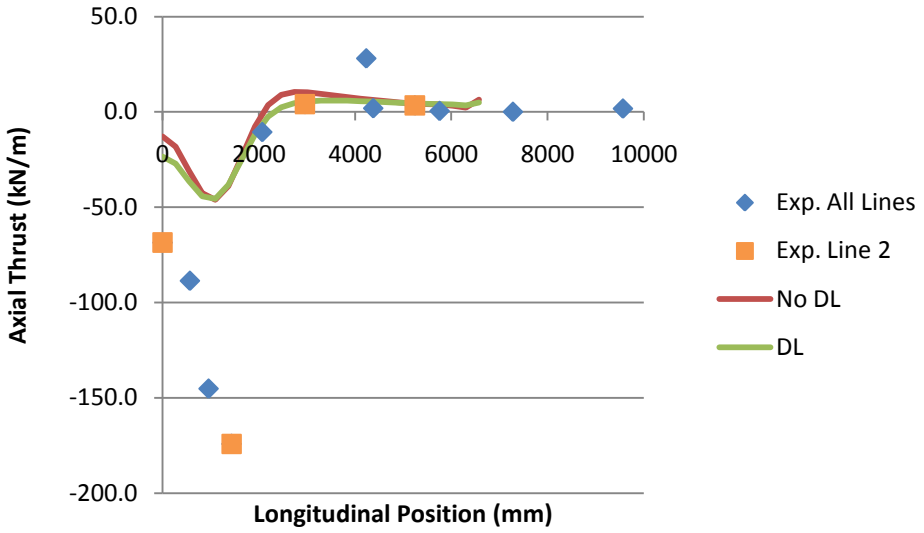

Figure 23 – Curve description model, longitudinal axial thrust profile, 0.75 m backfill

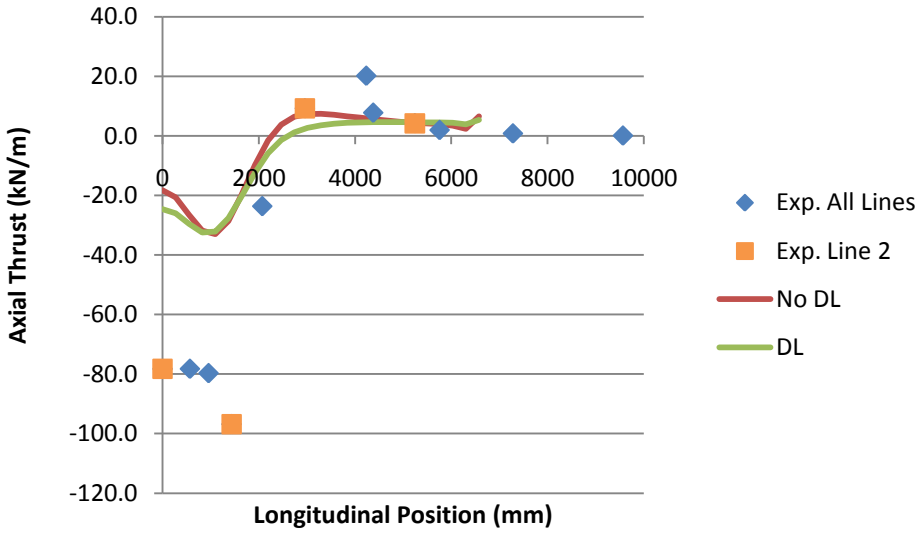

Figure 24 – Curve description model, longitudinal axial thrust profile, 1.05 m backfill

3. Layered Linear Elastic

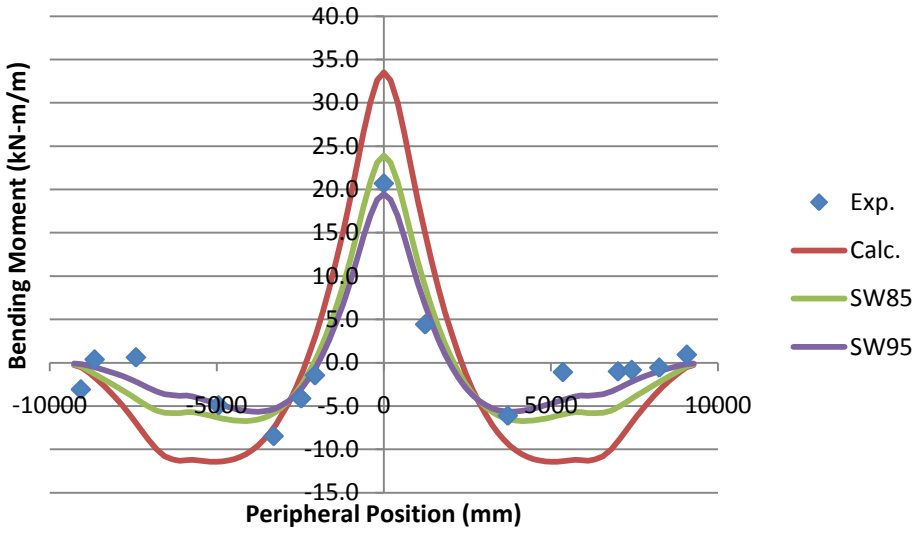

Figure 25 – Layered linear elastic model, transverse bending moments, 0.45 m backfill

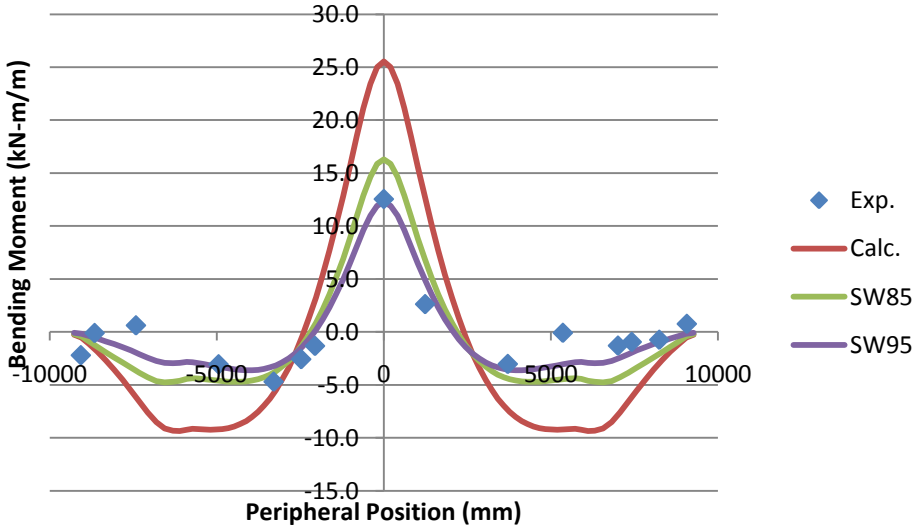

Figure 26 – Layered linear elastic, transverse bending moments, 0.75 m backfill

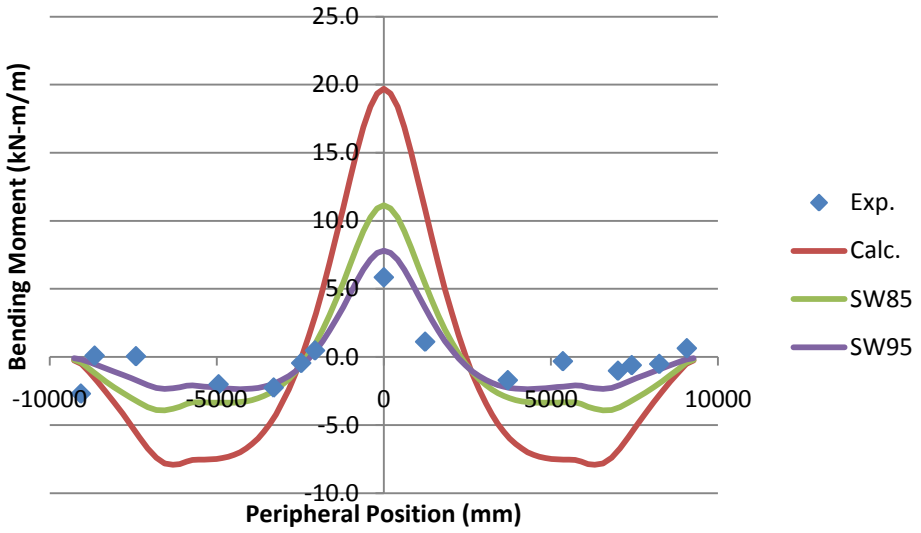

Figure 27 – Layered linear elastic model, transverse bending moments, 1.05 m backfill

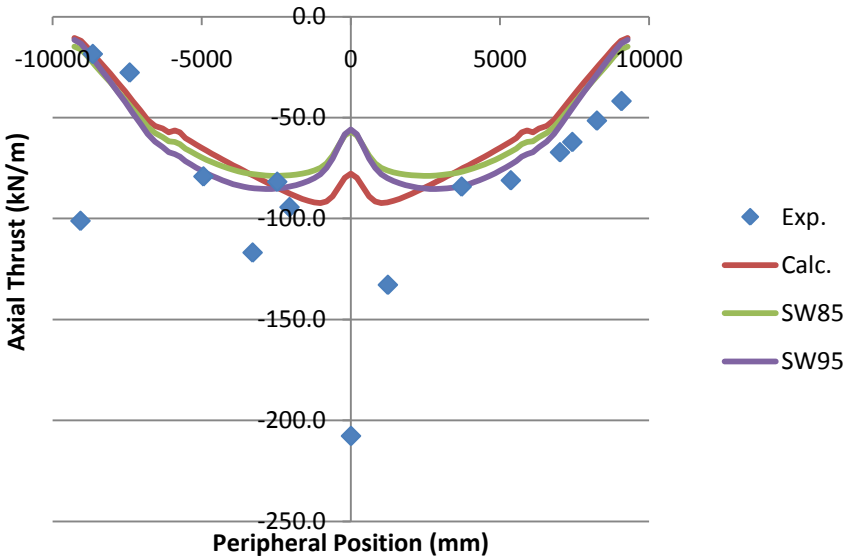

Figure 28 – Layered linear elastic, transverse axial thrust, 0.45 m backfill

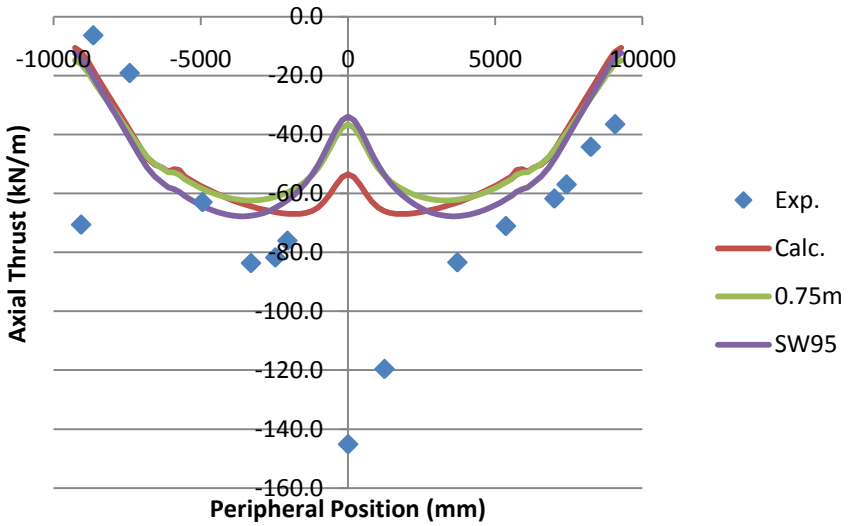

Figure 29 – Layered linear elastic, transverse axial thrust, 0.75 m backfill

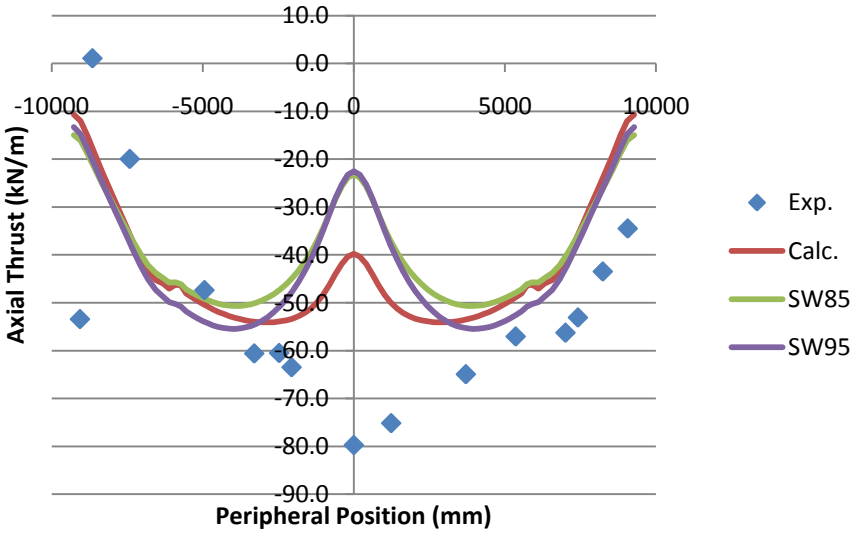

Figure 30 – Layered linear elastic model, transverse axial thrust, 1.05 m backfill

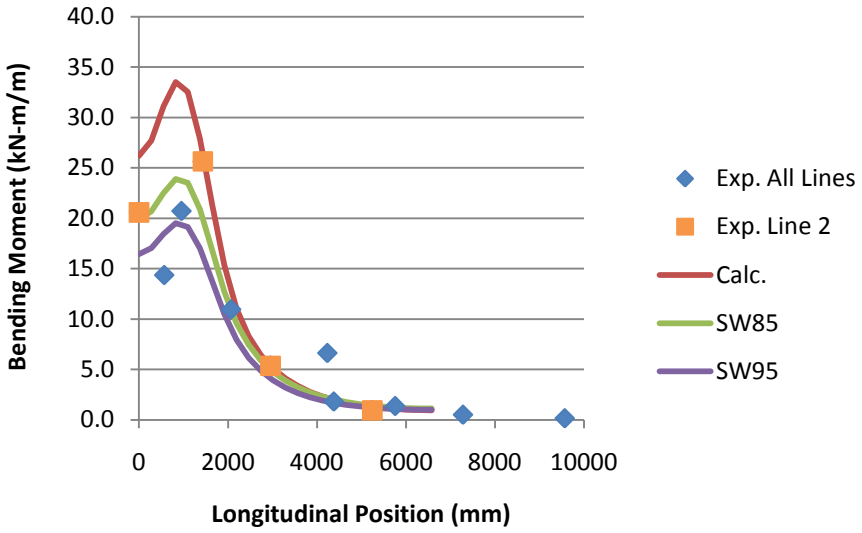

Figure 31 – Layered linear elastic model, longitudinal bending moment profile, 0.45 m backfill

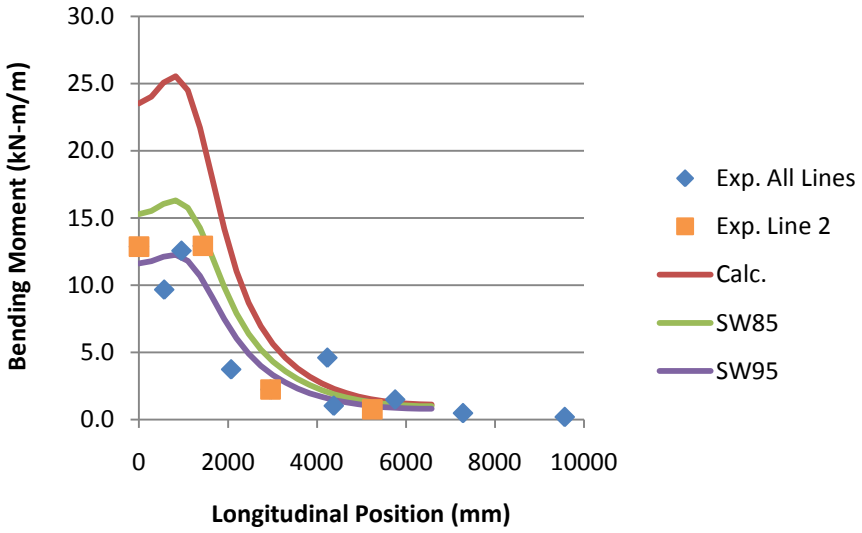

Figure 32 – Layered linear elastic model, longitudinal bending moment profile, 0.75 m backfill

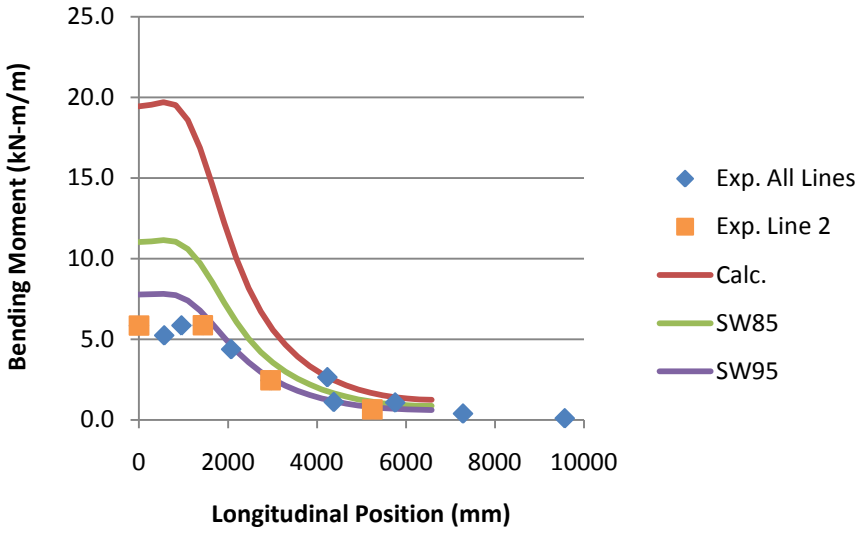

Figure 33 – Layered linear elastic model, longitudinal bending moment profile, 1.05 m backfill

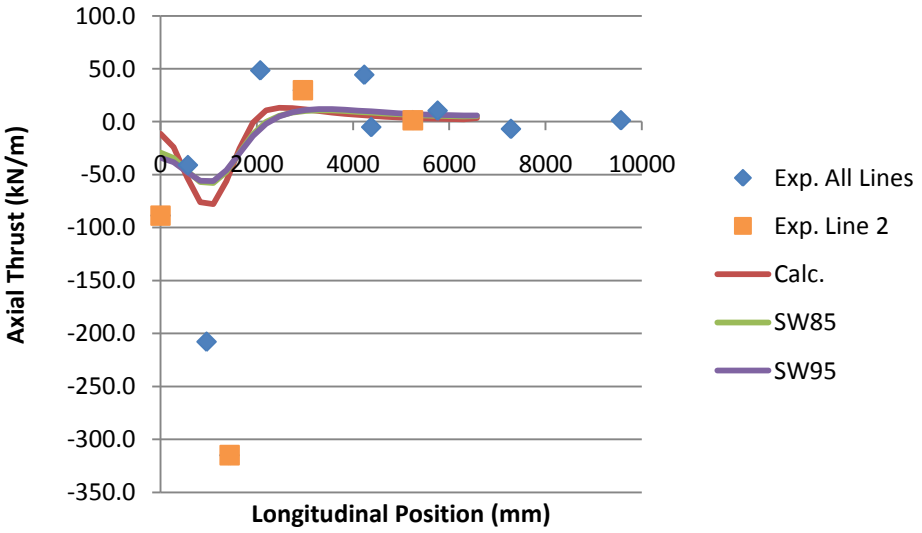

Figure 34 – Layered linear elastic model, longitudinal axial thrust profile, 0.45 m backfill

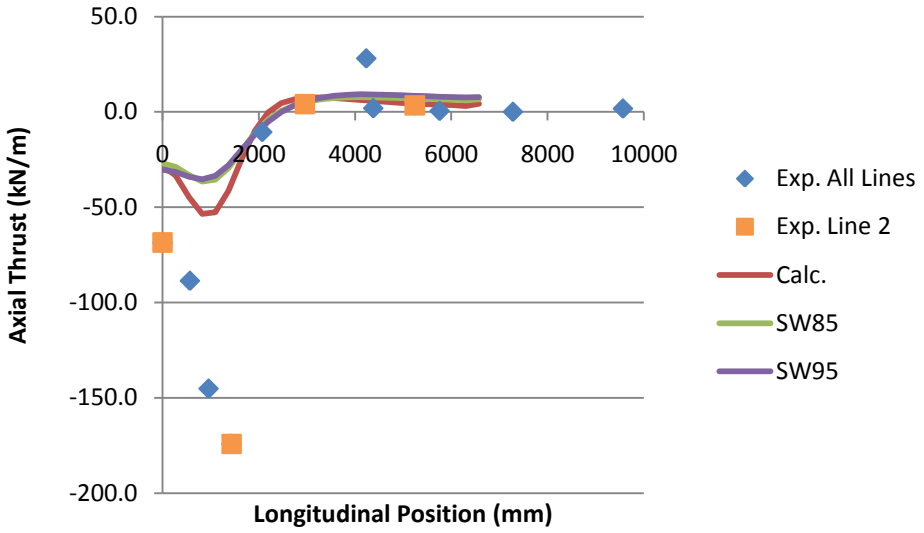

Figure 35 – Layered linear elastic model, longitudinal axial thrust profile, 0.75 m backfill

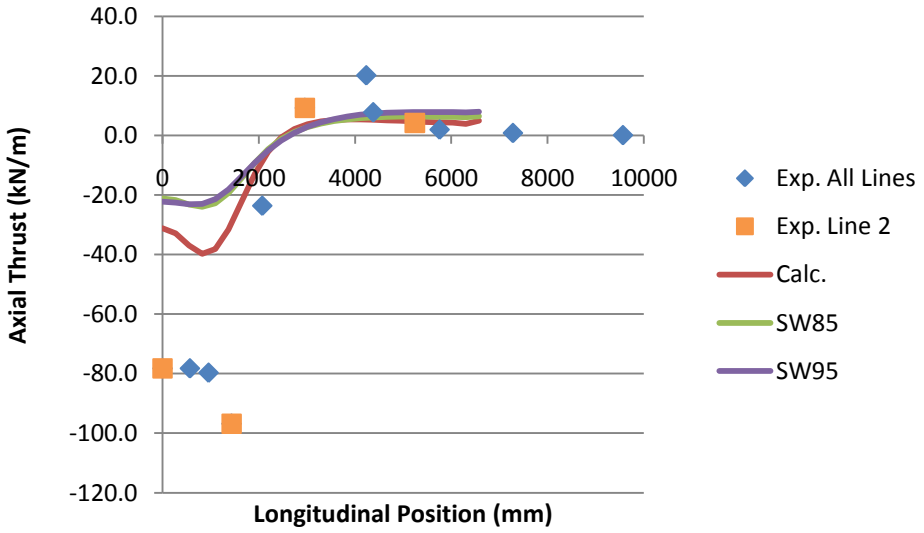

Figure 36 – Layered linear elastic model, longitudinal axial thrust profile, 1.05 m backfill

4. Layered Mohr-Coulomb

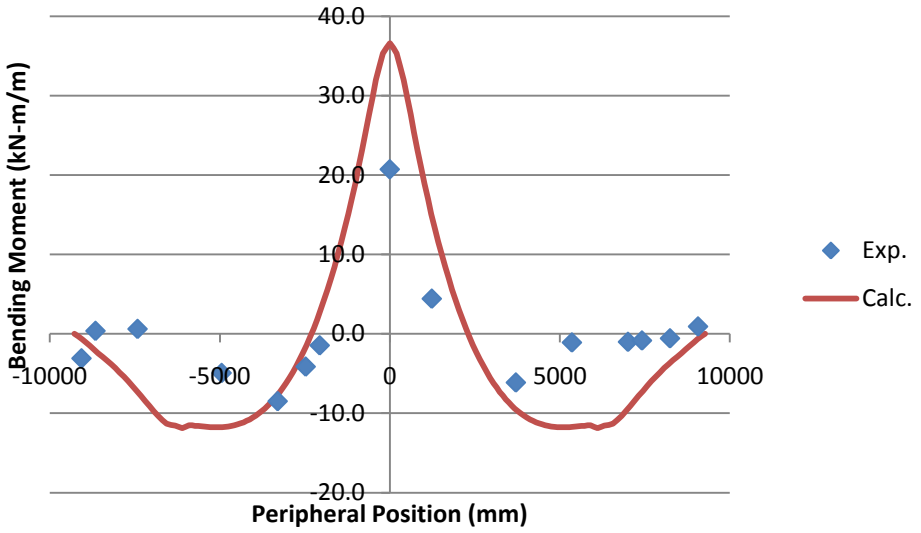

Figure 37 – Layered Mohr-Coulomb model, transverse bending moments, 0.45 m backfill

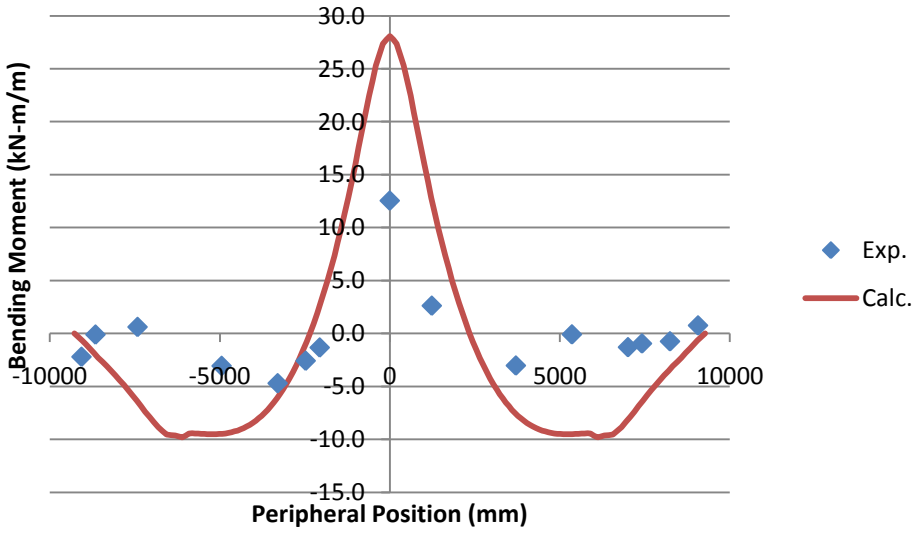

Figure 38 – Layered Mohr-Coulomb model, transverse bending moments, 0.75 m backfill

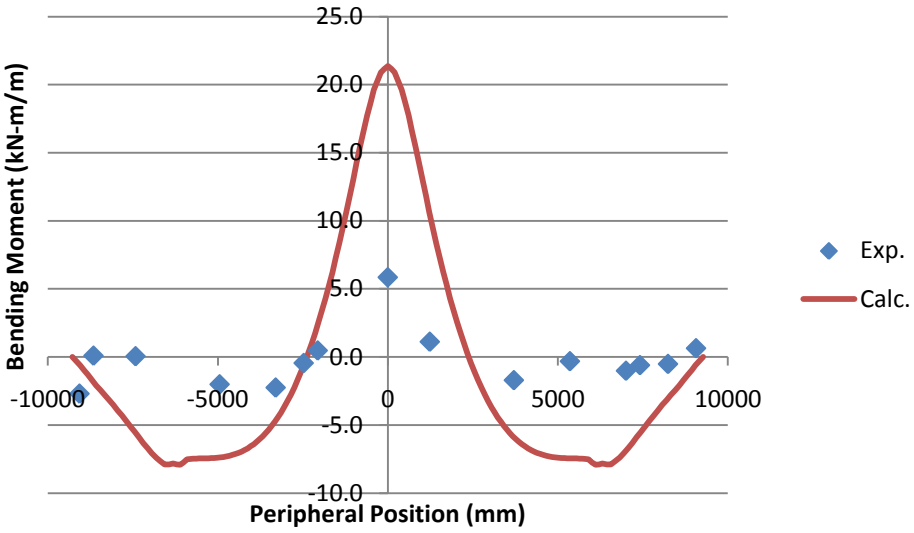

Figure 39 – Layered Mohr-Coulomb model, transverse bending moments, 1.05 m backfill

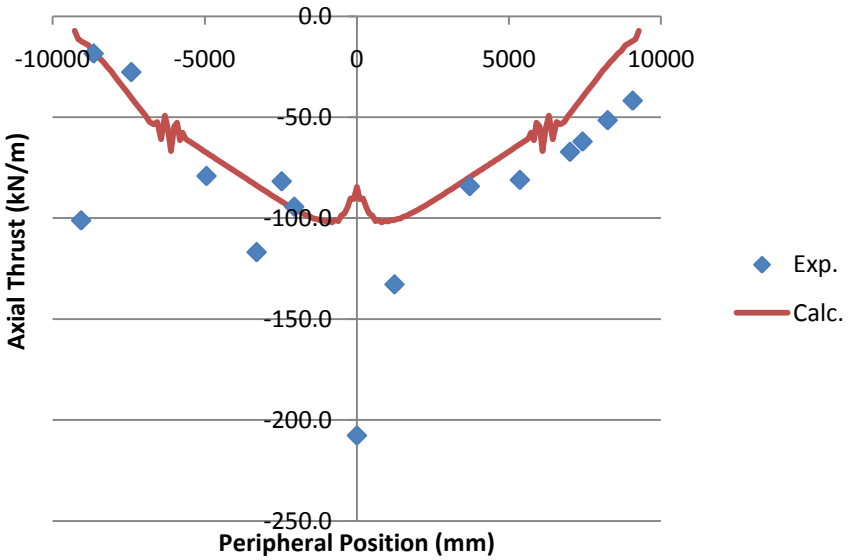

Figure 40 – Layered Mohr-Coulomb model, transverse axial thrust, 0.45 m backfill

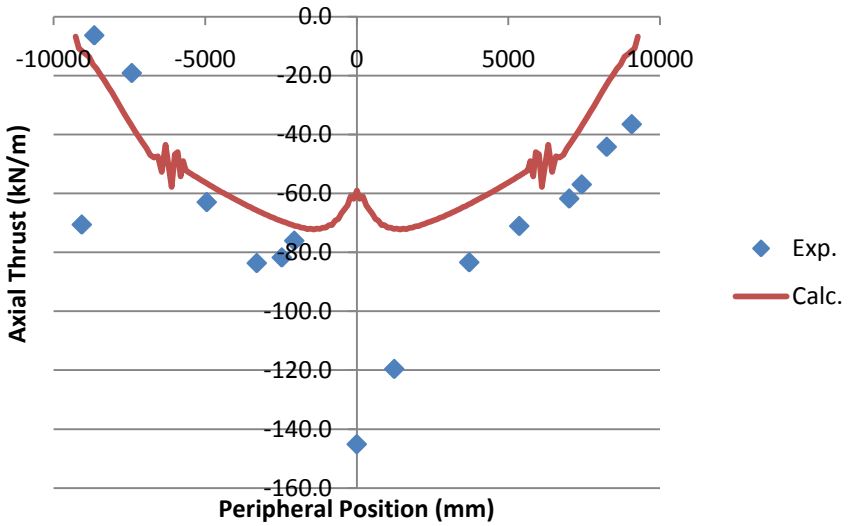

Figure 41 – Layered Mohr-Coulomb model, transverse axial thrust, 0.75 m backfill

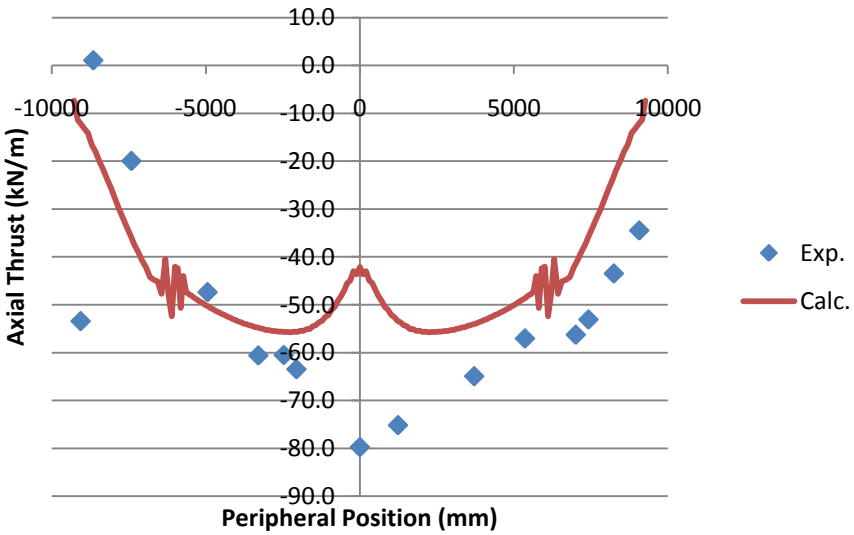

Figure 42 – Layered Mohr-Coulomb model, transverse axial thrust, 1.05 m backfill

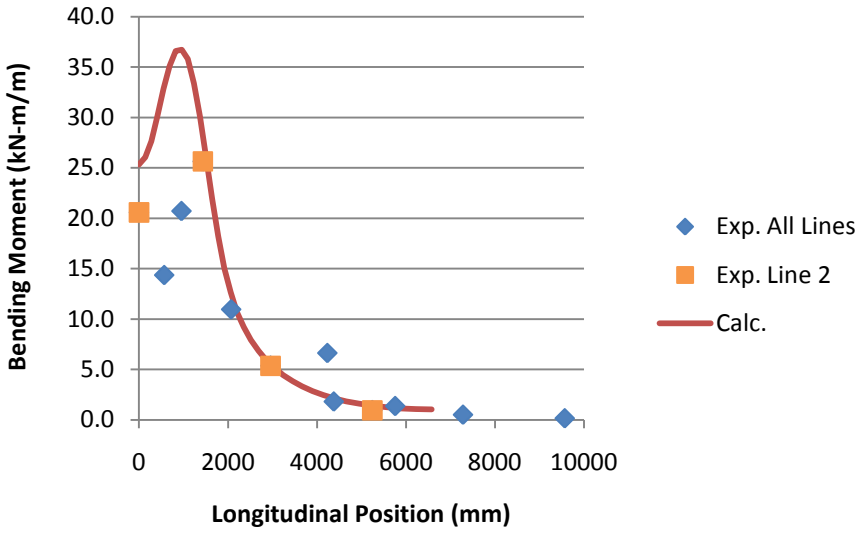

Figure 43 – Layered Mohr-Coulomb model, longitudinal bending moment profile, 0.45 m backfill

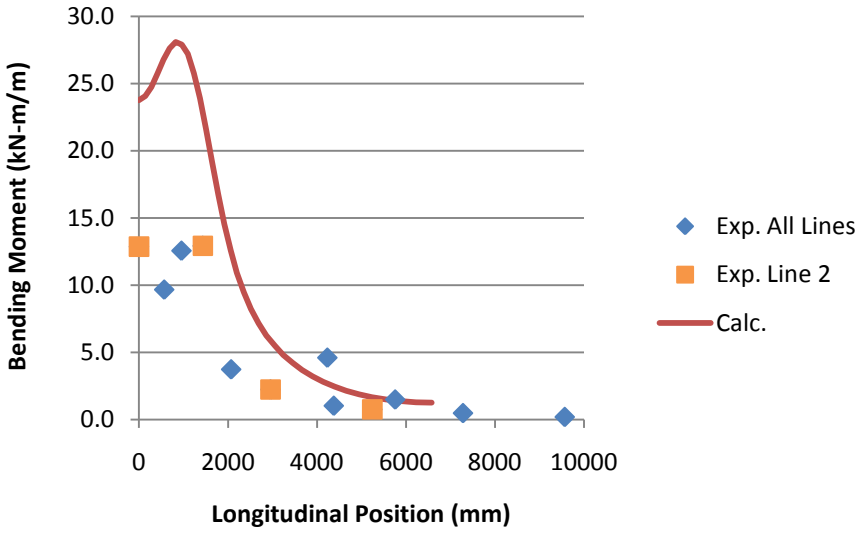

Figure 44 – Layered Mohr-Coulomb model, longitudinal bending moment profile, 0.75m backfill

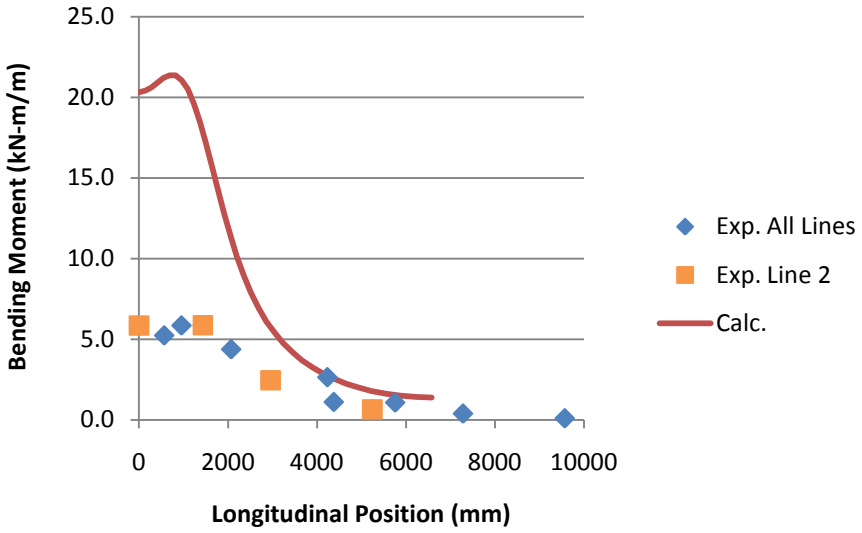

Figure 45 – Layered Mohr-Coulomb model, longitudinal bending moment profile, 1.05m backfill

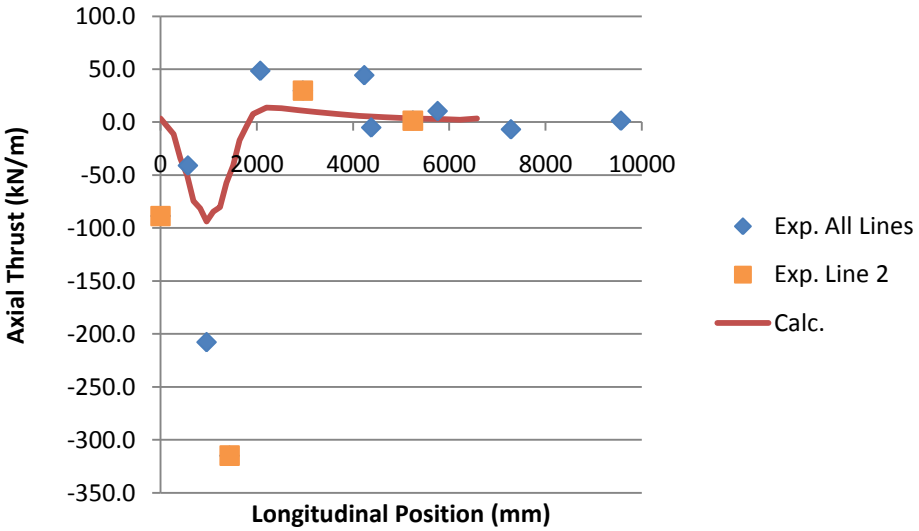

Figure 46 – Layered Mohr-Coulomb model, longitudinal axial thrust profile, 0.45 m backfill

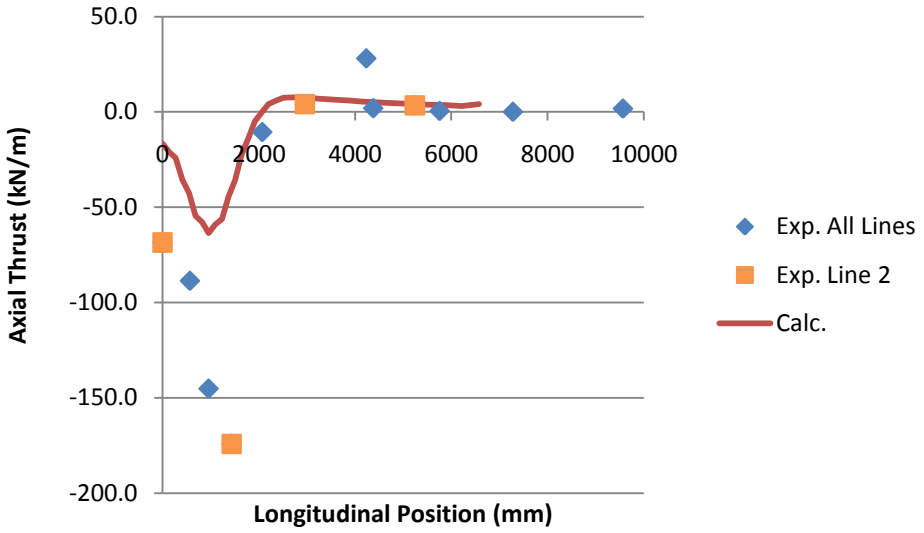

Figure 47 – Layered Mohr-Coulomb model, longitudinal axial thrust profile, 0.75 m backfill

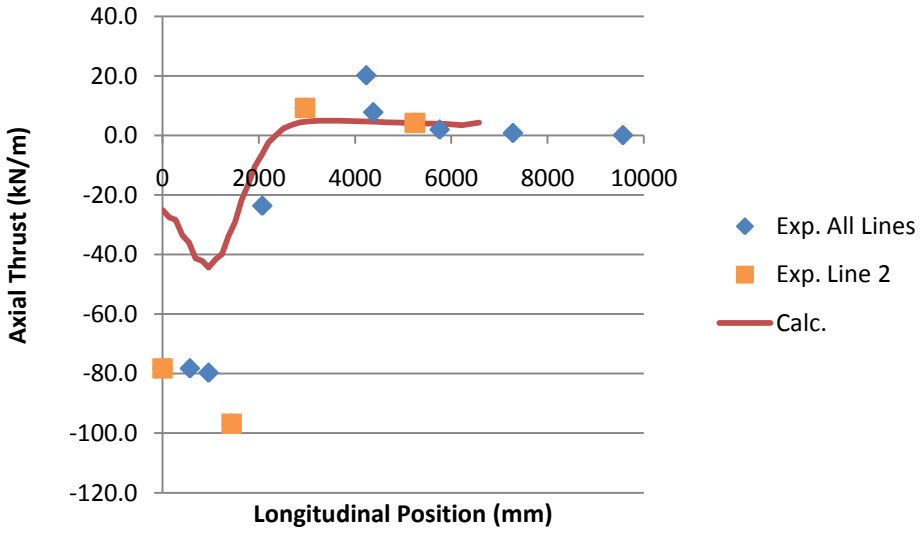

Figure 48 – Layered Mohr-Coulomb model, longitudinal axial thrust profile, 1.05 m backfill

5. Comparison Plots

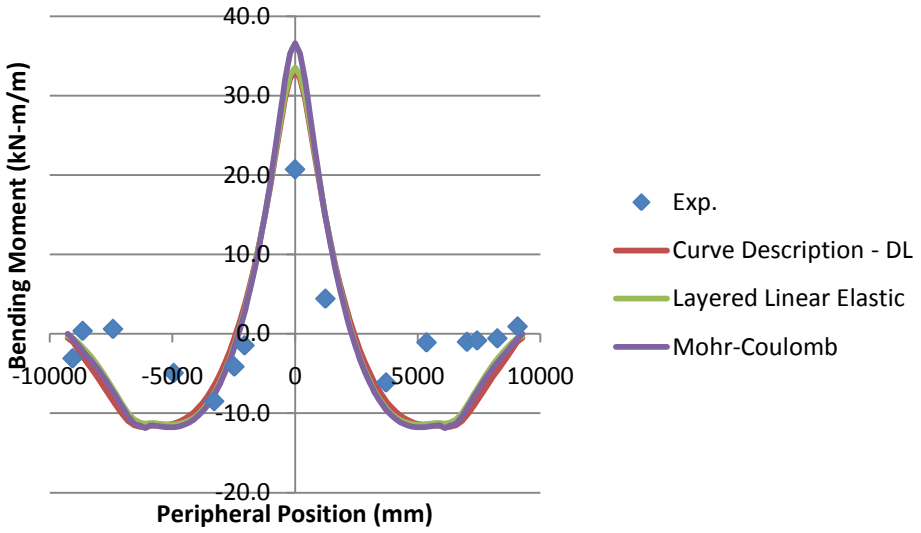

Figure 49 – Various soil models, transverse bending moment, 0.45m backfill

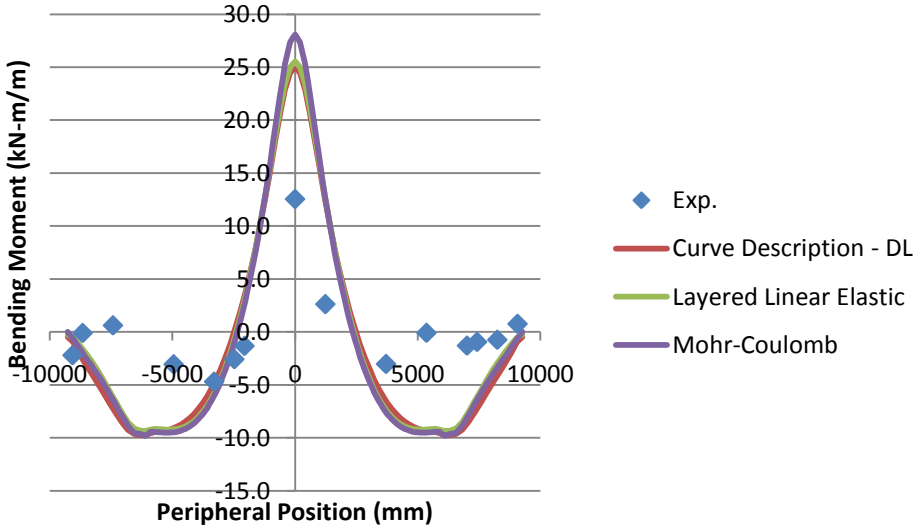

Figure 50 – Various soil models, transverse bending moment, 0.75m backfill

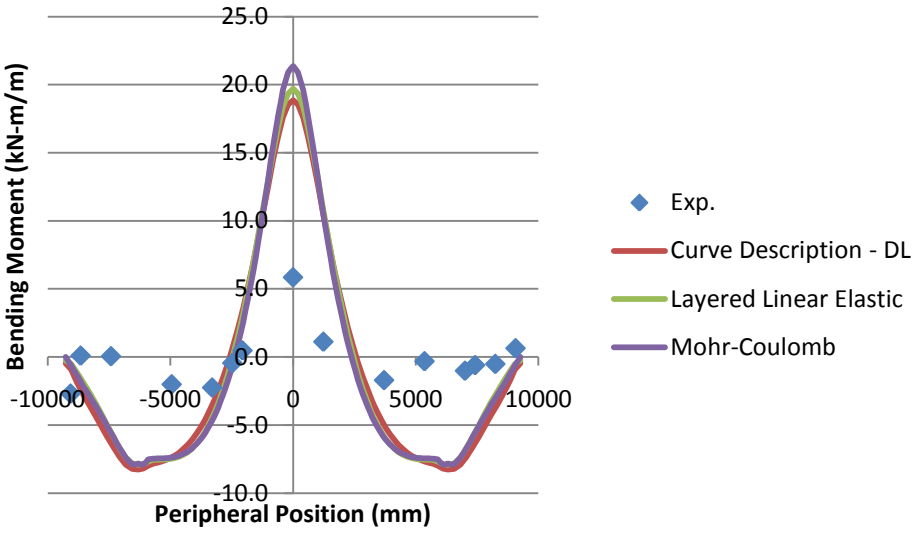

Figure 51 – Various soil models, transverse bending moment, 1.05m backfill

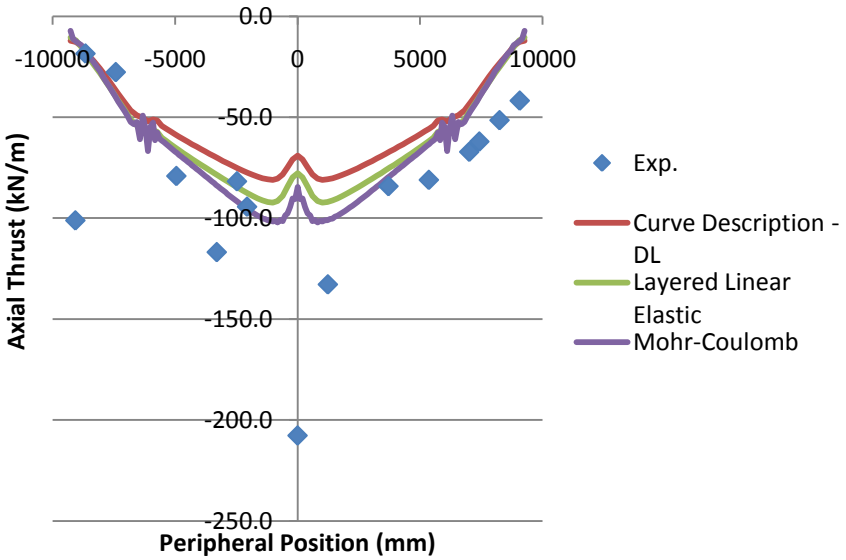

Figure 52 – Various soil models, transverse axial thrust, 0.45 m backfill

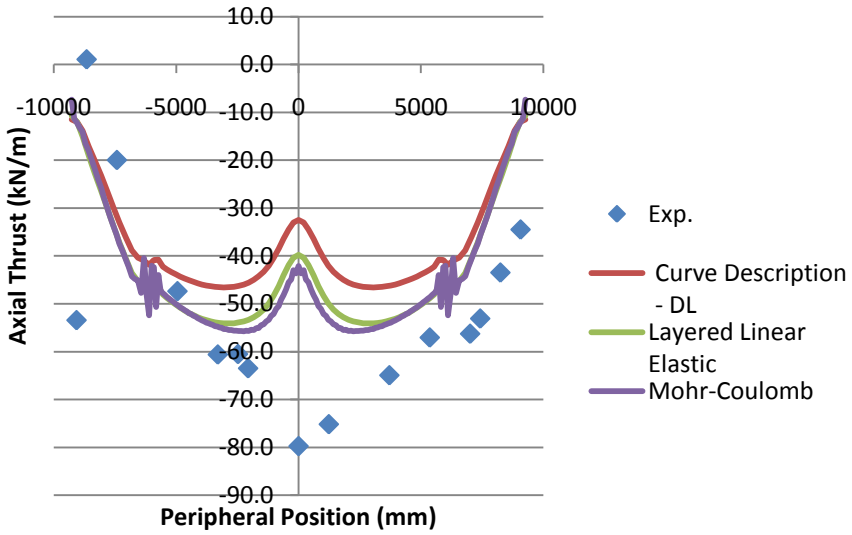

Figure 53 – Various soil models, transverse axial thrust, 1.05 m backfill

APPENDIX B - ADDITIONAL PLOTS FOR LAYERED LINEAR ELASTIC MODEL

1. Bending Moment

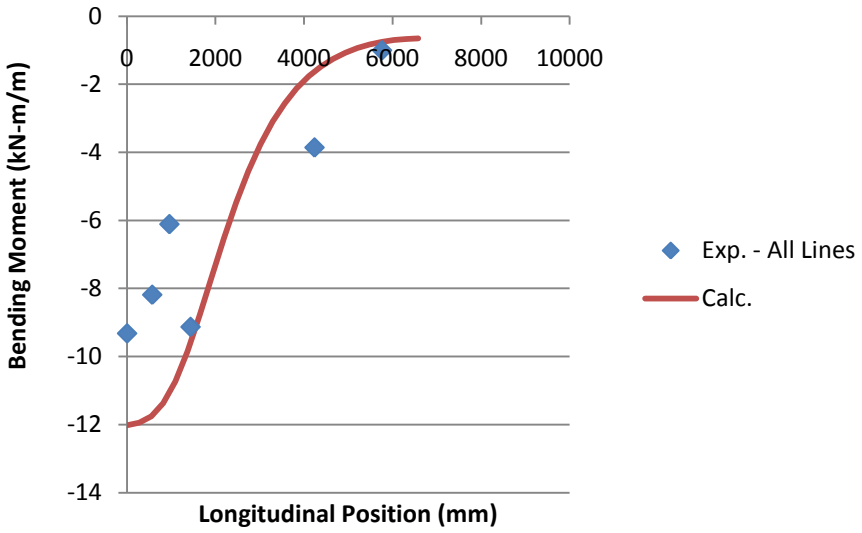

Figure 1 – Longitudinal bending moment profile at maximum negative moment, 0.45m

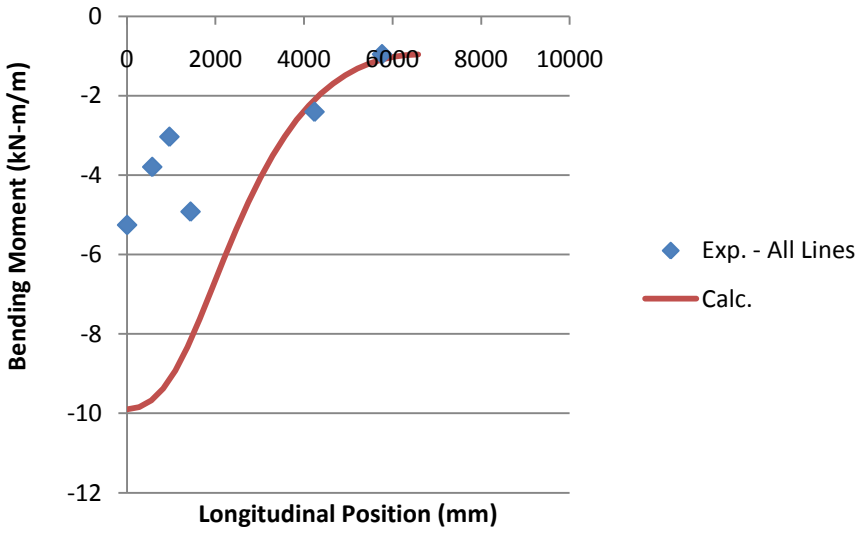

Figure 2 – Longitudinal bending moment profile at maximum negative moment, 0.75m

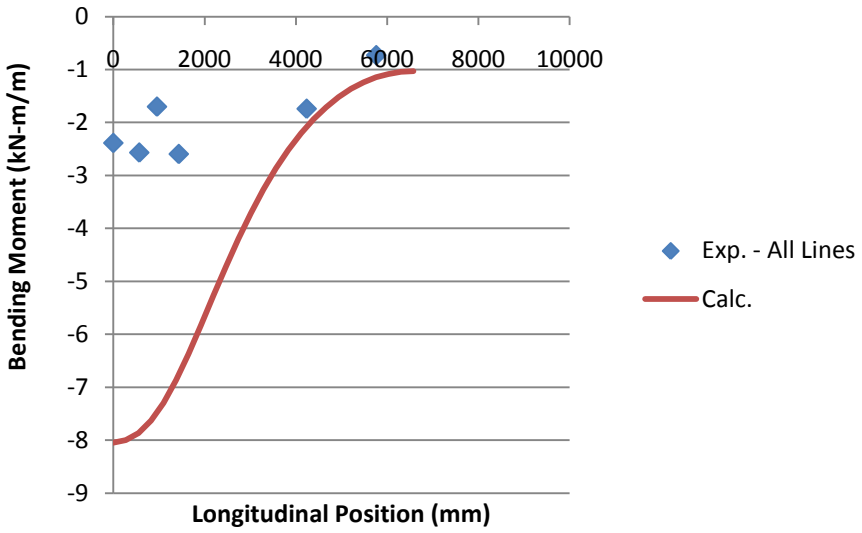

Figure 3 – Longitudinal bending moment profile at maximum negative moment, 1.05m

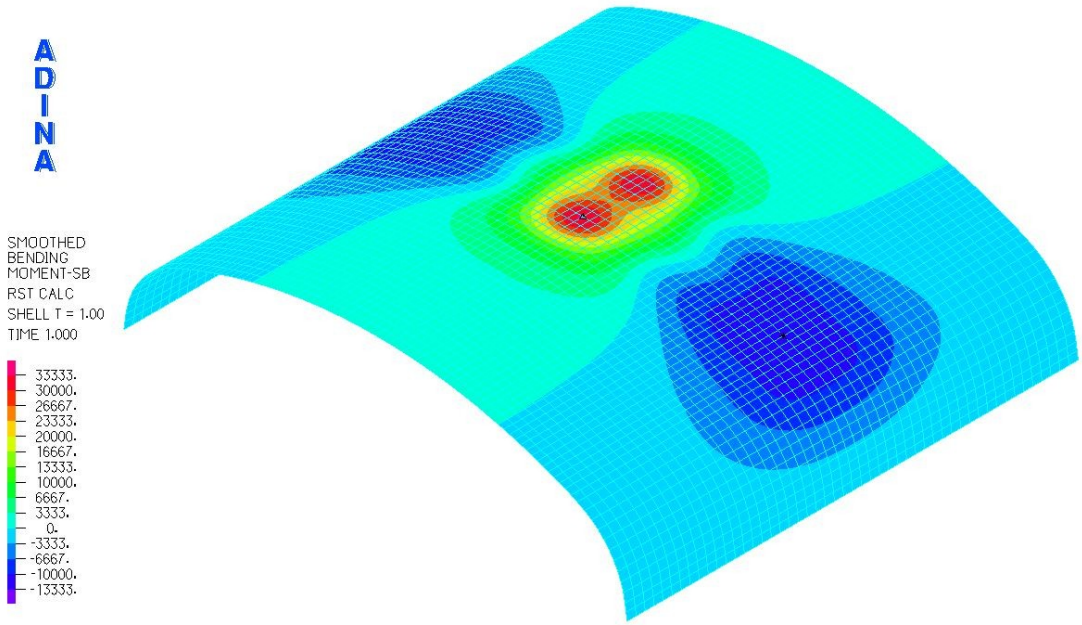

Figure 4 – Contour plot of bending moments, 0.45m backfill

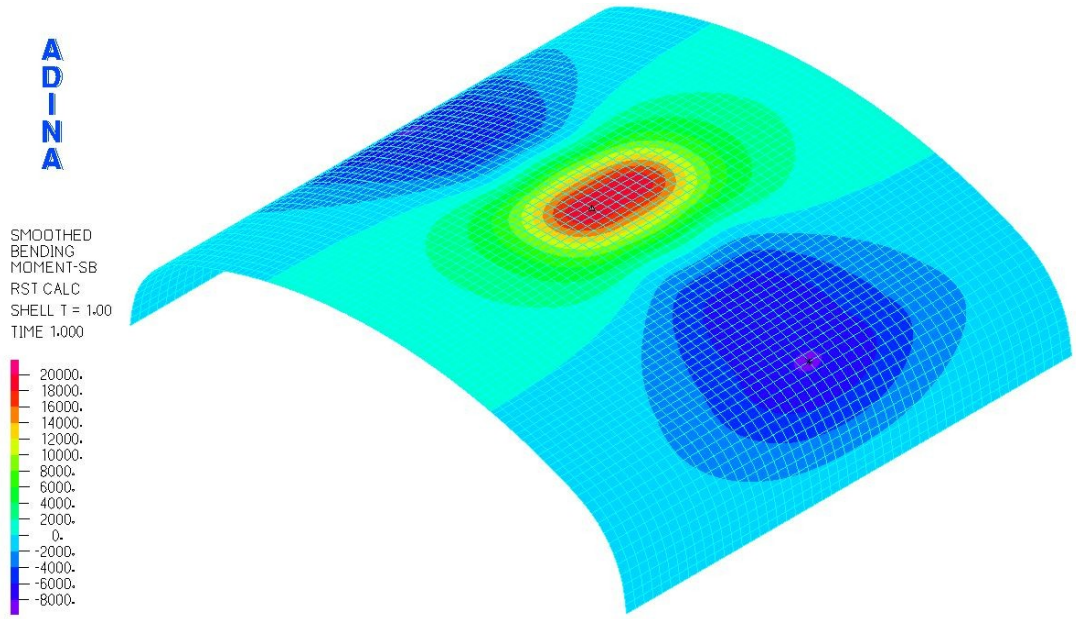

Figure 5 – Contour plot of bending moments, 1.05m backfill

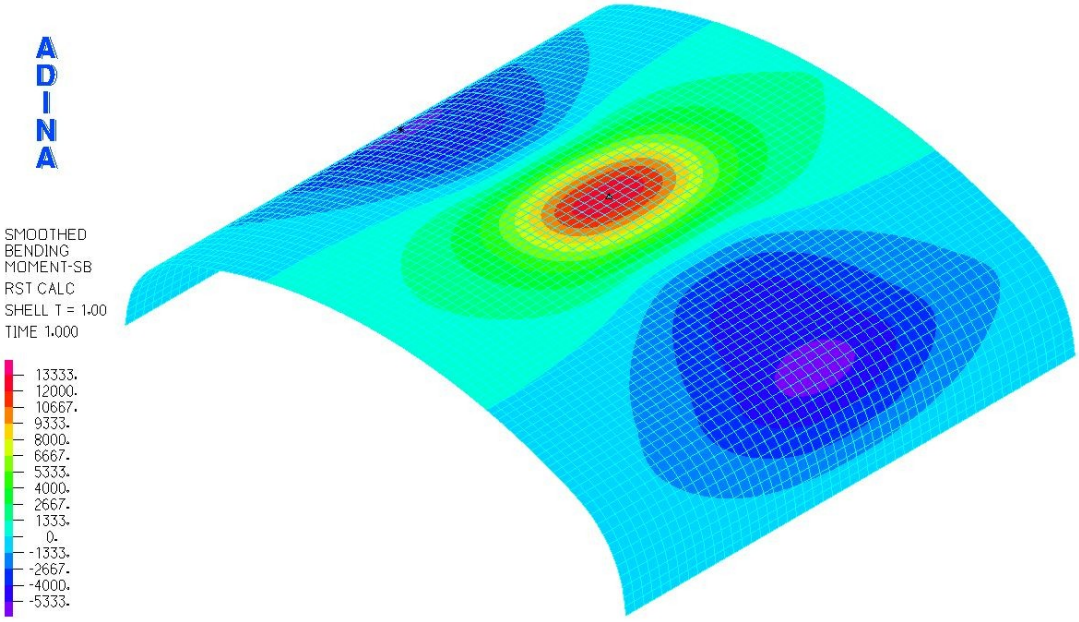

Figure 6 – Contour plot of bending moments, 1.55m backfill

2. Axial Thrust

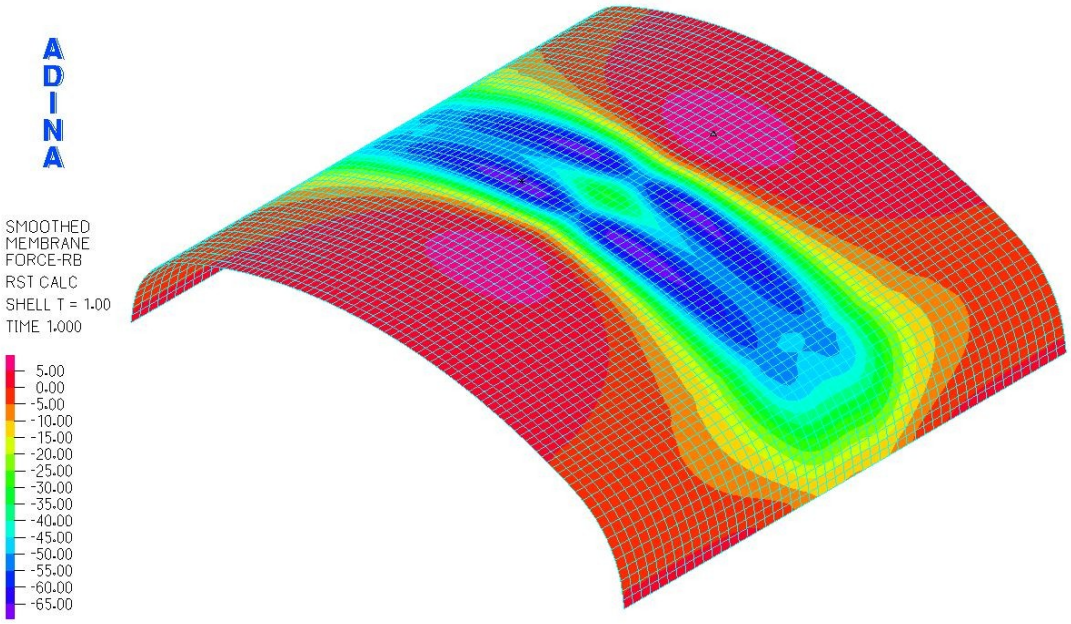

Figure 7 – Contour plot of axial thrust, 0.75m backfill

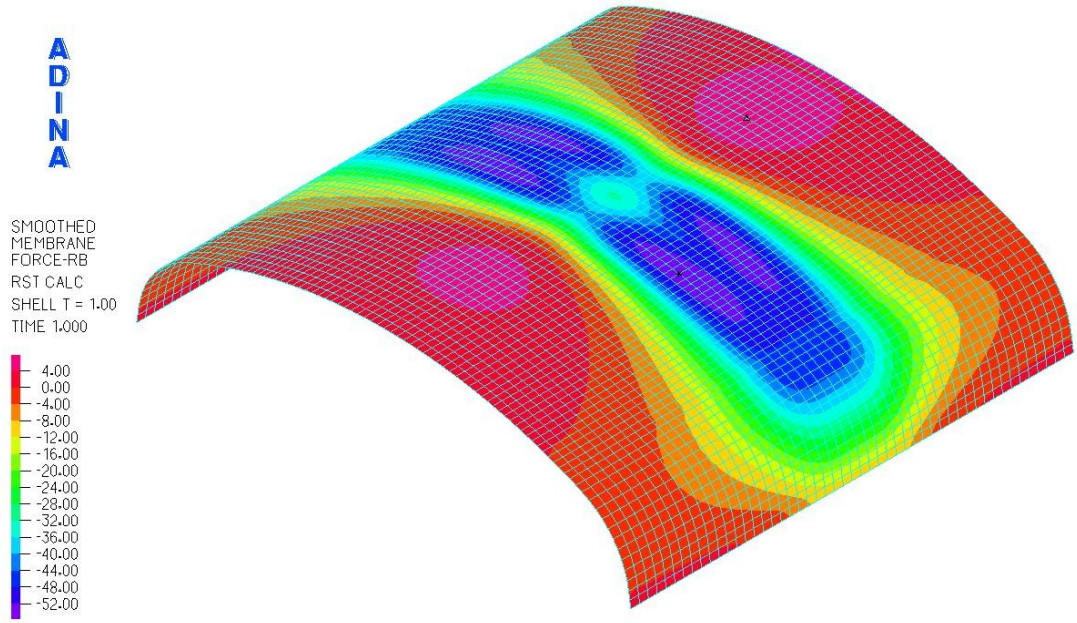

Figure 8 – Contour plot of axial thrust, 1.05m backfill

3. Vertical Displacement:

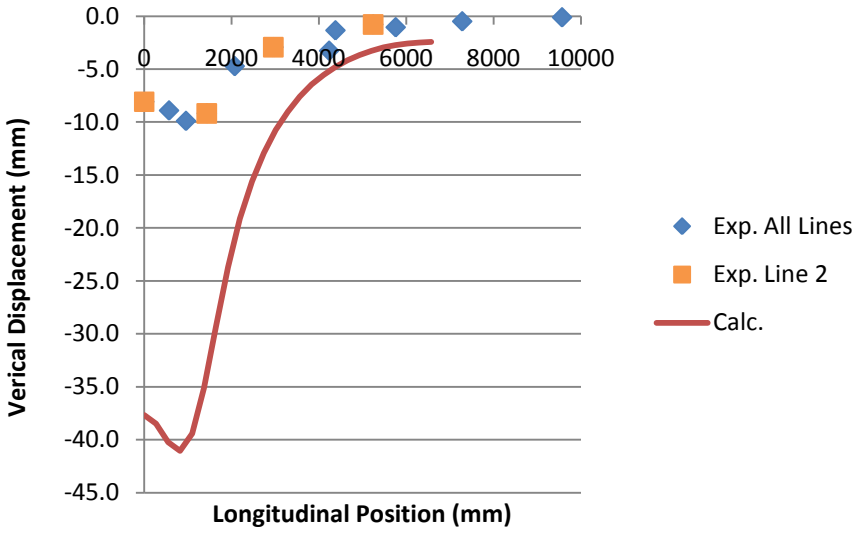

Figure 9 - Longitudinal vertical displacement profile, 0.45m backfill

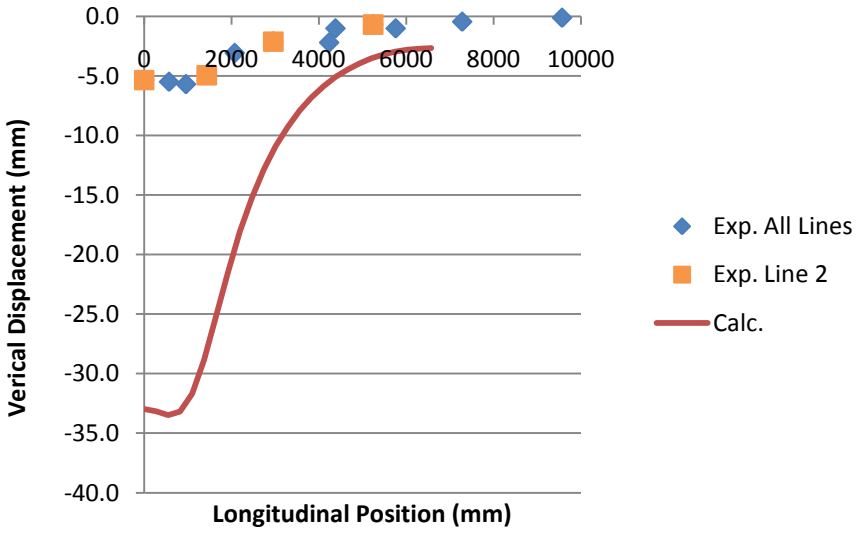

Figure 10 - Longitudinal vertical displacement profile, 0.75m backfill

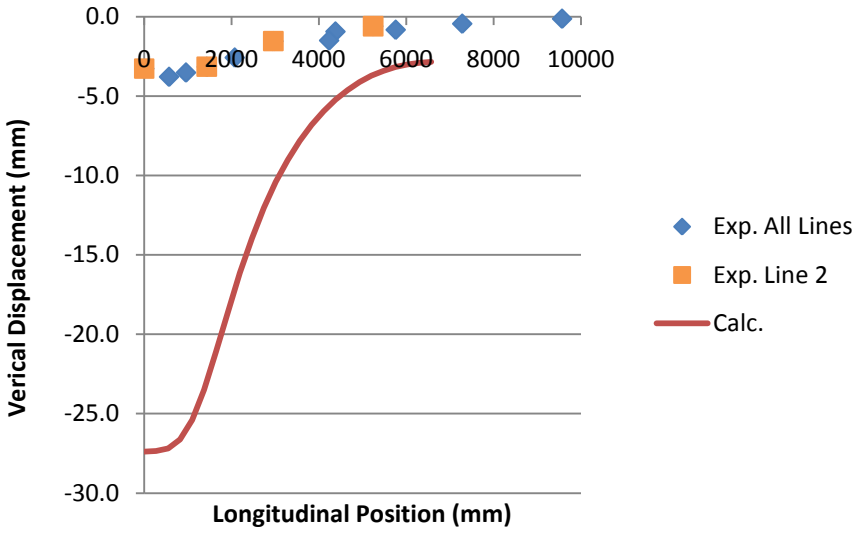

Figure 11 - Longitudinal vertical displacement profile, 1.05m backfill

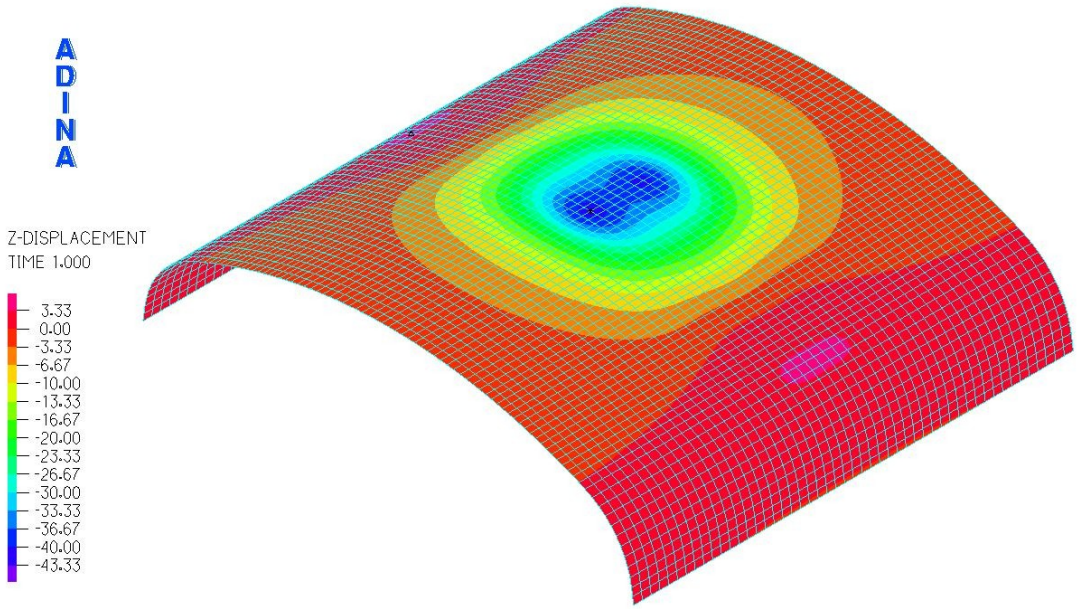

Figure 12 – Contour plot of vertical displacement, 0.45m backfill

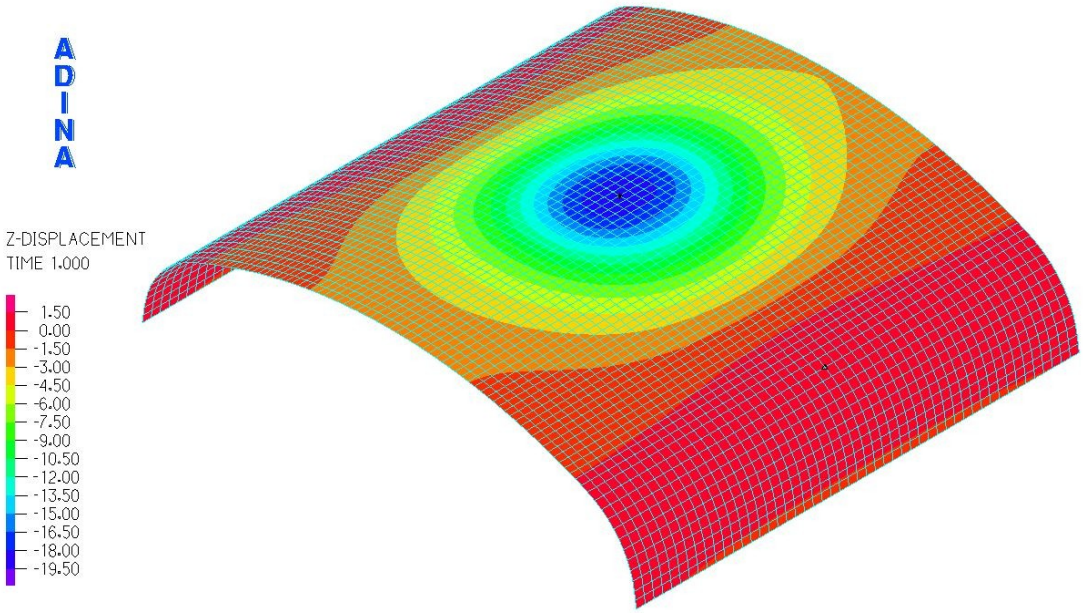

Figure 13 – Contour plot of vertical displacement, 1.55m backfill

4. Strain:

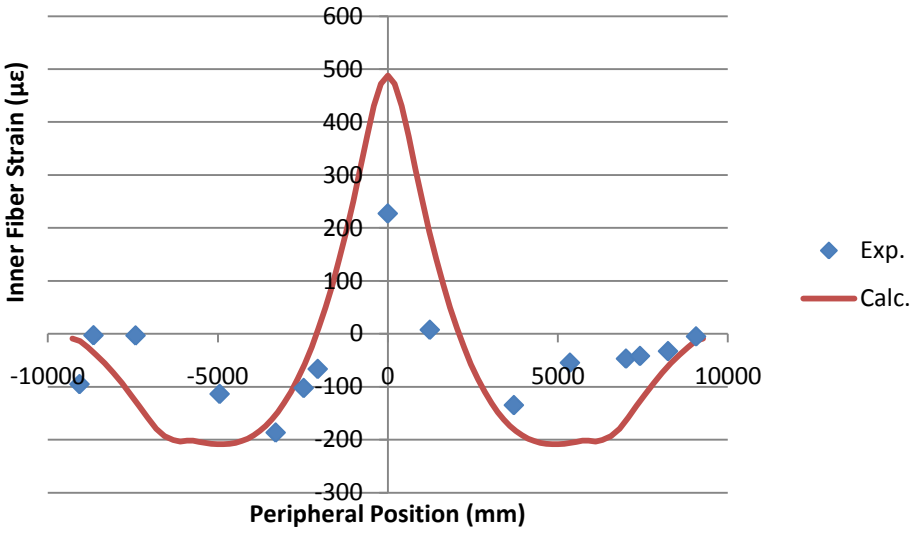

Figure 14 - Inner fiber strains around periphery of structure, 0.45m backfill

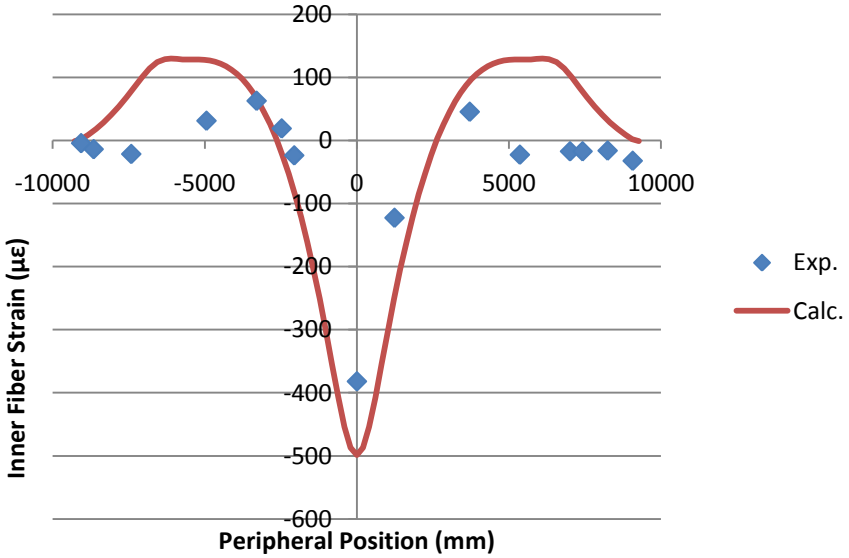

Figure 15 - Outer fiber strains around periphery of structure, 0.45m backfill

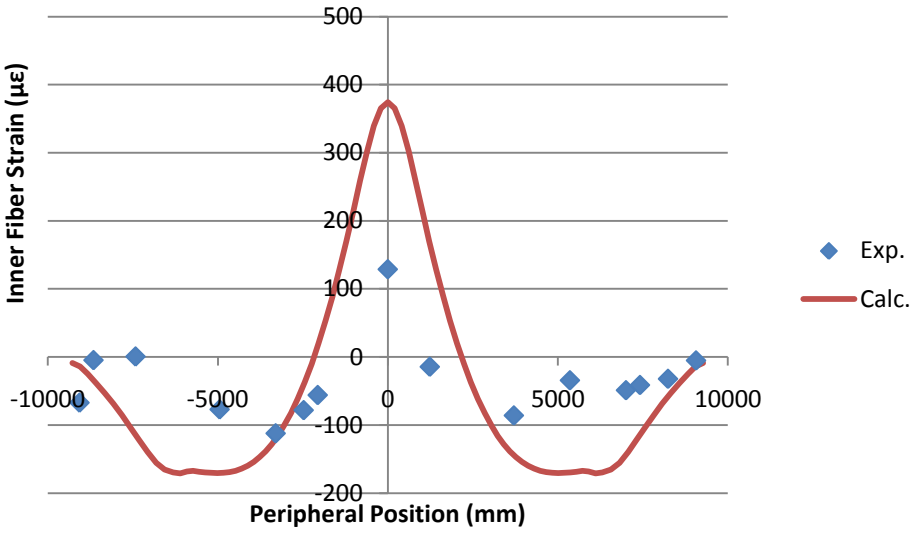

Figure 16 - Inner fiber strains around periphery of structure, 0.75m backfill

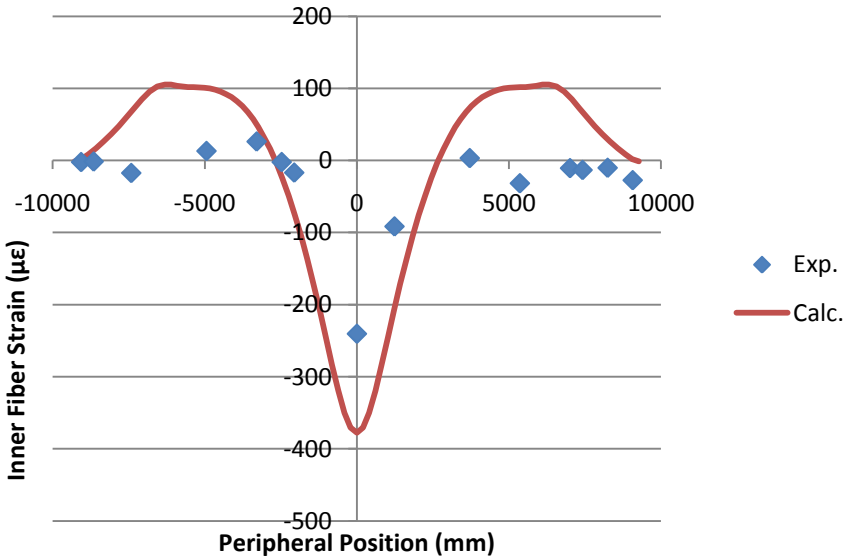

Figure 17 - Outer fiber strains around periphery of structure, 0.75m backfill

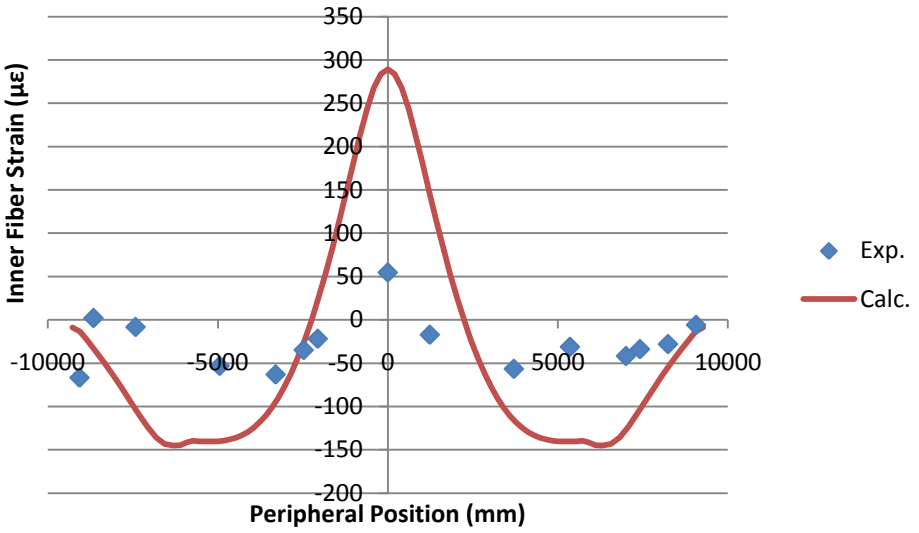

Figure 18 - Inner fiber strains around periphery of structure, 1.05m backfill

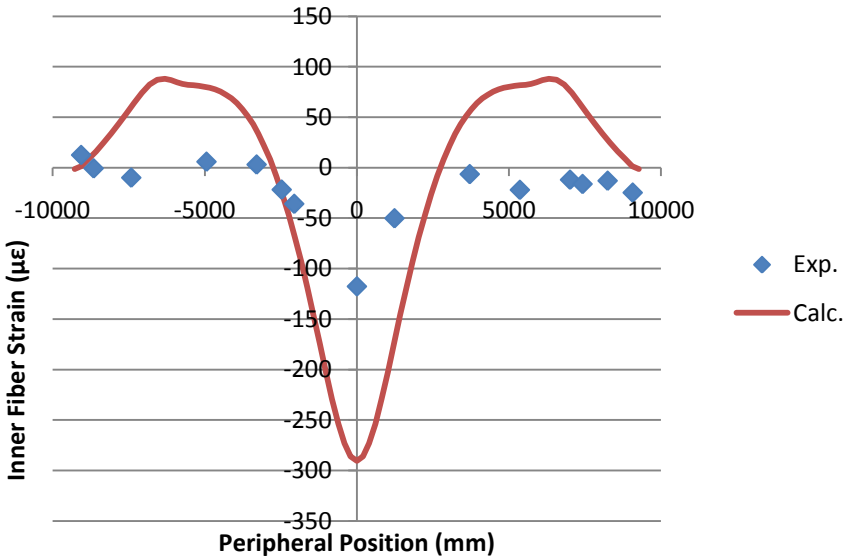

Figure 19 - Inner fiber strains around periphery of structure, 1.05m backfill

5. Soil Stresses

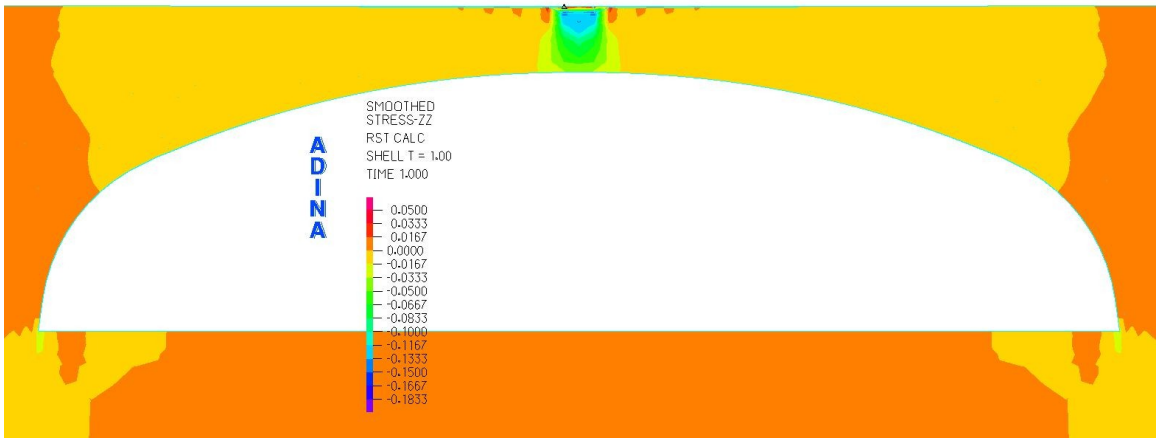

Figure 20 – Vertical soil stresses, transverse section, 0.75m backfill

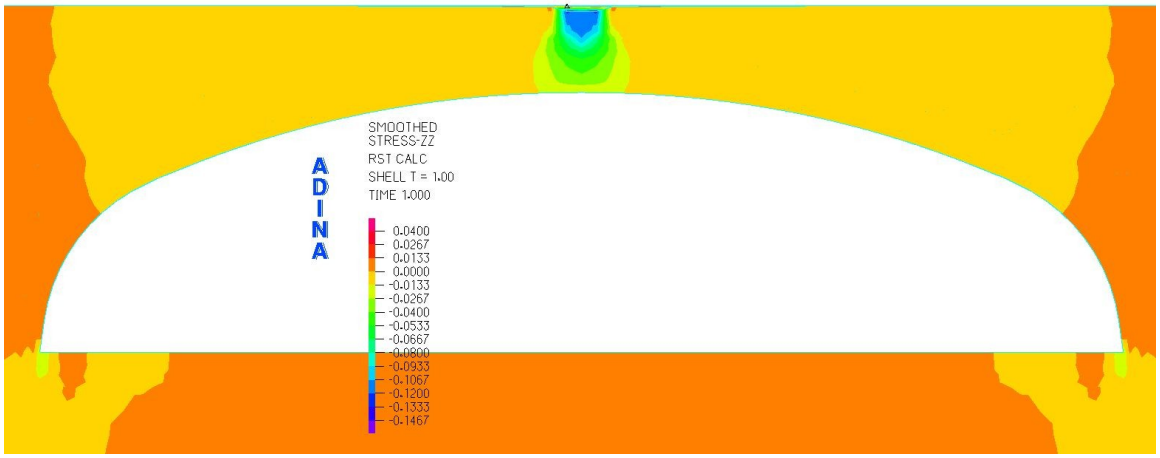

Figure 21 – Vertical soil stresses, transverse section, 1.05m backfill

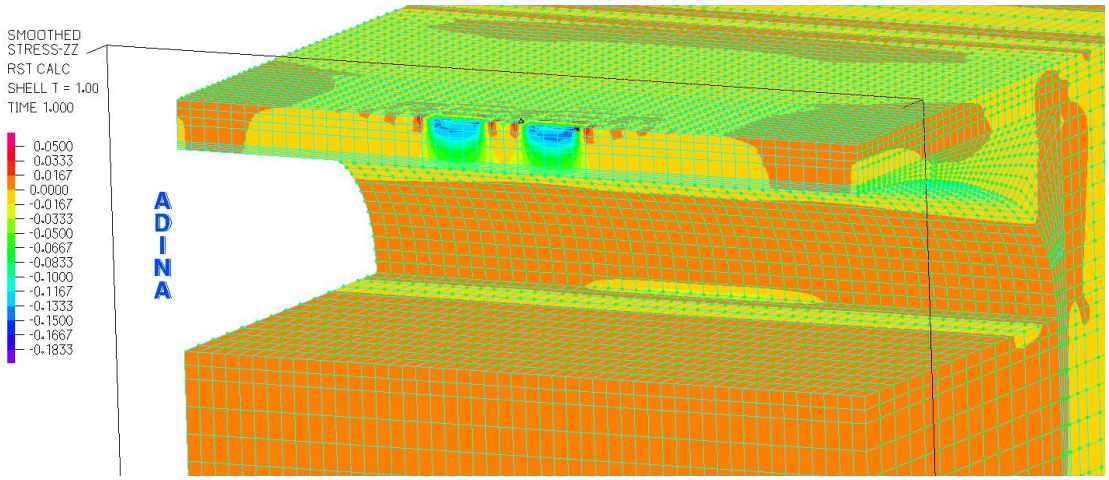

Figure 22 – Vertical soil stresses, longitudinal section, 0.75m backfill

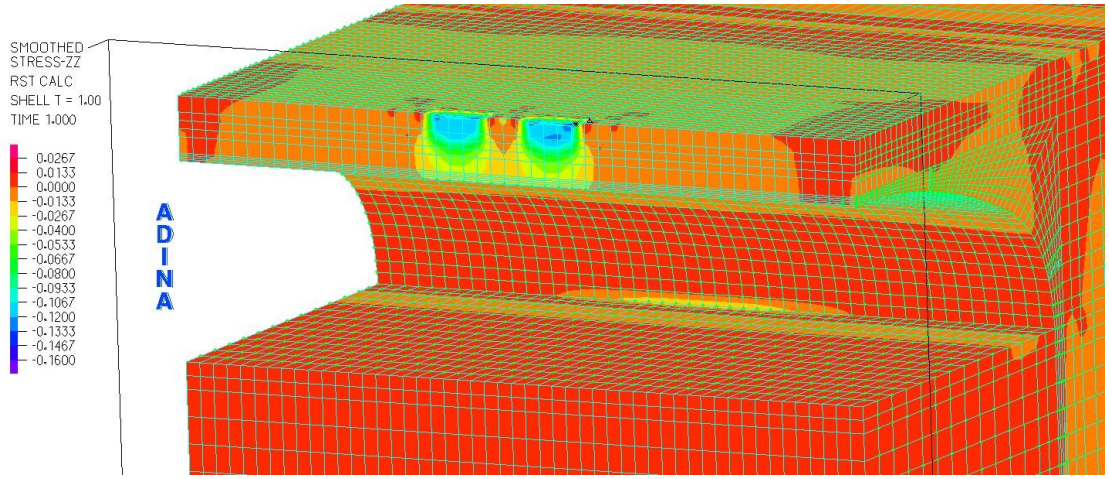

Figure 23 – Vertical soil stresses, longitudinal section, 1.05m backfill